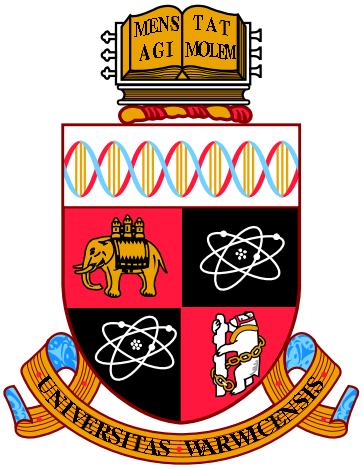

3D atmospheric models of helium-dominated atmosphere white dwarfs

by

Elena Cukanovaite

Thesis

Submitted to the University of Warwick

for the degree of

Doctor of Philosophy

Department of Physics

September 2020

Contents

List of Tables **v**

List of Figures **viii**

Acknowledgments **xx**

Declarations **xxi**

Abstract **xxii**

Chapter 1 Introduction **1**

1.1 Formation of a white dwarf 1

1.1.1 Protostar and the Main-Sequence 1

1.1.2 Red giant branch 3

1.1.3 Horizontal branch 5

1.1.4 Asymptotic giant branch 5

1.1.5 Formation of hydrogen-deficient white dwarfs 7

1.2 Composition of a white dwarf 8

1.2.1 Atmosphere 10

1.3 White dwarf evolution 14

1.3.1 Pre-white dwarf and gravitational contraction 15

1.3.2 Neutrino cooling 16

1.3.3 Convection 17

1.3.4 Pulsating white dwarfs 18

1.3.5 Crystallisation 18

1.3.6 Convective core coupling 19

1.3.7 Debye cooling 21

1.3.8 Remnant planetary systems 21

1.4 Atmospheric modelling 23

1.4.1 Radiative energy transport . . . 25
1.4.2 Temperature stratification . . . 26
1.4.3 Opacity . . . 27
1.4.4 Pressure stratification . . . 32
1.4.5 Convection . . . 33
1.4.6 Synthetic spectra . . . 36
1.5 Thesis layout . . . 40

Chapter 2 Methodology **41**
2.1 1D ATMO code . . . 41
2.1.1 Microphysics . . . 44
2.1.2 Line broadening . . . 45
2.2 3D CO^{5}BOLD code . . . 47
2.2.1 Hydrodynamics equations . . . 49
2.2.2 Boundaries . . . 50
2.2.3 Input and numerical parameters . . . 51
2.2.4 The equation of state . . . 52
2.2.5 Opacity binning . . . 52
2.2.6 Considerations in time . . . 54
2.2.7 Radiative transfer equation . . . 54
2.2.8 Average stratifications . . . 54
2.3 1D LHD code . . . 55
2.4 The Spectroscopic Technique . . . 55
2.5 Spectroscopic parallax . . . 56

Chapter 3 Spectroscopic 3D DB corrections **58**
3.1 Introduction . . . 58
3.2 Model atmospheres . . . 61
3.2.1 Numerical setup for CO^{5}BOLD simulations . . . 61
3.2.2 Input microphysics and 1D LHD code . . . 63
3.2.3 3D effects on atmospheric structures . . . 69
3.3 Model spectra . . . 76
3.3.1 Effect of opacity binning . . . 77
3.3.2 Mean 3D approximation . . . 78
3.4 Discussion . . . 81
3.4.1 3D corrections . . . 81
3.4.2 Sensitivity to input parameters . . . 89
3.4.3 Application to observations . . . 91

3.5 Conclusions . . . 93

Chapter 4 Spectroscopic 3D DBA corrections 94
4.1 Introduction . . . 94
4.2 Numerical setup . . . 97
4.2.1 3D atmospheric models . . . 97
4.2.2 1D atmospheric models . . . 98
4.2.3 3D synthetic spectra . . . 99
4.3 3D DBA corrections . . . 100
4.3.1 Fitting code . . . 100
4.3.2 Line cores . . . 102
4.3.3 3D correction function . . . 104
4.4 Discussion . . . 111
4.4.1 van der Waals line broadening . . . 116
4.4.2 Non-ideal effects . . . 121
4.4.3 Comparison between He- and H-atmosphere white dwarfs . . . 122
4.5 Conclusions . . . 126

Chapter 5 MLT parameter calibration for 3D DB and DBA white dwarfs 128
5.1 Introduction . . . 128
5.2 Numerical setup . . . 131
5.2.1 3D atmospheric models . . . 131
5.2.2 1D envelope models . . . 132
5.3 The convection zone . . . 136
5.4 The calibration method . . . 141
5.4.1 Closed bottom models . . . 141
5.4.2 Open bottom models . . . 144
5.5 Discussion . . . 147
5.5.1 Calibration of the entropy jump . . . 149
5.5.2 Calibration of the maximum convective flux . . . 152
5.5.3 Calibration of velocities . . . 153
5.5.4 Impact of metals on size of the convection zone . . . 154
5.6 Summary . . . 157

Chapter 6 Summary 160
6.1 3D spectroscopic corrections . . . 160
6.2 3D MLT calibration . . . 161

6.3 Future work 163

Appendix A Python 3D DBA spectroscopic correction functions 165

Appendix B Additional information on 3D DBA models 168

List of Tables

1.1 The Balmer series of hydrogen spectral lines. Data taken from Reader et al. [1980] 39
1.2 The optical He I lines. Data taken from Martin [1960] and Martin [1987]. 40

3.1 Selected parameters of the pure-helium 3D model atmospheres. The effective temperature is calculated from the spatially and temporally averaged emergent stellar flux and $\delta I_{\rm rms}/\langle I\rangle$ is the relative bolometric intensity contrast. 64
3.2 Our proposed 3D corrections for surface gravity and effective temperature derived from $\langle$3D$\rangle$ structures. A negative value indicates that 1D overestimates the parameter, while a positive value indicates underestimation. 83

4.1 The fitted coefficients of the 3D correction functions described in Eqs. 4.4 and 4.5. 108
4.2 The fitted coefficients of the van der Waals correction functions described in Eqs. 4.7, 4.8 and 4.9 119

5.1 Change in the convection zone mass from addition of metals (DBAZ) in a helium-rich DBA white dwarf. The DBAZ models use the metal abundances of SDSS J073842.56+183509.06 determined by Dufour et al. [2012]. 157

B.1 Select parameters of the 3D DB model atmospheres, where $\delta I_{\rm rms}/\langle I\rangle$ is the relative bolometric intensity contrast averaged over space and time. 169
B.2 Select parameters of 3D DBA model atmospheres with $\log {\rm H/He} = -7$. 171
B.3 Select parameters of 3D DBA model atmospheres with $\log {\rm H/He} = -5$. 172

B.4 Select parameters of 3D DBA model atmospheres with $\log \mathrm{H/He} = -4$. 173
B.5 Select parameters of 3D DBA model atmospheres with $\log \mathrm{H/He} = -3$. 174
B.6 Select parameters of 3D DBA model atmospheres with $\log \mathrm{H/He} = -2$. 175
B.7 MLT calibration for open bottom 3D DB models, where 3D s_{env} is the 3D adiabatic entropy used for calibration, ML2/α_{S} is the calibrated ML2/α value for Schwarzschild boundary, $\log(M_{\mathrm{CVZ}}/M_{\mathrm{tot}})_{\mathrm{S}}$ is $\log(M_{\mathrm{CVZ}}/M_{\mathrm{tot}})$ for Schwarzschild boundary, $(\log T_{\mathrm{b}})_{\mathrm{S}}$ is the 1D calibrated temperature at the Schwarzschild boundary, $(\log P_{\mathrm{b}})_{\mathrm{S}}$ is the 1D calibrated pressure at the Schwarzschild boundary. The same parameters are also given for the flux boundary and are denoted by subscript 'f'. 176
B.8 Same as Tab. B.7 but for MLT calibration of open bottom 3D DBA models with $\log \mathrm{H/He} = -7$. 177
B.9 Same as Tab. B.7 but for MLT calibration of open bottom 3D DBA models with $\log \mathrm{H/He} = -5$. 178
B.10 Same as Tab. B.7 but for MLT calibration of open bottom 3D DBA models with $\log \mathrm{H/He} = -4$. 179
B.11 Same as Tab. B.7 but for MLT calibration of open bottom 3D DBA models with $\log \mathrm{H/He} = -3$. 180
B.12 Same as Tab. B.7 but for MLT calibration of open bottom 3D DBA models with $\log \mathrm{H/He} = -2$. 181
B.13 MLT calibration for closed bottom 3D DB models, where $\langle 3\mathrm{D}\rangle$ $T_{\mathrm{b,\,S}}$ is the $\langle 3\mathrm{D}\rangle$ temperature at the bottom of the Schwarzschild boundary, $\langle 3\mathrm{D}\rangle$ $P_{\mathrm{b,\,S}}$ is the $\langle 3\mathrm{D}\rangle$ pressure at the bottom of the Schwarzschild boundary, ML2/α_{S} is the calibrated ML2/α value for the Schwarzschild boundary and $\log(M_{\mathrm{CVZ}}/M_{\mathrm{tot}})_{\mathrm{S}}$ is the $\log(M_{\mathrm{CVZ}}/M_{\mathrm{tot}})$ for the Schwarzschild boundary. The same parameters are also given for the flux boundary and are denoted with a subscript 'f'. 181
B.14 Same as Tab. B.13 but for MLT calibration of closed bottom 3D DBA models with $\log \mathrm{H/He} = -7$. 182
B.15 Same as Tab. B.13 but for MLT calibration of closed bottom 3D DBA models with $\log \mathrm{H/He} = -5$. 182
B.16 Same as Tab. B.13 but for MLT calibration of closed bottom 3D DBA models with $\log \mathrm{H/He} = -4$. 182
B.17 Same as Tab. B.13 but for MLT calibration of closed bottom 3D DBA models with $\log \mathrm{H/He} = -3$. 183

B.18 Same as Tab. B.13 but for MLT calibration of closed bottom 3D DBA models with $\log \mathrm{H/He} = -2$. 183

List of Figures

1.1 Experimental and theoretical initial mass functions for the Pleiades cluster. The theoretical initial mass functions for single and binary stars are shown in short-dashed and long-dashed lines, respectively. The squares, triangles and circles are data for the Pleaides cluster from three separate studies indicated in Chabrier [2003]. This figure illustrates the preference for formation of lower mass stars which occurs as a result of the process of fragmentation of the molecular cloud. Reproduced from Chabrier [2003]. 2

1.2 A typical Hertzsprung-Russell diagram following the evolution of $1M_{\odot}$ and $5M_{\odot}$ main sequence stars in terms of their luminosity and effective temperature. Adapted from Iben [1991]. 4

1.3 The mass distributions for DA and DB/DBA white dwarf samples are shown as black and red histograms, respectively. The DA and DB/DBA white dwarf samples are from Gianninas et al. [2010] and Rolland et al. [2018], respectively. The mean masses and their standard deviations are indicated on the plot. Adapted from Tremblay et al. [2019b]. 9

1.4 The typical elemental composition of a hydrogen-rich white dwarf with $T_{\rm eff}$= 12 000 K and mass of $0.56M_{\odot}$. Each coloured line represents a different element. The y-axis is the fractional abundance of the element and x-axis is the outer mass fraction, where M_r is the mass from the surface to a given depth, r, in the structure of the white dwarf and $M_{\star}$ is the total mass of the white dwarf. The explanations for the observed elemental abundances are given on the top of the plot. A He-rich white dwarf would have a much thinner outer hydrogen shell. Adapted from Córsico et al. [2019]. 11

1.5 Examples of different types of white dwarf spectra. The coloured lines indicate different types of spectral lines. In the case of DA white dwarfs the red dashes denote H lines, and for DB white dwarfs the green dashes mark the He I lines. DZ and DAZ spectra exhibit metal lines, in the examples shown here the blue dashes indicate calcium H and K lines, while the orange dash indicates the magnesium II line. The purple dashes identify the carbon Swan bands seen in DQ stars. The letter "H" is used to indicate white dwarf spectra that shows magnetic features. In this example the DAH spectrum contains hydrogen Balmer lines which are split due to Zeeman effect. Reproduced from Manser [2018]. 13

1.6 A comparison between theoretical and observational luminosity functions of white dwarfs. Open circles are observations from Liebert et al. [1988] and the solid line is the theoretical luminosity function of Iben and Laughlin [1989]. Luminosity can be used as a proxy for the age of the white dwarf. The number of white dwarfs in a given luminosity bin informs the time spent at a given luminosity. Several of the important stages in white dwarf evolution are indicated on the plot. Adapted from Koester and Chanmugam [1990]. 15

1.7 The luminosity as a function of effective temperature for DA white dwarf structures. Each separate thin line illustrates the evolution of a white dwarf with different total mass, starting from the top (right) line which is for a $0.4M_{\odot}$ white dwarf all the way down to the bottom line which is for a $1.2M_{\odot}$ white dwarf. The thick black lines indicate isochrones of constant age. The age of each isochrone in Gyr is specified nearby. The open circles near the top left corner indicate the effective temperature at which neutrino cooling becomes less important than thermal cooling. The onset of convective core coupling is shown as open circles at lower luminosities. The filled black circles designate the onset of crystallisation in the core of the white dwarf. This plot shows that for higher mass white dwarfs convective core coupling occurs later in the evolution than crystallisation, whereas for low mass white dwarfs the opposite is true. Reproduced from Fontaine et al. [2001]. 20

1.8 A schematic of limb darkening in stars. The line of sight of the observer is indicated by the black arrows. The observed photons are generated at $\tau_\lambda = 2/3$, where τ_λ is the optical depth at given wavelength, λ. However, this optical depth does not correspond to the same geometric depth. The photons travelling near the center of the disk (arrow a) come from a deeper atmospheric layer where temperature is higher and thus the disk appears brighter. Photons travelling near the limb (arrow b) come from a geometrically shallower depth, where temperature is lower and thus the limb appears darker. 24

1.9 The opacity as a function of wavelength for a DA white dwarf with $\log g = 8.0$ and $T_{\rm eff} = 13\,000$ K. The units of the variables are in cgs. Each opacity source is detailed in the label. The optical range is highlighted with the use of grey dashed lines. The opacity is heavily dominated by the hydrogen bound-free absorption and hydrogen spectral lines. 31

1.10 The opacities as a function of wavelength for a DB white dwarf with $\log g = 8.0$ and $T_{\rm eff} = 18\,000$ K. The units of the variables are in cgs. Each opacity source is detailed in the label. The optical range is highlighted with the use of grey dashed lines. The opacity is heavily dominated by the He I bound-free absorption and helium spectral lines. 32

2.1 An example of a box-in-a-star (local) model of the Sun's photosphere. It shows the convective granulation cells on the surface as emergent grey intensity (units of erg cm^{-}2 s^{-2}). On the sides of the box the convective down-drafts which extend from the upper layers are shown in units of entropy. Adapted from Freytag et al. [2002]. 48

2.2 An example of a star-in-a-box (global) simulation of a grey atmosphere of a mini-Sun, where the radius was artificially decreased to obtain a manageable number of convective cells at the surface. The entirety of the atmosphere is modelled in this case. Adapted from Freytag et al. [2002]. 48

3.1 The effective temperatures and surface gravities of our 3D model atmospheres with pure-helium compositions. Open and filled circles denote models with bottom boundaries that are open and closed to convective flows, respectively. 62

3.2 The total opacity as a function of the logarithm of wavelength for representative layers of two BW11 models with $\log g = 8.0$ at $T_{\rm eff} = 14\,000$ K (left) and $T_{\rm eff} = 34\,000$ K (right). We have selected reference temperature and pressure values (as indicated on the panels) that correspond to the plasma conditions at $\tau_{\rm R} = 1$. He I and He II line opacities are indicated by green and red colour regions. The Rosseland mean opacity (dashed grey) and the line region used for the derivation of the 3D corrections (dotted grey) are also shown. 65
3.3 Atmospheric line forming regions for 1D ATMO (solid red) and $\langle$3D$\rangle$ (dashed blue) spectra as defined by $\tau_{\rm R}(\tau_\nu = 1)$, where the plasma becomes optically thin for photons of frequency ν. 66
3.4 Temperature stratifications of spectral line forming regions for $\langle$3D$\rangle$ (dashed blue), 1D ATMO (dot-dashed red) and 1D LHD (dotted green) models. The line forming region is approximated by the grey vertical lines which represent the minimum and maximum $\tau_{\rm R}(\tau_\nu = 1)$ values in the range 3500 Å and 7200 Å according to Fig. 3.3. The black vertical lines represent the line forming region if the wavelengths that are within 0.5 Å of the line cores are ignored. The bottom boundaries do not change under this definition and therefore overlap with the grey lines. 67
3.5 Similar to Fig. 3.4 but for density stratifications of spectral line forming regions for $\langle$3D$\rangle$, 1D ATMO and 1D LHD models. 68
3.6 Entropy stratifications for 1D LHD (solid red) and $\langle$3D$\rangle$ (dashed blue) models with $\log g = 8.0$. All structures, apart from $T_{\rm eff} = 12020$ K, are offset from each other by 0.1×10^9 erg g^{-1} K^{-1} for clarity. 69
3.7 Temperature stratifications for 1D LHD (solid red) and $\langle$3D$\rangle$ (dashed blue) models with $\log g = 8.0$. All structures, apart from $T_{\rm eff} = 12020$ K, are offset from each other by 3000 K for clarity. 70
3.8 Bolometric emergent intensity for selected models with $\log g = 8.0$. The effective temperatures, surface gravities and intensity contrasts of the simulations are shown in the legends. The length of the bar on the top right of each panel is ten times the pressure scale height at $\langle\tau_{\rm R}\rangle = 1$. 72
3.9 The ratio of the characteristic granule size to the pressure scale height at $\langle\tau_{\rm R}\rangle = 1$ as a function of logarithm of the Mach number at $\langle\tau_{\rm R}\rangle = 1$ for 3D DB (filled circles) and 3D DA (unfilled circles) models. 73

3.10 Bolometric intensity contrast as a function of effective temperature for the pure-helium 3D model atmospheres. The points representing intensity contrasts for the same surface gravity are connected for clarity. 75
3.11 Bolometric intensity contrast as a function of the logarithm of the Mach number at $\langle \tau_{\rm R} \rangle = 1$ for our pure-helium 3D model atmospheres (filled circles) and the 3D DA atmospheres of Tremblay et al. [2013a, open circles]. 76
3.12 Fits of synthetic spectra based on 1D LHD structures with $\log g = 8.0$ that have been computed with two types of opacity tables: original (10 bins, solid red) and extended (16-20 bins, dashed blue). These model spectra were fitted with a grid of standard 1D ATMO spectra of BW11 to quantify the differences between the two types of 1D codes. The resulting effective temperature and surface gravity corrections are presented on the left and right panels, respectively. The external observational uncertainties of BW11 are also shown with dotted green lines. A dot-dashed horizontal black line representing a null correction has also been added to each panel for clarity. 78
3.13 1.5D and $\langle$3D$\rangle$ spectra with $\log g = 8.0$ are compared in terms of the differences between their respective effective temperatures (left panel) and surface gravities (right panel) corrections found by fitting the two types of spectra with the 1D LHD models. External fitting uncertainties from BW11 are also shown. A dot-dashed horizontal black line representing the equivalence of 1.5D and $\langle$3D$\rangle$ corrections (and therefore spectra) has also been added to each panel. 80
3.14 Proposed 3D corrections for pure-helium white dwarf atmospheres when compared with 1D model spectra using the ML2/α = 1.25 parameterisation. The horizontal dashed lines indicate $\log g = [7.5, 8.0, 8.5, 9.0]$, whereas the intersections between the dashed lines and the blue lines are the reference 1D atmospheric parameters. If one follows a given blue line from the intersection, its length will give the 3D correction for the particular 1D effective temperature and surface gravity. For clarity, at high effective temperatures some of the corrections from Table 3.2 are not shown. This figure can be compared to 3D DA corrections from Tremblay et al. [2015a]. 82
3.15 Comparison of 1D LHD (solid red), 1.5D (dotted green) and $\langle$3D$\rangle$ (dashed blue) spectra at $T_{\rm eff} = 18\,081$ K and $\log g = 8.0$. The spectra have been normalised at 2400 Å. 88

3.16 Comparison of a ⟨3D⟩ (dashed blue) spectrum and 1D LHD spectra computed with ML2/α = 1.25 (solid red) and 1.75 (dotted green) for $T_{\rm eff}$ = 21 989 K and $\log g = 8.0$. The spectra have been normalised at 2400 Å. 89
3.17 The temperature and pressure stratifications of the original (solid blue) and extended (dashed red) simulations for models with $\log g$ = 8.0 and $T_{\rm eff} \approx$ 12 000 and 18 100 K. The spectral line forming regions are indicated by solid grey lines. Note that the 3D simulations extend deeper into the upper layers than shown here. 91
3.18 Examples of 1D LHD (top panel) and ⟨3D⟩ (bottom panel) fits to the spectrum of the DB white dwarf WD 0845−188. The continuum flux is fixed to unity by a fitting function at predefined wavelength points shown as green tick marks in the panels (see BW11). The best fit atmospheric parameters assuming a pure-helium composition are identified on the panels. 92

4.1 The atmospheric parameters of 3D DB and DBA models averaged over time and over contours of constant $\log \tau_{\rm R}$. 3D simulations with open and closed bottom boundaries are indicated as unfilled and filled circles, respectively. The hydrogen abundance of the models is indicated on each individual sub plot. 98
4.2 A comparison between the synthetic H_α and H_β lines calculated from 3D, 1D ATMO and 1D LHD models for a DBA white dwarf with $\log$ H/He = −2.0, $\log g = 8.0$ and $T_{\rm eff}$ = 12 044 K. The ⟨3D⟩ synthetic lines are shown in solid orange, 1D ATMO in dashed green and 1D LHD in dotted red. The center of a given line is indicated by a vertical dot-dashed blue line. 103
4.3 The difference between the effective temperature corrections derived from original spectra and from spectra with line cores removed for 3D DBA models with $\log$ H/He = −2.0. The $\log \tau_{\rm R}$ values indicated on each sub plot denote the atmospheric layer above which we remove any flux formed. The difference in corrections for models with $\log g$ = 7.5, 8.0, 8.5 and 9.0 are shown as orange circles, green triangles, red stars and blue diagonal crosses, respectively. Corrections for each surface gravity are joined for clarity. The errors from Genest-Beaulieu and Bergeron [2019b] are shown in dotted black. 104

4.4 A comparison between the results of the correction functions and the 3D DBA corrections for the grid with $\log \mathrm{H/He} = -5$. 3D corrections for models with $\log g = 7.5$, 8.0, 8.5 and 9.0 are shown as orange circles, green triangles, red stars and blue diagonal crosses, respectively. The results of the correction functions for models with $\log g = 7.5$, 8.0, 8.5 and 9.0 are shown as solid orange, dashed green, dotted red and dot-dashed blue lines, respectively. 109
4.5 3D correction functions for surface gravity shown for all hydrogen abundances, surface gravities and effective temperatures covered by our study. Dotted black lines represent the observational errors from Genest-Beaulieu and Bergeron [2019b]. In solid orange, dashed green, dotted red and dot-dashed blue we show the surface gravity corrections for $\log g = 7.5$, 8.0. 8.5 and 9.0 values, respectively. The abundances are indicated on each sub plot. 110
4.6 Same as Fig. 4.5, but for 3D effective temperature corrections. 111
4.7 A comparison between the *Gaia* parallaxes and the parallaxes derived from spectroscopic parameters without (top panel) and with (bottom panel) 3D DB and DBA corrections for the Genest-Beaulieu and Bergeron [2019b] SDSS sample. The orange filled circles represent fractional difference between the observed and theoretical parallax, ϖ, and in light grey we show the error on the difference. The dotted black line illustrates a perfect agreement. The running median of the fractional difference in bins of 1000 K is shown in dashed green. The block-coloured green area indicates the 95% confidence limit of the median, which has been calculated using bootstrapping. 113

4.8 A comparison between the spectroscopically- and photometrically-determined effective temperatures for the Genest-Beaulieu and Bergeron [2019b] sample. The spectroscopic parameters have been computed without (top panel) and with (bottom panel) 3D effective temperature corrections taken in to account. The photometric parameters are from Gentile Fusillo et al. [2019a]. They are calculated based on *Gaia* data alone and include a reddening correction. The orange filled circles represent the fractional difference between the spectroscopic and photometric effective temperatures, and the error on the difference is shown in light grey. The dotted black line illustrates a perfect agreement. The running median of the fractional difference in bins of 1000 K is shown in dashed green. The block-coloured green area indicates the 95% confidence limit on the median. 115
4.9 Similar to Fig. 4.8 but for spectroscopically- and photometrically-determined surface gravities. 116
4.10 The corrections between two types of van der Waals line broadening. The intersections of the light grey lines denote the atmospheric parameters determined using the adapted Deridder and van Rensbergen [1976] broadening. The coloured lines which extend from the intersections indicate the size of the correction. The end-point away from the intersection gives the values of the corresponding atmospheric parameters when Unsold [1955] broadening is used. The colours of the lines represent the hydrogen abundance correction, which are omitted for very low hydrogen abundances. 118
4.11 A comparison between the spectroscopically and photometrically-derived surface gravities corrected for van der Waals broadening only (top plot) and corrected both for van der Waals broadening and 3D effects (bottom plot). Solid orange circles represent the difference in surface gravities with errors shown in light grey. The running median in bins of 1000 K is shown in dashed green, with the 95% confidence limit being represented by the green colour blocked area. For reference, the dotted black line illustrates a one-to-one agreement. 120

4.12 The corrections in surface gravity and effective temperature arising from varying the value of the multiplying factor to the Bohr radius, $r_{\rm B}$, in the Hummer and Mihalas [1988] non-ideal gas theory with respect to the standard value of 0.5. In solid orange, dotted green and dashed red we show the corrections for $r_{\rm B} = 1.0$, 0.75 and 0.25, respectively. The hydrogen abundance is indicated on each sub plot. 122
4.13 A comparison between the effective temperatures derived using spectroscopic and *Gaia* photometric observations for samples of DA and DB/DBA white dwarfs. The median fractional difference of each sample was plotted in bins of 2000 K for $T_{\rm eff} \leq 20\,000$ K and of 5000 K above that temperature. The difference in effective temperatures for the SDSS DA sample of Tremblay et al. [2019b], with spectroscopic S/N > 20 and 3D corrections, is shown in dashed orange. The dashed green curve corresponds to the DA sample of Gianninas et al. [2011] with 3D corrections (see Tremblay et al. 2019b for the comparison with *Gaia*). In dashed red and dashed blue the difference is shown for the SDSS DB/DBA sample of Genest-Beaulieu and Bergeron [2019b] and the DB/DBA sample of Rolland et al. [2018], respectively, both corrected for 3D effects presented in this work. The Genest-Beaulieu and Bergeron [2019b] sample is also corrected for Unsold [1955] van der Waals broadening (using corrections from Section 4.4.1), while Rolland et al. [2018] is already using this type of line broadening. The coloured areas represent the corresponding 95% confidence limit on the medians calculated using bootstrapping. The dashed black line indicates a perfect agreement between spectroscopy and photometry. 123
4.14 Same as Fig. 4.13 but for a comparison between the surface gravities derived using spectroscopic and *Gaia* photometric observations for samples of DA and DB/DBA white dwarfs. 126

5.1 The abundances, surface gravities and effective temperatures of the 3D models presented in this paper. Open and filled circles denote the models with open and closed bottom boundaries, respectively. 132

5.2 The specific entropy at the bottom of the convection zone defined by the Schwarzschild criterion as a function of effective temperature for 3D DB open (open circles) and closed (filled circles) bottom models, and for 1D DB envelopes with different values of the mixing length parameter. The value of the mixing length parameter decreases by increments of 0.1 from the dark blue line (ML2/$\alpha = 1.4$) all the way up to the dark purple line (ML2/$\alpha = 0.4$). We show the 1D entropies with (solid lines) and without (dashed lines) partial degeneracy effects taken into account. The surface gravities of the models are indicated on the panels. 134
5.3 The fraction of the convection zone mass to the total mass of the white dwarf as a function of effective temperature for 3D DB models and 1D DB envelopes (solid lines) with different values of the mixing length parameter. The value of the mixing length parameter decreases by increments of 0.1 from the dark blue line (ML2/$\alpha = 1.4$) all the way up to the dark purple line (ML2/$\alpha = 0.4$). The Schwarzschild boundaries for the 3D open bottom models are indicated by open circles; filled circles represent the Schwarzschild boundary for closed bottom 3D models; open squares represent the flux boundary for closed bottom 3D models. 135
5.4 Same as Fig. 5.3, but for a DBA grid with $\log \mathrm{H/He} = -2.0$. 136
5.5 Entropy stratifications of two 3D closed bottom models with $\log g = 8.0$ and $\log \mathrm{H/He} = -10.0$ are shown as solid blue lines. The dashed black lines indicate the flux-forming region for wavelengths 3500 Å to 7200 Å, representing the atmosphere of the white dwarf in terms of visible light. 1D models calculated at calibrated ML2/α_{S} are shown as dashed red lines. According to the Schwarzschild criterion, at $T_{\mathrm{eff}} \approx 28\,000$ K there are two convectively unstable regions due to He I and He II ionization. The top and bottom of the first convective region is denoted by right- and left-pointing triangles, respectively. The second convective region is indicated by upward- and downward-pointing triangles. The two convective regions are separated by a small region which is convectively stable in terms of the Schwarzschild criterion. At $T_{\mathrm{eff}} \approx 34\,000$ K, according to the Schwarzschild criterion there is only one convective region (He II) left, which is denoted by the upward- and downward-pointing triangles. 139

5.6 The ratio of the convective-to-total flux as a function of the $\log \tau_{\rm R}$ for two 3D closed bottom models with $\log g = 8.0$ and $\log {\rm H/He} = -10.0$ is shown in solid blue. The upward- and downward-pointing triangles denote the top and bottom flux boundaries of the convection zone, respectively. The dashed black lines represent the flux-forming region for wavelengths 3500 Å to 7200 Å. Red dashed lines show the 1D models calculated at calibrated ML2/$\alpha_{\rm f}$, and green dotted lines show 1D models calculated at ML2/$\alpha_{\rm F_{max}}$ (see Sect. 5.5.2). Unlike the Schwarzschild boundary, at $T_{\rm eff} \approx 28\,000$ K the two convectively-unstable regions are inseparable in terms of the flux due to the dynamics of the downdrafts. Beyond the flux boundary, a region of negative flux related to convective overshoot is observed. 140

5.7 The logarithm of the temperature at the base of the convection zone as a function of effective temperature for DB white dwarfs. The solid lines are 1D envelope temperatures at the Schwarzschild boundary for varying values of the mixing length parameter. The value of the mixing length parameter decreases by increments of 0.1 from the dark blue line (ML2/$\alpha = 1.4$) all the way down to the dark purple line (ML2/$\alpha = 0.4$). The solid circles represent the temperature of closed bottom 3D models at the Schwarzschild boundary, the open squares are the temperatures of closed bottom 3D models at the flux boundary. The surface gravities are indicated on the plots. 142

5.8 Similar to Fig. 5.7 but for pressure at the base of the convection zone. 143

5.9 The spatially- and temporally- resolved entropy for 3D open bottom models with $\log g = 8.0$. The top two plots show the entropy stratification when only the He I convection is present, whereas the bottom two panels show models with both He I and He II convection zones. In green we plot the averaged entropy over constant geometric depth and time. Although the average entropy does not reach the adiabatic value near the bottom of the simulation, it is clear that the spatially- and temporally- resolved entropy has a plateau at deeper layers, which corresponds to the inflowing entropy, an input parameter of our 3D models. 146

5.10 The calibrated mixing length parameter based on the Schwarzschild boundary is plotted as solid colour points which are connected for clarity for the same surface gravity. The hydrogen abundance is indicated on each panel. 148

5.11 Same as Fig. 5.10 but for the flux boundary. 149
5.12 The calibrated mixing length parameter based on the entropy jump for open bottom 3D DB models. The solid colour points represent the ML2/$\alpha_{\rm s_{jump}}$ values and are connected for clarity based on their surface gravity. 151
5.13 Same as Fig. 5.12, but for calibration of the mixing length parameter based on the maximum convective flux for 3D closed bottom models. 153
5.14 The vertical root mean square velocity as a function of $\log \tau_{\rm R}$ at two different effective temperatures for DB models with $\log g = 8.0$. The $\langle$3D$\rangle$ $v_{z,\rm rms}$ is shown in solid blue. The 1D models with ML2/α = ML2/$\alpha_{\rm S}$ and ML2/$\alpha_{\rm f}$ are shown as dotted green and red dashed lines, respectively. The bottom of the Schwarzschild and flux boundaries are shown as downward- and upward-pointing triangles. The dashed black lines indicate the top and bottom of the optical light forming region. The 1D structures are unable to reproduce $\langle$3D$\rangle$ velocities especially outside the convective regions. In the upper layers ($\log \tau_{\rm R}<$ -3), the $\langle$3D$\rangle$ convective velocities have an important contribution from waves in the simulation. 155
5.15 Temperature stratification of 3D models with and without metals at two different effective temperatures. The $\langle$3D$\rangle$ structures for 3D DBAZ models are shown in solid blue, whereas the metal-poor 3D models are in plotted in solid red. 158

Acknowledgments

Ačiū Mamai ir Andriui už viską. Pati geriausia šeima pasaulyje! Myliu jus labai stripriai! Спасибо папа за все тоже.

I want to thank my partner Chris from the bottom of my heart for being so loving and supportive.

Thanks to everyone in the department for being so friendly and supportive. A huge thank you to Pier for being the best supervisor imaginable. My PhD brother Tim, thank you for all your help during the PhD, for all your fun stories and for the amazing Hawaii holiday! I want to thank my PhD little brother Jack for doing the best angry nerd impersonation and being a cool person. Thanks to the New Orleans crew: Matt Green, Matt Hoskin, Odette, Nicola and Mark. It was an awesome holiday! Ashley, Ry and James Jackman: you were the best people to start my PhD with! James Blake and Patrick, you guys made the back office bearable! George and Henry, thanks for being awesome older PhD students. A thanks to Sam and Tom for the best parties. Sabrina, thanks for being my MCR buddy and not making fun of my BTS obsession!

For my undegraduate friends who will never read this: Rabyah, Martin, Julian, DJ Hadden and David T, love you all.

And to my secondary school peeps: Anna, Wai Yee and Aarani.

Cheers,

Elena

Declarations

I have compiled this thesis and I am submitting it to the University of Warwick graduate school for the degree of Doctor of Philosophy. It has not been submitted to any other university.

A large amount of work in this thesis has been published:

- Chap. 3 relies on work published in Cukanovaite et al. [2018].
- Chap. 4 relies on work that has not yet been published, but is in preparation.
- Chap. 5 relies on work published in Cukanovaite et al. [2019].

The introduction, methodology and summary also rely on the above published and in preparation to be published works.

The work presented in this thesis has been done by me, except for these instances:

- The 3D DB and DBA atmospheric models were run by Pier-Emmanuel Tremblay, which I then analysed and if needed extended their computation time.
- In Chap. 4 the EOS and opacity tables for metal-rich white dwarf simulations were provided by D. Koester and O. Toloza.
- Co-authors on papers also contributed to the general discussion of the manuscripts.

Abstract

All stars below around $10 M_{\odot}$ will eventually become white dwarfs, making them the most common type of stellar remnant. Due to the large densities of white dwarfs, their atmospheres are dominated by the lightest element present, with around 80% of white dwarfs in magnitude-limited samples possessing hydrogen-dominated atmospheres. A significant portion of the remaining white dwarfs posses helium-dominated atmospheres, which are the result of born-again or late thermal pulse scenarios, where hydrogen is either completely burned or is diluted during or after the AGB phase. These white dwarfs are the subject of this thesis.

A major uncertainty in the current 1D atmospheric models of white dwarfs lies in the treatment of convective energy transport, usually modelled under the mixing length approximation, which depends on a free parameter called the mixing length parameter, ML2/α. 3D simulations improve upon this by treating convection from first principles and by not relying on any free parameters, resulting in more physical models. In this thesis, I present the first 3D atmospheric models of white dwarfs that posses cool pure-helium atmospheres (DB) and helium-dominated atmospheres with traces of hydrogen (DBA). These models were calculated with the CO^{5}BOLD radiation-hydrodynamics code and cover the hydrogen-to-helium number ratios of $-10.0 \leq \log \mathrm{H/He} \leq -2.0$, surface gravities of $7.5 \leq \log g \leq 9.0$ and effective temperatures of $12\,000 \text{ K} \lesssim T_{\mathrm{eff}} \lesssim 34\,000$ K.

To determine the 3D effects on spectroscopic parameters, I compare the synthetic spectra computed from 3D and 1D models. In 1D models, the mixing length parameter is set to a commonly used value of 1.25. The 3D corrections on spectroscopically-derived values of hydrogen abundance and effective temperature are similar in magnitude to typical observational errors. However, the 1D models overestimate the surface gravity for $T_{\mathrm{eff}} \lesssim 22\,000$ K. By increasing hydrogen abundance in the atmosphere, the surface gravity corrections shift to a lower effective temperature range.

To test the 3D spectroscopic corrections, the Sloan Digital Sky Survey (SDSS) spectroscopic sample of DB and DBA white dwarfs is used, alongside the astrometric and photometric data from *Gaia* data release 2. Both 1D and 3D spectroscopic parameters are found to agree with *Gaia* within 1-3σ for individual white dwarfs, yet neither type of model produces a perfect agreement.

The uncertainty in line broadening caused by the effect of the neutral helium atom on its own species is also investigated to better understand additional systematic issues in current 1D and 3D model spectra. By comparing several samples of DA and DB/DBA white dwarfs, I show that the precision and accuracy of both types of 3D models are similar.

To extend the usefulness of 3D atmospheric models, I perform the calibration of the mixing length parameter for the bottom of the convection zone in order to determine more accurate bulk properties of the convection zone, such as its mass. Thus, the calibration is applicable for studies of planetary debris around white dwarfs, carbon dredge-up from the core, envelope and asteroseimological models. Overall, the calibrated value of the mixing length parameter is found to be around 0.8 and is much lower than the commonly used value of ML2/$\alpha = 1.25$ in DB and DBA 1D modelling, meaning that convective efficiency was previously overestimated by a significant factor. This is the first step in investigating convective overshoot in helium-dominated atmosphere white dwarfs.

Chapter 1

Introduction

I came from very far
A little unknown star, hello
I don't know what to do
It feels so cold and blue, without you

Sitting on the Moon
Enigma

1.1 Formation of a white dwarf

1.1.1 Protostar and the Main-Sequence

It is a well-established fact that the majority of stars in our galaxy will conclude their lives by evolving into white dwarfs [Althaus et al., 2010]. Main sequence stars below $\sim 10M_{\odot}$ are destined to follow this path [Woosley and Heger, 2015; Ibeling and Heger, 2013]. The stars of this mass range are born in a typical fashion. Their emergence begins with the collapse of a giant molecular cloud, which splits into smaller clumps via the process of fragmentation. Fragmentation prefers the formation of smaller mass stars, leading to what is known as the initial mass function, an example of which is shown in Fig. 1.1 [Chabrier, 2003]. The collapse results in an increase of the pressure inside a given clump, as well as the increase in temperature due to conversion of gravitational potential energy into heat. Such conditions bring forth the creation of a protostar [Hayashi, 1966].

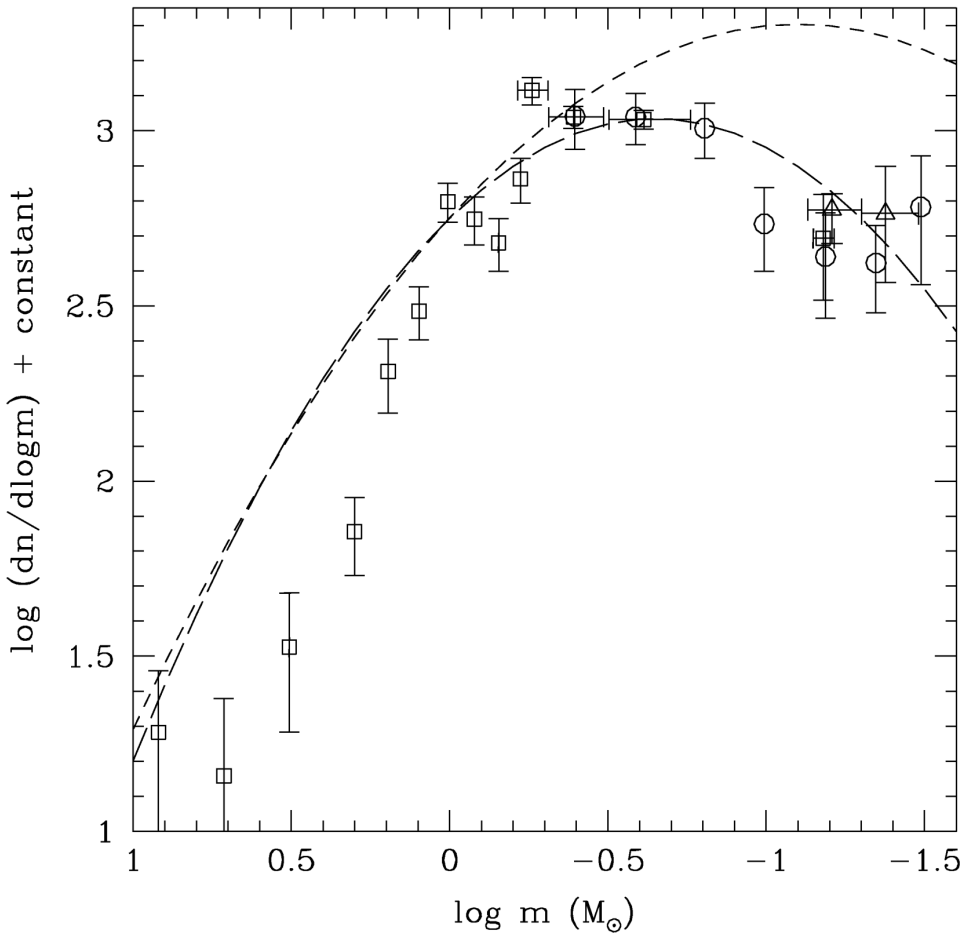

Figure 1.1: Experimental and theoretical initial mass functions for the Pleiades cluster. The theoretical initial mass functions for single and binary stars are shown in short-dashed and long-dashed lines, respectively. The squares, triangles and circles are data for the Pleaides cluster from three separate studies indicated in Chabrier [2003]. This figure illustrates the preference for formation of lower mass stars which occurs as a result of the process of fragmentation of the molecular cloud. Reproduced from Chabrier [2003].

The protostar grows in mass through the accretion of the remainder of the clump, until its internal temperature reaches around 10^7 K [Carroll and Ostlie, 2007, Chap. 13]. At this point, hydrogen, the element that makes up the majority of the cloud, begins fusing into helium via the proton-proton chain reaction or the CNO

cycle [Bethe, 1939]. Which reaction is preferred depends on the object's mass, since stars with mass above $1.2M_{\odot}$ have hot enough cores to burn hydrogen via the CNO cycle. Hereupon, the ongoing fusion inside the core is enough to support the protostar against the forces of gravity and thus a main-sequence star is formed. Indeed, the majority of a star's evolution is governed by the interplay of the forces of gravity and nuclear energy production.

The main sequence is the longest nuclear burning stage in the evolution of a star, as hydrogen provides a stable source of fuel that can sustain a star like the Sun for around 10 billion years [Carroll and Ostlie, 2007, Chap. 13]. For stars with masses below $1.2M_{\odot}$ the region of hydrogen-burning grows as the star evolves. This is because the growing mass of helium causes the mean molecular mass of the core to increase, thus raising the density and temperature of the core and the surrounding shell. It also means that as time passes more energy will be released via the CNO cycle [Carroll and Ostlie, 2007, Chap. 13]. More massive stars have convective cores, which means that the material inside the core is well mixed and there is no chemical gradient.

1.1.2 Red giant branch

Once the hydrogen in the core of a white dwarf progenitor is depleted, fusion ceases there. As the core can no longer support itself against the mass of the overlying layers, it will begin to contract, releasing gravitational potential energy into the envelope, causing the envelope to expand. The contraction also results in the unburned hydrogen from higher up layers to be brought down into the shell surrounding the core, where the temperature is high enough for fusion to begin [Carroll and Ostlie, 2007, Chap.13]. This stage is known as hydrogen-shell burning and will also contribute to envelope expansion. For white dwarf progenitors the expansion causes the temperature of the envelope to decrease, leading to formation of H^- ions in the photosphere, increasing the opacity and resulting in the formation of a convection zone [Iben, 1991]. The zone extends all the way down to the hydrogen-burning shell, allowing for efficient energy transport straight to the surface and the transportation of the products of nuclear reactions to the photosphere. This is known as the first dredge up and is indicated in Fig. 1.2 [Iben, 1991]. The nuclear products can then be observed in the spectra of such stars and can be used to test our understanding of stellar evolution [Lambert, 1981].

Once the contribution of the hydrogen-shell burning makes the mass of the helium core exceed the Schönberg-Chandrasekhar limit, the core will become degenerate and will contract further [Schönberg and Chandrasekhar, 1942]. The increase

of the temperature boosts the rate of hydrogen-burning, rising the luminosity of the star, explaining the position of the red giant branch in the Hertzsprung-Russell diagram (Fig. 1.2).

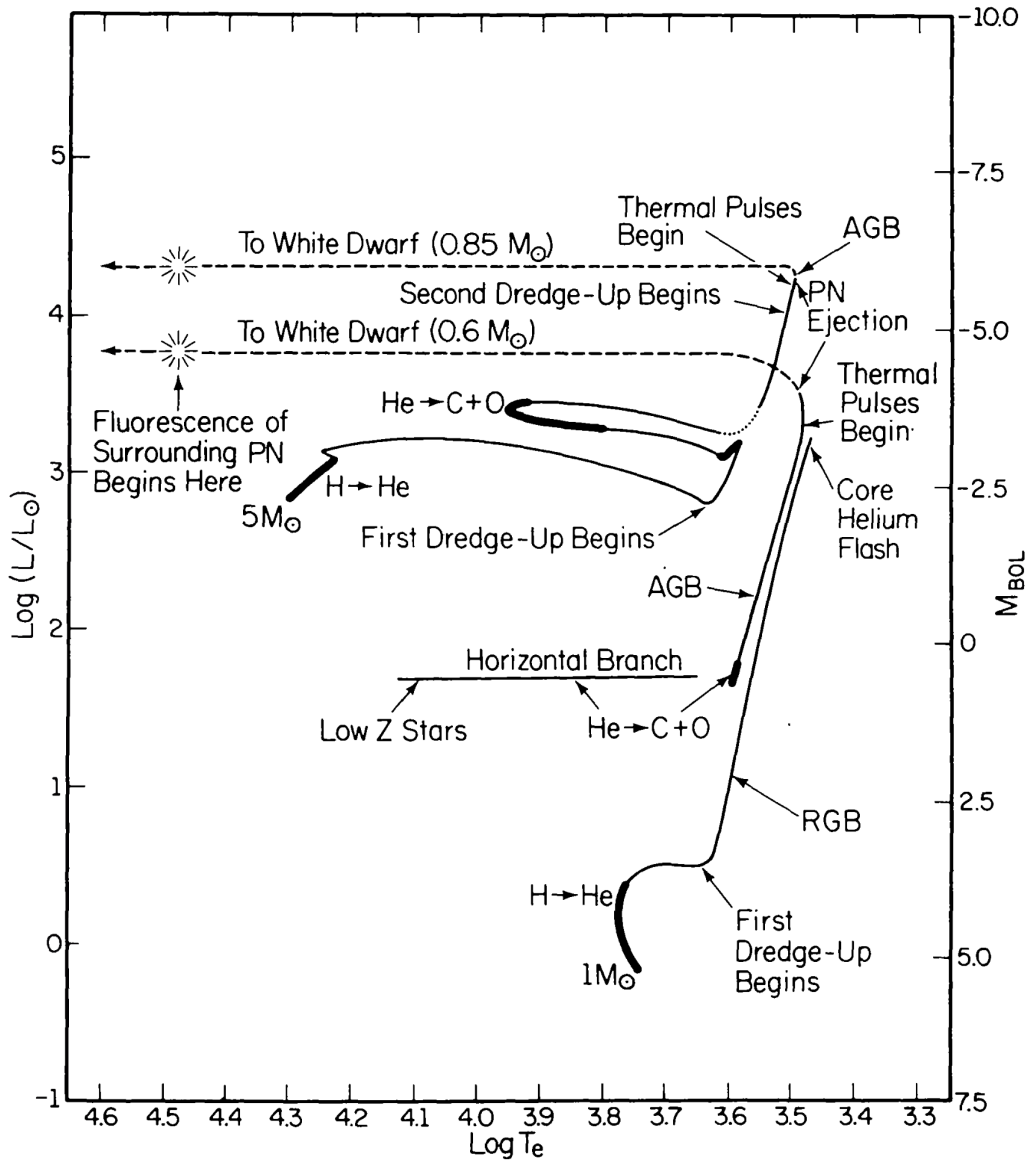

Figure 1.2: A typical Hertzsprung-Russell diagram following the evolution of $1M_\odot$ and $5M_\odot$ main sequence stars in terms of their luminosity and effective temperature. Adapted from Iben [1991].

At the tip of the red giant branch, helium fusion will begin in the core through the triple-α process, which converts helium into carbon [Bethe, 1939]. The onset of helium-burning releases vast amounts of energy with the luminosity produced rivalling the luminosity of an entire galaxy. However, the majority of this energy is used to lift the degeneracy of the core and therefore cannot be observed [Taam, 1980; Iben, 1991]. The energy release will expand the core and the hydrogen-burning shell, decreasing the shell's temperature and decreasing the energy production there. The luminosity of the star decreases, the envelope contracts and effective temperature increases.

1.1.3 Horizontal branch

The star now joins the horizontal branch (Fig. 1.2). The helium-burning horizontal branch is an analogue to the hydrogen-burning main sequence. The fusion of helium is not as long lived as the fusion of hydrogen. Thus, the Sun will spend around 10^8 years at this evolutionary stage [Iben, 1991].

During this part of stellar evolution, the star can exhibit pulsations in its luminosity, temperature and radius due to instabilities. This type of stars are known as RR Lyrae variables [de Vaucouleurs, 1978]. The pulsations can be observed and are quasi-periodic [Christy, 1966]. They can also be used to test the stellar evolutionary models (see e.g. Bellinger et al. [2020]). Similarly to the end of the main sequence, the end of the horizontal branch will see core contraction and an increase in the temperature of the shell around the core, resulting in a helium-burning shell surrounding the core. Due to this energy production, the material above will expand, resulting in lower temperature and thus the cessation of hydrogen-burning [Iben, 1991].

1.1.4 Asymptotic giant branch

The asymptotic giant branch (AGB) is a helium analogue to the red giant branch (see Fig. 1.2). At the start of this stage, the energy production is dominated by helium-burning in the shell surrounding the core [Iben, 1991]. This causes the envelope to expand, decreasing its temperature. As a result, a deep convection zone is formed, extending down to the region between the helium and hydrogen burning shells, bringing up the products of nuclear burning to the surface once again [Eldridge et al., 2007]. This is known as the second dredge up event (see Fig. 1.2). It occurs only for stars with masses above $4M_\odot$ [Carroll and Ostlie, 2007, Chap.13].

At some point, helium is exhausted in the helium-burning shell. Contraction and subsequent temperature increase allows for the hydrogen-burning shell to once

again become active [Carroll and Ostlie, 2007, Chap.13]. Eventually, helium will be dumped from the hydrogen-burning shell onto the quiescent helium-shell, leading to a helium shell flash and the resumption of helium-burning [Schwarzschild and Härm, 1965]. This cycle of helium- and hydrogen-burning is repeated resulting in quasi-periodic helium flashes. With each subsequent flash, the pulse amplitude and the convection zone depth increases [Carroll and Ostlie, 2007, Chap.13]. A third dredge up event will follow, once the convection zone becomes deep enough to reach the region where carbon is synthesised. Stars below $4M_\odot$ will only experience the first and third dredge-up events [Carroll and Ostlie, 2007, Chap.13]. This dredge-up event can occur multiple times due to helium flashes and can be observed in stars known as carbon stars [Iben and Renzini, 1983].

As more helium is converted into carbon, and some carbon is also further synthesised into oxygen, the carbon-oxygen core will grow. Eventually, it will contract and the density increase will mean that the electron degeneracy pressure will dominate the total pressure of the core [Carroll and Ostlie, 2007, Chap.13]. For more massive stars, between $4 < M < 8$ $M_\odot$, additional nucleosynthesis will occur, creating a final core of oxygen, neon and magnesium [Oswalt and Barstow, 2013, Chap. 11].

During the AGB, a star with a mass below $\approx 10M_\odot$ will lose around 10^{-6} $M_\odot$ per year through stellar wind and superwind [Höfner and Olofsson, 2018]. As the expelled material is cool enough, dust will be able to form inside it. Earlier stages of this part of the evolution will experience stellar wind while the later stages will also experience superwind, where a large amount of mass is expelled [Höfner and Olofsson, 2018]. Post-AGB the envelope of the star is expelled forming a planetary nebula, leaving behind only the core and the two burning shells [Iben, 1991]. The burning stops, decreasing the luminosity and what is left of the star is now a white dwarf. This is the most common type of white dwarf observed.

For very low mass stars with $M \lesssim 0.5$ $M_\odot$, the core never becomes a carbon-oxygen core, since the burning of helium into carbon cannot occur. Instead, such stars become white dwarfs with helium cores [Oswalt and Barstow, 2013, Chap. 11]. These white dwarfs cannot currently exist, because the time taken for this evolution to occur is longer than the present age of the Universe. Low mass white dwarfs have been observed, however, but they are assumed to be a result of binary evolution [Oswalt and Barstow, 2013, Chap. 11]. For massive stars with $4 < M < 8$ $M_\odot$, the formed white dwarfs will have oxygen, neon and magnesium cores.

For main sequence stars with larger masses than 10 $M_\odot$, the core of carbon-oxygen will be able to undergo further fusion, such as carbon into neon and neon

into iron [Heger et al., 2003]. The core will grow in mass and eventually will exceed the possible mass that can be supported by degeneracy pressure. A core-collapse supernova will then follow, producing a different type of compact object, either a neutron star or a black hole [Carroll and Ostlie, 2007, Chap. 13].

1.1.5 Formation of hydrogen-deficient white dwarfs

The subject of this thesis are white dwarfs with no outer hydrogen shell. The formation of these stellar remnants can be explained by either the born-again scenarios or the AGB final thermal pulse (AFTP). There are two types of born-again scenarios, the late thermal pulse (LTP) and the very late thermal pulse (VLTP). Both types of thermal pulses are caused by the reignition of the helium-burning shell, returning the post-AGB star back to the AGB, hence the born again name [Herwig, 2001].

VLTP occurs following the star's departure from the AGB, while it is becoming a white dwarf. The helium-burning creates enough energy to develop a convection zone between the helium- and hydrogen-shells [Werner and Herwig, 2006]. The absence of fusion in the dormant hydrogen shell, means that the convection zone can extend into the hydrogen shell, transporting the hydrogen downwards into a region where the temperature is high enough for hydrogen fusion to begin [Blöcker, 2001]. This results in the surface being completely depleted of hydrogen. Sakurai's object is a famous example of a star undergoing a VLTP [Asplund et al., 1999]. As the VLTP channel results in a complete elimination of hydrogen, it is predicted to result in the formation of pure-helium atmosphere white dwarfs [Metcalfe et al., 2005; Miller Bertolami and Althaus, 2006].

The LTP scenario is hypothesised to occur earlier in the star's evolution than VLTP, when hydrogen is still fusing [Blöcker, 2001]. This means that the convection zone cannot spread into the hydrogen layer. Instead, the helium flash will cause the star to expand, cooling the outer layers and causing a convection zone to form near the surface [Werner and Herwig, 2006]. This convection zone is able to dilute the hydrogen on the surface into the envelope, effectively producing a hydrogen-poor white dwarf [Herwig, 2001].

Unlike the born again scenarios, an AFTP occurs while the star is still on the AGB. It is related to the third dredge up event, such that the nuclear products brought up from the deep layers dilute the hydrogen at the surface, making the surface of the star hydrogen-poor [Herwig, 2001]. After this final pulse, the star will leave the AGB and will eventually become a hydrogen-deficient white dwarf.

In order to be able to determine which evolutionary path is true for hydrogen-poor white dwarfs, models are created for all three scenarios and the outputs of

these models are compared to observations [Werner and Herwig, 2006]. The study of hydrogen in the helium-atmosphere dominated white dwarfs, known as DBA stars, can shed light on the two processes which do not completely remove the hydrogen from the atmosphere. The hydrogen abundance can also allow us to study the amount of residual hydrogen that is left over from the AGB stage and thus give information on the nuclear burning rates in those stars [Werner and Herwig, 2006].

Asteroseismology can be used to probe the deep interior of white dwarfs. Since the different formation scenarios result in different interior chemical profiles, asteroseismology of pulsating helium-dominated atmosphere white dwarfs can also be used to distinguish the different formation scenarios [Battich et al., 2020].

The above discussion encapsulates the importance of helium-dominated atmosphere white dwarfs in the overall picture of stellar evolution, specifically for the AGB and post-AGB stages.

1.2 Composition of a white dwarf

On average, a white dwarf's mass is around 0.6 $M_{\odot}$ (see e.g. Tremblay et al. 2019b) and its size is comparable to that of the Earth (see e.g. Joyce et al. 2018). Typical mass distributions of DA and DB/DBA white dwarfs are shown in Fig. 1.3. Considering their masses and radii, one can easily deduce that white dwarfs are extremely dense. The average mass of a white dwarf also highlights the mass loss a star experiences during its previous evolutionary stages, since all stars below around $10M_{\odot}$ will become white dwarfs. This is summarised in the initial-to-final mass relations (see e.g. Cummings et al. 2018).

A white dwarf is made up of an electron and nucleon plasma, which is supported against the force of gravity by electron degeneracy pressure of the core [Fowler, 1926]. The pressure is a consequence of the fermion nature of electrons. Due to the Pauli exclusion principle, two electrons cannot occupy the same quantum state [Pauli, 1925]. This means that even at zero temperature, electrons cannot be all confined to the lowest energy level, and instead have to distribute themselves across all available lowest energy levels. Thus, at 0 K, such a system will have a non-zero energy, known as Fermi energy [Fermi, 1926]. The pressure comes about due to the gravitational compression of a white dwarf, as this increases the number of electrons in a given volume. The Heisenberg uncertainty principle defines the lowest possible uncertainty in a particle's momentum and position [Heisenberg, 1927], which in combination with the Pauli exclusion principle means that the uncertainty in electron's position cannot be larger than the separation of electrons [Carroll and Ostlie,

2007, Chap. 16]. The decrease in their separation due to compression decreases this uncertainty, increasing the electron's momentum, kinetic energy and therefore the outward pressure which supports the white dwarf.

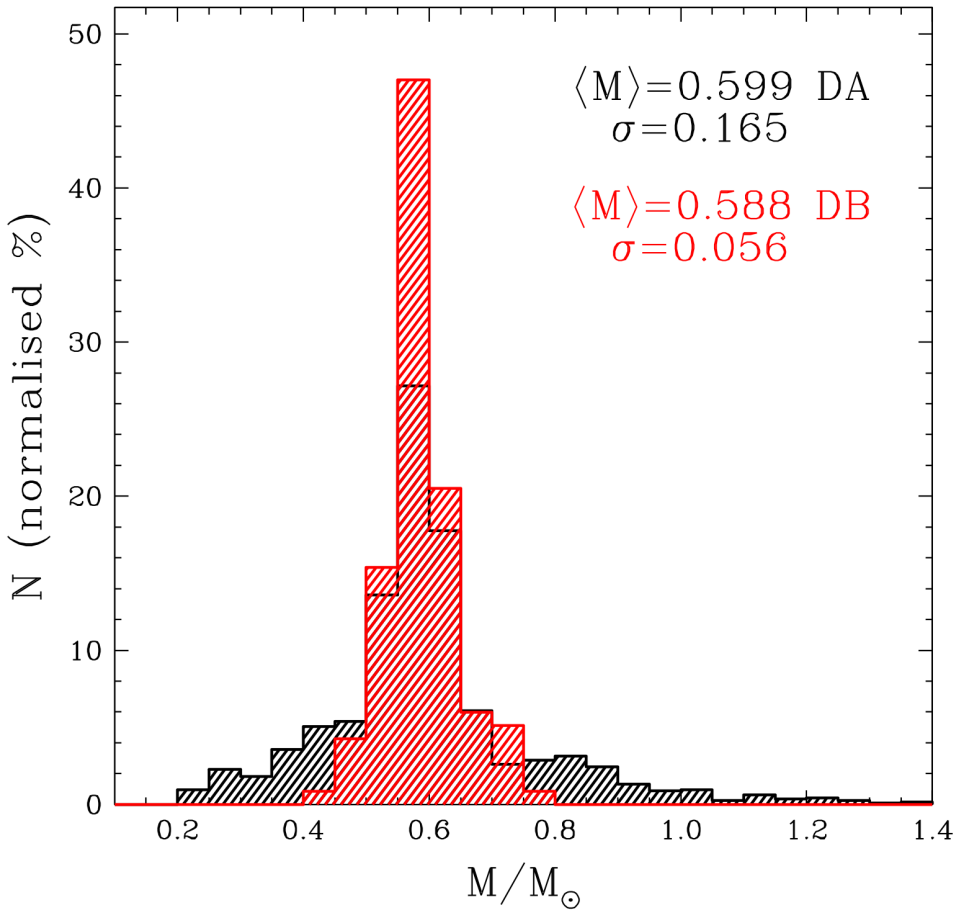

Figure 1.3: The mass distributions for DA and DB/DBA white dwarf samples are shown as black and red histograms, respectively. The DA and DB/DBA white dwarf samples are from Gianninas et al. [2010] and Rolland et al. [2018], respectively. The mean masses and their standard deviations are indicated on the plot. Adapted from Tremblay et al. [2019b].

As the mass of the white dwarf increases, its radius decreases (see e.g. Joyce et al. 2018), since the density increase following compression causes electrons to get closer together. At infinite mass, the white dwarf's radius will become zero, however, if relativistic effects are taken into account due to electron velocity approaching the speed of light, a zero volume can be achieved with a finite mass. This is the maximum

mass of a white dwarf allowed by electron degeneracy pressure and it is known as the Chandrasekhar mass of $1.44M_{\odot}$ [Chandrasekhar, 1931]. Above this mass, the white dwarf would become a neutron star through a core-collapse supernova. Other effects, such as rotation, can increase the value of the Chandrasekhar limit. No white dwarfs above the Chandrasekhar mass limit are observed (see Fig. 1.3).

For temperatures and densities of white dwarfs the assumption of complete degeneracy is valid even though it is not completely true, since the core is not at 0 K. As the temperature is higher, a number of electrons will be able to jump to higher energy levels if their energy is larger than the Fermi energy [Oswalt and Barstow, 2013, Chap. 11]. White dwarf cores are therefore partially degenerate [Wares, 1944].

The core has high thermal conductivity due to the degenerate nature of the electrons [Oswalt and Barstow, 2013, Chap. 11]. Therefore, energy is mostly transported by electron conduction, which is done via collisions between particles. In white dwarfs conduction is an efficient energy transport, thus the core is isothermal and has a uniform temperature of around 10^7 K [Fontaine et al., 2001]. It also means that the core does not cool fast. The cooling is instead moderated by the outer layers, which transport the energy from the conductive core to outer space [Fontaine et al., 2001].

1.2.1 Atmosphere

In most cases, the core of the white dwarf is surrounded by two separate and pristine layers of helium and hydrogen, the remains of the burning shells of the previous evolutionary stages [Koester and Chanmugam, 1990]. This type of white dwarfs have hydrogen-dominated atmospheres. If the hydrogen shell has been lost during the AGB or immediately following it, the core will only be surrounded by an envelope of helium and thus it will have a helium-dominated atmosphere [Werner and Herwig, 2006]. Fig. 1.4 shows the typical elemental composition of a hydrogen-rich white dwarfs.

The core makes up most of the mass of the white dwarf [Fontaine et al., 2001]. Therefore, the depth of the atmosphere is much smaller than the radius of the stellar remnant. The strong stratification of a white dwarf is due its immense gravity, which sinks the heaviest elements to the core, leaving the lightest material in the upper layers. This is known as gravitational settling and is a diffusion process [Schatzman, 1948; Koester and Chanmugam, 1990].

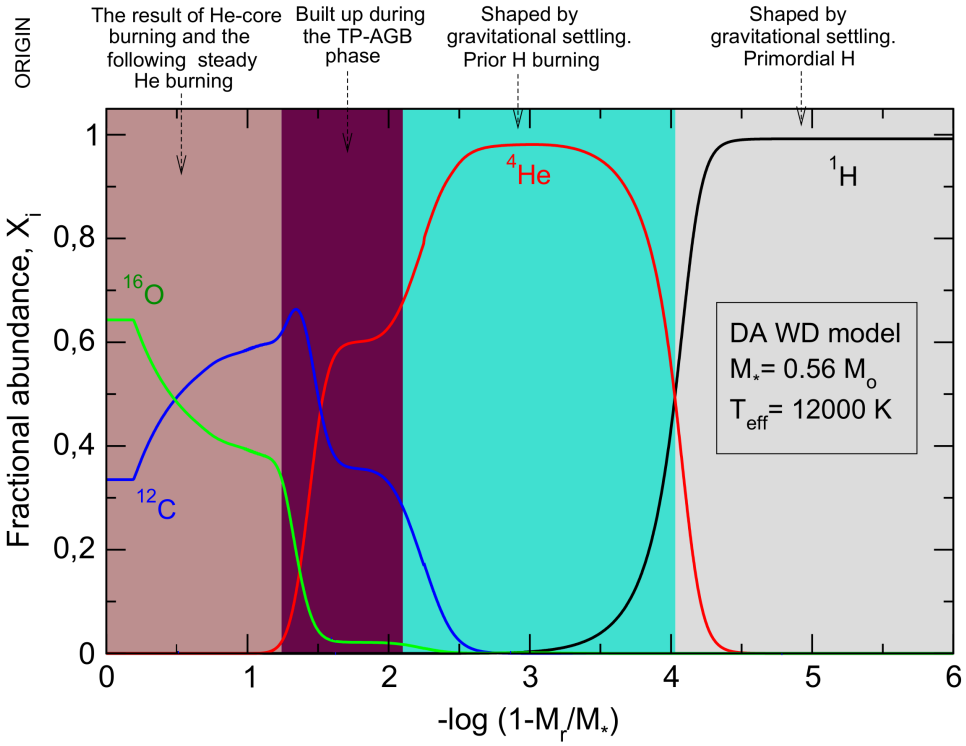

Figure 1.4: The typical elemental composition of a hydrogen-rich white dwarf with $T_{\rm eff}$= 12 000 K and mass of 0.56$M_{\odot}$. Each coloured line represents a different element. The y-axis is the fractional abundance of the element and x-axis is the outer mass fraction, where M_r is the mass from the surface to a given depth, r, in the structure of the white dwarf and $M_{\star}$ is the total mass of the white dwarf. The explanations for the observed elemental abundances are given on the top of the plot. A He-rich white dwarf would have a much thinner outer hydrogen shell. Adapted from Córsico et al. [2019].

White dwarfs are classified based on their spectra as their atmospheric composition can be deduced from the spectral lines [Sion et al., 1983], which are pressure-broadened due to the large surface gravities. Fig. 1.5 shows examples of typical white dwarf spectra. The majority of white dwarfs show hydrogen Balmer lines in the optical (see e.g. Kepler et al. 2019) and are classified as DA. The letter "D" stands for degenerate, owing to the degenerate nature of the majority of the white dwarf, "A" mirroring main sequence star classification [Oswalt and Barstow, 2013, Chap. 11]. The helium-pure atmosphere white dwarfs can be classified into more subcategories, for example the DO white dwarfs which show He II lines or the DB white dwarfs which show He I lines. The second most numerous class is DC, whose spectra is composed only of continuum [Kepler et al., 2019]. Any helium-dominated

atmosphere white dwarf will cease exhibiting helium lines below around 10 000 K and thus appears as DC [Oswalt and Barstow, 2013, Chap. 11]. Hydrogen-dominated atmosphere white dwarfs will no longer show hydrogen lines below around 5 000 K. Therefore, DC stars with effective temperatures below around 5 000 K cannot be differentiated as having hydrogen- or helium-dominated atmospheres [Bergeron et al., 1997]. This highlights the fact that the spectral classification does not always determine the atmospheric composition.

Other notable spectral classifications of white dwarfs are DQ, which show only carbon lines in their spectra [Pelletier et al., 1986], and DZ white dwarfs which only show metal lines [Koester et al., 1990]. The classifications can be combined, for example a white dwarf with a helium-dominated atmosphere that has traces of hydrogen would have both helium and hydrogen lines, and would be classified as DBA, "B" being the first letter given that the helium lines are the strongest.

DA white dwarfs are found in a large effective temperature range, from around 5 000 K to 100 000 K. DO white dwarfs are found at temperatures that are high enough for helium to singly ionize and subsequently be excited, which is around $45\,000 \lesssim T_{\text{eff}} \lesssim 100\,000$ K [Oswalt and Barstow, 2013, Chap. 11]. The upper limit of effective temperature is due to previous evolution. DB white dwarfs are found in the temperature range $10\,000 \lesssim T_{\text{eff}} \lesssim 35\,000$ K where neutral helium can be excited.

Due to their large surface gravities, white dwarf spectra can be used as laboratories to study the behaviour of different elements in extreme conditions that cannot be currently replicated in laboratories (see e.g. Kritcher et al. 2020). If the models do not match observations, a possible explanation can therefore be missing physics. Thus, white dwarf observations can pinpoint issues in our understanding of atomic physics.

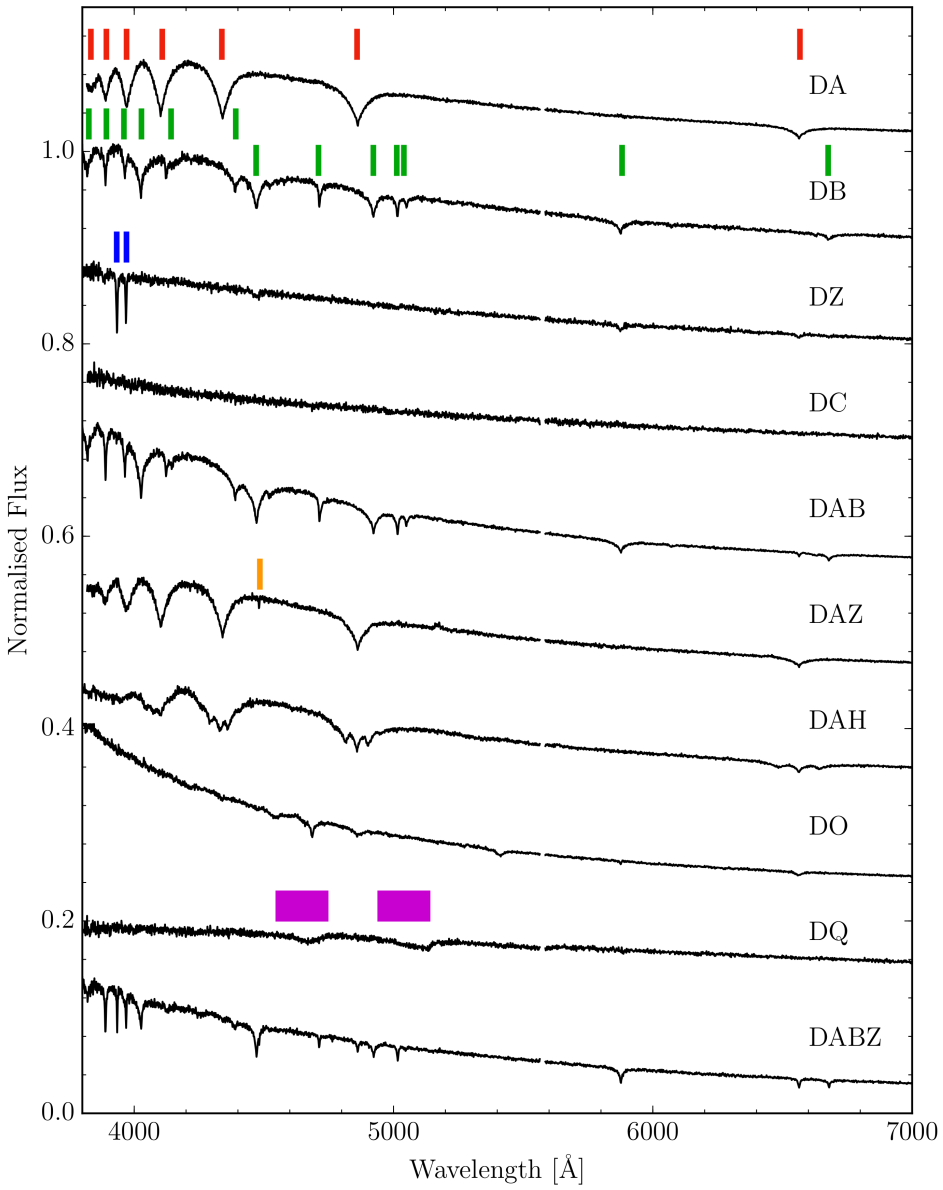

Figure 1.5: Examples of different types of white dwarf spectra. The coloured lines indicate different types of spectral lines. In the case of DA white dwarfs the red dashes denote H lines, and for DB white dwarfs the green dashes mark the He I lines. DZ and DAZ spectra exhibit metal lines, in the examples shown here the blue dashes indicate calcium H and K lines, while the orange dash indicates the magnesium II line. The purple dashes identify the carbon Swan bands seen in DQ stars. The letter "H" is used to indicate white dwarf spectra that shows magnetic features. In this example the DAH spectrum contains hydrogen Balmer lines which are split due to Zeeman effect. Reproduced from Manser [2018].

1.3 White dwarf evolution

Unlike stars, single white dwarfs do not undergo any nuclear burning. Thus, the energy that powers their luminosity must come from somewhere else. This source is the thermal energy stored in their nuclei [Koester and Chanmugam, 1990]. Due to their degenerate nature, electrons are unable to provide thermal energy as they already occupy the lowest available energy states [Mestel, 1952]. As white dwarfs cool with age their evolution is commonly referred to as cooling and thus their effective temperature can be used to estimate their age [Fontaine et al., 2001]. The thermal energy of a white dwarf results in long cooling times of around 10^6-10^9 years [Oswalt and Barstow, 2013, Chap. 11].

The cooling time also depends on the mass of the white dwarf. The more massive the white dwarf is, the bigger its thermal energy reservoir and the longer its cooling time [Fontaine et al., 2001]. Additionally, it also depends on the composition of the core since a white dwarf that has a pure-carbon core will take longer to cool than a white dwarf with a pure-oxygen core. This happens because the specific heat per gram is larger for carbon than oxygen [Fontaine et al., 2001].

The processes that take place in white dwarf atmospheres are also important for cooling, since the atmosphere governs how the internal energy of the white dwarf is released into space [García-Berro and Oswalt, 2016]. This highlights the need for accurate atmospheric models of white dwarfs.

There is a potential in being able to predict the evolution of a white dwarf to a great degree of accuracy. It means that white dwarfs can be used as accurate clocks to age different stellar populations, such as local stars (see e.g Tremblay et al. 2014; Fantin et al. 2019), the galactic inner halo (see e.g. Kalirai 2012) or disk [Winget et al., 1987]. An example comparison between the theoretical evolutionary predictions and white dwarf observations can be seen in Fig. 1.6. It shows both the theoretical and observational luminosity functions. As white dwarfs cool with age, their luminosity also decreases, therefore this type of plot can be used as an indication of white dwarf evolution (see Koester and Chanmugam 1990 for more detailed explanation).

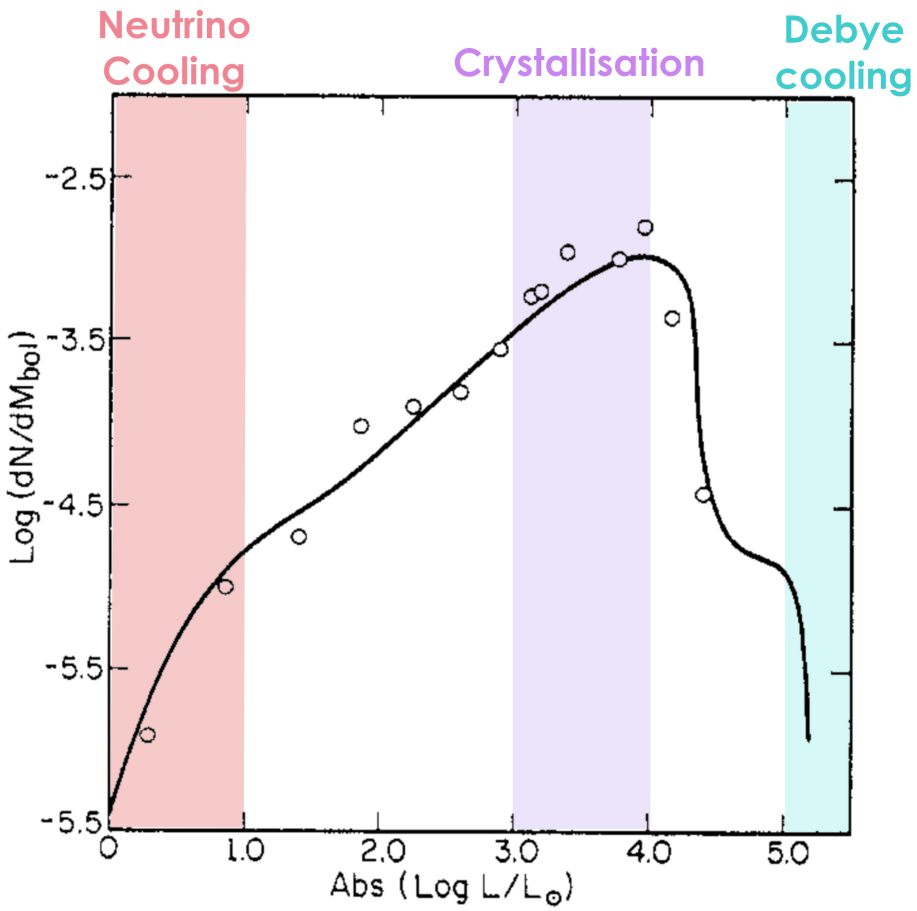

Figure 1.6: A comparison between theoretical and observational luminosity functions of white dwarfs. Open circles are observations from Liebert et al. [1988] and the solid line is the theoretical luminosity function of Iben and Laughlin [1989]. Luminosity can be used as a proxy for the age of the white dwarf. The number of white dwarfs in a given luminosity bin informs the time spent at a given luminosity. Several of the important stages in white dwarf evolution are indicated on the plot. Adapted from Koester and Chanmugam [1990].

1.3.1 Pre-white dwarf and gravitational contraction

At the pre-white dwarf stage where the remnant leaves the AGB and converges onto the white dwarf track, the gravitational contraction of the outer layers is important as it can contribute significantly to the luminosity, slowing down the cooling [Iben, 1991]. Due to its degeneracy the core does not contract significantly. This is because the difference between the core's radii when it is partially degenerate and when it is fully degenerate is small [Koester and Chanmugam, 1990].

Gravitational contraction becomes less important after the pre-white dwarf

stage, but its contribution to the energy released is never zero. Because of this reason, it is said that white dwarfs evolve at almost a constant radius [Koester and Chanmugam, 1990].

1.3.2 Neutrino cooling

In the first stage of white dwarf evolution, accelerated cooling is experienced through the loss of neutrinos from the degenerate core [Fontaine et al., 2001]. In Fig. 1.6 this is observed below $\mathrm{Abs}(\log \mathrm{L}/\mathrm{L}_{\odot}) \approx 1.0$ [Koester and Chanmugam, 1990], where there is a sharp decrease in white dwarfs. This is because this stage is so fast that it is not likely for us to observe a significant amount of white dwarfs with these luminosities.

The neutrinos are created via the plasmon neutrino process, which dominates the energy loss due to the hot and dense conditions of the core [Koester and Chanmugam, 1990]. In this process, a plasma photon, known as a plasmon, decays into a neutrino and an antineutrino pair. It is not possible for a normal photon to do this since it possesses no mass. However, in a dense plasma the interactions between the photon and surrounding free electrons slow the photon down, making it behave as if it has mass [Koester and Chanmugam, 1990]. As these plasmons are unstable, they quickly decay into a neutrino and an antineutrino without violating mass conservation laws [Oswalt and Barstow, 2013, Chap. 11]. The neutrinos are then able to quickly and efficiently leave the white dwarf since they have small interaction cross sections, leading to accelerated cooling of the white dwarf. Indeed, such cooling leaves the core cooler than the layer surrounding it, since photon cooling in the outer layers is not as efficient [Fontaine et al., 2001].

When the density of the core of the white dwarf exceeds 10^4 g cm^{-3} and its temperature is above 10^8 K, neutrino cooling dominates the energy release [Lamb and van Horn, 1975]. This occurs in the early stages of white dwarf evolution. The mass of the plasmon is proportional to the square root of the plasma density, so the large density of the core means that larger mass plasmons are created and they decay into more energetic neutrinos, which leave the white dwarf possessing a larger amount of energy [Winget et al., 2004]. The temperature also increases the number of plasmons, as the photons are interacting more with matter [Winget et al., 2004]. Since white dwarfs are dense and at this stage hot, they have large neutrino flux leading to significant cooling. Once the white dwarf cools enough, its loss through neutrino cooling reduces and normal thermal cooling via photons becomes dominant. Variable DB white dwarfs, known as DBV, can potentially be used to test our understanding of the plasmon neutrino process, as it is predicted to affect the pulsation periods of the hottest DBV stars [Winget et al., 2004].

1.3.3 Convection

As explained earlier, white dwarfs with hydrogen-rich and hydrogen-deficient atmospheres have different progenitors. However, from observations it is apparent that during its evolution a white dwarf is able to change its atmospheric composition and thus its spectral type. The reason for this is closely linked with convection.

One example of such a transformation is the deficiency of hydrogen-poor white dwarfs in the temperature range $30\,000 \lesssim T_{\rm eff} \lesssim 45\,000$ K, formally known as the DB gap [Wesemael et al., 1985; Eisenstein et al., 2006]. A gap of this sort cannot be explained by a different progenitor. Instead, it is assumed that in this temperature range the helium-dominated atmosphere white dwarfs transform into hydrogen-dominated white dwarfs [Fontaine and Wesemael, 1987]. It is proposed that the reason for this lies in any remaining hydrogen floating up to the surface at $T_{\rm eff} \approx 45\,000$ K, causing the atmosphere to become hydrogen-dominated. At $T_{\rm eff} \approx 30\,000$ K, the helium convection zone becomes large enough to dilute the hydrogen, turning the star back into a DB or a DBA.

Another way a convection zone impacts the evolution of white dwarfs can be seen at low effective temperatures. The ratio of DA to DB/DBA white dwarfs decreases significantly below $T_{\rm eff} \lesssim 12\,000$ K, implying that DA stars transform into helium-dominated white dwarfs. Around this temperature the hydrogen convection zone reaches the underlying helium layer, bringing up large amounts of helium to the atmosphere and transforming it [Strittmatter and Wickramasinghe, 1971].

It is theorised that the progenitors of cool DQ white dwarfs are helium-dominated, because the atmospheres of cool DQ white dwarfs are helium-dominated atmospheres with traces of carbon. It is assumed that for these white dwarfs, the helium convection zone becomes deep enough to penetrate the underlying carbon layer, bringing up carbon to the surface [Pelletier et al., 1986].

These examples highlight the importance of convection in the evolution of white dwarfs. Therefore, any uncertainties in our understanding of convection reflect themselves in our inability to fully understand white dwarf evolution. Additionally, the population analysis can be used as a useful indicator of the thickness of the hydrogen layer, a needed parameter in white dwarf evolution models, asteroseismology and planetary system studies [Fontaine et al., 2001]. Lastly, these examples also show the importance of helium-dominated atmosphere white dwarfs in the overall picture of white dwarf evolution.

1.3.4 Pulsating white dwarfs

As white dwarfs cool they go through a region of effective temperature where they experience non-radial gravity wave pulsations with periods on the order of minutes [Fontaine and Brassard, 2008]. The two main types of white dwarf pulsators are DAV stars which are found at $11\,000 \lesssim T_{\text{eff}} \lesssim 13\,000$ K [McGraw, 1977] and DBV white dwarfs found at $25\,000 \lesssim T_{\text{eff}} \lesssim 30\,000$ K [Winget et al., 1981, 1982]. As the names imply they are hydrogen-dominated and helium-dominated atmosphere white dwarfs, respectively. Asteroseismology can be used to study the interior of white dwarfs as the waves penetrate deep into the star [Giammichele et al., 2018].

The pulsations are due to the recombination of the main constituent of the atmosphere [Fontaine and Brassard, 2008]. If a star is compressed, the temperature and density will increase. If opacity increases with compression, i.e. with temperature, less heat is allowed to escape. This pushes the outer layers, causing the star to expand and become unstable against pulsations, since this cycle would repeat until conditions change enough for the cycle to stop [Carroll and Ostlie, 2007, Chap. 14]. However, in most stars opacity decreases with temperature. If a gas is partially ionized, the energy released during compression will go into ionizing the gas, thus opacity will increase with compression and therefore with temperature [Fontaine and Brassard, 2008]. Recall that partial ionization is also responsible for the formation of convection zones in white dwarfs, so the onset of pulsations is closely related to convective energy transport becoming dominant. Pulsations will eventually cease when convective energy transport becomes efficient, allowing the photons to escape, stopping the cycle [Carroll and Ostlie, 2007, Chap. 14]. This process is not well understood as it involves time-dependent convection, a process difficult to model in 1D [Van Grootel et al., 2012], highlighting the need for better models of convection.

The frequency of pulsations is proportional to the temperature of the core [Koester and Chanmugam, 1990]. This in turn means that as the white dwarf ages its pulsation period increases, introducing another way to estimate the ages of white dwarfs.

1.3.5 Crystallisation

Once enough thermal energy is lost by the white dwarf and the temperature of the core reaches its freezing point, it is energetically favourable for the ions in the core to form a crystalline structure [van Horn, 1968]. This is known as crystallisation. The gas undergoes a first-order phase transition to become a solid and latent heat is released slowing down the cooling of the white dwarf [van Horn, 1968]. Crystallisation

begins in the center of the white dwarf. Over time the crystallisation front moves upwards until the entire star becomes solid. This process is gradual and slows down the cooling over a long period of time [Koester and Chanmugam, 1990]. In Fig. 1.6 this is seen around $\mathrm{Abs}\log \mathrm{L/L}_{\odot} \approx 3$ [Koester and Chanmugam, 1990].

Most white dwarfs possess carbon-oxygen cores. The freezing point of oxygen is higher than carbon's and therefore it crystallizes first. As solid oxygen is more dense than carbon gas, it moves inwards releasing gravitational energy. This becomes an additional source of heat that slows down the cooling [Isern et al., 1997]. Signatures of both effects have been confirmed by the recent *Gaia* DR2 observations [Tremblay et al., 2019a], which also showed that the presence of neon and its sedimentation in high mass white dwarfs can affect the observed luminosity function and thus needs to be taken into account when modelling white dwarf evolution [Camisassa et al., 2020].

The temperature at which crystallisation occurs is proportional to the cube-root of density. Therefore, more massive white dwarfs solidify at higher effective temperatures and thus at an earlier stage in their evolution [van Horn, 1968].

1.3.6 Convective core coupling

Another significant event in the evolution of a white dwarf happens when the convection zone reaches the degenerate core. This couples the core directly to the surface, leading to significant energy losses which accelerate the cooling [Böhm, 1968]. This is known as convective core coupling. Before this occurs, the core is well insulated by the opaque, radiative layers in the envelope. When convection becomes dominant the opacity decreases, releasing large amounts of stored thermal energy. Thus, the cooling is initially slowed down compared to purely-radiative models [Fontaine et al., 2001]. Once this energy is freed, due to the lower insulation, convection will accelerate the cooling as energy is efficiently transported from the core directly to the surface. Similarly, cool white dwarfs with hydrogen-dominated atmospheres cool slower than helium-dominated white dwarfs because hydrogen acts as a better insulator compared to helium [Hansen, 1999].

Convective coupling occurs when the convection zone is adiabatic. This means that the changes happening at the surface directly impact the base of the convection zone [Fontaine et al., 2001]. Adiabatic convection is well modelled in 1D and therefore the theoretical predictions at this evolutionary stage are not affected by issues with the modelling of convection.

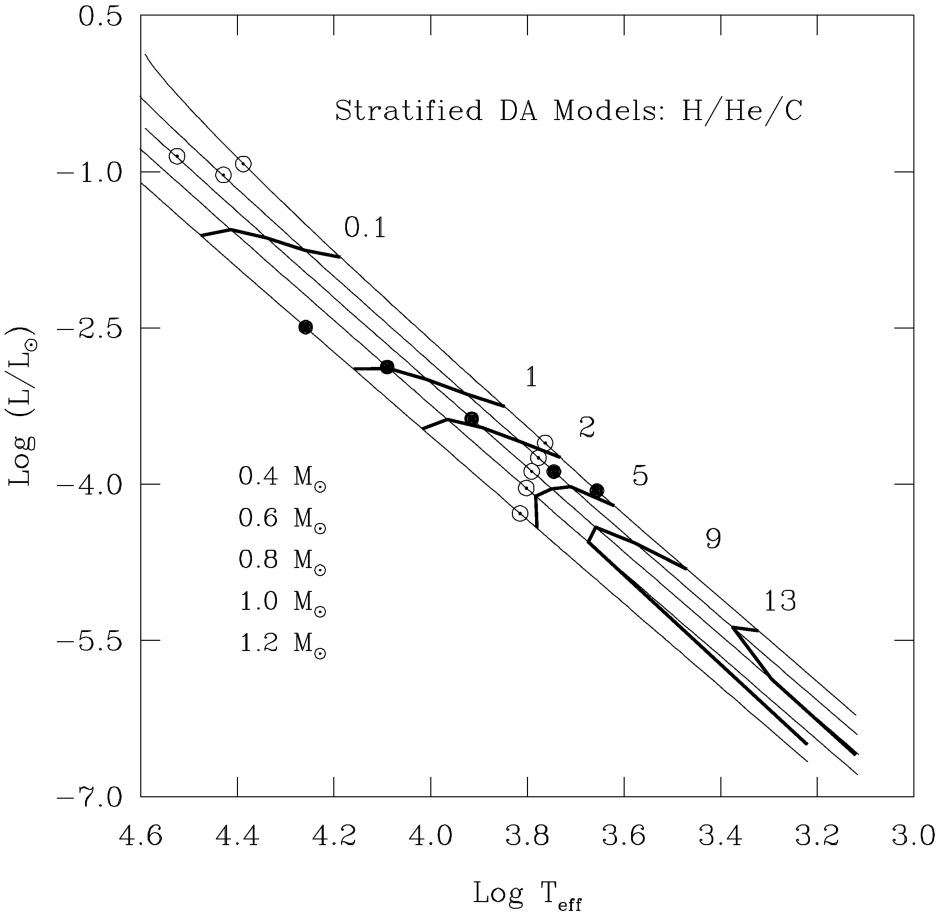

Figure 1.7: The luminosity as a function of effective temperature for DA white dwarf structures. Each separate thin line illustrates the evolution of a white dwarf with different total mass, starting from the top (right) line which is for a $0.4M_{\odot}$ white dwarf all the way down to the bottom line which is for a $1.2M_{\odot}$ white dwarf. The thick black lines indicate isochrones of constant age. The age of each isochrone in Gyr is specified nearby. The open circles near the top left corner indicate the effective temperature at which neutrino cooling becomes less important than thermal cooling. The onset of convective core coupling is shown as open circles at lower luminosities. The filled black circles designate the onset of crystallisation in the core of the white dwarf. This plot shows that for higher mass white dwarfs convective core coupling occurs later in the evolution than crystallisation, whereas for low mass white dwarfs the opposite is true. Reproduced from Fontaine et al. [2001].

As shown in Fig. 1.7 for larger mass white dwarfs, crystallisation occurs earlier than convective core coupling and these two processes can be observed as two separate peaks in the theoretical luminosity function due to the separation in age when the onset occurs [Fontaine et al., 2001]. This means that for these white dwarfs the two processes can be distinguished. For lower mass white dwarfs this is not possible as the two processes overlap in time. The signature of convective core coupling is also more significant on the luminosity function, because the latent heat release of crystallisation occurs over a larger period of time [Fontaine et al., 2001]. Therefore, its effect is averaged over a larger range, reducing its signature. This is illustrates in more detail in Fig. 5 of Fontaine et al. [2001].

1.3.7 Debye cooling

Once the white dwarf becomes cool enough, it will once again experience acceleration in its cooling. This time due to quantum effects, in a process known as Debye cooling [Lamb and van Horn, 1975]. In the crystallised solid that is now the white dwarf's core the specific heat is determined by the phonons which are created by the vibrations of the ions in the lattice [van Horn, 1971]. This specific heat is low, leading to accelerated cooling. In Fig. 1.6 this stage is seen around $\mathrm{Abs}\log \mathrm{L/L_{\odot}} \approx 5.0$ [Koester and Chanmugam, 1990].

Debye cooling will set in faster for more massive white dwarfs due to their larger density [Fontaine et al., 2001]. This means that massive white dwarfs will cool faster to the same luminosity than average mass white dwarfs. This will also happen if the oxygen content of the core is enriched [Fontaine et al., 2001].

Gravitational contraction of the outer layers becomes significant once again, when the Debye cooling has removed a large portion of white dwarf's thermal energy [Fontaine et al., 2001]. Eventually, a white dwarf will lose the entirety of its thermal reservoir, leaving it devoid of light in a state known as a black dwarf.

1.3.8 Remnant planetary systems

Since the majority of stars will become white dwarfs, a question arises regarding the fate of planetary systems. There is now plenty of evidence that such systems do survive into the white dwarf stage. A transit of a disintegrating planet has been observed around the white dwarf WD1145+0170 [Vanderburg et al., 2015]. An evaporating giant planet has been inferred to orbit WDJ0914+1914 [Gänsicke et al., 2019]. The short-term variations of emission lines in the spectrum of SDSS1228+1040 have also provided evidence for the existence of a planetesimal which is causing a 20

year precession in the gas disk around the star [Manser et al., 2019].

Evidence also comes from the observations of metals in the spectra of DZ (or DBZ, DAZ etc) white dwarfs [Jura, 2003; Farihi et al., 2010]. Due to the immense densities and surface gravities, metals should rapidly diffuse out of the atmosphere as the diffusion timescales are much less than the lifetime of the white dwarf [Koester and Chanmugam, 1990]. Thus the presence of metals in the spectra hints that there has been recent or ongoing accretion of metals from an external source. Some have argued that the interstellar medium (ISM) could be such a source [Dupuis et al., 1992]. However, studies have shown that typical accretion rates from ISM are not enough to counteract diffusion [Koester and Chanmugam, 1990]. Additionally, there does not seem to be any correlation between metal abundances observed and the white dwarf position in relation to interstellar material [Farihi et al., 2010].

Radiative levitation is another possible explanation. In this scenario it is assumed that the radiation field of the white dwarf gives momentum to the metals depending on their absorption coefficients [Oswalt and Barstow, 2013, Chap. 11]. As the temperature of the star decreases from the core to the surface, the metals would experience higher momentum from the bottom than the top, overcoming diffusion making them float in the atmosphere. The absorption coefficient can vary many orders of magnitude across different metals. Therefore, radiative levitation can lead to relative diffusion, where some metals diffuse faster out of the atmosphere than others [Oswalt and Barstow, 2013, Chap. 11]. However, the majority of metal-rich white dwarfs are convective, and are found below the effective temperature where radiative levitation is said to occur. Thus, it is not a likely explanation.

The most favoured explanation is the accretion of metals from planetesimals orbiting a white dwarf. These planetesimals can be perturbed onto highly eccentric orbits that brings them into the tidal disruption radius of the white dwarf, disrupting the planetesimal, creating a planetary debris disk that eventually gets accreted onto the white dwarf [Jura, 2003]. Such debris disks have been observed around white dwarf by studying them in infrared [Zuckerman and Becklin, 1987; Jura, 2003].

The identification of the metal lines and the ability to measure the metal abundances allows for unique determination of the interior compositions of exoplanetary systems [Zuckerman et al., 2007]. No other such method exists. However, to transform the observed abundances into masses, it is necessary to know the volume over which the metals are distributed. Convection efficiently mixes the metals homogeneously over the entirety of the convection zone and increases the diffusion timescales of metals. Provided we know the size of the convection zone, we can therefore deduce the masses of the metals. The size of the convection zone is closely

related to the efficiency of convection, which is difficult to determine in 1D. Therefore, 3D models can also be used to improve this aspect of white dwarf modelling.

Helium-atmosphere white dwarfs are important for remnant planetary systems as the diffusion timescales in helium-dominated atmospheres are longer than in hydrogen-dominated atmospheres [Oswalt and Barstow, 2013, Chap. 11]. This means that it is easier to observe rarer metals in helium-dominated atmosphere white dwarfs [Girven et al., 2012]. The combination of observations of metals in helium-dominated and hydrogen-dominated atmosphere white dwarfs can also be used to determine the lifetimes of the debris disks [Girven et al., 2012]. There is also evidence that the presence of hydrogen in helium-dominated atmosphere white dwarfs is correlated with the presence of metals, giving evidence for accretion of water-rich planetesimals [Gentile Fusillo et al., 2017].

1.4 Atmospheric modelling

The observed spectroscopic and photometric data of a star is made up of light that was generated in its deep interior and left through its envelope and atmosphere. The atmosphere is the last point of contact with the star for the observed photons, thus in order to decode the information stored in spectroscopic and photometric observations, we must understand the path of the light as it travels through the atmosphere [Böhm-Vitense, 1989, Chap. 5]. This is achieved by modelling the stellar atmospheres. Assumptions are used to simplify the calculations involved.

We know that stars are not in thermodynamic equilibrium, because there is a net outward energy flow which we observe. When modelling the atmospheres of cool white dwarfs we use the assumption of local thermodynamic equilibrium [Oswalt and Barstow, 2013, Chap. 11]. However, this assumption is not valid for white dwarfs with high effective temperatures of around $T_{\rm eff} > 50\,000$ K [Barstow et al., 1993; Dreizler and Werner, 1993]. We do not consider such white dwarfs in this thesis. Local thermodynamic equilibrium means that a portion of a star's atmosphere at a given geometric depth can be considered to have the same temperature, such that thermodynamic equilibrium can be assumed at that depth [Böhm-Vitense, 1989, Chap. 4]. For cool white dwarfs this is a good assumption, because the distance over which temperature changes considerably is much larger than the mean free path of photons [Carroll and Ostlie, 2007, Chap. 9]. This is due to the high density of white dwarfs causing frequent collisions between the photons and particles in the atmosphere.

The net movement of photons from the deep interior to the surface is caused

by the outwardly decreasing temperature and pressure stratifications. An example of observational evidence for this comes from limb darkening in stars. This occurs due to line of sight allowing us to see deeper into the star near its center than its limb as can be seen in Fig. 1.8. The center of the star's disk will appear brighter than its limb because the temperature of the deeper layers is higher [Carroll and Ostlie, 2007, Chap. 9]. Although, temperature and pressure decrease outwardly, each layer must transmit the same amount of flux, meaning that the star is in thermal equilibrium [Böhm-Vitense, 1989, Chap. 6]. If this was not the case, then the observed temperature of the star would vary greatly from one moment to next, which does occur in pulsating white dwarfs.

Another assumption that can be made in white dwarf atmosphere modelling is the plane-parallel geometry of the atmosphere [Oswalt and Barstow, 2013, Chap. 11]. This is a good assumption because the depth of the atmosphere is much smaller than the radius of the white dwarf. This assumption is needed to define the vertical optical depth, so that it is independent of the angle of the light beam [Böhm-Vitense, 1989, Chap. 4].

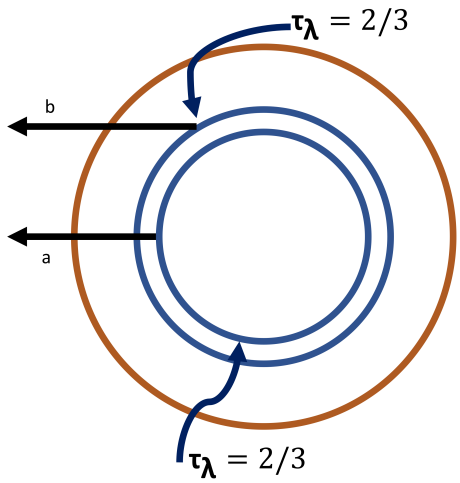

Figure 1.8: A schematic of limb darkening in stars. The line of sight of the observer is indicated by the black arrows. The observed photons are generated at $\tau_\lambda = 2/3$, where τ_λ is the optical depth at given wavelength, λ. However, this optical depth does not correspond to the same geometric depth. The photons travelling near the center of the disk (arrow a) come from a deeper atmospheric layer where temperature is higher and thus the disk appears brighter. Photons travelling near the limb (arrow b) come from a geometrically shallower depth, where temperature is lower and thus the limb appears darker.

In atmosphere modelling we have to use these approximations to determine the temperature, pressure, density and opacity stratifications in order to be able to calculate synthetic energy distributions that can be used to compare with observed spectra or photometric magnitudes [Oswalt and Barstow, 2013, Chap. 11].

1.4.1 Radiative energy transport

The total flux radiated by a star is given by the Stefan-Boltzmann law

$$\pi F(0) = \sigma T_{\text{eff}}^4, \tag{1.1}$$

where $\pi F(0)$ is the total flux per cm^{-2} emitted at the surface and σ is the Stefan-Boltzmann constant equal to 5.67×10^{-8} W m^{-2} K^{-4} [Boltzmann, 1884]. This is also the amount of flux that has to be transmitted by each layer of the atmosphere [Böhm-Vitense, 1989, Chap. 6]. This law allows for the determination of the effective temperature of a star, which is defined as the temperature of a blackbody emitting the same amount of flux.

We first assume the flux is carried by photons alone, which get absorbed and re-emitted in random directions by gas particles in the atmopshere. This happens in a radiative equilibrium. In the prescription of radiative energy transport we only need to consider the radial direction of the star because for a spherically symmetric star other components are equal to zero [Böhm-Vitense, 1989, Chap. 5]. This is a good assumption for white dwarfs since the depth of the atmosphere is much smaller than the total radius of the white dwarf [Oswalt and Barstow, 2013, Chap. 11]. Although photons are massless, they carry momentum and thus exert radiation pressure that supports the atmosphere against gravitational collapse [Böhm-Vitense, 1989, Chap. 4].

The energy of the light beam is defined as

$$E_\lambda = I_\lambda \, \mathrm{d}\lambda \, \mathrm{d}\omega \, \mathrm{d}A \, \mathrm{d}t, \tag{1.2}$$

where E_λ is the energy of the photons at a given wavelength, λ, I_λ is the specific intensity, ω is the solid angle, A is the cross sectional area of the light beam and t is time [Böhm-Vitense, 1989, Chap. 4]. This equation defines the specific intensity of the light beam. It is the amount of energy carried by photons at a given wavelength in a unit time and per unit solid angle. Since it is defined per unit solid angle, the specific intensity of a light beam does not change with the beam spreading out as it travels. An example of specific intensity is the Planck function which determines the specific intensity for a blackbody.

For the Sun we are able to observe its specific intensity as its surface is resolvable. For stars that are not resolvable with a telescope, we are observing the specific intensity integrated over all angles, which is the flux [Böhm-Vitense, 1989, Chap. 5].

The intensity transmitted by radiation is given by

$$\cos\theta \frac{\mathrm{d}I_\lambda}{\mathrm{d}\tau_\lambda} = -I_\lambda + S_\lambda, \tag{1.3}$$

where θ is the angle between the light beam and the radial direction of the star, τ_λ is the optical depth of photons with given wavelength, S_λ is the source function and is defined as $S_\lambda = \epsilon_\lambda/\kappa_\lambda$, where ϵ_λ is the emissivity coefficient (at given wavelength) and κ_λ is the absorption coefficient which is also known as the opacity [Böhm-Vitense, 1989, Chap. 5]. This is the radiative transfer equation and it considers what happens to the intensity of the light beam as it travels through matter. Emission will increase the intensity of the light beam, whereas absorption will decrease it. Therefore, the source function describes how the intensity of the light beam changes as the original photons from the light beam are removed and are replaced by photons from the surrounding gas.

From Eq. 1.3 we can deduce three scenarios. The first is when intensity does not change and this occurs when the intensity of the light beam is equal to the source function [Böhm-Vitense, 1989, Chap. 5]. This happens in a blackbody. As the intensity is equal to the source function, the blackbody's source function is equal to the Planck function.

If the intensity of the beam is larger than the source function, then the intensity will decrease as the beam moves through the atmosphere. On the other hand, if the source function is larger, then the intensity will increase. In general the intensity tends to change in order to represent the local source function, i.e. the local photons in the surrounding gas [Böhm-Vitense, 1989, Chap. 6]. This is not always possible, especially if the source function varies too rapidly with distance for equality to be attained.

The radiative flux can then be found by integrating the specific intensity with respect to the solid angle.

$$\pi F_\lambda = \int I_\lambda \cos\theta \, \mathrm{d}\omega. \tag{1.4}$$

1.4.2 Temperature stratification

The temperature stratification of the atmosphere is determined by the flux transport. To determine it, we can use the Eddington approximation as a simplification, where

the intensity varies linearly as a function of $\cos\theta$ [Böhm-Vitense, 1989, Chap. 6]. This leads to the Eddington-Barbier relation where the surface flux is defined by

$$F_\lambda(0) = S_\lambda(\tau_\lambda = 2/3). \tag{1.5}$$

This means that the observed flux at the surface of the star comes from photons at an optical depth $\tau_\lambda = 2/3$ (see Fig. 1.8). If local thermodynamic equilibrium is assumed then the source function at a given depth is equal to the Planck function and with the assumption of a grey atmosphere, where the opacity is independent of wavelength, one finds

$$T_{\text{eff}}^4 = T^4(\tau = 2/3). \tag{1.6}$$

This indicates that the effective temperature of a star is its temperature at $\tau = 2/3$ [Böhm-Vitense, 1989, Chap 6.].

In reality, however, a more rigorous calculation, which takes into account the non-greyness of the atmosphere, leads to a temperature stratification that can be written as

$$T^4(\tau) = \frac{3}{4} T_{\text{eff}}^4(\tau + q(\tau)), \tag{1.7}$$

where $q(\tau)$ is a slow-varying function of τ [Böhm-Vitense, 1989, Chap. 6]. When computing atmospheric models, the grey atmosphere solution is found first in order to be able to determine the value of $q(\tau)$.

1.4.3 Opacity

As a photon travels through the star it constantly gets absorbed and re-emitted by gas particles. This means that photons do not travel through a star at the speed of light in vacuum. Instead, they follow a path characterised by a random walk with a small mean free path [Carroll and Ostlie, 2007, Chap. 9]. The absorption coefficient of photons with given wavelength, κ_λ, is the collisional cross section of a photon which determines how it interacts with particles in the atmosphere. It is also known as opacity. The optical depth, τ_λ, is defined as the number of mean free paths a photon will travel from its original position to the surface [Carroll and Ostlie, 2007, Chap. 9]. This means that we will not see light that has been formed deeper than around $\tau_\lambda \approx 1$. An optically thick gas is therefore defined by $\tau_\lambda \gg 1$, whereas optically thin is defined by $\tau_\lambda \ll 1$. The optical depth is written as

$$\tau_\lambda = \int_0^z \kappa_\lambda \mathrm{d}z, \tag{1.8}$$

where z is the geometric depth with $z = 0$ defining the surface.

There are four ways photons can be absorbed by particles. True absorption involves the complete removal of photons from the light beam and surroundings, but opacity also takes into account scattering, where a photon is removed from the light beam by changing its direction of travel [Böhm-Vitense, 1989, Chap. 7]. In true absorption the energy of the photon is completely deposited into the thermal energy of the surrounding gas.

The first type is known as bound-bound absorption and it is due to the transition of a bound electron between two energy levels of an atom or an ion [Bohr, 1913]. This is also known as excitation. In true absorption the photon will be lost. However, if a photon is first absorbed by an electron and then is re-emitted following de-excitation, it becomes a scattering process since it is unlikely that the emitted photon will be travelling in the same direction as the light beam [Böhm-Vitense, 1989, Chap. 7]. This type of opacity contributes only at wavelengths corresponding to energy differences between the levels. Therefore, it is responsible for the formation of lines in the spectra of stars.

Another source of opacity is the bound-free absorption or photoionisation. This happens when a photon has enough energy to ionize a particle by providing the energy for an electron to become unbound. The resulting thermal energy of the electron will then be equal to $E_\nu - E_{\text{ionisation}}$, where E_ν is the energy of the photon and $E_{\text{ionisation}}$ is the ionisation energy [Böhm-Vitense, 1989, Chap. 7]. This means that unlike the bound-bound absorption, bound-free absorption contributes to the opacity at many wavelengths as long as the wavelength of the photon corresponds to $E_\nu > E_{\text{ionisation}}$. Therefore, these transitions contribute to the continuum opacity. For large wavelengths and therefore low photon energies, only high energy levels of the atom or ion can contribute to bound-free absorption [Böhm-Vitense, 1989, Chap. 7].

Free-free absorption occurs when a free electron in a presence of an ion absorbs a photon. This leads to an increase of the thermal energy of the electron. The presence of an ion is needed to conserve both energy and the momentum [Böhm-Vitense, 1989, Chap. 7]. This, again, contributes to the opacity of the continuum as this type of process can occur at any wavelength. For the largest wavelengths only free-free absorption is able to contribute to the opacity.

As mentioned earlier, scattering also contributes to the opacity of the gas. If the temperature of the atmosphere is large, then bound atoms cannot exist and therefore electron scattering dominates the opacity. There are three main types of scattering processes. The first is Thomson scattering, which happens when a free

electron scatters a photon. It has a constant, small cross section at all wavelengths, which is smaller than the hydrogen cross-section for photoionisation [Böhm-Vitense, 1989, Chap. 7]. This type of scattering is most dominant when the electron density is large and thus it is important for white dwarfs. Compton scattering is the scattering of a photon by a loosely bound electron. This occurs if the photon's wavelength is much smaller than the atom's radius [Böhm-Vitense, 1989, Chap. 7] and could be relevant for hot white dwarfs [Madej, 1994; Suleimanov et al., 2007]. Rayleigh scattering happens when the photon's wavelength is larger than the atom's radius. Rayleigh scattering dominates in the UV and the blue part of the optical spectrum of white dwarfs.

All these processes can also lead to emission of light, if instead of absorbing the photon, a photon is emitted. In the case of free-free absorption, the emission process is known as bremsstrahlung.

If the atmosphere becomes denser for a given constant temperature, the chance of an interaction between a photon and a particle increases, leading to larger atmospheric opacity. At higher temperatures, more of the gas will be ionised, affecting the opacity. This indicates that opacity is both a function of density and temperature [Carroll and Ostlie, 2007, Chap. 9].

As the opacity depends on the interactions between photons and atoms or ions, we need to know the number of atoms in different quantum states and the degree of ionization of the gas in order to accurately calculate the opacity of the atmosphere. The Boltzmann and Saha equations allow us to do that, respectively [Böhm-Vitense, 1989, Chap. 7]. The Boltzmann equation is given by

$$\frac{N_n}{N_1} = \frac{g_n}{g_1} e^{-\chi_n / kT}, \tag{1.9}$$

where N_1 and N_n are the number of atoms in the ground state and n-th energy level, respectively; g_1 and g_n are the statistical weights for the ground and n-th energy level, respectively; χ_n is the transition energy between the two levels; k is the Boltzmann constant and T is the temperature of the gas. The statistical weight of an energy level is given by the number of combinations of the quantum numbers that result in the same energy. The number of atoms in different quantum states is also known as the occupation number [Böhm-Vitense, 1989, Chap. 7]. The number of ions present in a gas will decrease the number of atoms in the ground state.

The Saha equation is derived from Boltzmann equation and is defined as

$$\frac{N^+ n_e}{N} = \frac{u^+}{u} 2 \frac{(2\pi m)^{3/2}}{h^3} (kT)^{3/2} e^{-\chi_{\text{ion}} / kT}, \tag{1.10}$$

where N^+ and N are the number of ionised and neutral atoms in their ground state, respectively; n_e is the electron density; u^+ and u are the partition functions for the ionised and neutral atoms, respectively, and they depend on the statistical weights of the energy levels; m is the mass of the electron; h is the Planck constant and χ_{ion} is the ionisation energy of the atom [Böhm-Vitense, 1989, Chap. 7]. For the same number of particles, the opacity can vary greatly depending on the degree of excitation and ionisation of the gas, as the interaction between the photons and particles will change.

For a given atmospheric layer with particular temperature and electron density or pressure, we can calculate the degree of ionization for all atoms and ions present and therefore the opacity. In general, larger opacity means that we cannot see deep into the star. Therefore, the light observed at wavelengths where the gas is opaque comes from higher up atmospheric layers where the temperature is lower and thus the emitted intensity is lower for larger opacity.

The Rosseland mean opacity, κ_{R}, is a flux-weighted harmonic mean of opacities over all wavelengths and is defined as

$$\frac{1}{\kappa_{\text{R}}} = \frac{\int_0^\infty \frac{1}{\kappa_\lambda} \frac{\mathrm{d}B_\lambda}{\mathrm{d}T} \, \mathrm{d}\lambda}{\int_0^\infty \frac{\mathrm{d}B_\lambda}{\mathrm{d}T} \, \mathrm{d}\lambda}, \tag{1.11}$$

where B_λ is the Planck function. As small opacities result in larger flux, low opacities are weighed most heavily. Therefore, the Rosseland mean opacity is closest to the smallest value of κ_λ [Böhm-Vitense, 1989, Chap. 8]. The Rosseland mean opacity also defines the Rosseland optical depth, τ_{R}, which can be used as a depth indicator of an atmosphere. If one were to use a constant opacity over all wavelengths when computing a stellar atmosphere, then the result would be a grey atmosphere. A non-grey atmosphere is thus one that considers the opacity as a function of wavelength and is the most physical model atmosphere. Rosseland mean opacity is constructed such that it results in a calculation of a grey atmosphere with the same emitted flux as the non-grey atmosphere [Böhm-Vitense, 1989, Chap. 8].

One effect caused by non-greyness is called backwarming [Böhm-Vitense, 1989, Chap. 8]. Non-greyness will cause lines to appear in a star's spectrum by removing flux at certain wavelengths. Therefore, an atmosphere with the same temperature stratification but with absorption lines will produce less flux and therefore will have smaller effective temperature. In principle grey and non-grey atmospheres must produce the same amount of total flux for a given star. This means that in a non-grey atmosphere more flux has to be emitted at other (non-spectral line) wavelengths with smaller opacities, i.e. the continuum. To produce more energy at

smaller opacities, the temperature has to be higher in deeper layers where continuum is formed, changing the overall temperature stratification. Therefore, the continuum will now resemble the continuum of a hotter star.

The typical opacities are shown in Figs. 1.9 and 1.10. These have been taken from the Montréal white dwarf atmospheric code [Bergeron et al., 1995]. The opacity is made up of various sources, each highlighted in the figure. Both in DA and DB white dwarfs the bound-free opacities dominate the continuum.

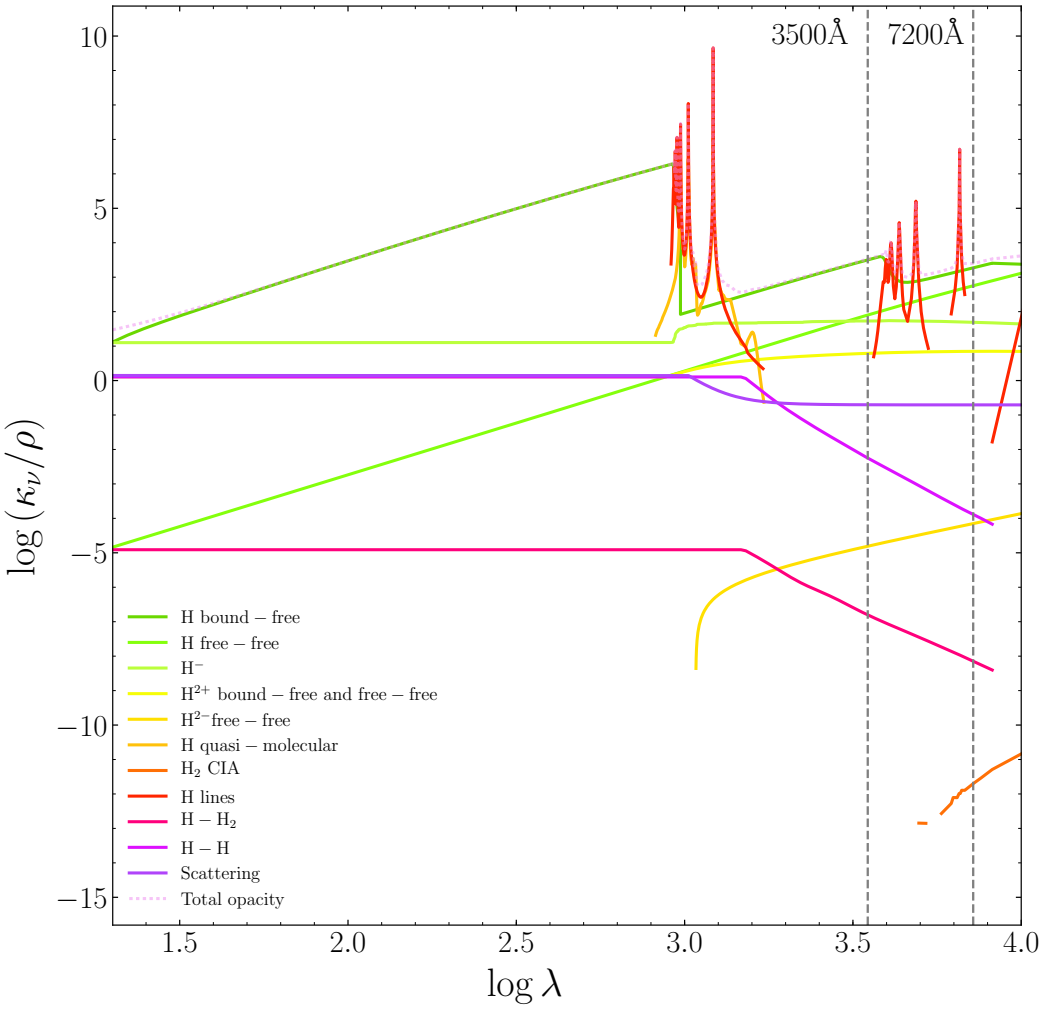

Figure 1.9: The opacity as a function of wavelength for a DA white dwarf with $\log g = 8.0$ and $T_{\rm eff} = 13\,000$ K. The units of the variables are in cgs. Each opacity source is detailed in the label. The optical range is highlighted with the use of grey dashed lines. The opacity is heavily dominated by the hydrogen bound-free absorption and hydrogen spectral lines.

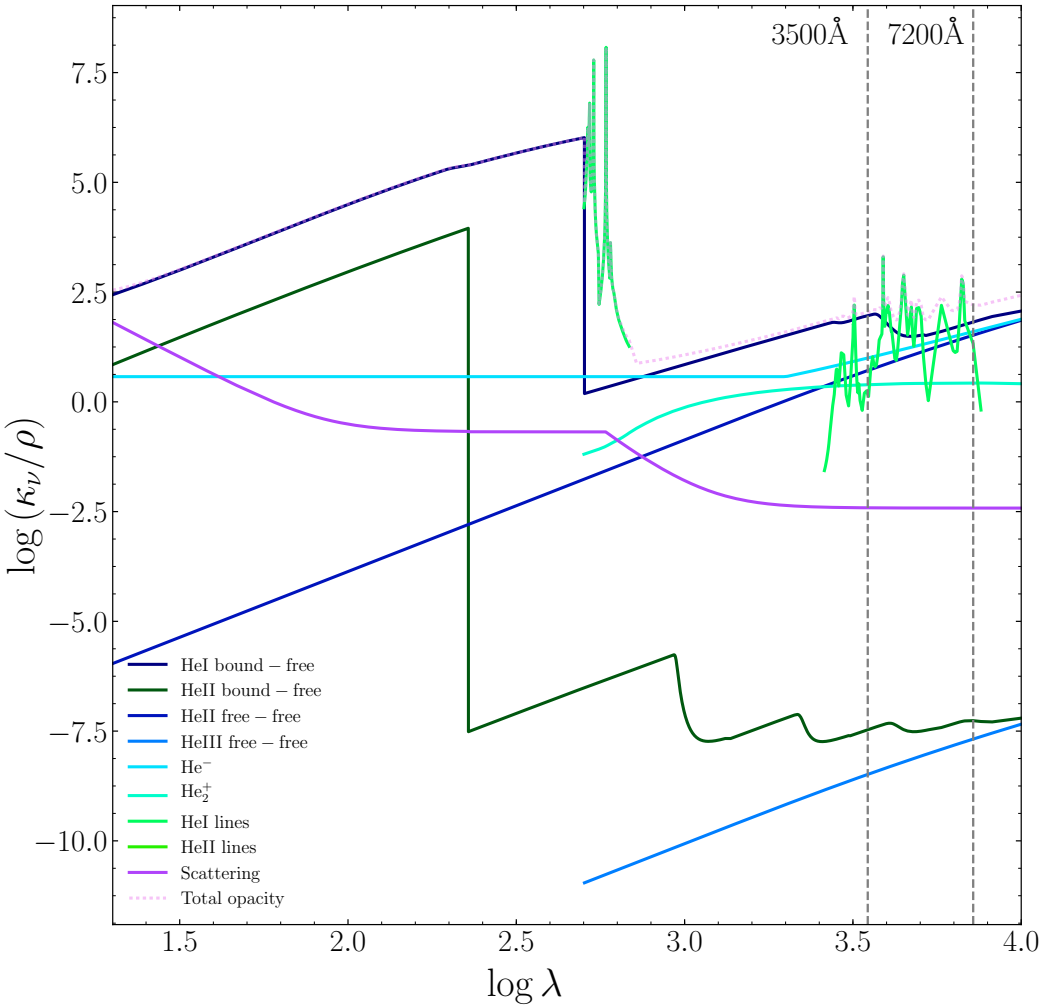

Figure 1.10: The opacities as a function of wavelength for a DB white dwarf with $\log g = 8.0$ and $T_{\rm eff} = 18\,000$ K. The units of the variables are in cgs. Each opacity source is detailed in the label. The optical range is highlighted with the use of grey dashed lines. The opacity is heavily dominated by the He I bound-free absorption and helium spectral lines.

1.4.4 Pressure stratification

When modelling the atmosphere of a star we have to consider that the outward force from the pressure exerted by the gas must be balanced by the gravitational force. If this was not the case, the star would either expel its outer layers if the outward pressure overcomes gravity or collapse if the opposite is true. Thus, we assume stars

are in hydrostatic equilibrium such that

$$\frac{\mathrm{d}P_g}{\mathrm{d}z} = g\rho, \tag{1.12}$$

where P_g is the gas pressure, g is the gravitational acceleration and ρ is the density of a given layer [Böhm-Vitense, 1989, Chap. 9]. As the atmosphere is thin compared to the radius of the white dwarf we can assume that the value of g in the atmosphere is constant. Additionally, we can also include the turbulent gas pressure which arises from particles having bulk momentum, and the radiation pressure which comes about due to photons possessing large momenta if radiation is particularly strong [Böhm-Vitense, 1989, Chap. 9].

When modelling the stellar atmospheres, we solve the equations of radiative transfer, state and hydrostatic equilibrium. This is done numerically due to the complex dependency of various parameters on opacity. The inputs for such modelling include effective temperature, surface gravity and atmospheric composition. First, a temperature stratification is assumed, and with the equation of state and hydrostatic equilibrium, the opacities and the stratifications of pressure and density are determined. This process is iterated until the temperature stratification satisfies the equation of radiative transfer, usually to a level of less than 1%.

In order to find the pressure of a given atmospheric layer, we have to integrate the right hand side of Eq. 1.12, therefore the procedure described in the above paragraph is made slightly more complicated. Numerical integration is used and is started at a small optical depth where the initial gas pressure is much smaller than the gas pressure of the atmospheric layer to be found [Böhm-Vitense, 1989, Chap. 9]. Once the pressure of the layer is found, we can continue integrating stepwise for a layer below. This is repeated until the entire pressure stratification is found.

1.4.5 Convection

In the atmosphere of a white dwarf, energy can either be transported by radiation or convection. Which process is dominant depends on the Schwarzschild criterion. A layer inside a star is said to be unstable against convection if

$$\left|\frac{\mathrm{d}T}{\mathrm{d}P}\right|_{\text{radiative}} > \left|\frac{\mathrm{d}T}{\mathrm{d}P}\right|_{\text{adiabatic}}, \tag{1.13}$$

where T and P are the temperature and gas pressure of the layer [Böhm-Vitense, 1989, Chap. 14]. This particular form of Schwarzschild criterion assumes that we started with a radiative atmosphere. The energy can be carried by both processes

at the same time, with one being dominant or both transporting equal amounts of energy flux.

Convection transports energy via the movement of a fluid. In general, if a parcel of gas that is less (or more) dense than its surroundings receives a kick, it will move upwards (or downwards). The Schwarzschild criterion then determines whether this parcel of gas will carry with this motion or if it travel back to its original position [Böhm-Vitense, 1989, Chap. 14]. If the motion carries on, then the gas is said to be unstable against convection causing convective energy transport to set in. During its travel, the bubble of gas must be in pressure equilibrium with its surroundings, thus for it to be less dense it has to be hotter. Therefore, in convection hot gas rises to the surface while cold gas falls to the center [Böhm-Vitense, 1989, Chap. 14]. This can be observed in the convection zone of the Sun or in Earth's atmosphere. The parcel of gas will eventually reach a layer where the density of the surroundings matches its own. There it will deposit (or absorb) its excess (or deficit) of energy and dissipate into the surroundings [Böhm-Vitense, 1989, Chap. 14].

The amount of energy that can be transported depends on the temperature gradient, with larger gradients needed to transport larger amounts of energy. Radiative energy transport can also be made difficult by a large opacity, which then requires an increase in the radiative temperature gradient of the gas and thus fulfils the Schwarzschild criterion. Therefore, if either the opacity or the temperature gradient becomes too large, this will result in the onset of convection [Carroll and Ostlie, 2007, Chap. 10]. Convection will also kick-in if the adiabatic gradient is low, which happens when the specific heat of the gas is large. For example, this occurs in the ionization zone, where energy is used to ionize the gas rather than heat it [Carroll and Ostlie, 2007, Chap. 10]. This is the main reason for convection zones in the atmospheres of white dwarfs [Fontaine et al., 2001]. Hydrogen ionization is responsible for the formation of a convection zone in the atmospheres of DA white dwarfs. For DB white dwarfs both the He I and He II ionization takes place, leading to the formation of two convection zones in the atmosphere.

For the bubble of gas to keep rising or sinking, it must not have the same density as its surroundings. To achieve this, it has to travel fast enough not to be able to exchange heat with the material surrounding it. Due to these high velocities the convection is turbulent, leading to complete mixing of the material inside the convection zone [Carroll and Ostlie, 2007, Chap. 10]. This occurs when the star's temperature gradient is the same as the adiabatic temperature gradient, leading to what is known as adiabatic convection. In white dwarfs such convection happens in the deeper layers of the star [Tassoul et al., 1990]. In the upper layers of a

star, where the opacity is lower and the star's temperature gradient is larger than the adiabatic temperature gradient, radiative energy transfer will transport energy alongside convection, leading to what is known as superadiabatic convection [Tassoul et al., 1990]. From this it is clear that convection is a time-dependent 3D process and needs the treatment of fluid dynamics. However, because of computational limitations in the majority of atmosphere modelling, convection is treated using 1D approximations.

In white dwarf 1D atmosphere modelling the ML2/α version [Tassoul et al., 1990] of the mixing length theory [Böhm-Vitense, 1958], MLT, is used to treat convection. This approximation depends on a free parameter that defines how far a parcel of gas will travel before it dissipates (or absorbs) its excess (or deficit) of energy [Böhm-Vitense, 1989, Chap. 14]. The characteristic distance travelled is known as the mixing length, l, and is characterised in modelling by the mixing length parameter, $\alpha = l/H_p$, where H_p is the pressure scale height. However, this is not the only free parameter used in MLT. There are three additional parameters denoted as a, b, c that define the average speed of convective elements, the energy flux and the convective efficiency, respectively [Tassoul et al., 1990]. The ML2/α version of MLT sets these values to $a, b, c = 1, 2, 16$ [Tassoul et al., 1990]. For DA white dwarfs the commonly used value of the mixing length parameter is 0.8 [Tremblay et al., 2010]. For DB and DBA white dwarfs the value of 1.25 is used instead [Bergeron et al., 2011]. These values were determined from observations as the theory does not define them. Observations also show that deeper layers have more efficient convection which results in larger values of mixing length parameter, highlighting the fact that no one choice of the mixing length parameter can describe all of the convection zone. One such example comes from asteroseismological studies, where the observed blue edge of the instability strip is located at a higher effective temperature than the theoretical blue edge calculated at ML2/$\alpha = 1.25$. Therefore, to raise the effective temperature of the theoretical blue edge, the convective efficiency must be increased at the bottom of the convection zone compared to the value of 1.25, which has been calibrated from spectroscopic observations that originate from higher up layers (see e.g. Bergeron et al. 2011; Van Grootel et al. 2012; Hermes et al. 2017; Van Grootel et al. 2017; Giammichele et al. 2018). This leads to the conclusion that MLT is a poor approximation of convective energy transport. A recent improvement in the prescription of convection in white dwarfs has been achieved with the introduction of 3D atmosphere modelling which treats convection from first principles with no need for free parameters [Tremblay et al., 2011, 2013b]. 3D modelling is especially important for those layers that experience superadiabatic convection. The subject

of this thesis revolves around the use of such modelling to simulate the atmospheres of DB and DBA white dwarfs.

In 1D atmosphere modelling convection is included according to the following procedure. For each layer, the temperature and pressure is determined following the calculations described in above sections. With these values the Schwarzschild criterion is then checked to determine whether convection sets in. If it does, then the flux transported by that layer is modified as

$$\pi F = \pi F_r + \pi F_c = \sigma T_{\text{eff}}^4, \tag{1.14}$$

where F_r is the radiative flux and F_c is the convective flux. Convection affects the total transported flux and thus the temperature stratification. Convective flux is proportional to the density [Böhm-Vitense, 1958, Chap. 14]. In the upper layers of the atmosphere where density is low, convection will transport less of the flux. These are the layers where superadiabatic convection occurs.

1.4.6 Synthetic spectra

The continuum of a star's spectrum is defined by slow changes in opacity. Rapid changes cause the formation of spectral lines which remove (or add in the case of emission lines) intensity at specific wavelengths from (or to) the continuum. For absorption lines to be able to form the temperature of the star must decrease outwards [Böhm-Vitense, 1989, Chap. 10]. Absorption lines are caused by large opacity at specific wavelengths determined by the bound-bound transitions of electrons, which need significant amounts of energy [Böhm-Vitense, 1989, Chap. 10]. Therefore, spectral lines are often observed at shorter wavelengths of the star's spectrum. This means that the inclusion of lines tends to make colours of the star redder as it removes intensity from the bluer parts of the spectrum.

A useful tool to measure the strength of a given line is called the equivalent witdh, W_λ. It is the width of a rectangle with height equal to one that would have the same area as the line. It is defined as

$$W_\lambda = \int_{\text{line}} \frac{F_{\text{continuum}} - F_\lambda}{F_{\text{continuum}}} \, \mathrm{d}\lambda, \tag{1.15}$$

where $F_{\text{continuum}}$ and F_λ are the continuum and line flux, respectively [Böhm-Vitense, 1989, Chap. 10]. The integral is performed over the wavelength range of the line. The depth of the line thus depends on the continuum and line opacity, and the temperature gradient of the atmosphere.

The core of the line denotes the highest opacity region and therefore is formed highest up in the atmosphere. As one moves away from the core of the line to its wings, the opacity decreases. Therefore, the wings are formed progressively deeper in the star until they reach the depth where the continuum is formed, merging the wings into the continuum.

Line broadening

One would assume that the lines seen in the spectra of stars should occur at one specific wavelength corresponding to the difference in energy between the two energy levels of the electron bound to an atom or ion. However, the observed spectral lines are spread over a range of wavelengths. This happens due to line broadening processes.

The first is natural broadening and it is due to the Heisenberg's uncertainty principle, which can be written as

$$\sigma_t \sigma_E \geq \frac{\hbar}{2}, \tag{1.16}$$

where σ_t and σ_E are the standard deviations of time and energy, and $\hbar$ is the reduced Planck constant [Heisenberg, 1927]. As the electron occupies an energy level for an instant of time, it means that the energy of the level has some uncertainty. Both levels in the transition will have such uncertainty, resulting in a line that extends over a range of wavelengths. The larger the amount of radiation, the shorter the lifetime of an electron in a given energy level and therefore the broader the line. The shape of this line profile is known as a Lorentzian or damping profile [Carroll and Ostlie, 2007, Chap. 9]. As the transitions can be described using a classical oscillator, the strength of the transition is referred to as its oscillator strength. These can be either measured in lab or derived theoretically.

Another type of broadening comes from the movement of atoms or ions in the gas. It is known as Doppler broadening, since it arises from the Doppler shift of the wavelength of the line caused by motion of particles [Carroll and Ostlie, 2007, Chap. 9]. The shape of a Doppler broadened line is a Gaussian. In thermal equilibrium, the motion of the particles is described by the Maxwell-Boltzmann distribution. As the distribution has an exponential tail, the wings of the Doppler broadened line fall-off exponentially as one moves away from the line core [Böhm-Vitense, 1989, Chap. 10]. This is a faster drop off than observed in naturally broadened lines. Therefore, a spectral line broadened by both natural and Doppler broadening will be dominated by Doppler broadening near the line core and dominated by natural

broadening in the wings [Carroll and Ostlie, 2007, Chap 9.]. Other motions can contribute to Doppler broadening. Convection is one type of large scale motion contributor. It affects the broadening in two ways. First is macroturbulence and it is due to the granulation of the convection zone [Böhm-Vitense, 1989, Chap. 10]. Granulation means that different parts of the star's surface have different velocities. Within each granule the absorption does not change, thus the line profile is the same. However, when all granules are considered together, the apparent line profile seems wider as the lines from different granules are centred at different wavelengths. The second is microturbulence and it is caused by particles having different velocities due to convective motions, resulting in photons which interact differently compared to an atmosphere with no convection [Böhm-Vitense, 1989, Chap. 10]. This alters the opacity and therefore changes the line profile. In 1D modelling these effects are taken into account using free parameters. In 3D these parameters are not needed since the motions are taken into account from first principles. Other sources of Doppler broadening include stellar rotation, pulsations and mass loss [Böhm-Vitense, 1989, Chap. 10].

The most important type of broadening in the spectra of cool white dwarfs is pressure broadening [Oswalt and Barstow, 2013, Chap. 11]. It occurs due to the collisions between atoms or due to the influence of electric fields of ions [Böhm-Vitense, 1989, Chap. 10]. Both of these effects perturb the energy levels of atoms or ions. It has the same profile as natural broadening. It is also called the damping profile as the shape can be described mathematically as an electric charge experiencing damped simple harmonic motion. In some stars, natural and pressure broadening are comparable. However, the width of pressure broadening is proportional to the number of collisions that occur, therefore in environments of high density (e.g. white dwarfs), this type of broadening is most significant.

A combination of Doppler and damping profiles is known as Voigt profile and it describes the total line profile [Böhm-Vitense, 1989, Chap. 10]. As mentioned before, this profile will have a Doppler broadened core and damped wings due to either natural broadening or pressure broadening.

Additional broadening can occur due to factors outside the stellar atmosphere. These include issues with the finite resolution of a spectrograph and instrumental profiles, amongst others [Böhm-Vitense, 1989, Chap. 10].

Hydrogen and helium spectral features

One of the features observed in the spectra of stars that have hydrogen in their atmosphere is known as the Balmer jump [Böhm-Vitense, 1989, Chap. 8]. It occurs

Table 1.1: The Balmer series of hydrogen spectral lines. Data taken from Reader et al. [1980]

	H_α	H_β	H_γ	H_δ	H_ϵ	H_ζ	H_η
Transition	$2 \rightarrow 3$	$2 \rightarrow 4$	$2 \rightarrow 5$	$2 \rightarrow 6$	$2 \rightarrow 7$	$2 \rightarrow 8$	$2 \rightarrow 9$
Wavelength (Å)	6563	4861	4340	4102	3970	3889	3835

at 3646Å due to the bound-free absorption of electrons from the $n = 2$ orbital which increases the opacity causing a sharp decrease in continuum intensity for wavelengths larger than 3646Å. The size of the jump will depend on the number of hydrogen atoms in the $n = 2$ orbital. The presence of the Balmer jump in the near ultraviolet part of the spectrum increases the U-B colour in the UBV magnitude system [Böhm-Vitense, 1989, Chap. 8].

In cool DA white dwarfs Balmer hydrogen lines are observed in the optical part of spectrum. Similarly to the Balmer jump, these lines are caused by bound-bound transitions of electrons from the $n = 2$ energy level [Böhm-Vitense, 1989, Chap. 8]. Table 1.1 shows more in depth information regarding the Balmer series. The hydrogen lines in DA white dwarfs are broadened by the Stark effect which is caused by the electric fields of passing ions and electrons [Tremblay and Bergeron, 2009]. This is a type of pressure broadening. The Stark effect acts in two ways [Böhm-Vitense, 1989, Chap 11]. Firstly, the electric field causes a shift to the energy levels as they decrease the lifetime of an electron in a given energy level. Secondly, the electric field lifts the degeneracy of the energy levels, resulting in formation of not one, but several lines. These new lines occur in the wings of the central line, such that the resultant line looks broadened. The closer the ion passes, the larger the energy level splitting and therefore the larger the broadening. The splitting also increases with n^2, so higher energy levels have more splitting and therefore the associated lines appear broader. Stark broadening is dependent on pressure and thus is important in the atmospheres of white dwarfs.

In the spectra of cool helium-dominated atmosphere white dwarfs, He I lines are observed. The lines listed in Table 1.2 are the He I lines observed in the optical and similarly to hydrogen are due to electron transitions from the $n = 2$ level. Stark broadening is important above $T_{\rm eff} > 16\,000$ K. Below around $T_{\rm eff} < 16\,000$ K the dominant broadening is due to van der Waals forces from neutral helium atoms and therefore it is known as van der Waals or neutral broadening [Beauchamp et al., 1996]. This happens because the temperature of the atmosphere is low enough for a significant number of neutral atoms to form.

Table 1.2: The optical He I lines. Data taken from Martin [1960] and Martin [1987].

3587, 3614, 3634, 3705, 3733, 3820,
3889, 3965, 4009, 4026, 4121, 4144,
4388, 4438, 4471-4472, 4713, 4922, 5016,
5048, 5876, 6678, 6867, 7065-7066, 7281

Calculation of synthetic spectra

Once the temperature and density (or pressure) stratifications are calculated, they can be used to determine the energy distribution of the star [Böhm-Vitense, 1989, Chap. 10]. This is essentially a synthetic spectrum that can be utilised to fit observations of a star in order to find its effective temperature, surface gravity and composition. To model a synthetic spectrum one has to solve the radiative transfer equation wavelength by wavelength.

Not all electron transitions are as likely to occur. Transitions where an electron moves from its initial level to a closer level are more likely to occur than to an energy level further away. These probabilities are known as f-values or oscillator strengths and will determine the opacity of a given line. The oscillator strengths are defined such that they give the number of electrons per atom or ion involved in the transition [Böhm-Vitense, 1989, Chap. 10].

Once the synthetic emergent energy distribution is calculated, it can be integrated to determine synthetic magnitudes and/or colours, which can also be compared to observations in order to find the atmospheric parameters.

1.5 Thesis layout

In this thesis, the work I carried out to improve the current modelling of helium-dominated atmosphere white dwarfs will be presented. Chapter 2 describes the computation of 1D and 3D models using multiple atmosphere modelling codes. Chapter 3 reviews the computation of the 3D atmospheric models of DB white dwarfs. In it I also derive the corrections to the spectroscopic parameters based on the better treatment of convection. In Chapter 4 the 3D DBA models are introduced and the resulting corrections are applied to observations. The implications of such analysis in terms of further model improvements are also discussed. In Chapter 5 the 3D models are used to calibrate the mixing length parameter in terms of the large scale properties of the convection zone. The work is summarised in Chapter 6.

Chapter 2

Methodology

She was taken under, drowning in her sea
Running like an angel, she was crying and could not see,
Now see everyone's watching as she starts to fall
They want her to breakdown, be a legend of her fall

Mona Lisa
Britney Spears

2.1 1D ATMO code

A large part of the work presented in this thesis has relied on the 1D white dwarf atmosphere code created by the Montréal group. In the following, this code is referred to as ATMO. The ATMO model grid covers the following parameter range: $-2.0 \geq \log \mathrm{H/He} \geq -10.0$ dex, $7.5 \leq \log g \leq 9.0$ dex and $11\,000 \leq T_{\mathrm{eff}} \leq 40\,000$ K, with a step size of $\Delta \log \mathrm{H/He} = 0.5$ dex, $\Delta \log g = 0.5$ dex and $\Delta T_{\mathrm{eff}} = 1\,000$ K. All units are in cgs. In some cases the grid has been expanded and this is mentioned in the relevant chapters. For DB and DBA white dwarfs ML2/α = 1.25 is used, unless otherwise stated. The code assumes a plane-parallel atmosphere in LTE with a constant value of gravity [Saumon et al., 1994]. The models are non-grey and include hydrogen and helium only [Bergeron et al., 1995].

When calculating a model atmosphere and a synthetic spectrum, the input parameters are hydrogen-to-helium number ratio (or abundance), surface gravity and effective temperature. The code is split into two parts. In the first part a model atmosphere is calculated. The input file for this part of the code is shown in Listing 2.1. The second part of the code calculates a synthetic spectrum for a given

temperature and pressure stratification. The input file for this part of the code is shown in Listing 2.2. Thus, one would run a model using the first part of the code and use the output in the second part to calculate a synthetic spectrum.

Listing 2.1: A typical input file for calculating a model atmosphere in ATMO. The first line indicates a file that contains a frequency grid needed for calculating the model. The second line specifies a file which contains the effective temperatures of the grid to be calculated. On the third line, the first, second and third numbers specify the smallest surface gravity of the grid, the largest surface gravity and the step size for surface gravities considered. On the fourth line, the first and second numbers are numerical switches for linearisation in temperature and pressure stratifications, and for calculation of non-grey atmosphere. Fifth line specifies the number of maximum iterations and a numerical parameter that can be used to start the model from a pre-existent model. If this parameter is equal to 1 as shown here, then the model is run from scratch. The next line specifies the helium-to-hydrogen number ratio, the number of grid points in the atmosphere and a numerical switch which indicates whether to print the output on the terminal during the run. The following line indicates whether to include line blanketing of H, He I and He II. However, the code now automatically includes blanketing when needed and thus these indicators are obsolete. The last number on this line is a numerical parameter that determines what type of neutral broadening to use. When running an atmospheric model, this is not important and thus should be set to 0 as shown in the example. The next line gives the four parameters of the mixing length theory. In this example it is set to ML2/α = 1.25. Last line specifies the suffix for the file name of the output model atmospheres.

```
grid_DA_FINAL
tgrid
7.5   9.0    0.5    logg1,loggn,dlogg
1      1   lineartp, nongray
100    1   niter,igris
1.0e+7   100     1    y,ndepth,iprnt
1   1   1   0    ihblk,ihe1blk,ihe2blk,ivdw
1.25    1.000  2.000  16.0      mixlen,mla,mlb,mlc
1.000e-06  2.000e+02    tau1,taun
_radiative
```

Listing 2.2: A typical input file for calculating a synthetic spectrum using the ATMO code. The first line provides a file name which contains the values of frequency to be used in calculating the spectrum. The second line indicates the format of the numbers in the frequency file. The third line specifies the type of the input model, 0 is for models calculated with ATMO, 1 is for 3D models, 2 is for models calculated with the 1D LHD code (described in next section). The next line indicates whether to include H, He I and He II lines. For example, one can calculate a spectrum for a DB model, but without any spectral lines. Such model is not physical, but can be useful for some applications. The last number of the same line indicates the type of neutral broadening to include, 0 is for no van der Waals broadening, 1 is for Unsold [1955] broadening and 2 is for Deridder and van Rensbergen [1976] broadening (described later on in this section). The following line gives the output file name, whereas the last line is the file name of the input atmospheric model.

```
grid_DB
0              0 = f8 format, 1 = f10 format
0              0 = regular mode (1 file per model)
1   1   1   2   ihblk,ihe1blk,ihe2blk,ivdw
950120_radiative_spectra
950120_radiative
```

In general, the following procedure is used when running a model in the ATMO code [Bergeron et al., 1991]. First, a grey atmosphere is calculated using the Rosseland mean opacity. When the convection zone forms it leads to numerical instabilities. This is due to radiative and convective energy transport being treated using separate equations leading to instabilities when a radiative layer turns convective [Bergeron et al., 1991]. The instabilities are combated with corrections ensuring a smooth model convergence. A converged grey atmosphere is then used as an input for calculating the non-grey atmosphere. The model is then run until the following convergence is achieved at each depth

$$\begin{aligned} \Delta P/P &< 10^{-2}, \\ \Delta T/T &< 10^{-3}, \\ \Delta H/H &< 10^{-3}, \end{aligned} \tag{2.1}$$

where Δ denotes the difference in a given parameter between the current and previous iteration; P, T and H are the pressure, temperature and integrated Eddington flux [Bergeron et al., 1991].

To calculate a synthetic spectrum, a model atmosphere must be provided as an input parameter to the second part of the ATMO code. This input file must

contain the values of temperature and pressure as functions of depth in the atmosphere. The values of temperature and pressure are then used to calculate opacity as a function of frequency at each layer in the atmosphere. With this information the radiative transfer equation is solved to find intensity at each frequency. The shape of the lines are determined and various line broadening mechanisms are taken into account. Thus, the calculation of a synthetic spectrum is complete.

2.1.1 Microphysics

ATMO is similar to other stellar atmospheric codes in the way it solves radiative transfer and hydrostatic equations. However, it has been specifically adapted to deal with the microphysics of white dwarfs, namely DA, DB and DBA white dwarfs. In general, both the Bolztmann and Saha equations depend on the partition function, which for isolated atoms diverge to infinity as isolated atoms have an infinite number of energy levels available for transitions [Bergeron et al., 1991, 1995]. ATMO uses the equation of state, EOS, from Hummer and Mihalas [1988], which provides a prescription for the treatment of the dissolvement of upper energy levels due to interactions with neighbouring particles [Bergeron et al., 1991]. Thus, these atoms do not have infinite energy levels and the partition function converges.

The Hummer and Mihalas [1988] equation of state treats non-ideal effects and allows for self-consistent calculation of level populations and opacities [Bergeron et al., 1991]. For this equation of state an important ingredient is the occupation probability formalism, which can be calculated in the following fashion. First, it is assumed that an electron has a finite probability of being bound or ionised. Interactions with neighbouring atoms lead to the decrease of bound probability. There are two types of interactions considered, those with neutral and those with charged neighbouring particles. The neutral interactions are treated using the hard sphere model, where each energy level in an atom is modelled as a sphere of given radius, r_n,

$$r_n \approx f_n^2 a_0, \tag{2.2}$$

where a_0 is the corresponding Bohr radius of a given energy level of the atom under consideration and f_n is a free parameter. In ATMO f_n is set to 0.5, a value that has been calibrated based on observations of DA white dwarfs [Bergeron et al., 1991]. An atom's energy level is effectively destroyed if its r_n is bigger than the interparticle distance. The value of f_n is important for DB/DBA white dwarfs with effective temperatures below 16 000 K where the helium atom is neutral [Bergeron et al., 1995].

The interactions with charged particles are treated using a screened Coulomb potential. It assumes that a given atom experiences an electric field generated by surrounding charged particles, and if the electric field exceeds a critical value the atom becomes ionized [Bergeron et al., 1991]. The critical field value roughly corresponds to a condition where a transition to an energy level n, which has been affected by the Stark effect, has the same energy as a transition to the n-1 energy level.

In ATMO the included bound-free opacities are due to H^-, H, He and He^+ atoms and ions [Bergeron et al., 1991]. Note that in the pure-helium case, there are no hydrogen atoms and therefore the opacity does not depend on hydrogen. The included free-free absorptions are due to H^-, H, He^+ (He I), He^{++} and He^- atoms and ions [Bergeron et al., 1991]. The free-free absorption of He^- ion is from John [1994]. The He_2^+ molecule absorption is described using Stancil [1994] [Beauchamp et al., 1995]. Hummer and Mihalas [1988] is used to calculate bound-bound, bound-free to true continuum and pseudo-continuum opacities, which are described below [Bergeron et al., 2011].

2.1.2 Line broadening

When calculating a synthetic spectrum an important ingredient is the description of line broadening. Helium starts to be ionised at $T_{\rm eff} \gtrsim 16\,000$ K, therefore below this effective temperature, the helium lines are dominated by neutral broadening. Neutral broadening can be split into two subcategories: resonance and van der Waals broadenings [Bergeron et al., 1991]. Above $T_{\rm eff} \approx 16\,000$ K, Stark broadening dominates the helium lines [Beauchamp et al., 1996]. Both neutral and Stark broadening are examples of pressure broadening [Bergeron et al., 1991]. For helium lines the profile of resonance broadening is calculated using the Ali and Griem [1965, 1966] prescriptions. The van der Waals broadening is described using either Unsold [1955] or Deridder and van Rensbergen [1976] prescriptions [Beauchamp et al., 1996; Genest-Beaulieu and Bergeron, 2019a,b]. In the regime where both broadenings are important, the neutral broadening profiles are convolved with Stark broadening profiles [Bergeron et al., 1991].

The following procedure is used to calculate neutral broadening of helium lines [Beauchamp et al., 1996; Genest-Beaulieu and Bergeron, 2019a]. First, van der Waals broadening is calculated for each spectral line using both Unsold [1955] and Deridder and van Rensbergen [1976] prescriptions. The width of a line broadened by van der Waals broadening, $\omega_{\rm vdw}$, is then decided based on

$$\omega_{\rm vdw} = \max(\omega_{\rm U}, \omega_{\rm D}), \tag{2.3}$$

where $\omega_{\rm U}$ and $\omega_{\rm D}$ are the widths of Unsold [1955] and Deridder and van Rensbergen [1976] line broadening, respectively. However, the helium lines at 4121Å and 4713Å are always treated using Unsold [1955] broadening, as they agree better with observations [Beauchamp et al., 1996; Genest-Beaulieu and Bergeron, 2019a]. The width of a neutrally broadened line, $\omega_{\rm neutral}$, is then decided based on

$$\omega_{\rm neutral} = \max(\omega_{\rm resonance}, \omega_{\rm vdw}), \tag{2.4}$$

where $\omega_{\rm resonance}$ and $\omega_{\rm vdw}$ are the widths of resonance and van der Waals broadened lines, respectively. In the following, this procedure is simply referred to as Deridder and van Rensbergen [1976] van der Waals line broadening [Beauchamp et al., 1996; Genest-Beaulieu and Bergeron, 2019a]. The shape of the resultant broadened line is Lorentzian [Genest-Beaulieu and Bergeron, 2019a].

In general, Stark broadening causes the splitting of an energy level into multiple levels. Therefore, for a transition involving an energy level that has been split by the Stark effect, we get not one spectral line but several. These individual lines are not seen separately as the electric field varies with time and position. What is seen is the integral of all possible fields causing the line to appear broadened. If Stark broadening is large enough, the higher lines of the hydrogen series can merge into a pseudo-continuum [Bergeron et al., 1991]. The equation of state of Hummer and Mihalas [1988] treats Stark broadening using three types of transitions: the bound-bound, bound-free to a true continuum and bound-free to a pseudo-continuum, where a transition happens from a lower level to a destroyed upper level. For helium-rich white dwarfs, helium lines overlap significantly (see Fig. 1.5), thus pseudo-continuum is also important [Bergeron et al., 1991; Beauchamp et al., 1997]. Additionally, the larger the pressure in the atmosphere, the more upper levels will be destroyed, thus correct treatment of the pseudo-continuum is important for white dwarf spectra overall [Bergeron et al., 1991].

Linear Stark broadening can also lead to transitions which are usually prohibited by selection rules [Beauchamp et al., 1997]. Such transitions can be seen in the spectra of DB/DBA white dwarfs as well-isolated forbidden lines [Beauchamp et al., 1995]. These forbidden lines are treated using the prescription described in Beauchamp et al. [1995] and Beauchamp et al. [1997].

If hydrogen is present in the atmosphere, it gets ionised at $T_{\rm eff} \gtrsim 10\,000$ K. Thus, above this effective temperature and indeed for all DBA stars considered in this thesis, the hydrogen lines are Stark broadened due to the presence of electrons and protons. In ATMO the Stark broadening of Balmer lines follows the prescription

of Tremblay and Bergeron [2009].

2.2 3D CO^{5}BOLD code

The 3D simulations of DB and DBA white dwarfs presented in this thesis have been calculated with the 3D radiation-hydrodynamics code called CO^{5}BOLD [Freytag et al., 2002; Wedemeyer et al., 2004; Freytag et al., 2012; Freytag, 2013, 2017] version "*002.02.2012.11.XX*". This code allows the calculation of two types of stellar atmosphere models: local models with the box-in-a-star set-up and global models with the star-in-a-box set-up [Freytag et al., 2002]. The box-in-a-star set-up simulates a portion of a stellar atmosphere in a Cartesian box with x, y and z coordinates, where z is the vertical axis. An example of a stellar atmosphere calculated with the box-in-a-star model is shown in Fig. 2.1. Star-in-a-box simulates the entirety of a stellar atmosphere and example of this is shown in Fig. 2.2. The star-in-a-box models can only be run for stars with convection zones made up of large convective cells, such as red giants [Freytag et al., 2002]. This set-up is not applicable for white dwarfs due to computational limitations and thus will not be discussed any further.

For white dwarfs the convective cells are much smaller than the radius of the white dwarf, therefore box-in-a-star set-up is used. Akin to 1D, these models ignore spherical symmetry and thus the gravitational field only acts in the negative z-direction. The variables are cell-centered and the cell spacings can be non-equidistant [Freytag et al., 2012]. For local models it is important that the vertical extent of the simulation box is deep enough to simulate both the optically thin upper layers, where radiative transfer dominates, and the optically thick convective layers. Radiative transfer in the upper layers causes radiative cooling, which creates down-drafts that have a significant effect on the deeper convective layers [Freytag et al., 2002]. These down-drafts also result in the appearance of convective cells at the surface of cool white dwarfs. For physicality of the simulation, the bottom layers of the simulation must be approaching adiabatic convection. As a consequence the bottom layers do not have much influence on the upper layers [Freytag et al., 2012]. In summary, both convective and radiative transfer have to be modelled correctly for the simulations to be physical.

In CO^{5}BOLD the equations of time-dependent hydrodynamics, which are used to treat convective energy transport, are solved alongside radiative transfer. Essentially, the stellar atmosphere is modelled as a compressible, homogeneous plasma under a constant gravitation field [Wedemeyer et al., 2004]. The microphysics are taken into account by using pre-computed equation of state and opacity tables [Frey-

tag et al., 2012]. OpenMP is used for linear parallelisation to decrease computational time.

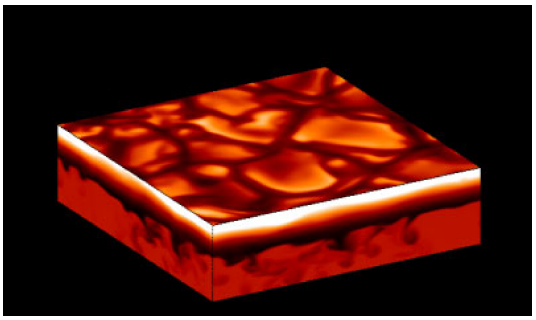

Figure 2.1: An example of a box-in-a-star (local) model of the Sun's photosphere. It shows the convective granulation cells on the surface as emergent grey intensity (units of erg cm^{-}2 s^{-2}). On the sides of the box the convective down-drafts which extend from the upper layers are shown in units of entropy. Adapted from Freytag et al. [2002].

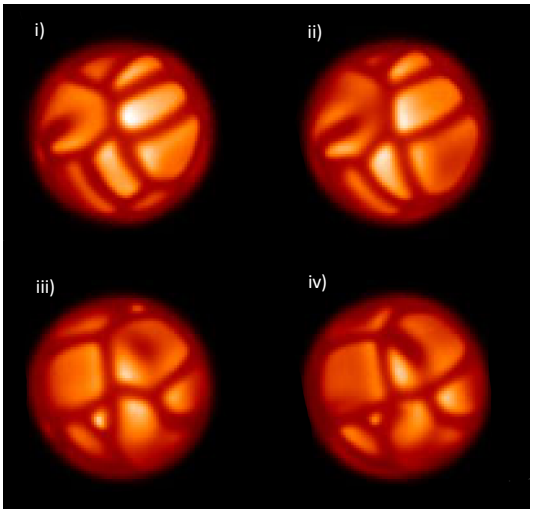

Figure 2.2: An example of a star-in-a-box (global) simulation of a grey atmosphere of a mini-Sun, where the radius was artificially decreased to obtain a manageable number of convective cells at the surface. The entirety of the atmosphere is modelled in this case. Adapted from Freytag et al. [2002].

2.2.1 Hydrodynamics equations

In order to simulate the convective energy transport, hydrodynamics equations are used [Freytag et al., 2002; Freytag, 2017]. These include the conservation of mass,

$$\frac{\partial \rho}{\partial t} + \frac{\partial \rho v_1}{\partial x_1} + \frac{\partial \rho v_2}{\partial x_2} + \frac{\partial \rho v_3}{\partial x_3} = 0, \tag{2.5}$$

where ρ is mass density, $x_{1,2,3}$ and $v_{1,2,3}$ are the spatial coordinates and velocity values for the three dimensions; conservation of momentum

$$\frac{\partial}{\partial t}\begin{pmatrix}\rho v_1\\ \rho v_2\\ \rho v_3\end{pmatrix} + \frac{\partial}{\partial x_1}\begin{pmatrix}\rho v_1 v_1 + P\\ \rho v_2 v_1\\ \rho v_3 v_1\end{pmatrix} + \frac{\partial}{\partial x_2}\begin{pmatrix}\rho v_1 v_2\\ \rho v_2 v_2 + P\\ \rho v_3 v_2\end{pmatrix} + \frac{\partial}{\partial x_3}\begin{pmatrix}\rho v_1 v_3\\ \rho v_2 v_3\\ \rho v_3 v_3 + P\end{pmatrix} = \begin{pmatrix}\rho g_1\\ \rho g_2\\ \rho g_3\end{pmatrix}, \tag{2.6}$$

where P is pressure and $g_{1,2,3}$ are the directional components of gravity defined as

$$\begin{pmatrix}g_1\\ g_2\\ g_3\end{pmatrix} = -\begin{pmatrix}\frac{\partial}{\partial x_1}\\ \frac{\partial}{\partial x_2}\\ \frac{\partial}{\partial x_3}\end{pmatrix}\Phi, \tag{2.7}$$

where Φ is the gravitational potential (local models ignore spherical symmetry thus gravity is only non-zero in the z-direction); and conservation of energy

$$\frac{\partial \rho e_t}{\partial t} + \frac{\partial (\rho e_t + P) v_1}{\partial x_1} + \frac{\partial (\rho e_t + P) v_2}{\partial x_2} + \frac{\partial (\rho e_t + P) v_3}{\partial x_3} + \frac{\partial F_{1,\,\mathrm{rad}}}{\partial x_1} + \frac{\partial F_{2,\,\mathrm{rad}}}{\partial x_2} + \frac{\partial F_{3,\,\mathrm{rad}}}{\partial x_3} = 0, \tag{2.8}$$

where $F_{1,2,3,\mathrm{rad}}$ are the directional components of radiative flux and e_t is the total energy defined as

$$\rho e_t = \rho e_i + \rho \frac{v_1^2 + v_2^2 + V_3^2}{2} + P\Phi, \tag{2.9}$$

where e_i is the internal energy. In CO^{5}BOLD these equations are solved for each grid cell in the Cartesian box and for each time-step. CO^{5}BOLD uses ρ, v_1, v_2, v_3 and e_i as independent variables. For stability, artificial tensor viscosity is introduced at each time-step [Wedemeyer et al., 2004]. The hydrodynamics equations are solved alongside the radiative transfer.

Operator splitting is used to simplify the numerical calculations, by separating each original hydrodynamics equation at a given time-step into several different sub-equations. These sub-equations are quicker to solve than the original equation. Once solved, operator splitting is then used to combine the solutions of the sub-equations into a solution to the original equation.

In CO^{5}BOLD the equations are solved using the Riemann solver of the Roe type [Freytag et al., 2012]. For solving the equations, it is imperative to interpolate over the grid cells. The interpolation method used is called a reconstruction scheme. For 3D DB and DBA models we use the FRWeno second-order reconstruction scheme, which provides better stability than the methods used in previous versions of CO^{5}BOLD, and means that less artificial viscosity needs to be added [Freytag, 2013].

2.2.2 Boundaries

The boundaries of the simulation box for a local model must be chosen such that the simulated atmosphere behaves like a real atmosphere, meaning that the boundaries have no effect on the final result [Freytag, 2017]. In general, it is recommended that both the top and bottom boundaries should be at least two pressure scale heights away from the atmospheric layer of interest [Grimm-Strele et al., 2015].

In CO^{5}BOLD ghost cells are added on all sides of the simulation box with the values of the ghost cells being dependent on the boundary conditions chosen [Freytag, 2017]. For the 3D DB and DBA simulations three ghost cells are used on each side.

Top boundary

In 3D DB and DBA simulations, the top boundary is always open both to material and radiative flows [Freytag et al., 2002]. For this type of boundary, the ghost cell values are set such that the three velocity components and the internal energy are constant. However, the density is exponentially extrapolated with a scale height equal to a fraction of the pressure scale height [Freytag, 2017]. The boundary can experience shocks which are either allowed to leave the simulation or which cause material to fall downwards [Wedemeyer et al., 2004].

Bottom boundary

Two types of bottom boundaries are used in this thesis. The first is an open bottom boundary, which allows both material inflows and outflows [Freytag et al., 2012]. However, the material flows have to be adjusted to conserve the total mass in the simulation [Wedemeyer et al., 2004]. This type of bottom boundary applies for white dwarfs whose convection zones are too large to be fully simulated vertically. Instead, only a portion of the atmosphere is vertically simulated. The bottom boundary must be deep inside the convection zone, where convection tends towards becoming adia-

batic [Wedemeyer et al., 2004]. The velocity of the up-flows at this bottom boundary is constant. The input parameter for controlling the boundary is the value of the inflowing entropy. It indirectly controls the effective temperature of the simulation. The entropy value is set to the entropy of the adiabatic up-flows [Freytag, 2017]. The ghost cell values are extrapolated from the bottom layer assuming constant gravitational potential.

The second type of bottom boundary is the closed bottom boundary, which is used for modelling white dwarfs whose convection zones are small enough to be vertically modelled. The input parameter that controls this type of boundary is the radiative energy flux at the boundary and it affects the effective temperature of the model. The values in the ghost cells are the same as in the bottom layer, the gravitational potential is set to zero and the vertical velocity is inverted [Freytag, 2017].

Side boundaries

The side boundaries of the simulation box are periodic [Freytag et al., 2002]. At each timestep of the simulation, the values from leftmost columns are copied to the ghost cells of the right side, and vice versa for left, front and rear sides [Freytag, 2017]. Side boundaries are used because they are easy to implement, they allow for the existence of standing and travelling waves, and they create no artefacts [Freytag, 2017]. When using periodic side boundaries, it is important to make sure that enough convective cells are simulated horizontally such that the final results are not affected by the boundaries [Freytag et al., 2012]. For DB and DBA models at least 4×4 convective cells were simulated. As discussed by Tremblay et al. [2013a], the number of simulated convective cells is chosen such that the power spectrum of intensity of the simulation is well resolved.

2.2.3 Input and numerical parameters

The input parameters of CO^{5}BOLD include surface gravity, microphysics in the form of an equation of state and opacity tables, the parameters that control the boundary conditions and the initial starting model [Freytag, 2017]. The initial starting model can be a 1D model with the same atmospheric parameters that has been extended into three dimensions. However, the best choice for a starting model is another 3D simulation with similar atmospheric parameters [Freytag et al., 2012]. It is important to make sure that the starting model is as close as possible to the final solution in order to save computational time.

The numerical parameters are numerous. They include the boundary conditions, reconstruction scheme used for the hydrodynamics solver, the number of rays used in solving radiative transfer, the magnitude of the tensor viscosity, resolution of the computational box and its size [Freytag et al., 2012; Freytag, 2017]. The numerical parameters have to be chosen such that the computational box behaves as if it is a real atmosphere and such that the parameters do not have an effect on the final result. The artificial viscosity is a parameter used to deal with shocks which sometimes occur in the simulation. Shocks cause significant variation in opacity, which affects the radiative transfer and can cause simulations to fail. Artificial viscosity dampens such shocks. The work presented in this thesis relies on the classical treatment of shocks in CO^{5}BOLD, which allows the shocks to pass through the top boundary into the ghost cells unaffected.

2.2.4 The equation of state

The equation of state is not computed by CO^{5}BOLD. Instead, it has to be provided as an input parameter in the form of a table of pre-computed values. The table is then interpolated over and the parameters are extracted by the code when they are required. The values of temperature, pressure, entropy and the first and third adiabatic coefficients must be provided in the equation of state table as functions of density and internal energy [Freytag et al., 2012]. The equation of state for DB and DBA white dwarfs were computed from information provided by the ATMO code.

2.2.5 Opacity binning

Although convective energy transport is important in the atmospheres of cool white dwarfs, radiative energy transport can be just as important, especially in the upper layers. Thus, both energy transfer modes need to be modelled to a good degree of accuracy. The radiative transfer equation must be solved at each point in the atmosphere, for each frequency under consideration and for each direction of the light ray [Vögler et al., 2004]. This is straightforward to achieve in 1D models and in ATMO over 1000 individual frequencies are used. However, solving the equation for a large number of frequencies becomes computationally impossible to carry out when the dimensions of the models are increased, specifically in 3D modelling where we not only have two additional space dimensions, but also the dimension of time.

The easiest way to decrease the computational time is to reduce the number of frequencies considered when solving the radiative transfer equation. This is because for each grid cell in the simulation the radiative transfer equation will have to

be solved for all frequencies. In the radiative transfer equation the opacity is a function of frequency, therefore the number of frequencies considered must be decreased while preserving as much information as possible about the opacities. To do this CO^{5}BOLD uses the opacity binning procedure [Nordlund, 1982; Ludwig et al., 1994; Vögler et al., 2004]. One extreme case of this would be the calculation of a grey atmosphere, which only has one opacity bin because the opacity is considered to be constant over all frequency. As discussed in Sec. 1.4.3 the opacity in the stellar atmosphere is not constant and can significantly affect the atmospheric stratification, especially if lines are included [Vögler et al., 2004]. More sophisticated opacity binning allows for a realistic treatment of radiative transfer while saving computational time. It was first introduced by Nordlund [1982] and was later developed by Ludwig et al. [1994]. It relies on the assumption that the radiative transfer equation can be rewritten by introducing integrated quantities over a given bin, $I_i = \int_{\rm bin} I_\nu \, {\rm d}\nu$ and $B_i = \int_{\rm bin} B_\nu \, {\rm d}\nu$, such that it becomes

$$\frac{{\rm dI_i}}{{\rm ds}} = -\int \kappa_\nu \rho (I_\nu - B_\nu) {\rm d}\nu = -\bar{\kappa_{\rm i}} \rho ({\rm I_i} - {\rm B_i}), \tag{2.10}$$

where i subscript denotes values associated with i-th bin, ν subscript denotes values for a given frequency ν and $\bar{\kappa_i}$ is the bin-averaged opacity [Vögler et al., 2004].

The error of the calculated atmosphere is small only if the binned frequencies are grouped into bins such that the depth dependence of the opacity is similar for all frequencies in the bin and the opacities are of similar strength. The use of opacity binning in the work presented here reduces the number of frequencies considered from around 1000 to 10. In CO^{5}BOLD the method of sorting opacities is τ-binning [Ludwig et al., 1994], where a frequency ν is grouped into bin i if

$$\tau_{\rm R}^{i-1} \geq \tau_{\rm R}(\tau_\nu = 1) > \tau_{\rm R}^{i}. \tag{2.11}$$

Essentially, this method will group frequencies that become transparent at similar height in the atmosphere [Ludwig et al., 1994]. To achieve this we need the optical depth information for each frequency, which we can get from a reference 1D model. In the work presented here we use the 1D atmospheres calculated with ATMO. The 3D DB and DBA models use opacity tables that have been binned according to $\log \tau_{\rm R} = [99.0, 0.25, 0.0, -0.25, -0.5, -1.0, -1.5, -2.0, -3.0, -4.0, -5.0]$, unless otherwise stated. The bin for $\log \tau_{\rm R} = [-5.0, -99.0]$ has been omitted due to interpolation issues [Chap. 1 which has been published in Cukanovaite et al. 2018]. For CO^{5}BOLD the opacity table must be a function of temperature and pressure. The tables were computed for each value of hydrogen abundance, surface gravity and for

$T_{\rm eff} = [10\,000, 12\,000, 15\,000, 20\,000, 25\,000, 30\,000, 34\,000]$ K.

2.2.6 Considerations in time

During the simulation, the initial starting model will be run until relaxation occurs. If chosen correctly, the initial conditions will not impact the final result as the dynamics of convective flows act on short time-scales [Wedemeyer et al., 2004]. For relaxation, the simulation should be run for around ten convective turnover time-scales [Freytag et al., 2012]. In this thesis, the relaxation of simulations was confirmed by tracking the time evolution of total flux, of flux at all depths and of the velocity field.

To determine the size of the time-step that is appropriate for a simulation, the Courant-Friedrichs-Lewy (CFL) condition is used [Freytag et al., 2012]. Essentially, if the time-step of the simulation is larger than CFL time-scale, then the simulation fails. CFL time-scale is estimated as the sound crossing time.

2.2.7 Radiative transfer equation

In CO^{5}BOLD the atmosphere is assumed to be in LTE. For box-in-a-star simulations the radiative transfer equation is solved using the Feautrier scheme on a number of long rays [Wedemeyer et al., 2004]. The long rays traverse many inclinations with respect to the vertical and azimuthal angles, taking into account periodic side boundaries [Freytag et al., 2012]. The radiative transfer equation is solved for each grid point starting from the top of the simulation all the way to the bottom. Opacities are extracted from the pre-computed opacity table.

2.2.8 Average stratifications

For the work presented in this thesis, the 3D simulations were averaged temporally and over contours of constant optical depth (Chap. 3 and 4) or geometric depth (Chap. 5). For spectroscopic applications, the average over constant optical depth gives a better representation of how emergent flux is formed. For studies of the bulk properties of the convection zone and convective fluxes, the average over geometric depth is more appropriate. In general, it is found that temperature averages over optical depth result in higher temperature than the averages over geometric depth, because the temperature fluctuations are smoother over constant contours of optical depth [Wedemeyer et al., 2004]. This is due to the shock fronts in the simulations, which span small range of geometric depths, but a large range of optical depths.

By using the tests listed in Sec. 2.2.6, I made sure that each simulation is relaxed in the last half of the run. The temporal average is only performed in the last quarter of the run. For Chap. 3 and 4 at least 12 individual time-steps in the last quarter were used for the average. In Chap. 5, all time-steps in the last quarter were used. This is because the average over optical depth is time consuming compared to averaging over geometric depth.

2.3 1D LHD code

Another type of 1D atmospheric code used for the analysis presented in this thesis is called LHD [Caffau et al., 2007]. Similarly to ATMO, LHD uses the assumptions of a plane-parallel atmosphere in LTE. It is, however, a Lagrangian 1D hydrodynamical code, which uses the numerical solutions identical to CO^{5}BOLD, but simplified for 1D geometry. In LHD a hydrodynamical model is run until its thermal and dynamical evolution converges, creating a 1D hydrostatic model.

LHD is a sister code to CO^{5}BOLD and is useful in eliminating any issues with equation of state and opacity tables. This is because both LHD and CO^{5}BOLD treat microphysics in the same fashion, thus allowing for the elimination of any issues with microphysics when comparing the models calculated from these two codes. Sect 3.2.2 explains this in more detail. LHD has been adapted to treat convection in the same way as the 1D ATMO code (for white dwarfs), using ML2/$\alpha = 1.25$. As LHD treats the microphysics in the same way as CO^{5}BOLD, it means that the LHD code produces 1D models that can be differentially compared to CO^{5}BOLD simulations in order to derive differences that are only due to convective energy transport. On the other hand, when comparing ATMO with CO^{5}BOLD models we could find differences that are due to both 3D convective effects and microphysics.

The LHD code was used to calculate a grid of 1D models that cover $-2.0 \geq \log \mathrm{H/He} \geq -10.0$ dex, $7.5 \leq \log g \leq 9.0$ dex and $11\,000 \leq T_{\mathrm{eff}} \leq 40\,000$ K parameter range, with step sizes of $\Delta \log \mathrm{H/He} = 0.5$ dex, $\Delta \log g = 0.5$ dex and $\Delta T_{\mathrm{eff}} = 1\,000$ K. All units are in cgs.

2.4 The Spectroscopic Technique

A large portion of the work presented in this thesis is focused on trying to understand how spectroscopically-determined parameters of effective temperature, surface gravity and hydrogen abundance are affected by 3D models. In order to be able to derive the spectroscopic corrections due to 3D modelling, the differential approach

is used, where a given 3D spectrum is fitted with a grid of 1D LHD models to find the best matching 1D spectrum. The difference between the atmospheric parameters of the 3D model and the fitted parameters from the 1D fit gives the spectroscopic corrections. The fitting of the observed spectra is known as the spectroscopic technique. Some of the work presented in this thesis used the fitting code of the Montréal group, described in detail by Bergeron et al. [2011]. Other work has been done with a fitting procedure I have written and this code will be described later in Chap. 4. In the following a brief description is given for the Montréal fitting code, as it is a good example to illustrate the spectroscopic technique. The fitting procedure is also dependent on the type of the white dwarf [Genest-Beaulieu and Bergeron, 2019a], thus in the following we describe the case of DB/DBA stars only.

When fitting a white dwarf spectrum, both the observed and synthetic spectra are normalised. One such normalisation technique has been described by Liebert et al. [2005], where the observed spectrum is fitted by a model grid of synthetic spectra multiplied by a high-order polynomial function of wavelength or frequency. This allows for the determination of the continuum and the multiplication takes into account any issues with flux calibration [Bergeron et al., 2011]. Additionally, this procedure finds the line centres which can be then be adjusted to laboratory values. The flux at selected wavelengths, known as the normal points, is then set to unity and this normalised spectrum is used for fitting using linear least-squares minimization of Levenberg-Marquardt [Bergeron et al., 2011]. The normalised spectrum is first fitted for effective temperature and surface gravity only. These values are then fixed to fit for hydrogen abundance. This is repeated iteratively until the values converge. In the case of the Montréal fitting code iteration is used as the blue and red part of the spectrum are made up of separate observations. The hydrogen abundance is only fitted based on Hα, or if unavailable, Hβ. Sometimes only an upper limit can be found if for example, the hydrogen lines are too weak and noisy. The upper limit of hydrogen abundance as a function of effective temperature has been determined based on observations by Voss et al. [2007] and Bergeron et al. [2011].

In order to derive the 3D spectroscopic corrections, the 3D synthetic spectra replace the role of observed spectra. In this thesis this code was only used for fitting 3D DB models (Chap. 3), thus the fitting of hydrogen abundance was disabled.

2.5 Spectroscopic parallax

In this thesis, the data from the second data release (DR2) of the European Space Agency's *Gaia* satellite [Gaia Collaboration et al., 2018] are used to test the 3D

spectroscopic corrections. In some cases the *Gaia* observed parallaxes for several samples of DB and DBA white dwarfs are compared to spectroscopic parallaxes, which are derived from spectroscopic determinations of effective temperature and surface gravity [Holberg et al., 2008; Tremblay and Bergeron, 2009]. By integrating synthetic spectra over pre-selected band passes it is possible to calculate theoretical absolute magnitudes for any combination of effective temperature and surface gravity of a white dwarf. In the work presented here, the cooling table of the Montréal group which provides this information is used. It is interpolated over to find the absolute theoretical *Gaia* G magnitudes of the white dwarfs based on their spectroscopic effective temperatures and surface gravities. The G absolute magnitude can then be combined with the observed de-reddened (see Gentile Fusillo et al. 2019a) *Gaia* G magnitude via the distance modulus equation in order to find the spectroscopic distance and thus the spectroscopic parallax. The errors on the spectroscopic parallax depends on the errors of effective temperature and surface gravity, which have been propagated through the relevant equations. In this work, the procedure is performed for 1D and 3D spectroscopic effective temperatures and surface gravities, in order to calculate 1D and 3D spectroscopic parallaxes which can then be compared to observations.

An independent technique which can also be used to test the 3D spectroscopic corrections involves the effective temperatures and surface gravities derived from *Gaia* photometric G_{BP}-G_{RP} colours. These photometric values can then be directly compared to spectroscopically-derived effective temperatures and surface gravities.

Chapter 3

Spectroscopic 3D DB corrections

Yeah I'm you, you are me, now do you know
Yeah you are me, I'm you, now you do know
We are one body, sometimes we will clash
You can never break me off, this you must know
Yeah yeah can't break me off, whatever you do
Yeah you'll be at ease if you admit it too
Yeah succeed or fail, whichever way you flow
Yeah you can't escape, wherever you go
I am you, you are me, now you do know
You are me, I am you, now do you know
We are one body and we are gonna clash
We are you, we are me, this do you know

Interlude: Shadow
BTS

3.1 Introduction

In this chapter, I present the first 3D radiation-hydrodynamics simulations for pure-helium white dwarf atmospheres. The 3D simulations are used to compute synthetic DB spectra, which are then compared with 1D synthetic spectra. The full spectroscopic analysis of the existing data sets is postponed until Chap. 4 where grids of 3D model atmospheres with mixed He/H compositions are introduced. Even with this shortcoming, the predictions with a pure-helium equation-of-state (EOS) have been useful [Tremblay et al., 2019b] to interpret the independent stellar parameters (effective temperature, radius, luminosity) revealed from *Gaia* Data Release 2

[Tremblay et al., 2017; Bédard et al., 2017; Hollands et al., 2018]. This chapter is restricted to the atmospheric properties of DB white dwarfs; the calibration of the mixing-length theory for structure calculations will be presented in Chap. 5. In Section 3.2, the numerical setup of the 3D simulations is explained and some brief description of the structural differences between the 3D and 1D convection models is given. The calculation of synthetic spectra for both 3D and 1D structures is explained in Section 3.3. The proposed 3D corrections on effective temperature and surface gravity are presented and discussed in Section 3.4. A summary of the work is given in Section 3.5.

Although most white dwarfs have hydrogen dominated atmospheres as a result of gravitational settling [Schatzman, 1948], a significant number of degenerate stars have atmospheres dominated by helium, which is understood to be the consequence of late thermal pulses experienced by post-asymptotic giant branch (AGB) progenitors [Althaus et al., 2005; Werner and Herwig, 2006]. Indeed, about 20% of white dwarfs in magnitude limited samples [e.g. SDSS; Kleinman et al., 2013; Kepler et al., 2015] are of DB or DO spectral types. For volume-complete samples where the white dwarf luminosity function peaks at much cooler temperatures, the fraction of helium-dominated atmospheres is as large as 50% [Giammichele et al., 2018]. This increase of helium-rich stars below $T_{\rm eff} \sim 10\,000$ K is likely due to convective mixing events in hydrogen-line (DA) white dwarfs, resulting in their thin hydrogen blanket being fully mixed-in with the underlying helium layer [Tremblay and Bergeron, 2008].

For the majority of DB and DBA white dwarfs, the spectroscopic technique, which compares the observed line profiles to predictions from model spectra [Bergeron et al., 2011, henceforth BW11], is used to determine their atmospheric parameters (effective temperature, surface gravity and hydrogen-to-helium number ratio). These parameters coupled with evolutionary models allow for the determination of white dwarf masses and ages. While DB white dwarfs are not quite as frequent as DA or DC spectral types, their parameters are still essential to understand the local stellar formation history [Kalirai, 2012; Tremblay et al., 2014], the late thermal pulses in post-AGB progenitors [Reindl et al., 2014b,a], and the fraction of primordial hydrogen in white dwarfs [BW11; Koester and Kepler, 2015; Rolland et al., 2018]. Furthermore, a large fraction of white dwarfs polluted by asteroids and planetary debris [Veras, 2016] have helium-dominated atmospheres [Kleinman et al., 2013]. This is expected from the much larger diffusion timescales for the denser helium atmospheres [Paquette et al., 1986a,b; Koester, 2009; Fontaine et al., 2015]. As a consequence, DB white dwarfs are important objects for the understanding of

post-main-sequence planetary system evolution, and in particular the detection of water-rich asteroids [Farihi et al., 2013; Raddi et al., 2015; Gentile Fusillo et al., 2017].

In the last two decades, detailed spectroscopic analyses of DB and DBA white dwarfs have resulted in exquisite mass-effective temperature distributions, and sophisticated 1D model atmosphere and spectral synthesis codes which incorporate detailed line broadening schemes (see, e.g., Beauchamp et al. 1997; Voss et al. 2007; BW11; Koester and Kepler 2015). The importance of hydrogen in the helium-dominated atmosphere white dwarfs has also been made clear. These studies have determined that the fraction of DBAs in DB/DBA samples is up to 75%, and that perhaps all DB white dwarfs have traces of hydrogen with the abundance too low to cause observable spectral features [Koester and Kepler, 2015], illustrating the close link between the two spectral classifications. The presence of hydrogen, even if not observed, can significantly affect the derived effective temperature, especially for the boundaries of the V777 Her instability strip [Beauchamp et al., 1999], the region where pulsating DB/DBA white dwarfs are found.

Some issues remain in the spectroscopic analyses of DB white dwarfs. One such problem is observed at $T_{\rm eff} < 16\,000$ K, where the spectroscopically derived surface gravities are significantly higher than the predictions of evolutionary models, possibly due to incomplete treatment of line broadening by neutral helium [BW11; Koester and Kepler, 2015]. Beauchamp et al. [1996] have shown that better treatment of the van der Waals broadening implemented from Deridder and van Rensbergen [1976] does lower the surface gravities at low effective temperatures, yet the authors find that gravity is very sensitive to the exact treatment of this broadening. A similar high-$\log g$ problem was known for DA white dwarfs [Bergeron et al., 1990] for $T_{\rm eff} < 12\,000$ K, a temperature which corresponds to the onset of convective energy transfer in the photosphere of DAs. This problem was solved by computing the first-ever 3D model atmospheres of DA white dwarfs [Tremblay et al., 2013b,c] and corresponding 3D synthetic spectra, confirming the long-standing suspicion that convection is modelled too approximately in 1D model atmospheres.

Helium-atmosphere white dwarfs develop superficial convection zones at temperatures as large as 50 000 K and thus all currently known DB stars must rely on convective model atmospheres. Consequently, the high-$\log g$ problem for cool DB white dwarfs cannot be related to the onset of convection, but it could be caused by changes in the properties of convection that 1D models do not consider. Therefore, it is of great interest to look at the predictions of 3D DB model atmospheres, especially because of the success of modelling DA white dwarfs. In addition to the

derivation of masses and ages that are likely to be more precise, the sizes of the convection zones and overshoot regions [Tremblay et al., 2015b; Kupka et al., 2018] are of particular importance, since they determine the total mass of hydrogen or accreted metals in DBA and DBZ white dwarfs, respectively. Another critical aspect is the revision of the spectroscopic parameters to determine the empirical edges of the V777 Her instability strip and the connection to asteroseismic models [Van Grootel et al., 2017].

For DB and DBA white dwarfs the mixing-length parameter, ML2/α, is usually set to 1.25 [BW11; Koester and Kepler, 2015]. BW11 derived this value by looking at possibly unphysical clumping in the $\log g$-$T_{\rm eff}$ distribution arising from the different values of the mixing length parameter, and from the calibration of the effective temperature derived from fits of optical and UV spectra. Although ML2/α = 1.25 performed reasonably well in both tests, BW11 suggested that an improvement needs to be made in the treatment of convective transport itself, which is exactly what 3D models can provide. Thus, in this chapter I investigate the effect of the more physical 3D models on spectroscopically-determined atmospheric parameters of DB white dwarfs.

3.2 Model atmospheres

3.2.1 Numerical setup for CO^{5}BOLD simulations

The CO^{5}BOLD radiation-hydrodynamics code [Freytag et al., 2012] was used to compute 47 3D DB model atmospheres with surface gravities ranging between 7.5 and 9.0 in steps of 0.5 dex, and effective temperatures between 12 000 K and 34 000 K in steps of around 2000 K. The grid is illustrated in Fig. 3.1 and presented in Table 3.1. As discussed in Chap. 2 of this thesis, the effective temperature is not an input parameter, which results in the unevenly spaced values of effective temperature in the 3D grid. In Fig. 3.1, the models with open and closed bottom boundaries are indicated by open and filled circles, respectively. The bottom layer for all models is around $\log \langle \tau_{\rm R} \rangle = 3$, where $\langle \tau_{\rm R} \rangle$ is the Rosseland optical depth averaged over space and time. Some closed boundary models were extended deeper to include a larger overshoot region. The top $\langle \tau_{\rm R} \rangle$ value varies from model to model, ranging from $-8.5 \lesssim \log \langle \tau_{\rm R} \rangle \lesssim -4.8$, with all simulations covering the line forming region. All simulations also cover more than 4.5 pressure scale heights vertically, with the majority being more than 10 pressure scale heights deep. Apart from the EOS and opacities, our computational setup is the same as that used for DA white dwarfs [Tremblay et al., 2013b,c].

The simulations cover a minimum time of 60 turnover timescales at $\langle \tau_{\rm R} \rangle = 1$. We have confirmed that our models are relaxed in the last quarter of the simulation by monitoring total flux as a function of depth over time (including outgoing flux at the top). In all cases systematic variations within that time frame were less than the statistical noise due to periodic waves and the finite number of convective cells in our simulations. Convergence of the velocity field was also reached for all cases but the lowest effective temperature models, where the velocity field is still not in equilibrium in the uppermost layers ($\langle \log \tau_{\rm R} \rangle < -3$). As stated in Tremblay et al. [2013b,c], the upper layers never reach radiative equilibrium owing to very large Péclet number, Pe, defined as

$$\mathrm{Pe} = \tau_{\rm rad}/\tau_{\rm adv}, \tag{3.1}$$

where $\tau_{\rm rad}$ and $\tau_{\rm adv}$ are the radiative and convective turnover timescales, respectively. Instead, the entropy gradient in the upper layers slowly converges to a near-adiabatic structure due to the weak convective overshoot.

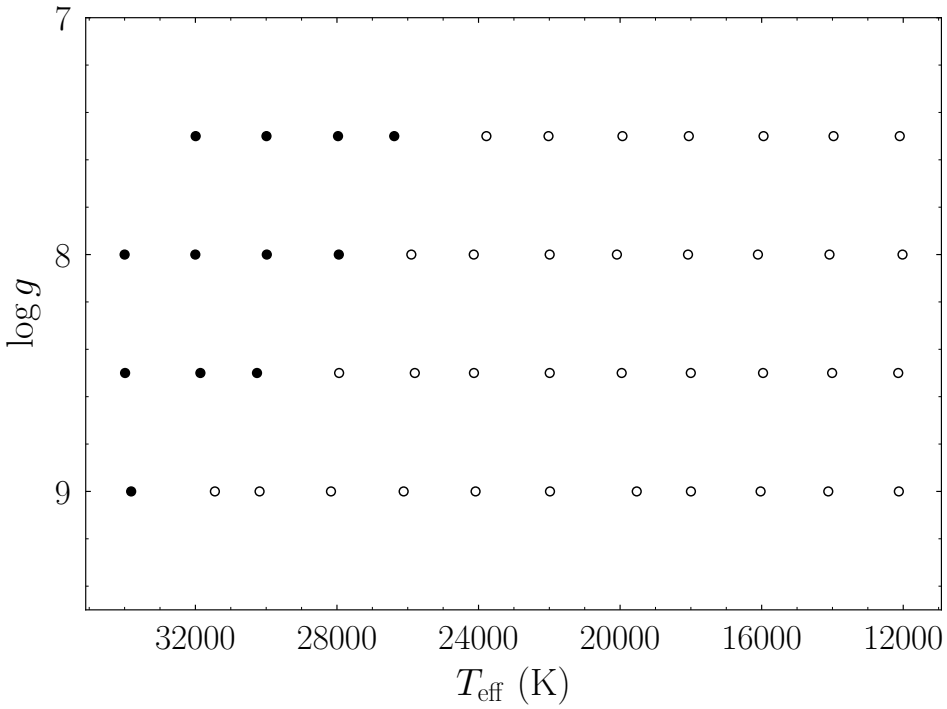

Figure 3.1: The effective temperatures and surface gravities of our 3D model atmospheres with pure-helium compositions. Open and filled circles denote models with bottom boundaries that are open and closed to convective flows, respectively.

In the following we employ $\langle 3D \rangle$ averages which are derived from spatial and temporal averages of the 3D simulations over constant τ_R surfaces. Twelve snapshots in the last one-fourth of each simulation were used. These average structures are useful both for a simple comparison with 1D structures and as inputs for the $\langle 3D \rangle$ spectral synthesis in Section 3.3. In Section 3.3.2 we report on the possibility of performing full 3D spectral synthesis instead of using $\langle 3D \rangle$ structures.

3.2.2 Input microphysics and 1D LHD code

Microphysics in the form of an EOS and opacity tables, are input parameters for CO^{5}BOLD. The EOS and opacity tables have been pre-calculated from reference 1D models, which in our case are the standard 1D DB model atmospheres of BW11 calculated using their 1D atmosphere code. In this thesis we refer to this code as ATMO. For reference, Fig. 3.2 shows the opacity as a function of wavelength for the photosphere of two BW11 models with $\log g = 8.0$. The optical depth at which plasma becomes optically thin for photons of frequency ν is defined by $\tau_R(\tau_\nu = 1)$ and is shown in Fig. 3.3 for selected 1D and mean 3D (hereafter $\langle 3D \rangle$) spectra (see Section 3) at $\log g = 8.0$. Each opacity table has been computed with 10 band-averaged opacity bins with boundaries at $\log \tau_R$ = [99.0, 0.25, 0.0, −0.25, −0.5, −1.0, −1.5, −2.0, −3.0, −4.0, −5.0]. We note that due to interpolation issues we did not include the extremely strong far-UV opacities whenever they were assigned to the missing $\log \tau_R$ = [−5.0,−99.0] opacity bin. As Fig. 3.2 shows, at low effective temperatures He I bound-free and He I lines from the ground level provide the far-UV opacities. At high effective temperatures He II bound-free and He II line opacities also contribute. These frequencies are fully opaque to light everywhere in the simulations and very little flux is transported at such short wavelengths in the photosphere, therefore this missing opacity has little impact on the resulting temperature and pressure stratifications that are used for spectral synthesis.

Another important difference between standard 1D structures and our 3D simulations comes from CO^{5}BOLD treating scattering as true absorption, again, due to current numerical limitations. Therefore, one may argue that any 3D effects we observe when comparing our 3D models with 1D ATMO structures are due to approximations with opacity tables, scattering and even the missing opacities mentioned earlier. To test this hypothesis, the ATMO structures were compared with stratifications calculated using a different 1D code called LHD [Caffau et al., 2007]. The LHD code treats microphysics by employing the same input tables as those used in CO^{5}BOLD, considers scattering as true absorption, and has been modified to rely on a mixing length parameterisation of ML2/$\alpha = 1.25$. Tremblay et al. [2013b] have

Table 3.1: Selected parameters of the pure-helium 3D model atmospheres. The effective temperature is calculated from the spatially and temporally averaged emergent stellar flux and $\delta I_{\rm rms}/\langle I \rangle$ is the relative bolometric intensity contrast.

$\log g$	$T_{\rm eff}$ (K)	Box size (km × km × km)	Time (stellar s)	$\delta I_{\rm rms}/\langle I \rangle$ (%)
7.5	12098	1.22×1.22×0.58	31.6	3.6
7.5	13969	1.98×1.98×0.67	31.6	8.9
7.5	15947	2.86×2.86×1.19	31.6	16.4
7.5	18059	6.09×6.09×1.46	31.6	21.3
7.5	19934	11.96×11.96×2.39	31.6	23.4
7.5	22023	21.75×21.75×4.51	31.6	25.5
7.5	23778	23.96×23.96×4.78	31.6	24.3
7.5	26382	37.47×37.47×10.88	31.6	22.9
7.5	27970	31.22×31.22×10.77	15.0	17.5
7.5	29992	31.22×31.22×11.86	20.0	9.4
7.5	31993	33.48×33.48×14.00	8.0	4.9
8.0	12020	0.70×0.70×0.10	10.0	2.1
8.0	14083	0.79×0.79×0.24	10.0	6.0
8.0	16106	0.94×0.94×0.18	10.0	11.9
8.0	18081	1.23×1.23×0.35	10.0	17.0
8.0	20090	2.00×2.00×0.58	10.0	19.4
8.0	21989	5.19×5.19×0.97	10.0	22.3
8.0	24135	8.62×8.62×1.41	10.0	23.8
8.0	25899	8.62×8.62×1.56	10.0	21.1
8.0	27948	17.69×17.69×3.04	10.0	20.6
8.0	29983	12.63×12.63×3.50	10.0	19.7
8.0	32002	12.63×12.63×3.28	10.0	14.8
8.0	33999	12.63×12.63×3.42	10.0	7.9
8.5	12141	0.25×0.25×0.05	3.2	1.5
8.5	14009	0.25×0.25×0.04	3.2	3.6
8.5	15961	0.34×0.34×0.05	3.2	7.6
8.5	18002	0.39×0.39×0.13	3.2	12.6
8.5	19955	0.60×0.60×0.20	3.2	15.5
8.5	21988	1.03×1.03×0.26	3.2	17.8
8.5	24130	1.78×1.78×0.37	3.2	22.1
8.5	25801	2.37×2.37×0.44	3.2	22.3
8.5	27939	2.53×2.53×0.59	3.2	20.6
8.5	30259	4.53×4.53×1.23	3.2	20.4
8.5	31859	4.53×4.53×1.23	3.2	19.7
8.5	33987	4.53×4.53×0.98	3.2	17.6
9.0	12124	0.06×0.06×0.01	1.0	0.8
9.0	14118	0.07×0.07×0.01	1.0	2.3
9.0	16030	0.11×0.11×0.02	1.0	5.0
9.0	17999	0.12×0.12×0.03	1.0	8.7
9.0	19530	0.12×0.12×0.03	1.0	11.2
9.0	21981	0.20×0.20×0.07	1.0	13.6
9.0	24084	0.39×0.39×0.10	1.0	17.2
9.0	26116	0.76×0.76×0.13	1.0	20.6
9.0	28169	0.76×0.76×0.16	1.0	20.6
9.0	30187	0.86×0.86×0.20	1.0	17.4
9.0	31449	0.86×0.86×0.20	1.0	17.2
9.0	33815	1.43×1.43×0.39	1.0	19.1

shown, from the comparison of pure-hydrogen structures, that differences between the LHD and ATMO codes are small apart from the input microphysics. Consequently, any difference observed between them in the case of pure-helium composition would likely be caused by approximations in the microphysics.

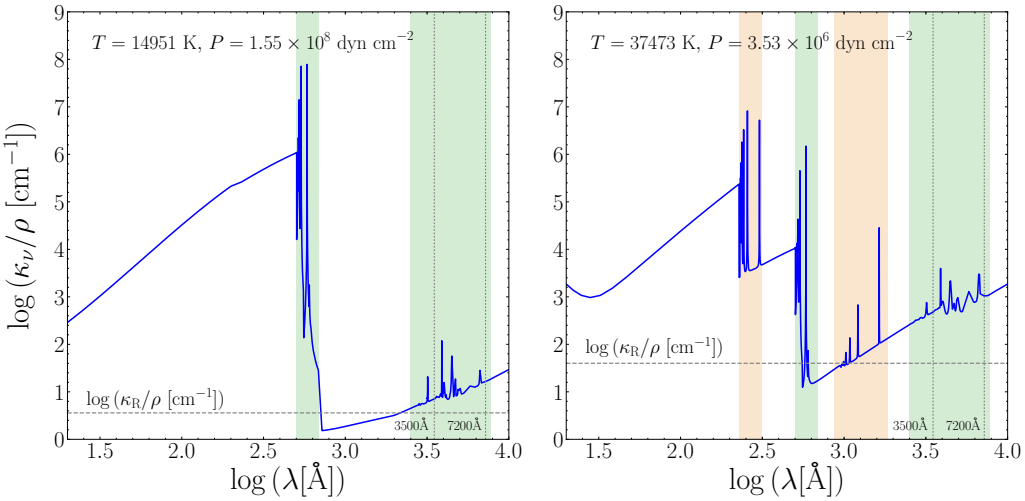

Figure 3.2: The total opacity as a function of the logarithm of wavelength for representative layers of two BW11 models with $\log g = 8.0$ at $T_{\rm eff} = 14\,000$ K (left) and $T_{\rm eff} = 34\,000$ K (right). We have selected reference temperature and pressure values (as indicated on the panels) that correspond to the plasma conditions at $\tau_{\rm R} = 1$. He I and He II line opacities are indicated by green and red colour regions. The Rosseland mean opacity (dashed grey) and the line region used for the derivation of the 3D corrections (dotted grey) are also shown.

Fig. 3.3 allows for the identification of the atmospheric layers where the continuum and lines between 3500 Å and 7200 Å are formed, so that a comparison can be made between ATMO, LHD and $\langle$3D$\rangle$ structures in the regions relevant to our spectral study. Such a comparison is shown in Figs. 3.4 and 3.5 for four models with $\log g = 8.0$ in terms of the temperature and density stratifications, respectively. On these figures we also indicate how the line forming region changes if the wavelengths that are closer than 0.5 Å from the line cores are not included. This boundary is more appropriate when models are used to fit typical low and medium resolution observations. As the line opacity increases significantly for the line cores, their removal causes the upper boundary of the line forming region to be significantly lower in the atmosphere.

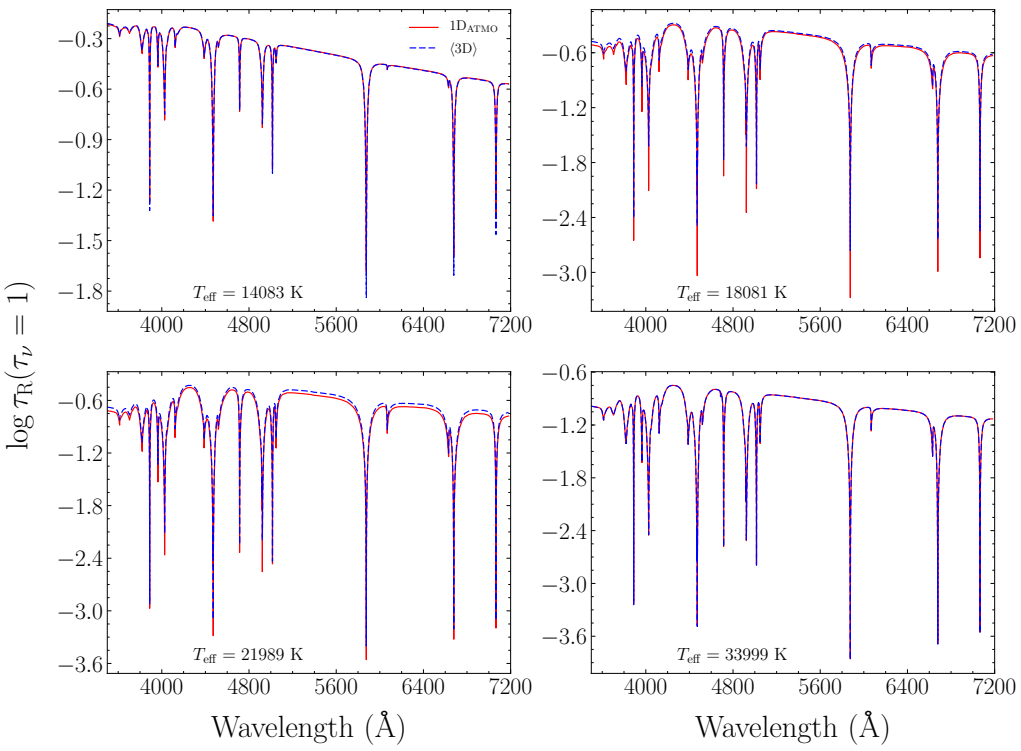

Figure 3.3: Atmospheric line forming regions for 1D ATMO (solid red) and ⟨3D⟩ (dashed blue) spectra as defined by $\tau_{\rm R}(\tau_\nu = 1)$, where the plasma becomes optically thin for photons of frequency ν.

The first observation from Figs. 3.4 and 3.5 is that for $T_{\rm eff} \sim 14\,000$, $18\,000$, and $22\,000$ K, the differences between the ⟨3D⟩ structures and their 1D counterparts are larger than the differences between 1D ATMO and LHD structures, i.e. the 3D corrections are more significant than the issues with microphysics. Nevertheless, there is some disagreement between ATMO and LHD models in this regime, especially at optical depths smaller than the inflexion point above which convection is abruptly switched off as per the prescription of the 1D mixing-length approximation (e.g. $\log \tau_{\rm R} \lesssim -1.7$ for the 18 000 K model). By calculating 1D ATMO structures with scattering treated as true absorption, we found that scattering only has a minor effect in the line forming region and does not significantly improve the agreement between ATMO and LHD. Therefore, we are left with opacity binning as the culprit for the small observed differences between 1D structures at cool temperatures.

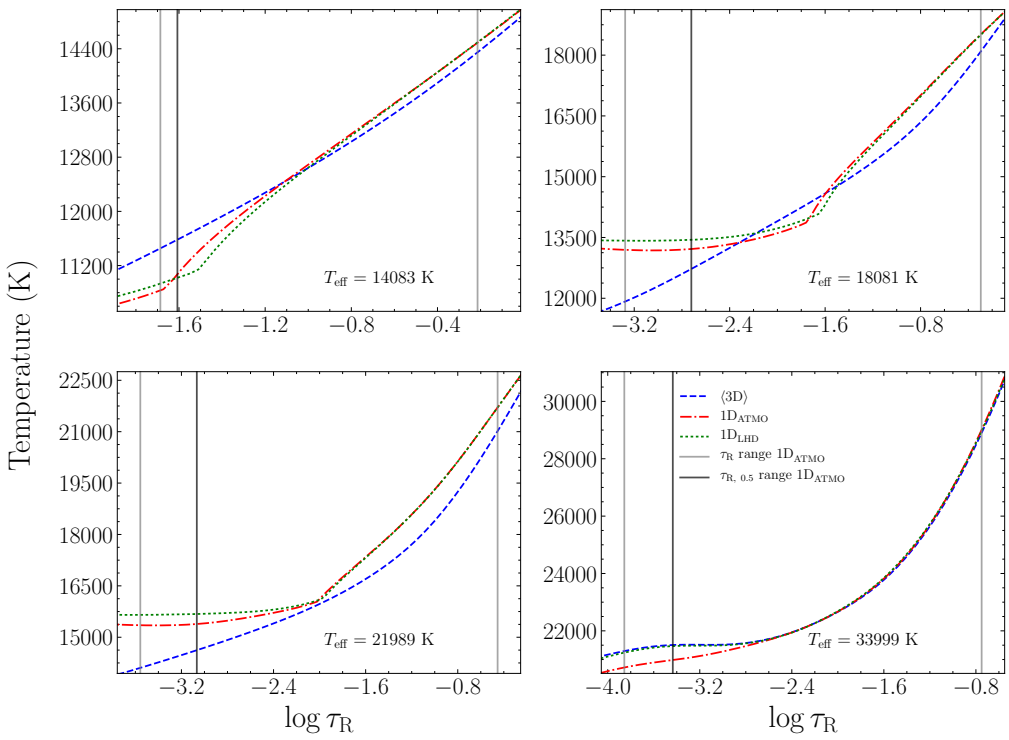

Figure 3.4: Temperature stratifications of spectral line forming regions for ⟨3D⟩ (dashed blue), 1D ATMO (dot-dashed red) and 1D LHD (dotted green) models. The line forming region is approximated by the grey vertical lines which represent the minimum and maximum $\tau_{\rm R}(\tau_\nu = 1)$ values in the range 3500 Å and 7200 Å according to Fig. 3.3. The black vertical lines represent the line forming region if the wavelengths that are within 0.5 Å of the line cores are ignored. The bottom boundaries do not change under this definition and therefore overlap with the grey lines.

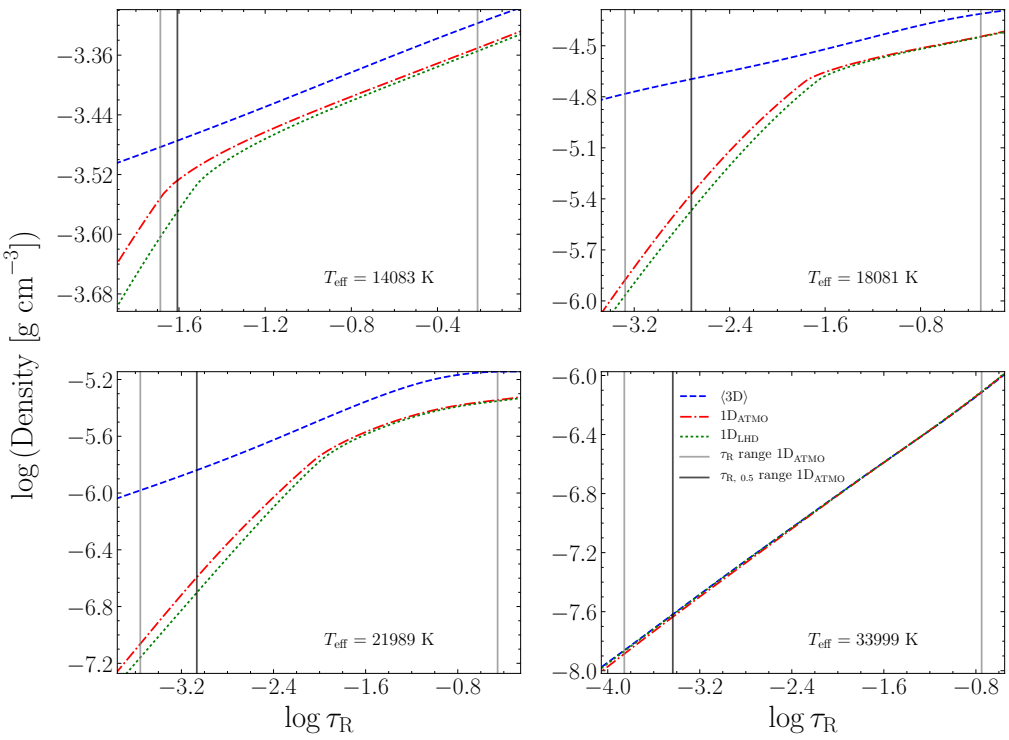

Figure 3.5: Similar to Fig. 3.4 but for density stratifications of spectral line forming regions for ⟨3D⟩, 1D ATMO and 1D LHD models.

At large temperatures (e.g. bottom right plot of Fig. 3.4 at $T_{\rm eff} \sim 34\,000$ K), the disagreement between LHD and ATMO structures becomes more severe in the line forming layers. Interestingly, the good agreement between LHD and ⟨3D⟩ structures demonstrates that 3D effects are expected to be small at these temperatures. We made attempts to improve the opacity binning procedure or include more bins in LHD (see Section 3.3.1), but the effect of this did not improve the agreement between ATMO and LHD significantly. Since the LHD and ATMO codes largely agree at cool temperatures and LHD converges to the 3D simulations in the warm radiative regime, we conclude that it is best to use 1D LHD structures to derive 3D corrections from CO^{5}BOLD simulations. One advantage of this differential analysis is the minimization of the uncertainties caused by the approximations in the microphysics discussed in this section. Furthermore, 3D corrections are generally used for DA white dwarfs rather than the 3D models being used for actual fitting [Tremblay et al., 2013c], suggesting that this method, which we refer to as the differential approach, is also advisable for DB white dwarfs. With these justifications, we proceed with 1D LHD structures in the following.

3.2.3 3D effects on atmospheric structures

To better understand the structural differences between 1D (LHD) and ⟨3D⟩ models, Figs. 3.6 and 3.7 compare the entropy and temperature stratifications for all 3D models with $\log g = 8.0$. Positive and negative entropy gradients as a function of $\tau_{\rm R}$ are indicative of atmospheric layers which are unstable and stable against convection, respectively.

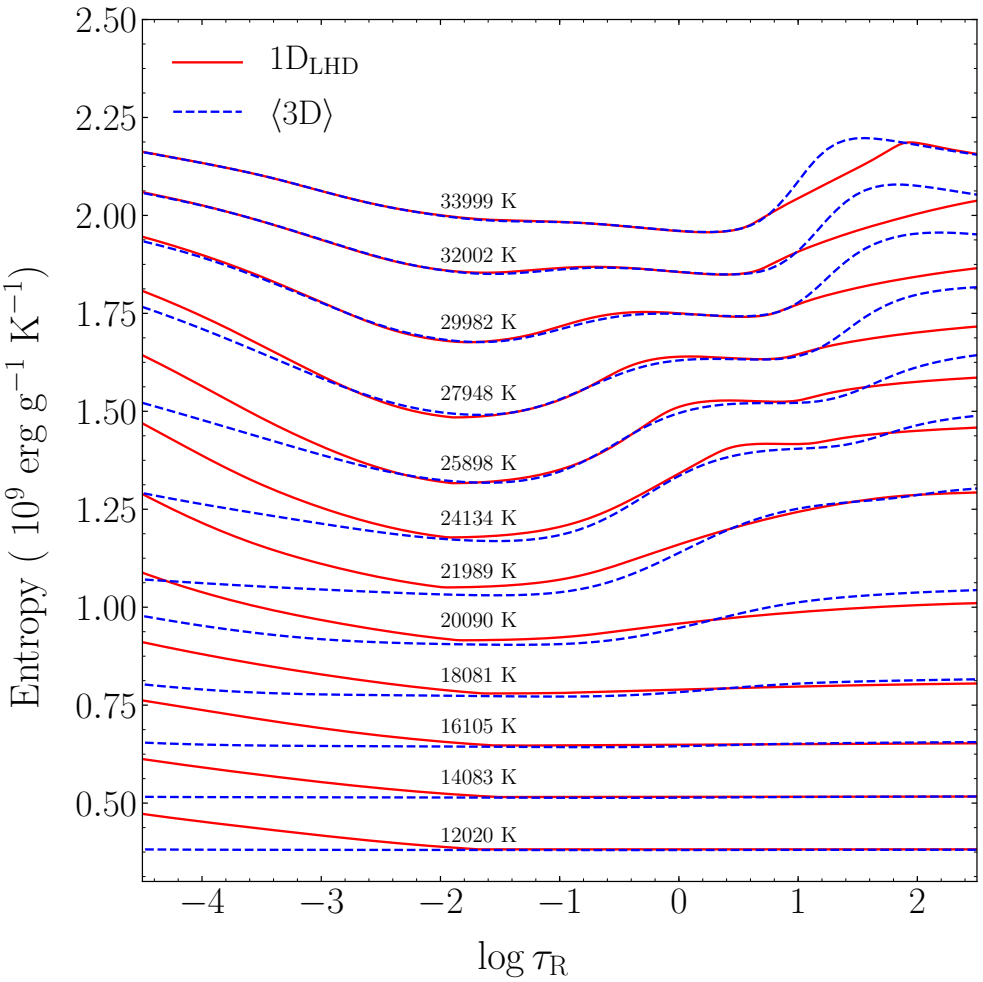

Figure 3.6: Entropy stratifications for 1D LHD (solid red) and ⟨3D⟩ (dashed blue) models with $\log g = 8.0$. All structures, apart from $T_{\rm eff} = 12020$ K, are offset from each other by 0.1×10^9 erg g^{-1} K^{-1} for clarity.

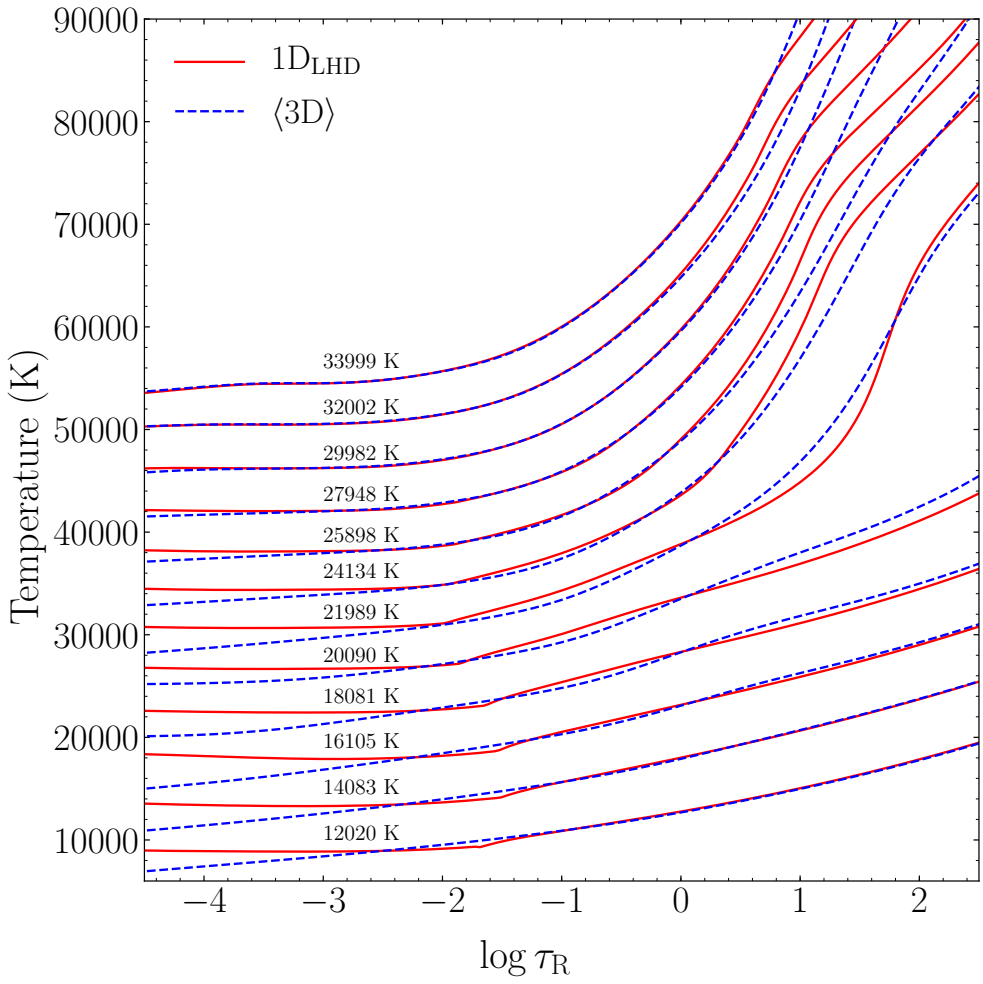

Figure 3.7: Temperature stratifications for 1D LHD (solid red) and ⟨3D⟩ (dashed blue) models with $\log g = 8.0$. All structures, apart from $T_{\rm eff} = 12020$ K, are offset from each other by 3000 K for clarity.

For the lowest effective temperatures, good agreement is observed between 1D and ⟨3D⟩ structures deeper than $\log \tau_{\rm R} = -1.6$, where convection is adiabatic and therefore both 1D and ⟨3D⟩ structures converge to the adiabatic gradient. Above these layers, however, the mixing-length approximation predicts no convection and the radiative equilibrium is reached. In the ⟨3D⟩ picture, overshoot contributes in cooling the upper layers and forces them to have an adiabatic stratification. Very similar results were found for cool DA white dwarfs [Tremblay et al., 2013b,c]. Above $T_{\rm eff} \sim 16\,000$ K, convection becomes non-adiabatic and sensitive to the prescription of the convective efficiency, resulting in emerging differences between 1D and ⟨3D⟩

models within the convection zone.

For effective temperature above 24 000 K but below 34 000 K, two convective zones develop as indicated by positive entropy gradients. These convection zones are associated with He I and He II ionization. This is observed for both 1D and ⟨3D⟩ structures in Fig. 3.6, though for the non-local 3D convection, the two convection zones are dynamically connected as the entropy gradient never becomes negative and the convective flux remains large in-between the two regions. In this regime the atmospheric structures of DB white dwarfs become more complex compared to DA stars. Convection is driven both by deep optically-thick He II convection and superficial optically-thin He I convection, with a thermally stable but dynamically active photosphere in between. For this DB temperature regime, Fig. 3.7 also shows that 3D effects become very small in the line forming layers owing to increasingly inefficient photospheric convection ($\tau_R < 1$). Figs. 3.6 and 3.7 do however suggest strong 3D effects near the bottom of the convection zone for warm simulations, which is related to 1D ML2/α = 1.25 models and 3D simulations predicting significantly different convection zone sizes. We note that this may not be limited to warmer simulations since we do not have access to the bottom of the convection zones for cooler models. The 1D models systematically overpredict the sizes of the convection zones, suggesting that a smaller mixing-length is necessary to match the deep 3D convection zones. We will report on the mixing-length calibration for 1D structures in Chap. 5. The mixing length calibration for the size of the convection zone has little to do with the mixing-length value that would be needed for the 1D models to match 3D structures in the line forming regions, $\tau_{\rm R}(\tau_\lambda = 1)$, which appears neither to be overestimated or underestimated according to Figs. 3.6 and 3.7.

Differences between 1D and ⟨3D⟩ structures can also be understood by looking at the resolved 3D simulations. Fig. 3.8 shows the bolometric intensity emerging at the top of the simulations for four of the 3D models with $\log g = 8.0$. The results are very similar at other surface gravities albeit with a shift in temperature. At low effective temperatures where adiabatic convection dominates, the boundaries of the granules are ill-defined. In this regime the lack of energy loss and the large densities make it possible for convection to transport the required stellar flux with a very small intensity contrast. For larger effective temperatures convection becomes non-adiabatic and the intensity contrast increases. The radiative timescale decreases such that only the largest granules survive, resulting in a granulation pattern of large cells and narrow intergranular lanes. At $T_{\rm eff} \sim 22\,000$ K, the surface of a DB star looks remarkably similar to a DA white dwarf at $T_{\rm eff} \sim 12\,000$ K [see Fig. 5 of Tremblay et al., 2013b]. At $T_{\rm eff} \sim 34\,000$ K, convection is very inefficient in the photosphere

and the contrast between the cells and intergranular lanes decreases.

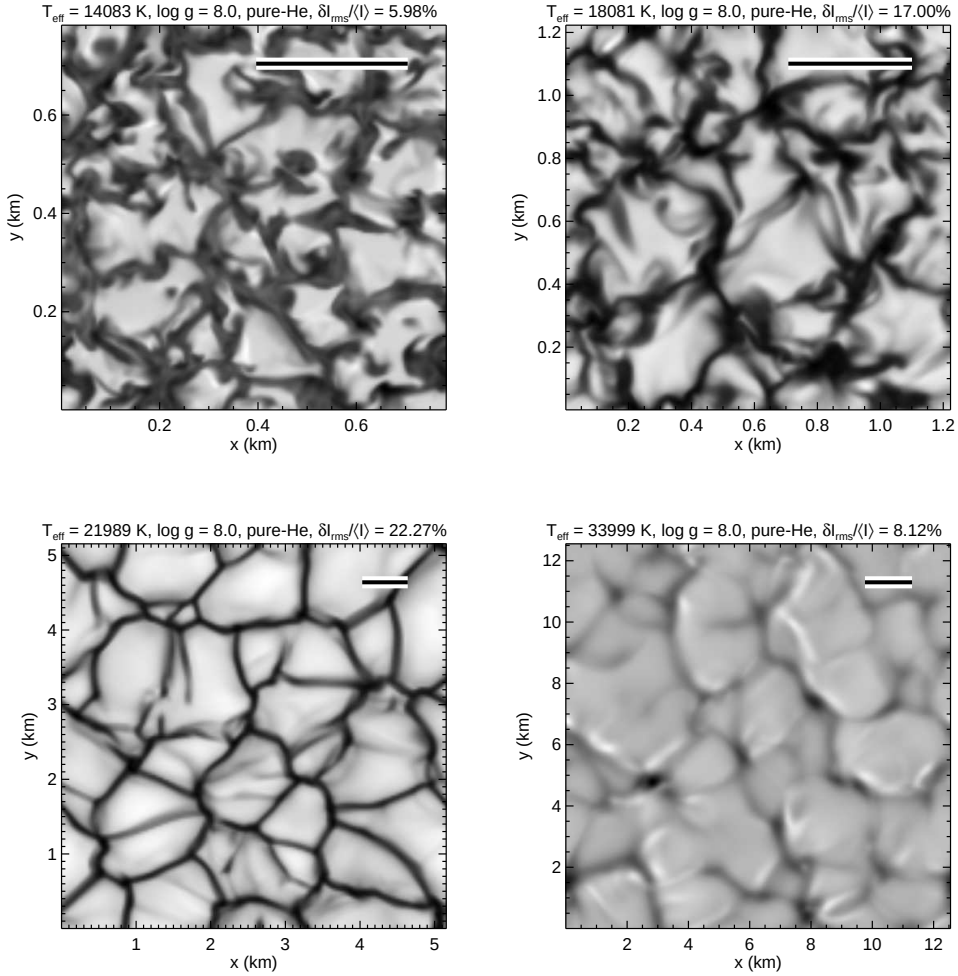

Figure 3.8: Bolometric emergent intensity for selected models with $\log g = 8.0$. The effective temperatures, surface gravities and intensity contrasts of the simulations are shown in the legends. The length of the bar on the top right of each panel is ten times the pressure scale height at $\langle \tau_{\rm R} \rangle = 1$.

In Fig. 3.9 we show the ratio of the characteristic granule size to the pressure scale height at $\langle \tau_{\rm R} \rangle = 1$ for 3D DA and DB models. In this section all quantities are averaged over constant geometrical depth. The characteristic granule sizes were calculated from the peaks of the emergent intensity power spectra [Tremblay et al., 2013a]. Hotter DB models with $T_{\rm eff} \gtrsim 22\,000$ K have granule sizes that are more than ten times the local pressure scale height. Almost all of the models with two convection zones have ratios above 10, suggesting that the presence of He II con-

vection zone is connected to this behaviour unique to DB white dwarfs. Following the procedure laid out in Tremblay et al. [2013a] we confirm that the sizes of the granules are consistent with conservation of mass flux, where the continuity equation reduces to

$$\frac{v_{\text{hor, rms}}}{v_{\text{z, rms}}} \propto \frac{L}{H}, \tag{3.2}$$

where $v_{\text{hor, rms}}$ and $v_{\text{z, rms}}$ are the horizontal and vertical root mean square velocities, respectively, L is the characteristic granule size and H is the scale height of momentum density.

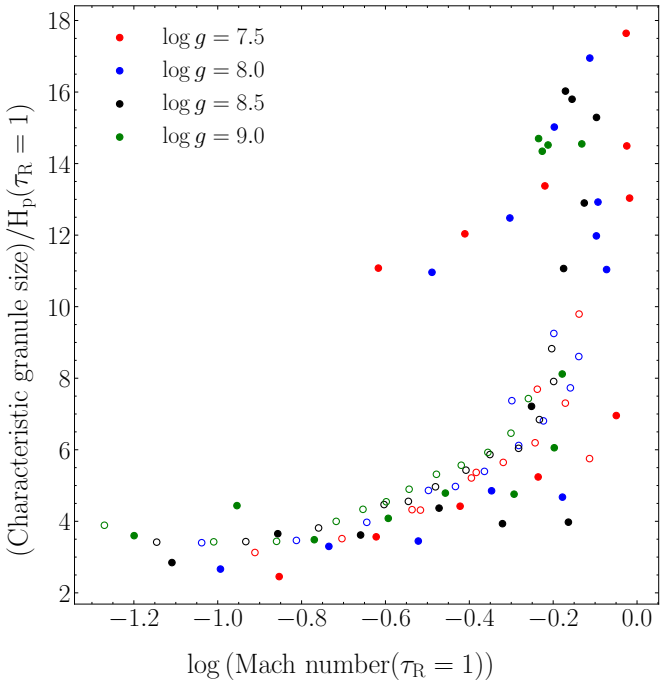

Figure 3.9: The ratio of the characteristic granule size to the pressure scale height at $\langle\tau_{\text{R}}\rangle = 1$ as a function of logarithm of the Mach number at $\langle\tau_{\text{R}}\rangle = 1$ for 3D DB (filled circles) and 3D DA (unfilled circles) models.

Figs. 3.10 and 3.11 show the intensity contrast as a function of effective temperature and as a function of the Mach number at $\langle\tau_{\text{R}}\rangle = 1$, respectively. The latter plot also includes data for 3D DA atmospheres from Tremblay et al. [2013a]. We define the Mach number as

$$\text{Mach} = \frac{v_{\text{rms}}}{c_{\text{sound}}} = \sqrt{\frac{\langle\rho\rangle v_{\text{rms}}^2}{\langle\Gamma_1\rangle\langle P\rangle}}\ , \tag{3.3}$$

where $v_{\rm rms}$ is the convective velocity, $c_{\rm sound}$ is the sound speed; $\langle\rho\rangle$, $\langle P\rangle$ and $\langle\Gamma_1\rangle$ are the geometric horizontal averages of density, pressure and the first adiabatic constant, respectively. Following Tremblay et al. [2013a] $v^2_{\rm rms}$ is

$$v^2_{\rm rms} = \langle v^2\rangle - \frac{[\langle\rho v_x\rangle^2 + \langle\rho v_y\rangle^2 + \langle\rho v_z\rangle^2]}{\langle\rho\rangle^2} \ , \tag{3.4}$$

where $\langle v^2\rangle$ is the horizontally averaged mean square velocity and $\langle\rho v_x\rangle^2$, $\langle\rho v_y\rangle^2$, $\langle\rho v_z\rangle^2$ are the three horizontally averaged mass fluxes. The density weighted mean velocity is removed due to its sensitivity to numerical parameters and oscillations.

Both the intensity contrast and the Mach number are measures of the strength of convection and they span a similar range in DA and DB white dwarfs. Helium-atmosphere simulations reach a maximum intensity contrast of about 25% compared to 20% for hydrogen-rich compositions. We note that the range in the former case is closer to that seen in main-sequence stars where He ionization is also of relevance [Tremblay et al., 2013a]. For a given intensity contrast or Mach number, the density is significantly higher for a DB white dwarf compared to any other convective star, owing to the smaller internal energy density per gram and the larger energy flux to transport. The peak in intensity contrast for DB models with $\log g = 8.0$ is observed at the effective temperature of 24 000 K, and above this temperature the peak significantly decreases and tends towards small intensity contrast for the models with $\log g = 8.0$ and $\log g = 7.5$. This is expected for models that are becoming fully radiative. Although it seems that the intensity contrast is useful to measure the strength of 3D effects on spectra, the link between 3D inhomogeneities and opacities (and thus predicted spectral lines) is highly non-linear. Furthermore, the strength of 3D effects on spectra also depends on how the different regions of the surface average.

The mean Mach number for a handful of 3D DB models approaches unity at the photosphere, indicating that the flows are close to being supersonic. As such, shocks can occur in the simulation and could imprint themselves on synthetic spectra. We note that the situation is no different for DA white dwarfs or main-sequence stars for which the mean Mach number can reach a value close to one.

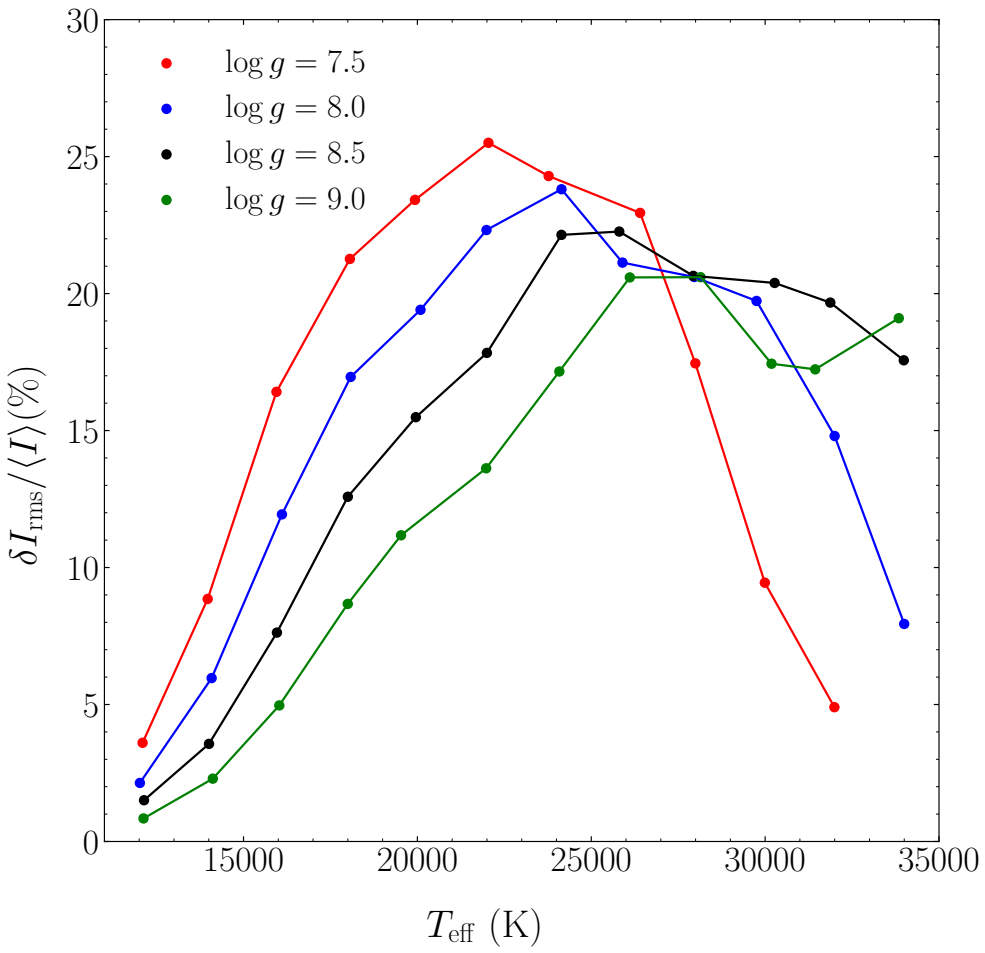

Figure 3.10: Bolometric intensity contrast as a function of effective temperature for the pure-helium 3D model atmospheres. The points representing intensity contrasts for the same surface gravity are connected for clarity.

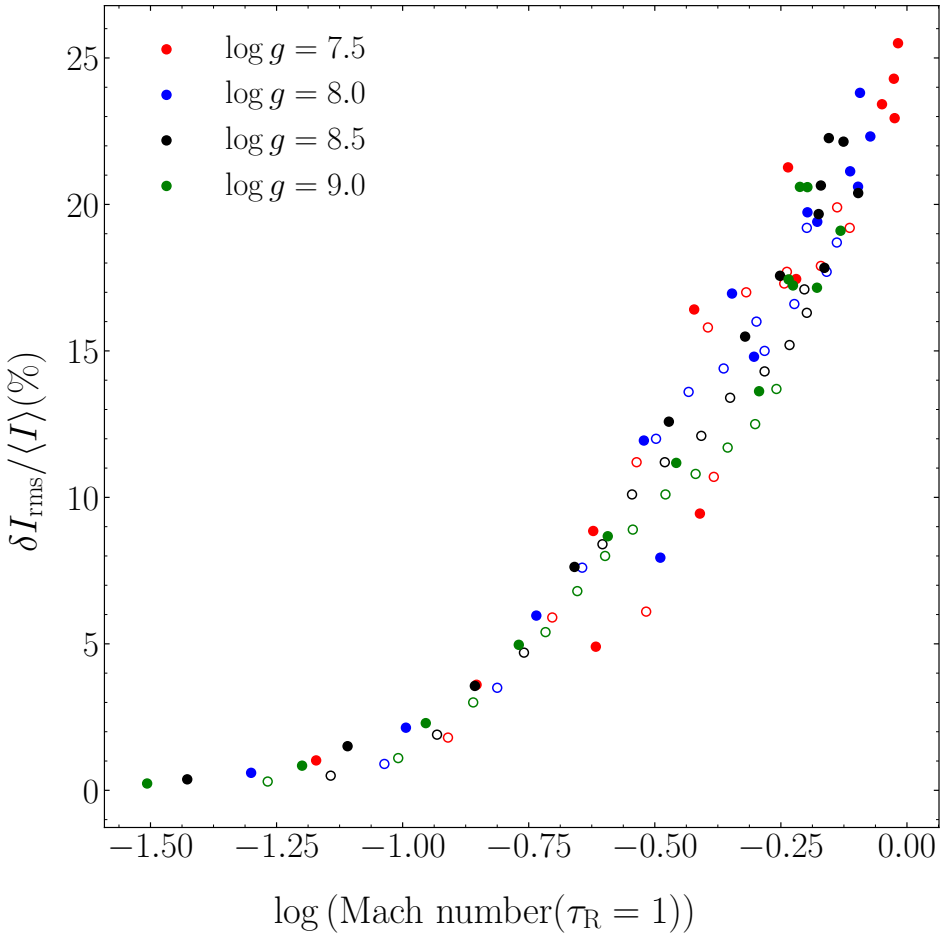

Figure 3.11: Bolometric intensity contrast as a function of the logarithm of the Mach number at $\langle \tau_{\rm R} \rangle = 1$ for our pure-helium 3D model atmospheres (filled circles) and the 3D DA atmospheres of Tremblay et al. [2013a, open circles].

3.3 Model spectra

Neither LHD nor CO^{5}BOLD can perform detailed spectral synthesis. Given our differential approach at comparing 1D LHD and $\langle$3D$\rangle$ structures, it is thus appropriate to use the ATMO code (BW11) to calculate synthetic spectra. We employ the same numerical setup as used by BW11 to compute their DB grid.

To calculate the differential 3D corrections on effective temperature and surface gravity, we use the DB fitting code of BW11 to fit $\langle$3D$\rangle$ synthetic spectra with a grid of 1D (LHD) spectral grid. This allows us to find a 1D spectrum that most

closely resembles a given 3D spectrum. We define the 3D corrections to be

$$T_{\rm eff,\ corr} = T_{\rm eff,\ 3D\ model} - T_{\rm eff,\ 1D\ fit}\ , \tag{3.5}$$

and

$$\log g_{\rm corr} = \log g_{\rm 3D\ model} - \log g_{\rm 1D\ fit}\ . \tag{3.6}$$

The use of BW11 fitting code ensures that we consider the same wavelength region and the same lines that BW11 analysed in their study. Since DBA stars were also included in their study, BW11 used the code to either fit hydrogen lines or to apply upper limits in the case of non-detection. As our models are pure-helium, we have instead adapted the code to have pure-helium composition as the only option. Before presenting our proposed 3D corrections, we first evaluate the uncertainties from the different approximations we have made, namely the opacity binning procedure and the mean 3D approximation.

3.3.1 Effect of opacity binning

Two sets of 1D LHD structures with $\log g = 8.0$ were computed with the same effective temperatures as the 3D models. The first set was computed with 10 bin opacity tables already employed for our 3D models and we shall refer to these as "$\rm LHD_{original}$". The other "$\rm LHD_{16-20bins}$" set was calculated using opacity tables with 16 to 20 bins, which do not remove the large far-UV opacity unlike the 10 bin opacity tables. We have derived synthetic spectra using ATMO for the two sets of LHD structures. The full grid of BW11 1D DB synthetic spectra is also used for our opacity binning analysis. This grid was calculated from 1D structures computed with the ATMO code and therefore all 1745 frequencies were used in the computation instead of opacity binning. To quantify the corrections arising from the opacity binning, the two types of LHD spectra were fitted with the 1D ATMO spectral grid and the differences between the atmospheric parameters are shown in Fig. 3.12. A negative difference indicates that ATMO overestimates the effective temperature and surface gravity of the LHD spectrum. BW11 determined external errors by fitting multiple spectra of the same white dwarf and using the scatter in the fitted values as the error. This was done using 28 individual white dwarfs. They found average uncertainties of $\langle \Delta T_{\rm eff}/T_{\rm eff} \rangle = 2.3\%$ and $\langle \Delta \log g \rangle = 0.052$ when obvious outliers are removed (see their Fig. 17). These errors are plotted on Fig. 3.12 and are referred to as BW11 errors. For comparison, the external uncertainties for the Koester and Kepler [2015] SDSS sample are $\langle \Delta T_{\rm eff}/T_{\rm eff} \rangle = 3.1\%$ and $\langle \Delta \log g \rangle = 0.12$. The reason why Koester and Kepler [2015] errors are larger than BW11 errors is because the

SDSS sample has on average a smaller signal-to-noise ratio.

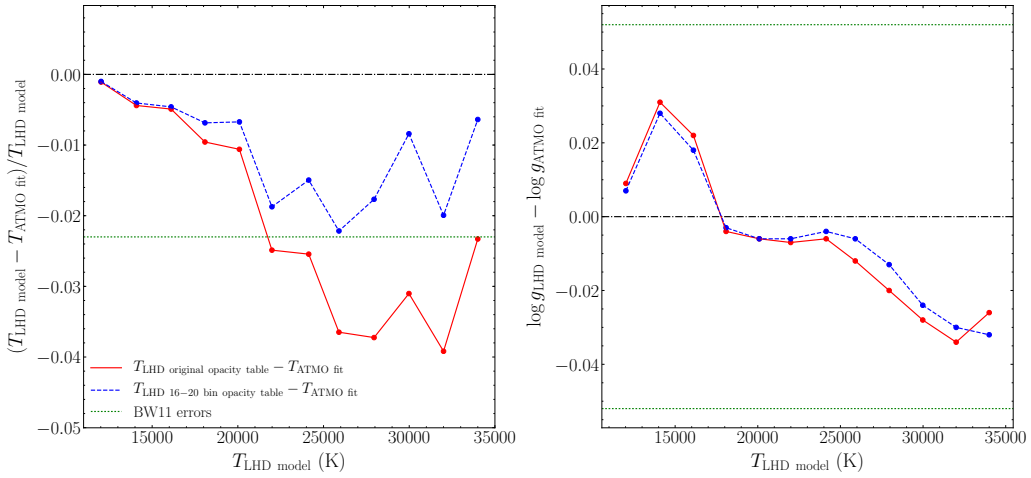

Figure 3.12: Fits of synthetic spectra based on 1D LHD structures with $\log g = 8.0$ that have been computed with two types of opacity tables: original (10 bins, solid red) and extended (16-20 bins, dashed blue). These model spectra were fitted with a grid of standard 1D ATMO spectra of BW11 to quantify the differences between the two types of 1D codes. The resulting effective temperature and surface gravity corrections are presented on the left and right panels, respectively. The external observational uncertainties of BW11 are also shown with dotted green lines. A dot-dashed horizontal black line representing a null correction has also been added to each panel for clarity.

The surface gravity corrections for models with original and extended opacity tables are well within fitting uncertainties (right panel of Fig. 3.12). For the effective temperature corrections only the LHD models with extended opacity tables fall within the uncertainties. As expected from our discussion around Figs. 3.4 and 3.5 and the comparison of ATMO and LHD structures, the largest differences are expected for the warmest simulations. Although the agreement improves when doubling the number of opacity bins, we did not pursue the possibility of improving the opacity binning procedure for LHD and by inference our CO^{5}BOLD simulations because of the dramatic increase in computation time. Instead we employ our 10 bin tables. This is because deriving 3D corrections with the help of 1D LHD models removes the offset observed in Fig. 3.12.

3.3.2 Mean 3D approximation

Ideally, 3D spectral synthesis is performed to compute a spectrum directly from a 3D data cube. One such code, Linfor3D [Ludwig and Steffen, 2008], was utilised

by Tremblay et al. [2011] to model synthetic 3D Hβ lines for DA white dwarfs. While the code could be adapted to synthesise selected 3D spectral lines for DB white dwarfs, it would be computationally expensive to create a full grid of 3D model spectra. Instead, we proceed with the comparison of two types of estimates for calculations of synthetic spectra from 3D simulations: the $\langle$3D$\rangle$ and 1.5D approximations. Our standard $\langle$3D$\rangle$ spectra are computed from the $\langle$3D$\rangle$ temperature and pressure structures using ATMO. On the other hand, the 1.5D method assumes that each 3D simulation, which is made up of $150 \times 150 \times 150$ grid points, is a collection 150×150 "1D" atmospheres, where the vertical extent of the simulation (z-axis) is the extent of these 1D atmospheres. For each of the "1D" atmospheres a spectrum is then calculated using ATMO and the resulting 150×150 spectra are simply averaged to produce a so-called 1.5D spectrum for a given 3D model. However, we found that some of the atmospheres exhibited pressure inversion due to the departure from hydrostatic equilibrium, which is expected in 3D simulations. ATMO is not adapted to handle such departures and therefore any structures with pressure inversion were removed from the 1.5D spectrum calculations. At most a couple of per cent of structures were removed. We also want the 1.5D spectrum to be representative of the entire simulation and not of one single time snapshot, and therefore we used several snapshots over the last quarter of the computation for the average. The $\langle$3D$\rangle$ and 1.5D methods represent the two extremes in neglecting or enhancing the 3D fluctuations, respectively, and thus the full 3D spectral synthesis is somewhere in between these two methods. For the majority of 3D DA models, with the exception of extremely low-mass (ELM) white dwarfs, it has been shown that 1.5D and $\langle$3D$\rangle$ corrections are equivalent [Tremblay et al., 2015a]. This results from a complex cancellation of the 3D fluctuations in spectral synthesis [Tremblay et al., 2013c] and there is no obvious reason to assume the same behaviour for DB white dwarfs.

To determine the uncertainties arising from not using the full 3D spectral synthesis, we fitted both the 1.5D and $\langle$3D$\rangle$ spectra with the 1D LHD model grid to find their respective corrections. Fig. 3.13 shows the differences between the $\langle$3D$\rangle$ and 1.5D corrections for models with $\log g = 8.0$, although similar results are obtained for other surface gravity models. The BW11 errors are also shown. A negative difference means that the 1.5D correction is larger and this is what we observe for 3D simulations below $\approx 24\,000$ K. Most of the differences are well within the BW11 external errors, with the maximum offset observed at $\approx 20\,000$ K. At this particular effective temperature, He I lines reach their maximum strength (depending on the assumed convective efficiency) giving rise to the hot/cool solution problem, where for

any given DB spectrum there are two possible fits with equivalent χ^2 values. BW11 have also shown that in the range $20\,000 \lesssim T_{\rm eff} \lesssim 28\,000$ K, the spectra are quite insensitive to the effective temperature. This suggests that fitting uncertainties may peak in this region even though we have employed a constant average uncertainty in percentage.

Another possibility for the disagreement between 1.5D and $\langle$3D$\rangle$ corrections could be related to the high Mach numbers of some of the DB simulations as 1.5D spectra are more sensitive to thermal fluctuations caused by shocks. However, for simulations with $\log g = 8.0$, the $T_{\rm eff} \approx 22\,000$ K model has the highest Mach number, and yet for this particular model the $\langle$3D$\rangle$ and 1.5D corrections do agree, suggesting that there is no obvious link.

We stress that since the full 3D spectral synthesis is expected to lie somewhere between the 1.5D and $\langle$3D$\rangle$ corrections, Fig. 3.13 likely overestimates the error of using the $\langle$3D$\rangle$ approximation. We conclude that the $\langle$3D$\rangle$ approximation is valid for DB white dwarfs, a result that is similar to that found for DA stars with $\log g \geq 7.0$.

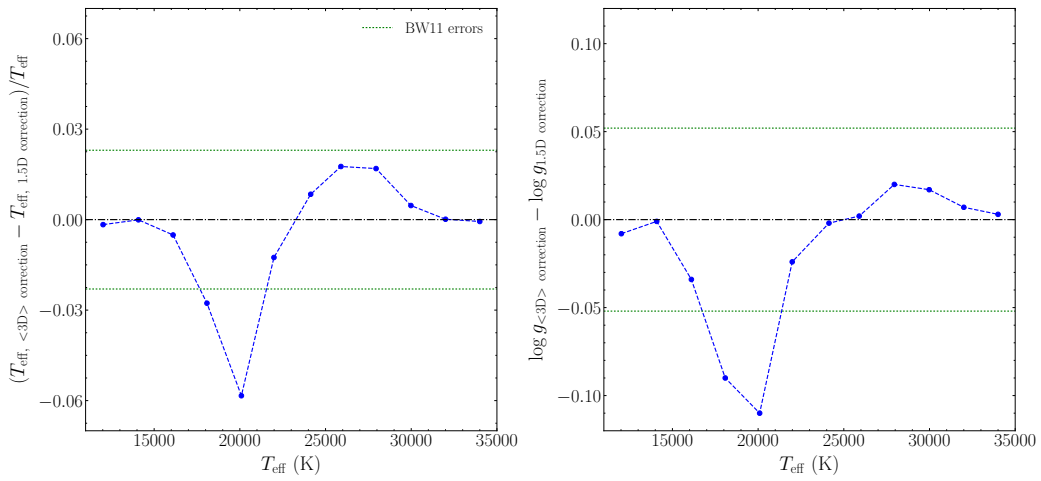

Figure 3.13: 1.5D and $\langle$3D$\rangle$ spectra with $\log g = 8.0$ are compared in terms of the differences between their respective effective temperatures (left panel) and surface gravities (right panel) corrections found by fitting the two types of spectra with the 1D LHD models. External fitting uncertainties from BW11 are also shown. A dot-dashed horizontal black line representing the equivalence of 1.5D and $\langle$3D$\rangle$ corrections (and therefore spectra) has also been added to each panel.

3.4 Discussion

3.4.1 3D corrections

Our proposed 3D corrections for pure-helium DB white dwarfs are shown in Fig. 3.14 and are tabulated in Table 3.2. To derive these corrections the original opacity tables with 10 bins were used. The corrections were derived using the reference 1D LHD spectral grid under the ML2/α = 1.25 parametrisation, and Eqs. 3.5 and 3.6. Since the effective temperatures of the 3D models can only be found after the simulation is run, resulting in uneven spacing in effective temperature range of the 3D models, we interpolated over the corrections to provide corrections that are spaced out by 1 000 K in effective temperature. In the figure, the dashed lines denote $\log g$ = [7.5, 8.0, 8.5, 9.0]. The intersection points between the dashed horizontal lines and the blue lines are the 1D effective temperatures and surface gravities. The blue lines then extend to the corresponding 3D parameters, such that the lengths of the blue lines represent our proposed 3D corrections for the 1D parameters. The main uncertainty in the 3D corrections resides in the $\langle$3D$\rangle$ approximation discussed in Section 3.2, but also important is the validity of the pure-helium atmosphere approximation when applying the corrections to specific DB white dwarfs.

At low effective temperatures, we do not observe significant temperature corrections. Above $\sim$ 22 000 K, especially for large surface gravities, the temperature corrections can reach up to 3000 K. For $\log g$ = 7.5 and 8.0, however, the effective temperature corrections become negligible at the highest effective temperatures, where the spectral line forming regions become radiative and therefore equivalent to their 1D counterparts. We do not observe any significant temperature corrections for the V777 Her instability strip [Fontaine and Brassard, 2008] at $\log g$ = 8.0. We remind the reader, however, that asteroseismic predictions could be impacted by the significantly different sizes for the 3D convection zones as discussed in Section 3.2.3. It is reassuring that the current ML2/α = 1.25 parameterisation for the optical spectra of DB white dwarfs, which mostly impacts the effective temperature scale, is in reasonable agreement with the 3D simulations.

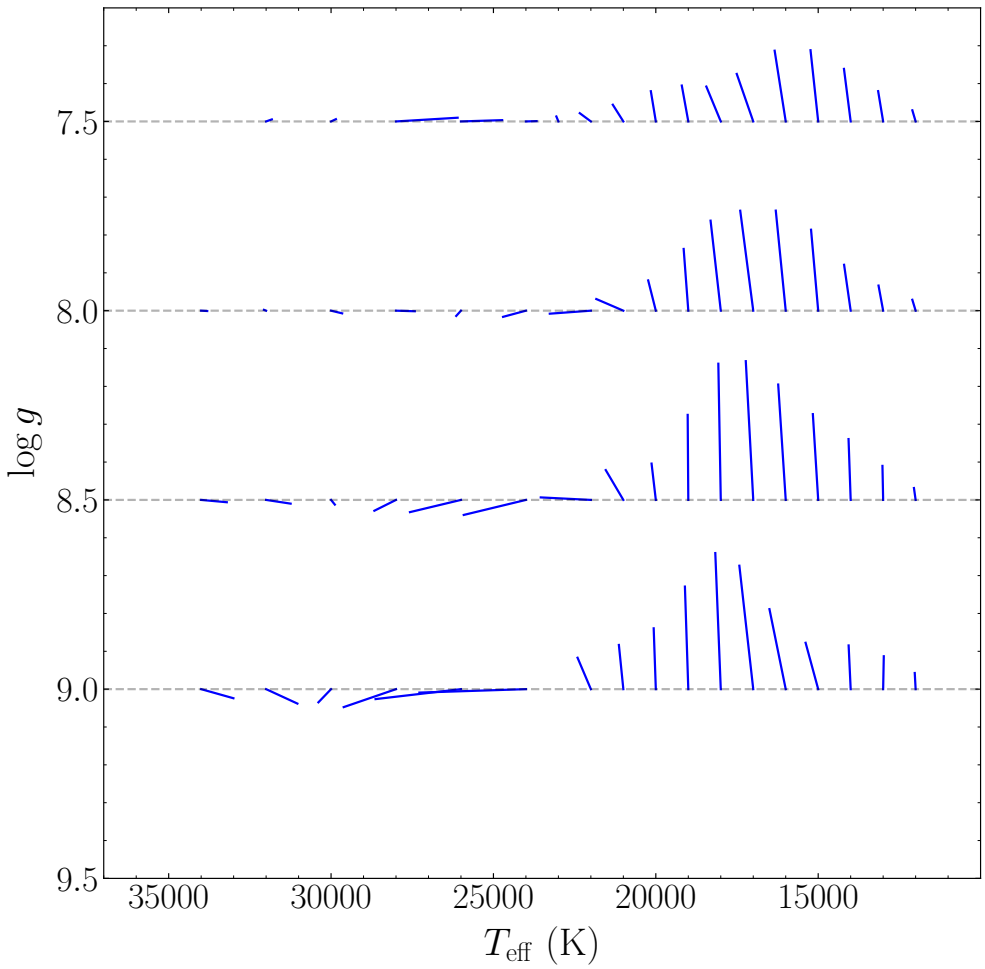

Figure 3.14: Proposed 3D corrections for pure-helium white dwarf atmospheres when compared with 1D model spectra using the ML2/α = 1.25 parameterisation. The horizontal dashed lines indicate $\log g = [7.5, 8.0, 8.5, 9.0]$, whereas the intersections between the dashed lines and the blue lines are the reference 1D atmospheric parameters. If one follows a given blue line from the intersection, its length will give the 3D correction for the particular 1D effective temperature and surface gravity. For clarity, at high effective temperatures some of the corrections from Table 3.2 are not shown. This figure can be compared to 3D DA corrections from Tremblay et al. [2015a].

Table 3.2: Our proposed 3D corrections for surface gravity and effective temperature derived from ⟨3D⟩ structures. A negative value indicates that 1D overestimates the parameter, while a positive value indicates underestimation.

1D $\log g$	1D $T_{\rm eff}$	3D $\log g$ correction (dex)	3D $T_{\rm eff}$ correction (dex)
7.5	12000	−0.029	100
7.5	13000	−0.080	154
7.5	14000	−0.139	206
7.5	15000	−0.188	236
7.5	16000	−0.187	340
7.5	17000	−0.126	507
7.5	18000	−0.092	444
7.5	19000	−0.095	200
7.5	20000	−0.080	153
7.5	21000	−0.044	324
7.5	22000	−0.022	341
7.5	23000	−0.013	62
7.5	24000	−0.001	−328
7.5	25000	0.002	−710
7.5	26000	−0.003	−1268
7.5	27000	−0.009	−1915
7.5	28000	−0.010	−1897
7.5	29000	−0.004	−201
7.5	30000	−0.006	−148
7.5	31000	−0.006	−165
7.5	32000	−0.005	−176
7.5	33000	−0.003	−218
7.5	34000	−0.000	149
8.0	12000	−0.029	101
8.0	13000	−0.066	142
8.0	14000	−0.121	202
8.0	15000	−0.214	219
8.0	16000	−0.264	306
8.0	17000	−0.264	400
8.0	18000	−0.238	314

Continued on next page

Table 3.2 continued.

1D $\log g$	1D $T_{\rm eff}$	3D $\log g$ correction (dex)	3D $T_{\rm eff}$ correction (dex)
8.0	19000	−0.163	142
8.0	20000	−0.080	234
8.0	21000	−0.031	833
8.0	22000	0.008	1264
8.0	23000	0.015	1055
8.0	24000	0.016	703
8.0	25000	0.017	558
8.0	26000	0.014	146
8.0	27000	0.011	−484
8.0	28000	0.001	−578
8.0	29000	0.003	−105
8.0	30000	0.007	−342
8.0	31000	0.003	−252
8.0	32000	−0.002	66
8.0	33000	−0.001	−627
8.0	34000	0.001	−186
8.5	12000	−0.031	51
8.5	13000	−0.090	21
8.5	14000	−0.161	65
8.5	15000	−0.227	164
8.5	16000	−0.305	231
8.5	17000	−0.367	229
8.5	18000	−0.360	75
8.5	19000	−0.225	18
8.5	20000	−0.096	130
8.5	21000	−0.079	541
8.5	22000	−0.007	1543
8.5	23000	0.032	1886
8.5	24000	0.040	1913
8.5	25000	0.033	1915
8.5	26000	0.032	1570
8.5	27000	0.037	1068

Continued on next page

Table 3.2 continued.

1D $\log g$	1D $T_{\rm eff}$	3D $\log g$ correction (dex)	3D $T_{\rm eff}$ correction (dex)
8.5	28000	0.029	666
8.5	29000	0.021	396
8.5	30000	0.012	−116
8.5	31000	0.004	−455
8.5	32000	0.010	−755
8.5	33000	0.011	−1580
8.5	34000	0.006	−789
9.0	12000	−0.043	26
9.0	13000	−0.087	−19
9.0	14000	−0.115	62
9.0	15000	−0.123	387
9.0	16000	−0.211	500
9.0	17000	−0.326	427
9.0	18000	−0.360	168
9.0	19000	−0.271	104
9.0	20000	−0.161	65
9.0	21000	−0.117	137
9.0	22000	−0.083	410
9.0	23000	−0.069	1042
9.0	24000	0.009	3279
9.0	25000	0.018	3071
9.0	26000	0.026	2629
9.0	27000	0.042	2119
9.0	28000	0.047	1610
9.0	29000	0.045	1110
9.0	30000	0.035	389
9.0	31000	0.030	−333
9.0	32000	0.038	−963
9.0	33000	0.040	−1434
9.0	34000	0.024	−993

Concluded

The 1D models tend to significantly overpredict the surface gravity in the range 14 000 K $\lesssim T_{\rm eff} \lesssim$ 21 000 K for $\log g = 7.5$ and 8.0, but this range does extend further to 22 000 K for $\log g = 8.5$ and to 24 000 K for $\log g = 9.0$. Above these effective temperatures, the 3D surface gravity corrections are within the BW11 errors. BW11 and Koester and Kepler [2015] have shown that DB and DBA white dwarfs in the range 12 000 K $\lesssim T_{\rm eff} \lesssim$ 16 000 K have larger than expected surface gravities, with maximum discrepancy between the spectroscopically derived surface gravities and those predicted by stellar evolutionary models occurring at around 13 000-14 000 K. Therefore, our proposed 3D surface gravity corrections are an incomplete solution to this problem. Many studies have attributed the high-$\log g$ problem in DB white dwarfs to issues with the line broadening by neutral helium and not with the treatment of convection. Our results provide support for this scenario. Furthermore, a smooth mass versus cooling age distribution for DB stars is expected from evolutionary models. When applying our 3D corrections to the 1D atmospheric parameters determined in BW11 and Koester and Kepler [2015] assuming pure-helium atmospheres as a very preliminary assessment, the 3D parameters are not in obviously better or worse agreement with evolutionary models. To fully understand the mass distribution of DB white dwarfs, we believe that 3D simulations with mixed helium and hydrogen compositions must first be calculated, even though Beauchamp et al. [1999] suggest that hydrogen does not significantly impact the atmospheric parameters in the range 14 000 K $\lesssim T_{\rm eff} \lesssim$ 20 000 K.

A study of the temperature and density stratifications (Figs. 3.4 and 3.5) in the line forming regions (Fig. 3.3) can be useful to understand the strong predicted 3D corrections at $T_{\rm eff} \sim$ 18 000 K. Fig. 3.3 (top right panel) illustrates that 3D effects on the mean structure are strong enough at this effective temperature that the 3D lines are formed in a significantly narrower range of the atmosphere. Fig. 3.5 shows that in the line forming region, the density is significantly larger in the 3D simulation. Since density correlates with surface gravity, it suggests that a higher gravity 1D structure is necessary to mimic the 3D density stratification, resulting in a negative surface gravity correction. We note that the spectral lines are formed largely within the convective zone and the 3D effects are especially strong in this regime. We have, therefore, no reason to doubt the accuracy of the 3D simulations or suspect that any approximation we have made would cause spurious 3D effects, especially in light of our success with pure-hydrogen 3D model atmospheres.

For DA white dwarfs, the 3D line cores of the deep lower Balmer lines were shown to be too deep when compared to observed white dwarf spectra [Tremblay et al., 2013c]. This 3D prediction is largely caused by adiabatic overshoot at large

Peclet number [see, e.g., Brummell et al., 2002; Kupka and Muthsam, 2017] cooling the 3D structures in the upper layers of the atmosphere, an effect that does not occur in 1D. This discrepancy led us to remove line cores for calculating more robust 3D corrections for DA white dwarfs. For 3D simulations of DB stars we do not observe any obvious issue with the line cores. One reason is that He I lines are weaker and the cores of the lines do not significantly extend into the overshoot regions. We have tried to remove the line cores from the fits, but this does not meaningfully change the 3D corrections, and thus we suggest keeping the full line shapes in the fitting procedure.

Fig. 3.15 compares the normalised 1D LHD, 1.5D and $\langle$3D$\rangle$ spectra for $\log g = 8.0$ and $T_{\rm eff} = 18\,081$ K, where the largest 3D corrections for surface gravity are observed (for models with $\log g = 8.0$). We find that all predicted spectra are very similar in terms of the broadband fluxes from the near-UV to the near-infrared. This suggests once again that the $\langle$3D$\rangle$ approximation is adequate, but also that 3D corrections are unnecessary for calculating broadband photometric fluxes in this regime. In Fig. 3.16 we compare our $\langle$3D$\rangle$ spectrum at $\log g = 8.0$, $T_{\rm eff} = 21\,989$ K with 1D LHD spectra using both ML2/α = 1.25 and 1.75. In this regime, BW11 have found (see their Figure 15) that a mixing-length of ML2/α = 1.75 provides a better agreement between the optical and near-UV temperatures, while a value of ML2/α = 1.25 results in a smoother mass distribution as a function of effective temperature. They attribute this behaviour to a potential shortcoming of the mixing-length theory. It is difficult to conclude yet about the possible improvements of a 3D spectral analysis, since the 3D effective temperature corrections are fairly mild in this regime and the predicted near-UV fluxes are all very similar in a relative sense.

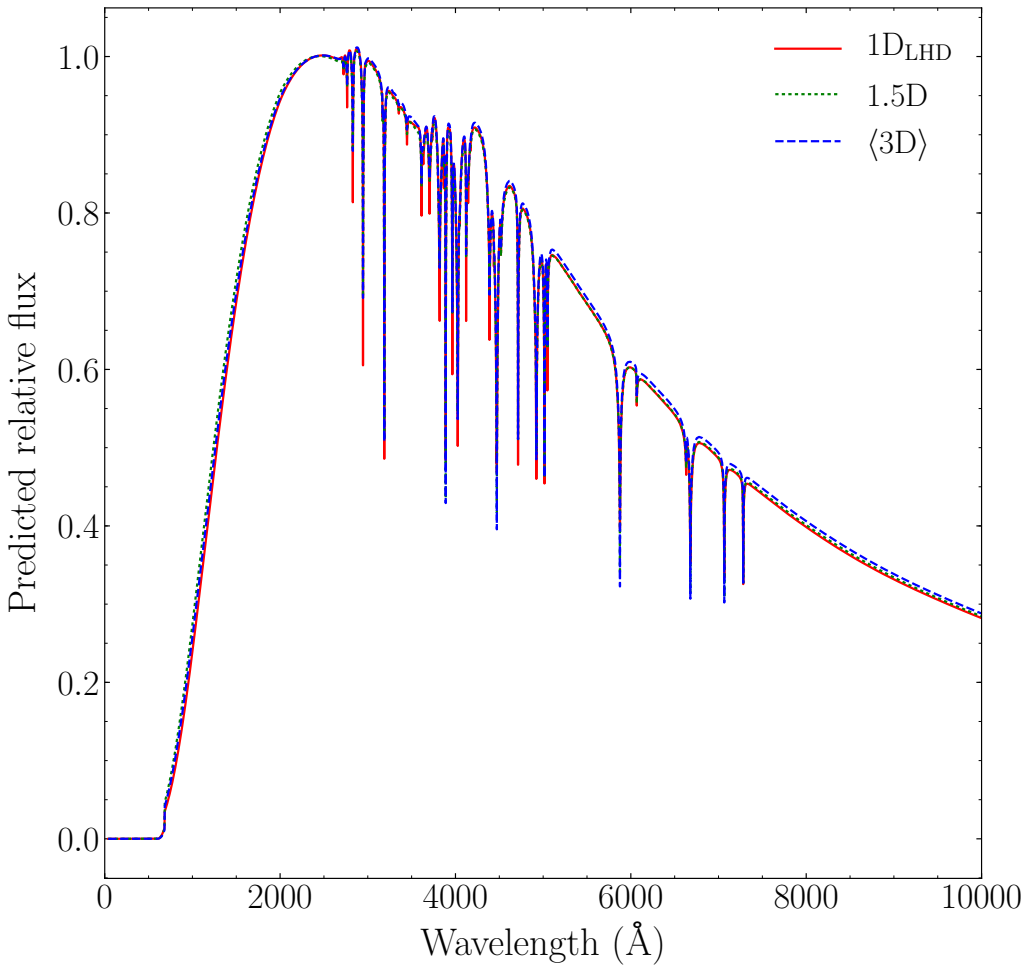

Figure 3.15: Comparison of 1D LHD (solid red), 1.5D (dotted green) and ⟨3D⟩ (dashed blue) spectra at $T_{\rm eff} = 18\,081$ K and $\log g = 8.0$. The spectra have been normalised at 2400 Å.

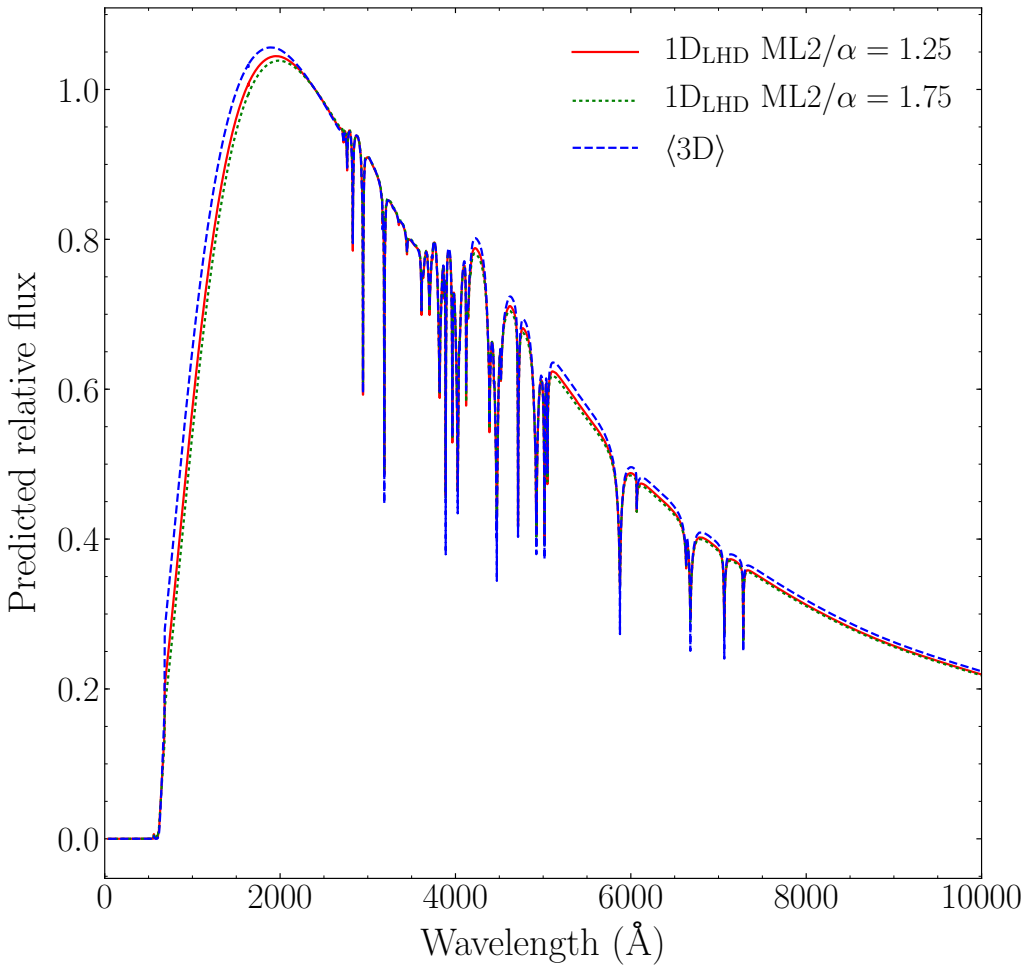

Figure 3.16: Comparison of a ⟨3D⟩ (dashed blue) spectrum and 1D LHD spectra computed with ML2/α = 1.25 (solid red) and 1.75 (dotted green) for $T_{\rm eff}$ = 21 989 K and $\log g$ = 8.0. The spectra have been normalised at 2400 Å.

3.4.2 Sensitivity to input parameters

⟨3D⟩ thermal structures of DA white dwarfs show little sensitivity to the input numerical parameters, which include the grid resolution, artificial viscosity, geometrical dimensions, and numerical schemes for the hydrodynamics solver (see Table 3 of Tremblay et al. [2013b] for more detail). This work relies on the same numerical setup. The change of the gas composition is not expected to have a significant impact on the precision of the thermal structures and numerical setup. Therefore, we conclude that the earlier numerical tests performed for DA white dwarfs also apply to the DB grid presented in this paper. This does not rule out, however, that there are untested numerical setups [e.g., very large grid sizes, see Kupka et al., 2018]

that could still have an effect on our results. These experiments were performed for a characteristic closed bottom simulation ($T_{\rm eff} = 12,000$ K, $\log g = 8.0$, pure-hydrogen). In this section we expand on these numerical experiments by quantifying how the open bottom boundary condition impacts our derived corrections.

Grimm-Strele et al. [2015] have shown that vertical boundary conditions can influence layers located two pressure scale heights above or below them. We extended two models with $\log g = 8.0$, and initially with $T_{\rm eff} = 12\,020$ and $18\,081$ K, by adding 60 and 50 more grid points to the bottom of the two simulations, respectively. The former case is the shallowest model at $\log g = 8.0$ with a total of 5 pressure scale heights. For both simulations we only focus on the lower boundary. This is because the top of each simulation is more than 3 pressure scale heights above the top of the spectral line forming region. These new simulations are run for 10 more seconds, and we make sure they have been properly relaxed using the tests described in Section 3.2.1. 12 snapshots over the last quarter of the simulations are used to calculate the mean structures and synthetic spectra. The two new synthetic spectra are fitted with the 1D LHD grid to derive 3D corrections.

In Fig. 3.17 we compare the temperature and pressure stratifications between the original and extended simulations. We find that the $\langle$3D$\rangle$ structure at $\approx 12\,000$ K does not change significantly with the extended simulation. The 3D spectroscopic corrections are well within fitting errors. Convection is very adiabatic everywhere in the simulation and we hypothesize that the mean stratification is rather insensitive to the treatment of convection (either in 1D or 3D). The standard and extended $\approx 18\,000$ K simulations differ marginally in the line forming regions according to Fig. 3.17. The shift in the 3D surface gravity correction is similar to the typical external observational errors (≈ 0.05 dex). The original simulation was already deep in terms of the number of pressure scale heights between the photosphere and the bottom boundary, and therefore the difference may not be directly caused by the change in the bottom boundary condition.

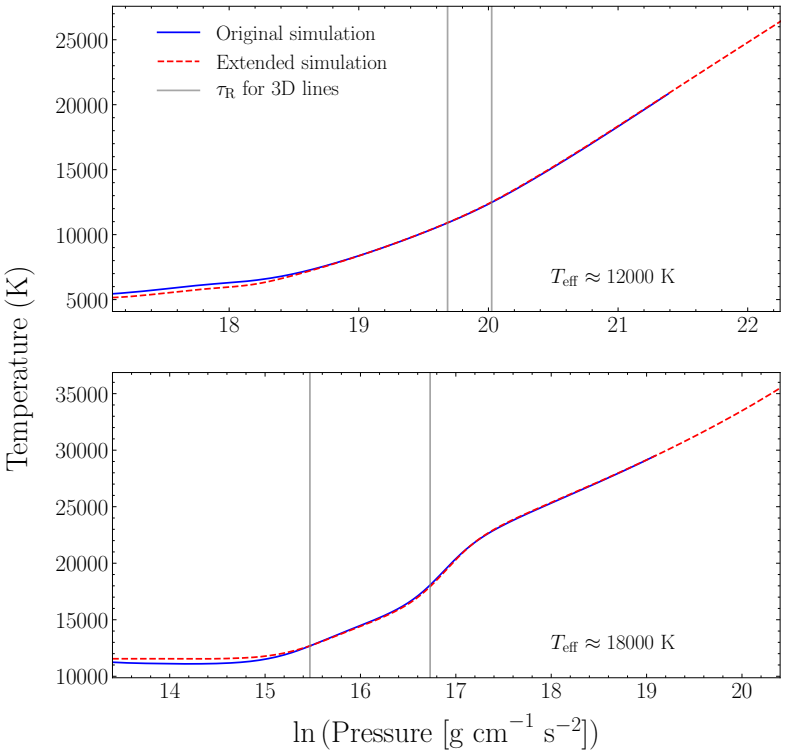

Figure 3.17: The temperature and pressure stratifications of the original (solid blue) and extended (dashed red) simulations for models with $\log g = 8.0$ and $T_{\rm eff} \approx 12\,000$ and 18 100 K. The spectral line forming regions are indicated by solid grey lines. Note that the 3D simulations extend deeper into the upper layers than shown here.

3.4.3 Application to observations

Fig. 3.18 shows 1D LHD and ⟨3D⟩ fits to WD0845−188, a selected DB white dwarf from BW11 with a hydrogen abundance small enough to assume pure-helium composition [Bergeron et al., 2015]. Fitting with ⟨3D⟩ spectra lowers the surface gravity by 0.24 dex, in line with the corrections proposed in Table 3.2. However, the effective temperature difference does not exactly match the corrections proposed in Table 3.2, but since the correction is of the same order as the internal errors we believe this inconsistency to be negligible.

If we fit WD0845−188 with 1D ATMO instead of 1D LHD, we recover parameters that are almost in complete agreement to LHD fitted parameters, reinforcing what is shown in Fig. 3.12, i.e. the difference between the 1D structures calculated from these two 1D codes are negligible at the given surface gravity and effective temperature.

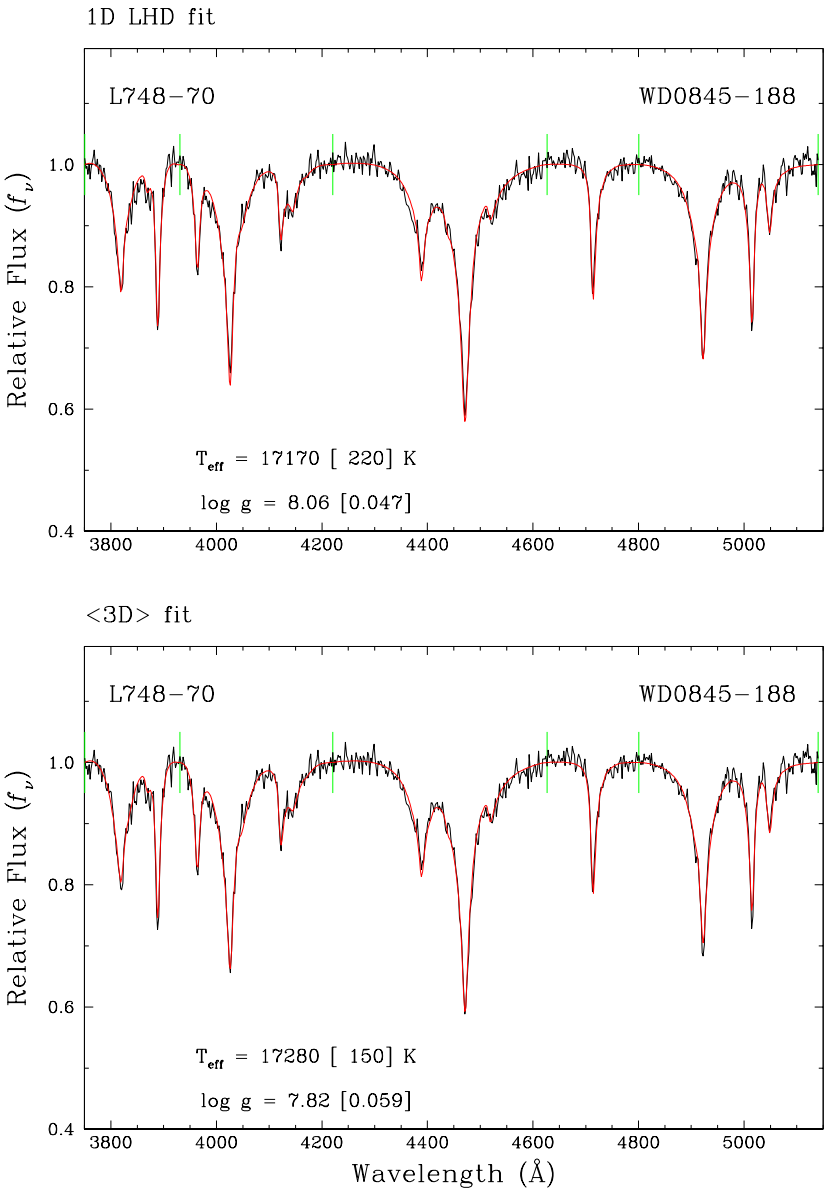

Figure 3.18: Examples of 1D LHD (top panel) and ⟨3D⟩ (bottom panel) fits to the spectrum of the DB white dwarf WD 0845−188. The continuum flux is fixed to unity by a fitting function at predefined wavelength points shown as green tick marks in the panels (see BW11). The best fit atmospheric parameters assuming a pure-helium composition are identified on the panels.

For this particular DB white dwarf, the χ^2 is marginally smaller in the ⟨3D⟩ case compared to the 1D LHD fit. However, looking at the whole BW11 sample excluding DBA white dwarfs, we do not find an obvious preference for either model

grid, suggesting that fits are of equivalent quality on average. This is in line with our earlier finding that there is no obvious line core problem for DB white dwarfs in comparison to DA stars. This suggests that the next step is to calculate a grid of mixed He/H 3D atmospheres and revisit earlier spectroscopic analyses.

3.5 Conclusions

We have presented the first-ever 3D radiation-hydrodynamics simulations of DB white dwarf atmospheres and discussed them in terms of the 3D effects on synthetic spectra. Briefly examined were the significant differences between these new 3D models and their previously available 1D counterparts in terms of the temperature and density stratifications. This distinction arises from the different models of convection; the 3D treatment derived from first principles and the more approximate mixing-length theory in 1D. Our 3D simulations are not without approximations either, but these issues can be largely overcome when computing 3D corrections with carefully selected reference 1D models. In our case, the sister-code of CO^{5}BOLD, LHD, was used, which treats opacity binning and scattering in the exact same fashion as CO^{5}BOLD.

The 3D corrections on the atmospheric parameters were constrained by using both 1.5D and $\langle 3D \rangle$ spectra, which represent the two extremes of enhancing or neglecting the 3D fluctuations, respectively. Corrections found with either method are similar, and the differences are within typical fitting uncertainties, suggesting that full 3D spectral synthesis is not required. The $\langle 3D \rangle$ spectra, drawn from $\langle 3D \rangle$ structures averaged over constant optical depth, have thus been used to estimate 3D corrections for pure-helium atmosphere white dwarfs. We find that current 1D synthetic spectra, under the ML2/α = 1.25 parameterisation of the mixing-length theory, overpredict surface gravity in the range 12 000 K $\leq T_{\rm eff} \leq$ 23 000 K by as much as 0.4 dex. It is a surprising result since DB white dwarf parameters have not been reported to be erroneous in this range of effective temperature.

Photometric fits using *Gaia* Data Release 2 have provided independent masses for all known DB stars, giving us a better description of the shortcomings in the line broadening or current 1D and 3D model atmospheres. In Chap. 4 the earlier 1D spectroscopic analyses are revisited by computing a grid of mixed He/H 3D simulations. This will account for the hypothesis that most if not all helium-rich atmosphere white dwarfs have hydrogen traces [Koester and Kepler, 2015].

Chapter 4

Spectroscopic 3D DBA corrections

> And when we go don't blame us, yeah
> We'll let the fires just bathe us, yeah
> You made us oh so famous
> We'll never let you go
>
> Mama
> *My Chemical Romance*

4.1 Introduction

In this chapter new 3D DBA models from Chap. 5 (from now on referred to as Cukanovaite et al. 2019 models) are introduced alongside the already discussed 3D DB models from Chap. 3 (referred to as Cukanovaite et al. 2018 models). These models are used to finalise the determination of the atmospheric parameters of DB and DBA white dwarfs with our accurate treatment of convective energy transport. We first introduce our 3D and reference 1D models in Sect. 4.2. The 3D spectroscopic corrections are determined in Sect. 4.3 and we apply them to observations in Sect. 4.4. In that section we also investigate van der Waals broadening and non-ideal effects and we conclude in Sect. 4.5.

The spectroscopically-determined atmospheric parameters of DB and DBA white dwarfs disagree with the results of photometric studies and evolutionary models. There is a small systematic difference between the parameters derived using spectroscopic and photometric techniques [Tremblay et al., 2019b; Genest-Beaulieu

and Bergeron, 2019a,b]. Before the advent of *Gaia* DR2 [Gaia Collaboration et al., 2018], the spectroscopic technique was assumed to be more precise, due to the uncertainties associated with white dwarf parallaxes and absolute magnitudes. With the use of much more accurate and precise parallaxes of *Gaia*, the photometric technique now rivals the precision of the spectroscopic technique. The surface gravities, $\log g$, (and therefore masses) of DB and DBA white dwarfs derived from photometry show a more uniform distribution as a function of effective temperature, compared to the surface gravity distribution of the spectroscopic technique, which suggests that spectroscopic results may be subject to additional uncertainties from the underlying convection model or input microphyics [Tremblay et al., 2019b]. Historically, the spectroscopic $\log g$ distribution of cool DB white dwarfs has been plagued by the so-called high-$\log g$ problem [Beauchamp et al., 1996; Bergeron et al., 2011; Koester and Kepler, 2015]. More recent results show that by calibrating the line broadening and eliminating very cool DB stars with weak lines and uncertain instrumental resolution, the high-$\log g$ problem is greatly diminished [Genest-Beaulieu and Bergeron, 2019b]. The photometric technique is much less sensitive to the details of line broadening, but the absolute accuracy of the stellar parameters depends more critically on the uncertain relative flux calibration, for which DA white dwarf models are often employed [Narayan et al., 2019; Gentile Fusillo et al., 2020].

In most studies the dominant uncertainty in the atmospheric parameters of cool DB white dwarfs ($T_{\rm eff} \lesssim 16\,000$ K) is attributed to the implementation of van der Waals line broadening due to the neutral helium atom [Beauchamp et al., 1996; Bergeron et al., 2011; Koester and Kepler, 2015]. The two most common implementations for this type of line broadening used in DB and DBA studies are the Unsold [1955] theory, used in, for example, Beauchamp et al. [1996] and Bergeron et al. [2011] and the modified Deridder and van Rensbergen [1976] treatment, used in Beauchamp et al. [1996] and Genest-Beaulieu and Bergeron [2019a,b]. Beauchamp et al. [1996] showed that the modified Deridder and van Rensbergen [1976] version produces a much smoother distribution of surface gravity as a function of effective temperature. Genest-Beaulieu and Bergeron [2019a,b] later showed that neither implementation gives a perfect agreement between the spectroscopic and the photometric technique or spectroscopic and evolutionary model predictions. However, from their samples it is clear that the modified Deridder and van Rensbergen [1976] treatment agrees better with *Gaia* data. Either way, a more accurate implementation is needed since the Deridder and van Rensbergen [1976] version of the line broadening has been tweaked by Beauchamp et al. [1996] to agree better with observations.

Additionally, there is the issue of non-ideal effects due to the neutral helium

atom, which also become significant for $T_{\rm eff} \lesssim 16\,000$ K. The current implementation used for white dwarf atmosphere models is the Hummer and Mihalas [1988] model, which depends on a free parameter, $r_{\rm B}$, that determines the radius of the hydrogen or helium atom as a fraction of atomic radius according to the Bohr model. The commonly utilized value is 0.5, which was calibrated based on DA white dwarf spectra, specifically the line profiles of the higher hydrogen Balmer lines [Bergeron et al., 1988, 1991]. A discussion on the effect of $r_{\rm B}$ on surface gravity can be found in Tremblay et al. [2010]. This free parameter can potentially be adjusted to obtain a smoother surface gravity distribution for DB and DBA white dwarfs.

The treatment of convective energy transport in atmospheric models of DB and DBA white dwarfs is another source of uncertainty influencing the spectroscopic parameters. Tremblay et al. [2013c] showed that it is precisely the shortcomings in the MLT theory that cause a similar high-$\log g$ problem for DA white dwarfs, which as a result can be solved with the help of 3D radiation-hydrodynamical models, because these models treat convection from first principles and do not depend on any free parameters. Cukanovaite et al. [2018] (Chap. 3) calculated the first 3D DB atmospheric models and found that while a single value of ML2/α = 1.25 can reproduce reasonably well the temperature distribution and UV fluxes of DB white dwarfs, no single value of the mixing length parameter can mimic the 3D spectra below $T_{\rm eff} \approx 18\,000$ K, resulting in strong 3D $\log g$ corrections[1]. Nevertheless, Cukanovaite et al. [2018] (Chap. 3) found that 3D $\log g$ corrections do not result in obviously more accurate stellar parameters. Tremblay et al. [2019b] cemented this by showing that 1D and 3D DB models provide spectroscopic parallaxes (calculated from spectroscopically-determined values of effective temperature and surface gravity, and observed magnitude) that are in similar agreement with *Gaia* parallaxes. It was postulated by Cukanovaite et al. [2018] (Chap. 3) that inclusion of traces of hydrogen in their 3D models could potentially lead to a better agreement with *Gaia*. However, given the known issues with the microphysics of line broadening in cool DB white dwarfs and concerns with the photometric calibration [Tremblay et al., 2019b; Maíz Apellániz and Weiler, 2018], it is unclear if *Gaia* can provide an accurate test of 3D convection. Thus in this chapter, the 3D DB and DBA spectroscopic corrections are applied to published samples, and the line broadenings are investigated in detail.

[1]See Cukanovaite et al. [2019] (Chap. 5) for an alternative calibration of the mixing length parameter, which is relevant for the size of the convection zone.

4.2 Numerical setup

4.2.1 3D atmospheric models

We computed 282 3D DB and DBA models using the CO^{5}BOLD radiation-hydrodynamics code [Freytag et al., 2002; Wedemeyer et al., 2004; Freytag et al., 2012; Freytag, 2013, 2017]. Our 3D grid of models covers the hydrogen-to-helium number ratio, $\log \mathrm{H/He}$, of $-10.0 \leq \log \mathrm{H/He} \leq -2.0$. Models at $\log \mathrm{H/He} = -10.0$ are the same as the pure-helium models discussed in Cukanovaite et al. [2018] (Chap. 3) and this hydrogen abundance is used for pure-helium atmosphere models since all known DB white dwarfs have upper limits on hydrogen larger than this value. Including even less hydrogen in the calculations makes no meaningful change to the predictions. The grid also spans 7.5 dex $\leq \log g \leq$ 9.0 dex in steps of 0.5 dex, and 12 000 K $\lesssim T_{\mathrm{eff}} \lesssim$ 34 000 K in steps of around 2 000 K. We show the exact values of the atmospheric parameters in Fig. 4.1. Additional data on the models can be found in Appendix 1 of Cukanovaite et al. [2019] (App. B of this thesis) .

The input parameters of CO^{5}BOLD include boundary conditions, surface gravity, an equation of state (EOS) and an opacity table. The EOS and opacity table define the hydrogen abundance of the DBA simulations. The opacity tables are binned and discussed in Cukanovaite et al. [2018] (Chap. 3). Due to interpolation issues we do not include the $\log \tau_{\mathrm{R}} = [-5.0,-99.0]$ bin.

For all models the top boundary is higher than $\log \tau_{\mathrm{R}} = -5.0$, such that the top of the photosphere is contained within the model. The bottom boundary for all models is around $\log \tau_{\mathrm{R}} = 3.0$, but in some cases the models had to be extended deeper to include the negative convective flux region found below the Schwarzschild boundary of the convection zone [Cukanovaite et al., 2019] (Chap. 5). In those cases, the vertical extent of the box was also increased, with some models extending to 250 grid points vertically compared to the original 150 grid points. We ensure that both the top and the bottom of the photosphere is at least $\sim 2H_p$ away from either top or bottom boundary of the simulation.

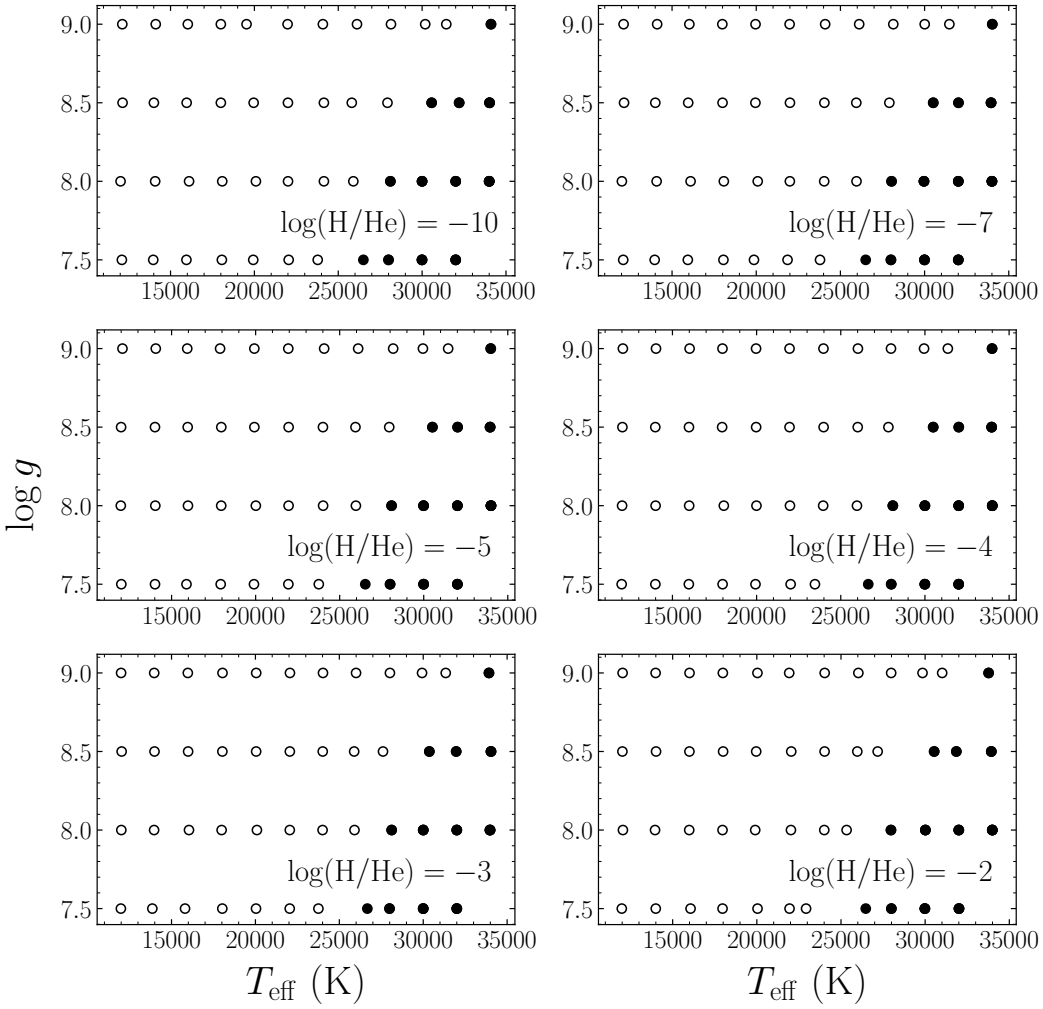

Figure 4.1: The atmospheric parameters of 3D DB and DBA models averaged over time and over contours of constant $\log \tau_{\rm R}$. 3D simulations with open and closed bottom boundaries are indicated as unfilled and filled circles, respectively. The hydrogen abundance of the models is indicated on each individual sub plot.

4.2.2 1D atmospheric models

In order to calculate 3D spectroscopic corrections, we use a differential fitting approach between 3D and reference 1D synthetic spectra. ATMO is used to calculated the EOS and opacity tables. However, we use the 1D LHD code [Caffau et al., 2007] for determining the 3D corrections.

Fig. 12 of Cukanovaite et al. [2018] (Fig. 3.12 of Chap. 3) shows that the differences between DB ATMO and LHD models are due to the binning procedure

used in opacity tables. We performed a similar comparison for the DBA grid of models with $\log \mathrm{H/He} = -2$ and $\log g = 8.0$. Two different grids of 1D LHD models were used, those calculated with 10-bin (same as 3D models) and 20-bin opacity tables. We fitted each type of LHD spectrum with our standard ATMO grid (See Sect. 4.3.1 for the fitting procedure) and found that as the number of bins increases, the agreement between 1D LHD and 1D ATMO DBA synthetic spectra does not improve. This is not necessarily unexpected as increasing the number of bins does not always produce more accurate structures [Tremblay et al., 2013c]. However, since it was determined that for DB structures the opacity binning can introduce artificial 3D corrections that have nothing to do with treatment of convective energy transport, we utilise the 1D LHD models for calculating 3D DBA spectroscopic corrections as a precaution.

To compute the spectra for 3D and 1D LHD structures, we use the 1D ATMO code. This is because neither CO^{5}BOLD nor LHD is capable of calculating synthetic spectra. We utilise ATMO consistently to calculate spectra for CO^{5}BOLD and LHD using the exact same numerical setup apart from the input temperature and pressure stratification.

Our 1D LHD grid spans a parameter space slightly extended compared to that of our 3D models. It covers $-10.0 \leq \log \mathrm{H/He} \leq -2.0$, $7.0 \leq \log g \leq 9.5$ and $10\,000 \leq T_{\mathrm{eff}} \leq 40\,000$ K. The models are in LTE and use ML2/α = 1.25. The input EOS and opacity tables are the same as those used in 3D models, which include the physics described in Bergeron et al. [2011] and Genest-Beaulieu and Bergeron [2019a,b]. In terms of van der Waals broadening we use the Unsold [1955] treatment, unless otherwise specified, such as in Sect. 4.4.1. We have tested and confirmed that the particular choice of line broadening theory does not impact the final 3D corrections if the line broadening is used consistently in both 1D and 3D models.

4.2.3 3D synthetic spectra

Ideally, one would calculate a synthetic spectrum from a 3D atmospheric model using a 3D spectral synthesis code such as Linfor3D [Ludwig and Steffen, 2008]. This way all of the information from a given 3D simulation would be used, including the horizontal fluctuations. However, this process is time-consuming and typically limited to a small portion of a spectrum, e.g. a few atomic lines. Instead, to calculate synthetic spectra of DB and DBA white dwarfs from 3D atmospheric models, we average the models spatially and temporally as explained in Sect. 4.2

to calculate the so-called ⟨3D⟩ structure, which we then feed into the ATMO code to calculate a ⟨3D⟩ synthetic spectrum. This completely neglects any horizontal fluctuations in the 3D models. For DA white dwarfs it was shown that synthetic spectra (Hβ line) derived from 3D and ⟨3D⟩ structures were identical within 1% level [Tremblay et al., 2013c]. However, for extremely low mass DA white dwarfs, the differences could reach a few per cent [Tremblay et al., 2015a]. For a discussion on why 3D and ⟨3D⟩ synthetic spectra can agree in some cases and disagree in others see Tremblay et al. [2013c] and Tremblay et al. [2015a].

To test whether the horizontal fluctuations have any effect on the derived 3D spectroscopic corrections, Cukanovaite et al. [2018] (Chap. 3) computed 1.5D spectra [Steffen et al., 1995]. This type of spectra is calculated by assuming that each column in the 3D simulation box is an individual model atmosphere, and for each of these atmospheres a separate spectrum is calculated. These individual spectra are then averaged together to calculate the final 1.5D spectrum. They also average over three different snapshots in time. In the 1.5D method the horizontal fluctuations are enhanced [Tremblay et al., 2015a] compared to a 3D synthetic spectrum which combines nearby grid points through inclined light rays. The 1.5D and ⟨3D⟩ spectra represent two extremes of combining grid points in a 3D model, such that these two type of spectra encompass a given 3D synthetic spectrum [Tremblay et al., 2013c].

For DB white dwarfs, 1.5D spectra were found to be identical to ⟨3D⟩ spectra within the observational errors and thus ⟨3D⟩ spectra were used for final 3D DB spectroscopic corrections. We performed the same test for DBA models with $\log \mathrm{H/He} = -2.0$ and $\log g = 8.0$ and found that the corrections derived using either type of spectra gave the same results. Therefore, this agrees with the conclusions reached for 3D DB corrections, with the difference between ⟨3D⟩ and 1.5D for DBA models being even smaller, resembling the results of 3D DA models. Therefore, we use ⟨3D⟩ synthetic spectra when calculating 3D DBA corrections, given also that it would give the minimum possible 3D correction.

4.3 3D DBA corrections

4.3.1 Fitting code

In order to determine 3D corrections, we want to find a 1D LHD synthetic spectrum that best matches a given ⟨3D⟩ spectrum. To do this, we wrote a code that fits a synthetic spectrum with a grid of different type of synthetic spectra. We

define the 3D spectroscopic corrections as

$$x_{\text{correction}} = x_{\langle 3\text{D}\rangle \text{ value}} - x_{\text{1D LHD fit}}, \tag{4.1}$$

where x can be $\log \text{H/He}$, $\log g$ or T_{eff}. The code fits the optical part of the spectrum, namely the wavelength range $3500 \leq \lambda \leq 7200$ Å. This is the same range used by Bergeron et al. [2011] for fitting observations and in Cukanovaite et al. [2018] (Chap. 3) for 3D DB corrections. All spectra are normalised by dividing the flux at all wavelengths by the flux value at 5500 Å, a wavelength at which there are no helium or hydrogen lines.

The code first fits for effective temperature and surface gravity assuming a value of hydrogen abundance. The initial value of the hydrogen abundance does not matter, but the code converges faster if the abundance is set closest to the actual 3D value. Once the effective temperature and surface gravity are found, the spectrum is then fitted for hydrogen abundance at fixed values of effective temperature and surface gravity, found in the previous step. This procedure is then repeated until convergence of 0.1% is achieved across all three parameters. If the hydrogen lines are not visible or insignificant then we do not fit for hydrogen abundance. This happens mostly for $\log \text{H/He} = -10.0$ and -7.0 models, as well as models with higher hydrogen abundances and large effective temperatures.

Using this fitting code, we can recover the 3D DB spectroscopic corrections of Cukanovaite et al. [2018] (Chap. 3). For $T_{\text{eff}} \gtrsim 20\,000$ K (depending on the surface gravity) Cukanovaite et al. [2018] (Chap. 3) reported sizeable effective temperature corrections, although they were smaller than the typical observational errors. We can now report that these corrections were dependent on the method used to normalise spectra in the fitting code utilised by Cukanovaite et al. [2018] (Chap. 3). With our new normalisation method, we keep the slope of the spectrum, which means that fitting retains its sensitivity to effective temperature, leading to smaller effective temperature corrections in that particular temperature range. Note that this is only possible in the case of fitting models with models. This normalisation method would be unreliable in the case of fitting observed spectra of white dwarfs as there can be issues with data reduction. Our goal in determining the spectroscopic corrections is to determine 1D spectrum that best matches given 3D spectrum. In terms of the surface gravity corrections, both the new and old codes agree within typical observational errors.

4.3.2 Line cores

Tremblay et al. [2013b,c] showed that convective overshoot cools the upper layers ($\log \tau_{\rm R} < -2.0$) of 3D DA models, causing them to deviate significantly from their 1D counterparts. The cores of Hα and Hβ appear too deep in 3D when compared to observations. It was found that the discrepancy is unlikely to be a numerical, structure averaging or microphysics issues with 3D DA models. Tremblay et al. [2013c] chose to remove the line cores from their fitting when determining 3D DA corrections. In contrast, Cukanovaite et al. [2018] (Chap. 3) determined that removal of line cores did not impact 3D DB corrections. This is because helium lines are not formed as high-up in the atmosphere as the hydrogen lines, despite a similar strength for convective overshoot. However, hydrogen lines do appear in the spectra of DBA white dwarfs and therefore we review the properties of the line cores in this section.

In Fig. 4.2 we compare the line cores between 3D, 1D LHD and 1D ATMO synthetic spectra at $T_{\rm eff} = 12\,000$ K, $\log g = 8.0$ and $\log {\rm H/He} = -2.0$. The 3D line core is deeper for Hα but the difference is less pronounced for Hβ compared to DA models at the same temperature. We also find that the 1D LHD synthetic spectrum has shallower cores than 1D ATMO. Therefore it appears that the EOS and opacity tables contribute to a significant uncertainty on the prediction of the line cores, but with an effect in the opposite direction compared to 3D convective overshoot.

In Fig. 4.3 we compare the 3D DBA effective temperature corrections for $\log {\rm H/He} = -2.0$ derived when fitting the spectrum with and without line cores. We remove line cores by removing any wavelength range corresponding to flux that was formed above a given value of $\log \tau_{\rm R}$. As shown in Fig. 4.3 the values of $\log \tau_{\rm R} = [-2.0, -3.0, -4.0]$ are tested. At low effective temperatures, this will mostly remove the cores of hydrogen lines, as helium lines are formed lower in the atmosphere than $\log \tau_{\rm R} = -2.0$, but as the effective temperature increases the cores of the helium lines will also be removed. We find that the removal of line cores does not affect the 3D corrections (not just effective temperature, but also hydrogen abundance and surface gravity). Therefore, we do not remove them in the rest of our analysis.

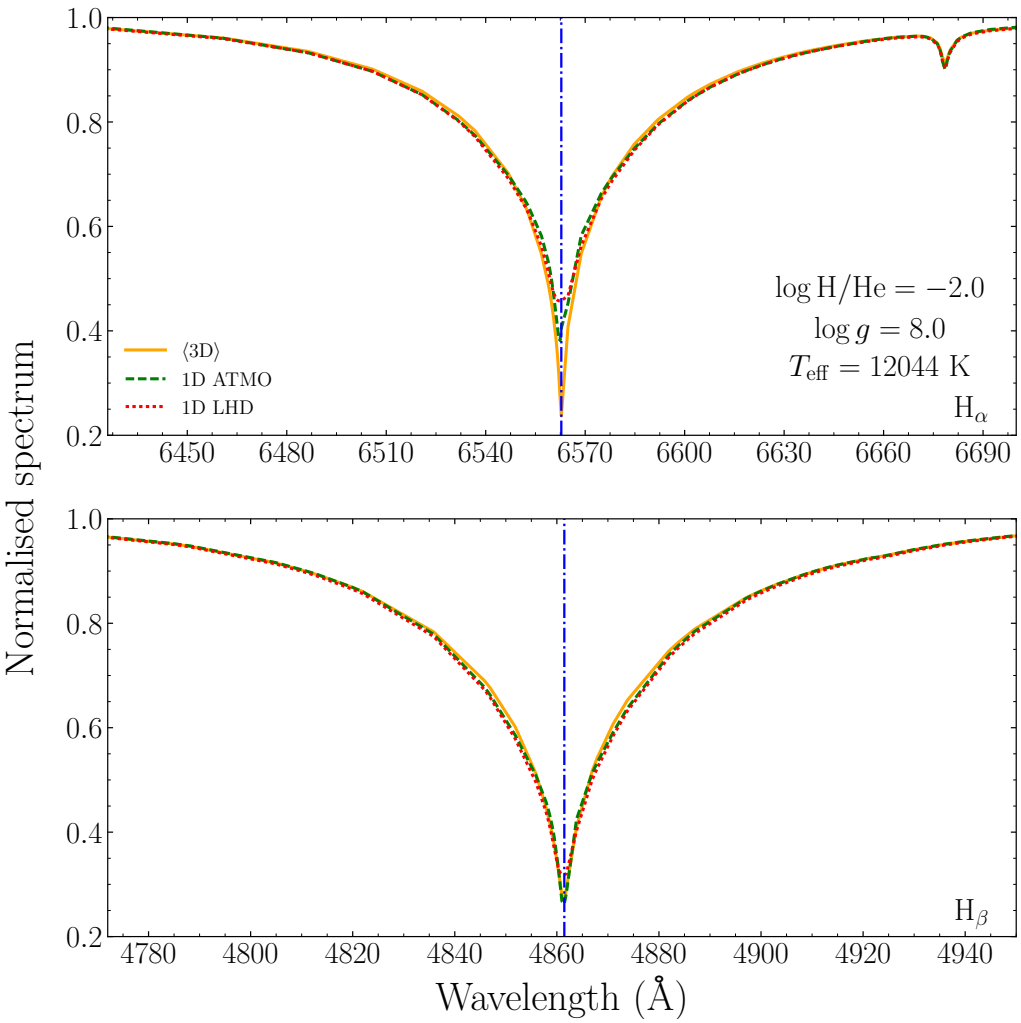

Figure 4.2: A comparison between the synthetic H_α and H_β lines calculated from 3D, 1D ATMO and 1D LHD models for a DBA white dwarf with $\log \mathrm{H/He} = -2.0$, $\log g = 8.0$ and $T_{\mathrm{eff}} = 12\,044$ K. The $\langle 3\mathrm{D} \rangle$ synthetic lines are shown in solid orange, 1D ATMO in dashed green and 1D LHD in dotted red. The center of a given line is indicated by a vertical dot-dashed blue line.

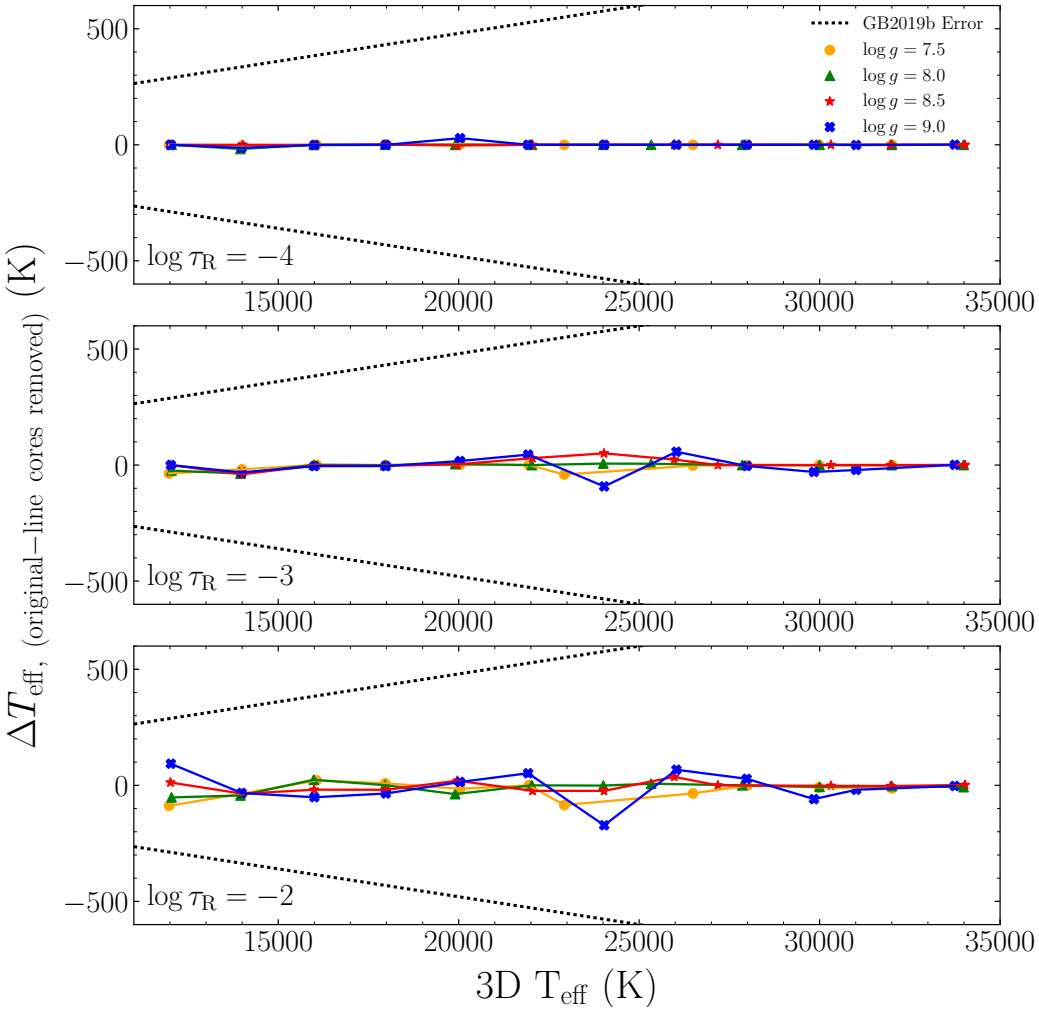

Figure 4.3: The difference between the effective temperature corrections derived from original spectra and from spectra with line cores removed for 3D DBA models with $\log \mathrm{H/He} = -2.0$. The $\log \tau_{\mathrm{R}}$ values indicated on each sub plot denote the atmospheric layer above which we remove any flux formed. The difference in corrections for models with $\log g = 7.5$, 8.0, 8.5 and 9.0 are shown as orange circles, green triangles, red stars and blue diagonal crosses, respectively. Corrections for each surface gravity are joined for clarity. The errors from Genest-Beaulieu and Bergeron [2019b] are shown in dotted black.

4.3.3 3D correction function

For the ease of user application of 3D DB and DBA corrections, we provide correction functions that can be applied directly to spectroscopically-determined 1D hydrogen abundances, surface gravities and effective temperatures. This removes

the need for users to interpolate the 3D DB and DBA corrections, and provides definitive corrections that do not vary between studies, since different studies can use non-identical interpolation methods. Our fitted corrections are not based in any physical arguments. Unlike interpolation, we do not aim to have an ideal fit between our correction functions and the 3D DB and DBA corrections. This is because we do not want to preserve the small fluctuations of our results, which could be the result of e.g. issues arising due to the finite size of the simulation or the effects of boundary conditions.

To determine our correction functions we have written a code following the description of the recursive fitting procedure from Ludwig et al. [1999], Sbordone et al. [2010] and Allende Prieto et al. [2013]. This code not only provides the values of the fitted coefficients but also determines the function to fit. Our aim is to determine three correction functions for 3D hydrogen abundance, surface gravity and effective temperature corrections, in the form $f(\log g, T_{\rm eff}, \log \mathrm{H/He}; \vec{A})$, where $\vec{A}$ is the vector of fitted coefficients. The fitting is recursive to allow for determination of initial values for the coefficient parameters and thus to ensure an efficient convergence to a solution.

The code begins by fitting a simple function of $f(\log g, T_{\rm eff}, \log \mathrm{H/He}; \vec{A}) = A_0$, where A_0 is the average of the corrections. The next step is then to replace A_0 with $(A_0 + A_1 \exp[A_2 + A_3 g x + A_4 T_x + A_5 y_x])$, where

$$\begin{aligned} g_x &= (\log g - 7.0)/7.0, \\ T_x &= (T_{\rm eff} - 10\,000.0)/10\,000.0, \\ y_x &= -\log(\mathrm{H/He})/(10.0). \end{aligned} \tag{4.2}$$

For this subsequent fit, the initial values are set as

$$\begin{aligned} A_0 &= A_0, \\ A_1 &= 0.7 \times A_0, \\ A_2 &= 0.5 \times A_0, \\ A_3 &= 0.2 \times A_0, \\ A_4 &= 0.1 \times A_0, \\ A_5 &= 0.01 \times A_0, \end{aligned} \tag{4.3}$$

and are all based on the value of A_0 found during the first fit. At this point, we begin our recursive fitting procedure, where each coefficient of A_i in the previous step is replaced one at a time by $(A_i + A_6 \exp[A_7 + A_8 g_x + A_9 T_x + A_{10} y_x])$, resulting

in six separate minimisations. The initial values of the five new unknown coefficients are set as described in Eq. 4.3, but with A_i replacing A_0. The best fitted correction function is then chosen by the smallest value of the cost function. This step is followed by a similar step where each parameter (11 at this point) is replaced by $A_j = A_j + A_{11} \exp[A_{12} + A_{13} g_x + A_{14} T_x + A_{15} y_x]$. The function with the smallest value of the cost function is then chosen as the final fitted correction function. In Fig. 4.4 we compare the 3D DBA corrections with the predictions of the correction functions for $\log \mathrm{H/He} = -5$. The correction functions are

$$\begin{aligned} \Delta \log g = a_0 + a_1 \exp \Big[a_2 + \\ a_3 g_x + \Big(a_4 + (a_6 + a_{11} \exp[a_{12} + a_{13} g_x + a_{14} T_x + a_{15} y_x]) \\ \times \exp[a_7 + a_8 g_x + a_9 T_x + a_{10} y_x] \Big) T_x + a_5 y_x \Big], \end{aligned} \tag{4.4}$$

$$\begin{aligned} \Delta T_{\mathrm{eff}} = b_0 + b_1 \exp \Big[\Big(b_2 + b_6 \\ \times \exp \big[b_7 + (b_8 + b_{11} \\ \times \exp[b_{12} + b_{13} g_x + b_{14} T_x + b_{15} y_x]) g_x + b_9 T_x + b_{10} y_x \big] \Big) + \\ b_3 g_x + b_4 T_x + b_5 y_x \Big], \end{aligned} \tag{4.5}$$

where $\Delta \log g$ is the 3D surface gravity correction and ΔT_{eff} is the 3D effective temperature correction. These corrections were derived using g_x, T_x and y_x, therefore they have to be added in the following way to the 1D spectroscopically-determined parameters

$$\begin{aligned} \log g_{\mathrm{3D}} &= \log g_{\mathrm{1D}} + 7 \times \Delta \log g \\ T_{\mathrm{eff,\ 3D}} &= T_{\mathrm{eff,\ 1D}} + 1000 \times \Delta T_{\mathrm{eff}}. \end{aligned} \tag{4.6}$$

The 3D hydrogen abundance corrections are insignificant, especially compared to typical observational errors and we do not discuss them further. Tab. 4.1 gives the values of the fitted coefficients (a_i and b_i). Note that outside the parameter range of our 3D corrections, these functions lose all meaning and should not be used. The parameter range for 1D derived spectroscopic values is $7.5 \leq \log g \leq 9.1$ dex, $11\,900 \leq T_{\mathrm{eff}} \leq 33\,900$ K and $-10.0 \leq \log \mathrm{H/He} \leq -2.0$ dex. In Appendix A we supply a Python code to apply our correction functions.

In Figs. 4.5 and 4.6 we show the 3D surface gravity and effective temperature correction functions for all hydrogen abundances, surface gravities and effective

temperatures considered in this study. There are significant 3D surface gravity corrections for effective temperatures below around 20 000 K depending on the hydrogen abundance, such that the 3D synthetic spectra predict lower surface gravities than 1D models. Uncertainties in the van der Waals broadening fall in a similar parameter range, $T_{\rm eff} \leq 16\,000$ K, which overlaps well with our 3D surface gravity corrections especially for $\log {\rm H/He} \geq -4.0$ models. Significant effective temperature corrections are observed for $18\,000 \leq T_{\rm eff} \leq 28\,000$ K depending on the surface gravity. This is the temperature range where the issue of cool/hot solutions appears [Bergeron et al., 2011]. In this region the He I lines reach maximum strength, such that the they look identical with decreasing or increasing effective temperature near this maximum point. This means that in this region the fitting becomes insensitive to effective temperature and this could explain the significant 3D effective temperature corrections. Nevertheless, the 3D effective temperature corrections could have a significant effect on the spectroscopically parameters of the white dwarfs in the V777 Her (DBV) instability region. There is currently an issue with the empirical blue edge, which is too cool in comparison with observations by around 2 000 K (at $\log g \approx 8.0$) [Shipman et al., 2002; Provencal et al., 2003; Hermes et al., 2017; Van Grootel et al., 2017]. However, our 3D effective temperature corrections at $\log g \approx 8.0$ and $T_{\rm eff} \approx 31\,000$ K (the atmospheric parameters of the empirical blue edge) are insignificant and therefore cannot solve the disagreement between theory and observations.

Table 4.1: The fitted coefficients of the 3D correction functions described in Eqs. 4.4 and 4.5.

Coeff.		Coeff.	
a_0	7.789804e-05	b_0	−1.507415e-03
a_1	−1.246790e-01	b_1	1.567231e-02
a_2	2.266438e-01	b_2	−4.028622e-01
a_3	7.346191e+00	b_3	−4.160986e+00
a_4	−4.956186e+00	b_4	3.087746e+00
a_5	9.319494e-01	b_5	2.172546e-01
a_6	−2.706825e-03	b_6	−1.773794e-02
a_7	8.474978e+00	b_7	−6.214232e-01
a_8	3.139169e+00	b_8	−1.388323e+01
a_9	−6.493254e+00	b_9	5.002702e+00
a_{10}	1.909074e+00	b_{10}	1.520483e-02
a_{11}	−5.272041e+00	b_{11}	4.749075e+00
a_{12}	9.791687e+00	b_{12}	9.447618e+00
a_{13}	2.150441e+00	b_{13}	−3.172587e+00
a_{14}	4.428345e+00	b_{14}	−2.922094e-01
a_{15}	−1.008931e+02	b_{15}	−3.898302e+01

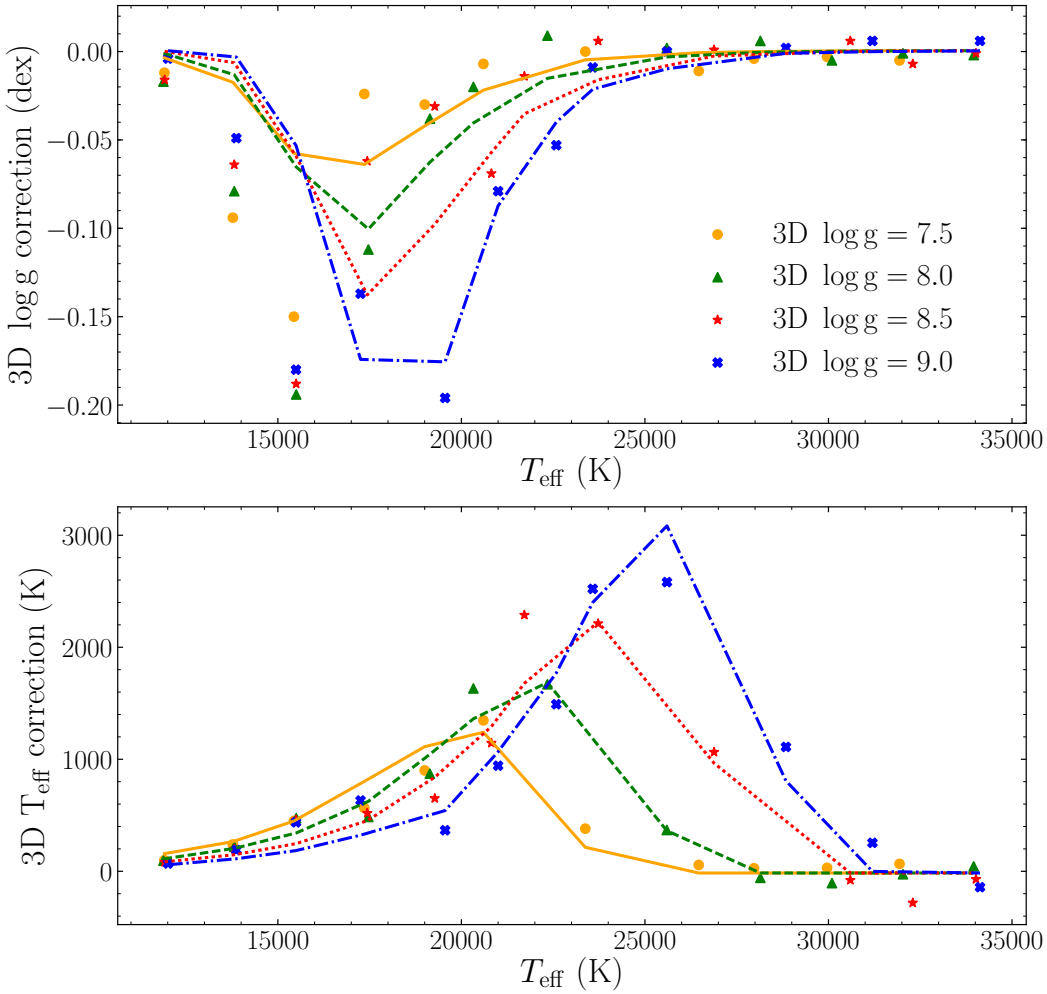

Figure 4.4: A comparison between the results of the correction functions and the 3D DBA corrections for the grid with $\log \mathrm{H/He} = -5$. 3D corrections for models with $\log g = 7.5$, 8.0, 8.5 and 9.0 are shown as orange circles, green triangles, red stars and blue diagonal crosses, respectively. The results of the correction functions for models with $\log g = 7.5$, 8.0, 8.5 and 9.0 are shown as solid orange, dashed green, dotted red and dot-dashed blue lines, respectively.

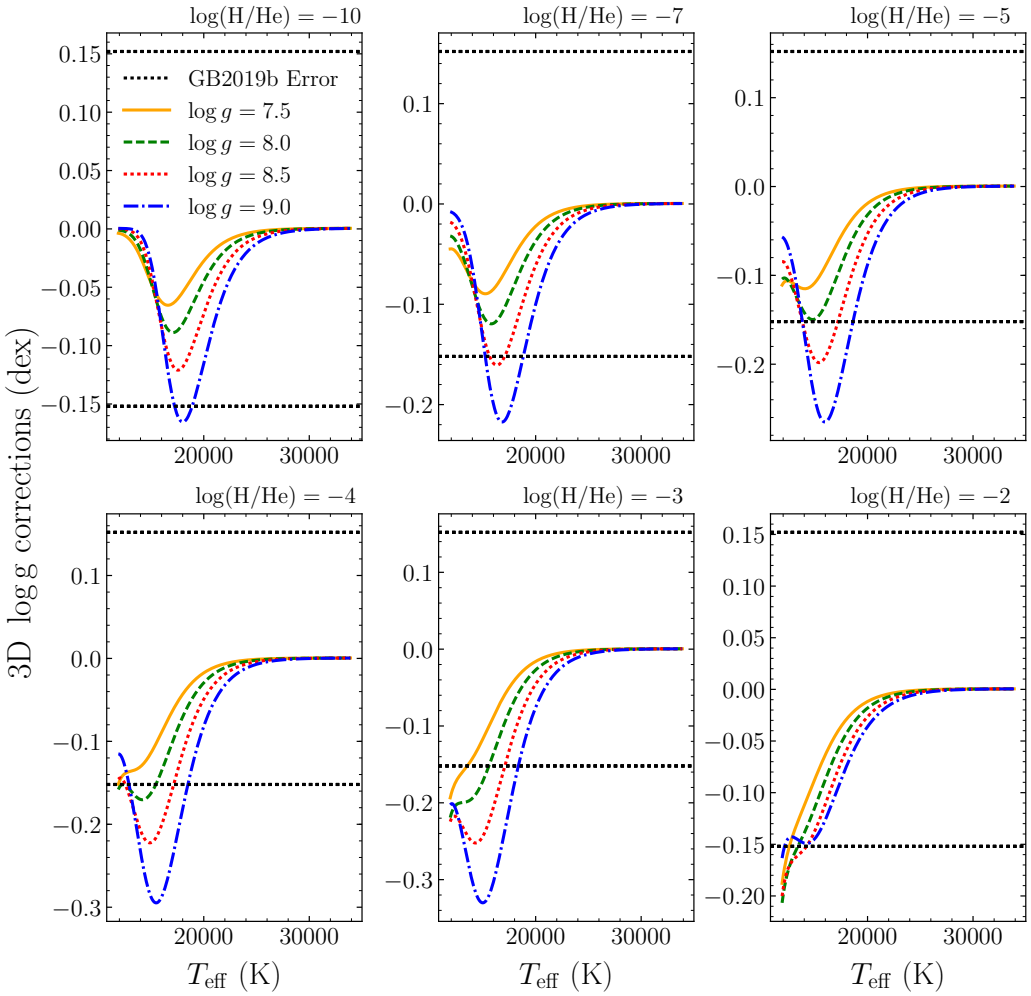

Figure 4.5: 3D correction functions for surface gravity shown for all hydrogen abundances, surface gravities and effective temperatures covered by our study. Dotted black lines represent the observational errors from Genest-Beaulieu and Bergeron [2019b]. In solid orange, dashed green, dotted red and dot-dashed blue we show the surface gravity corrections for $\log g = 7.5$, 8.0. 8.5 and 9.0 values, respectively. The abundances are indicated on each sub plot.

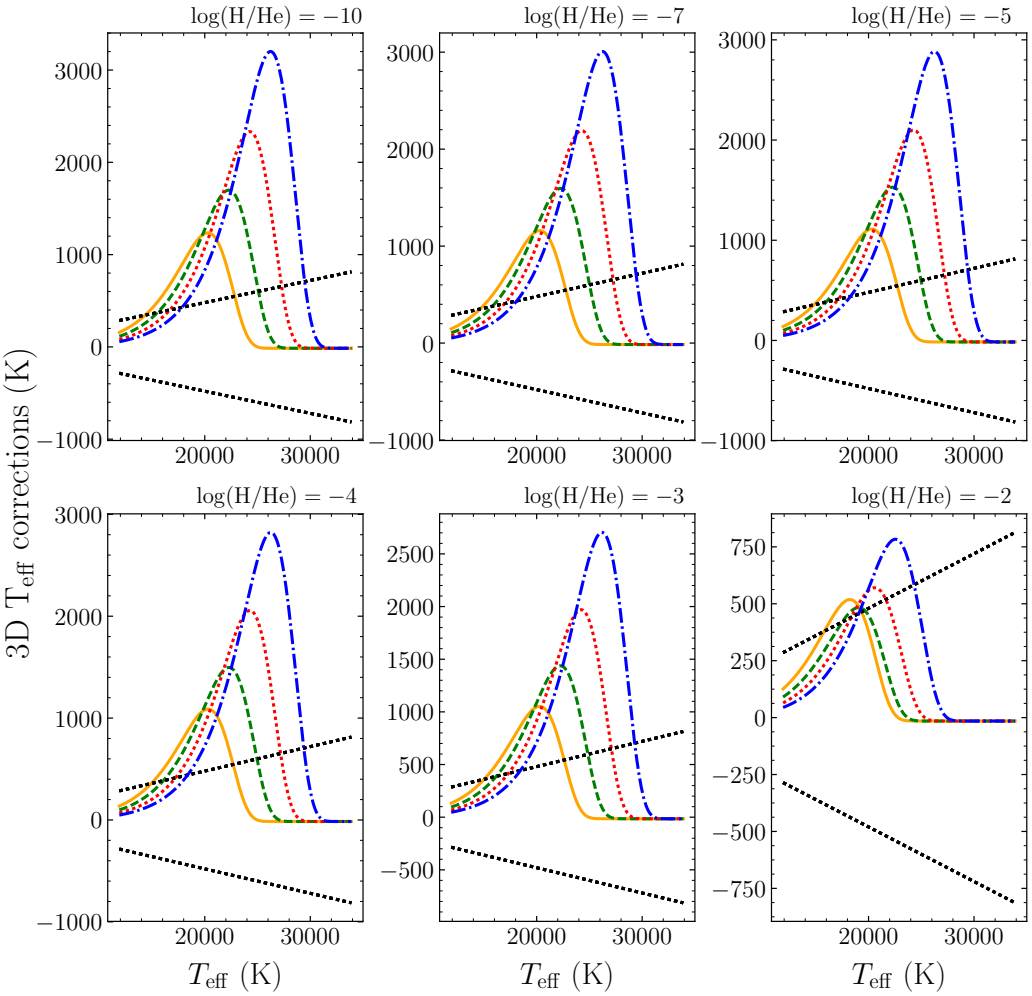

Figure 4.6: Same as Fig. 4.5, but for 3D effective temperature corrections.

4.4 Discussion

For a demonstration of 3D corrections, the sample of SDSS DB and DBA white dwarfs is by far the largest spectroscopic sample available [Koester and Kepler, 2015; Kepler et al., 2019; Genest-Beaulieu and Bergeron, 2019a,b]. We rely specifically on the 1D spectroscopic parameters published in Genest-Beaulieu and Bergeron [2019b]. We cross-matched this sample with the *Gaia* DR2 white dwarf catalogue [Gentile Fusillo et al., 2019a,b]. As Genest-Beaulieu and Bergeron [2019b] remarked, only around 90% of DB and DBA white dwarfs can be cross-matched with the *Gaia* white dwarf catalogue and we report a similar percentage. We removed all white dwarfs with spectroscopic signal-to-noise ratio (S/N) below 20. This results in a

sample of 126 DB and 402 DBA white dwarfs. We require data with the highest precision possible to apply the 3D corrections for an appropriate H/He ratio and in order to inspect systematic model issues.

We have used 1D and 3D corrected spectroscopic parameters to predict synthetic *Gaia* absolute G magnitudes from our model atmospheres[2]. From the distance modulus linking the observed apparent *Gaia* G magnitude with our predicted absolute magnitude, we derive so-called 1D and 3D spectroscopic parallaxes. These values can be compared to observed parallaxes. Fig. 4.7 (upper panel) shows the comparison between 1D spectroscopic parallaxes and *Gaia* parallaxes, which is similar to the results presented in [Genest-Beaulieu and Bergeron, 2019b]. Overall, for individual white dwarfs the agreement is satisfactory within 1-3σ. In general, spurious large spectroscopic surface gravities should appear above zero on the figure, because as surface gravity increases at a constant effective temperature, the absolute G magnitude also increases, i.e. the white dwarf becomes dimmer. Thus, for the same apparent G magnitude the white dwarf must be closer, and therefore its spectroscopic parallax must be larger. If we take the median of the parallax difference in bins of 1 000 K as shown in Fig. 4.7, it is clear that the so-called high-$\log g$ problem is not apparent in the spectroscopic parallax distribution unlike the results of previous studies of DB and DBA white dwarfs such as Koester and Kepler [2015] and Rolland et al. [2018]. In fact, it appears that the 1D spectroscopic results of Genest-Beaulieu and Bergeron [2019b] may have some leaning towards low surface gravities. Genest-Beaulieu and Bergeron [2019b] attribute the high-$\log g$ problem seen in earlier studies to the inclusion of DB and DBA white dwarfs with weak helium lines where the spectroscopic technique becomes unreliable, as well as the use of Unsold [1955] treatment of van der Waals line broadening in older studies. Neither of these two issues affecting spectroscopic parameters are fully resolved and may also depend on the flux calibration and instrumental resolution of the observations.

Before we investigate this further, in Fig. 4.7 we also compare the 3D spectroscopic parallaxes with *Gaia*. The 3D spectroscopic parallaxes where calculated as outlined previously, but with atmospheric parameters corrected for 3D effects. For individual white dwarfs, both 1D and 3D results are in satisfactory agreement with *Gaia*, suggesting it is not possible to differentiate between 1D and 3D models on a case by case basis, although 3D parameters should be favoured as a starting point because of the superior input physics. When looking at the median in bins of 1 000 K, the bump which is seen in the 1D-*Gaia* comparison and is centred around 19 000 K

[2]We use 1D ATMO model atmospheres to predict absolute G magnitudes in all cases as 3D effects on absolute fluxes are negligible.

seems to largely disappear with the use of 3D models. The range in effective temperature where the bump is observed largely agrees with the effective temperature range of 3D DB corrections discussed at length in Cukanovaite et al. [2018] (Chap. 3) and shown in Fig. 4.5. At lower effective temperatures, where the high-log g problem was historically reported, 3D models do not produce a better agreement with *Gaia*, since the 1D surface gravities are already on average too low in comparison with *Gaia* observations.

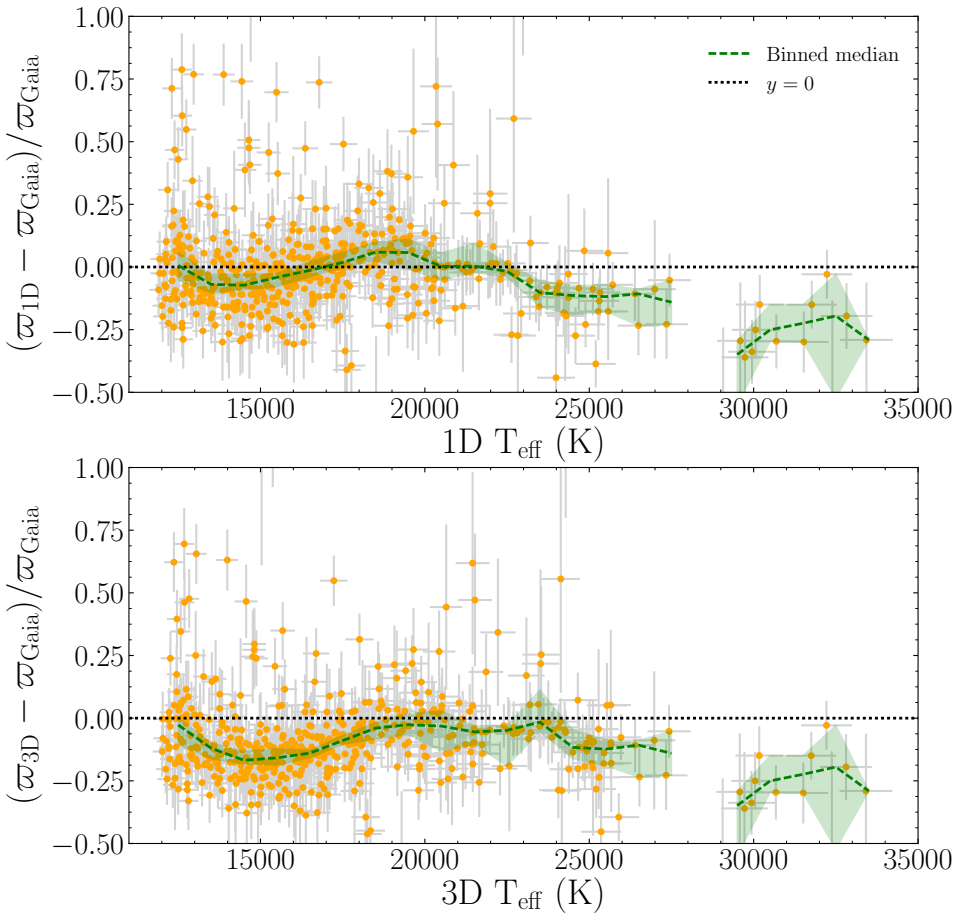

Figure 4.7: A comparison between the *Gaia* parallaxes and the parallaxes derived from spectroscopic parameters without (top panel) and with (bottom panel) 3D DB and DBA corrections for the Genest-Beaulieu and Bergeron [2019b] SDSS sample. The orange filled circles represent fractional difference between the observed and theoretical parallax, ϖ, and in light grey we show the error on the difference. The dotted black line illustrates a perfect agreement. The running median of the fractional difference in bins of 1000 K is shown in dashed green. The block-coloured green area indicates the 95% confidence limit of the median, which has been calculated using bootstrapping.

The spectroscopic parallaxes were computed from a combination of surface gravity and effective temperature, as well as *Gaia* G magnitudes. In order to investigate the current status of the accuracy of spectroscopic parameters in better detail, in Figs. 4.8 and 4.9 we plot a comparison of surface gravities and effective temperatures determined from spectroscopic (with and without 3D corrections) and photometric *Gaia* observations. The photometric parameters have been determined using only *Gaia* data and have been extracted from the *Gaia* DR2 white dwarf catalogue of Gentile Fusillo et al. [2019a,b]. The photometric parameters are based on pure-helium models but the presence of hydrogen makes a negligible contribution to the *Gaia* photometric parameters of DBA white dwarfs [Genest-Beaulieu and Bergeron, 2019b], which is not the case for cooler DC white dwarfs with much weaker helium opacity [Bergeron et al., 2019]. It was also previously shown that photometric parameters of DB and DBA white dwarfs have a fairly smooth $\log g$ distribution as a function of temperature, but the accuracy of the parameters is directly subject to the accuracy of photometric $G_{\rm BP} - G_{\rm RP}$ colour calibration [Tremblay et al., 2019b]. This is an additional uncertainty that did not play a role in our comparison of spectroscopic parallaxes as it only depends on the absolute flux calibration which is tied to the observed flux of Vega [Bohlin et al., 2014].

From Fig. 4.8 it is apparent that both 1D and 3D spectroscopic models result in higher effective temperatures when compared with photometrically derived values. It is unclear whether the offset is due to the photometric colour calibration, SDSS spectral calibration, reddening or any issue with the spectroscopic parameters. In Fig. 4.9, the comparison between surface gravities derived from spectroscopy and photometry is also shown. We confirm that within the errors of Genest-Beaulieu and Bergeron [2019b] the high-$\log g$ problem previously observed in Koester and Kepler [2015] and Rolland et al. [2018] is non-existent. The effect of 3D corrections on $\log g$ values is fairly similar to that of 3D corrections on spectroscopic parallaxes observed in Fig. 4.7. This is not surprising given that the photometric $\log g$ distribution is fairly smooth as a function of temperature [Tremblay et al., 2019b; Genest-Beaulieu and Bergeron, 2019a], and fluctuations appear to be related to spectroscopic $\log g$ values, which are employed in both Figs. 4.7 and 4.9. We now attempt to understand better the systematic differences between photometric and spectroscopic studies by reviewing the input microphysics and comparing to external data from DA white dwarfs with vastly different microphysics.

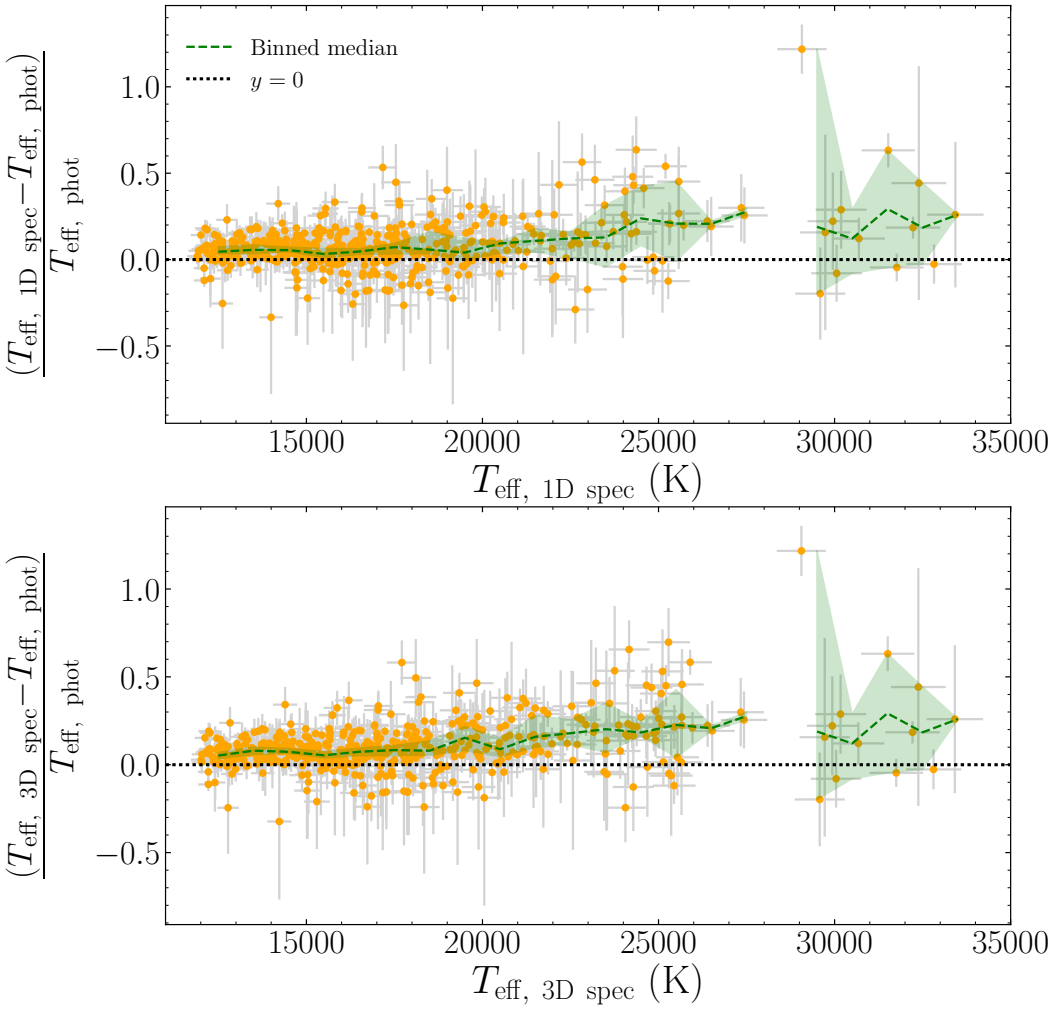

Figure 4.8: A comparison between the spectroscopically- and photometrically-determined effective temperatures for the Genest-Beaulieu and Bergeron [2019b] sample. The spectroscopic parameters have been computed without (top panel) and with (bottom panel) 3D effective temperature corrections taken in to account. The photometric parameters are from Gentile Fusillo et al. [2019a]. They are calculated based on *Gaia* data alone and include a reddening correction. The orange filled circles represent the fractional difference between the spectroscopic and photometric effective temperatures, and the error on the difference is shown in light grey. The dotted black line illustrates a perfect agreement. The running median of the fractional difference in bins of 1000 K is shown in dashed green. The block-coloured green area indicates the 95% confidence limit on the median.

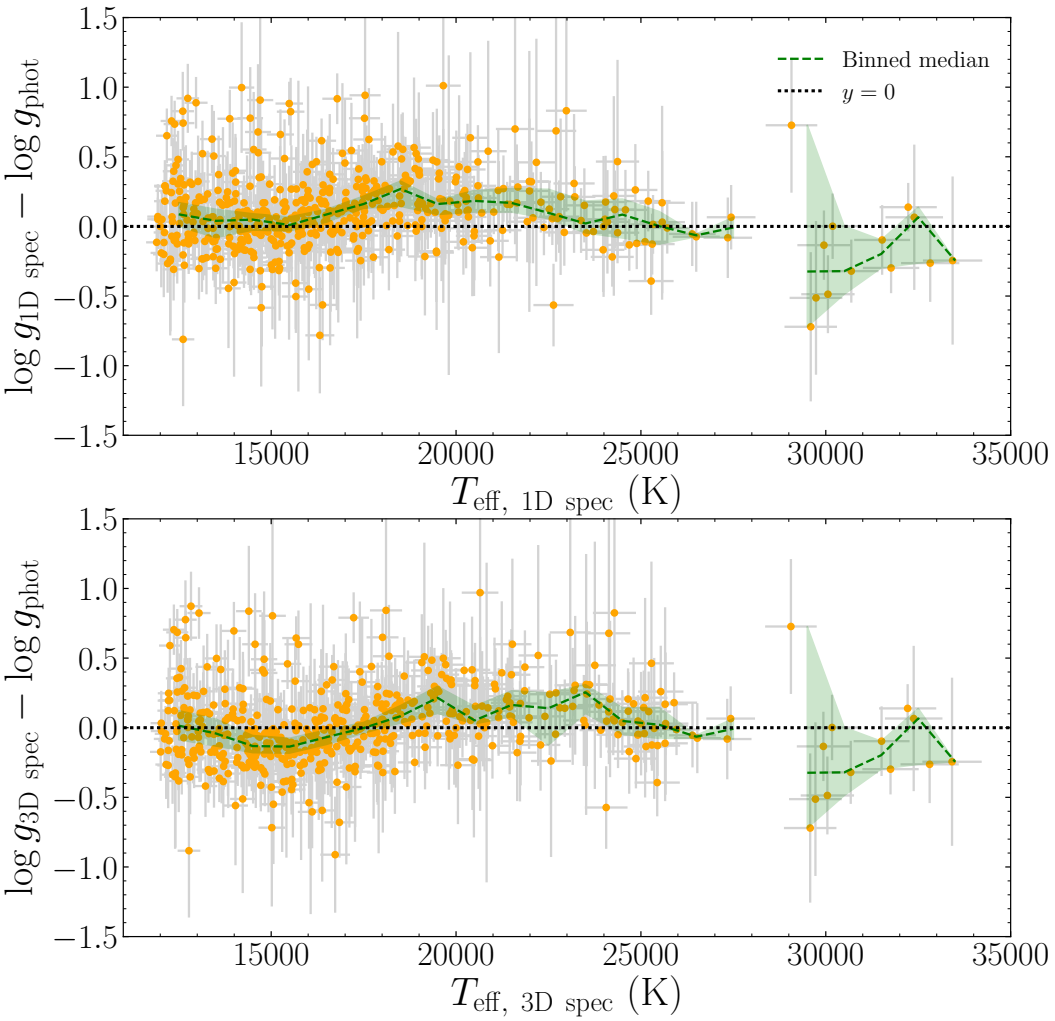

Figure 4.9: Similar to Fig. 4.8 but for spectroscopically- and photometrically-determined surface gravities.

4.4.1 van der Waals line broadening

There are two types of van der Waals line broadening commonly used in spectroscopic analyses of DB and DBA white dwarfs. These are the Unsold [1955] broadening, used in studies such as Bergeron et al. [2011], and the modified line broadening of Deridder and van Rensbergen [1976] recently resurrected by Genest-Beaulieu and Bergeron [2019a,b]. In this section, we aim to investigate the effect of van der Waals broadening on the values of the atmospheric parameters and explain the disappearance of the high-$\log g$ problem. In order to achieve this we employ the 1D ATMO code to calculate two grids of synthetic spectra, one utilising the

Unsold [1955] broadening theory and the other using Deridder and van Rensbergen [1976] with the prescriptions of Beauchamp et al. [1996]. We fit each spectrum of the Deridder and van Rensbergen [1976] grid with the Unsold [1955] grid to find the spectroscopic corrections due different prescription of line broadening. In Fig. 4.10 we show the van der Waals atmospheric parameter corrections. It is apparent that the surface gravity is most affected by the choice of the broadening, with Unsold [1955] broadening resulting in larger surface gravities. This has already been noted by Beauchamp et al. [1996].

To investigate further, we derive van der Waals correction functions for hydrogen abundance, surface gravity and effective temperature to transform from Deridder and van Rensbergen [1976] to Unsold [1955] spectroscopically-determined parameters. We use the same technique as before. The resulting corrections are

$$\begin{aligned}\Delta\log g_{\rm vdw} = d_0 + d_1 \\ \times \exp\Big[d_2 + d_3 g_x + d_4 T_x + \\ \Big(d_5 + (d_6 + d_{11}\exp\left[d_{12} + d_{13} g_x + d_{14} T_x + d_{15} y_x\right]) \\ \times \exp\left[d_7 + d_8 g_X + d_9 T_x + d_{10} y_x\right]\Big) y_x\Big],\end{aligned} \tag{4.7}$$

$$\begin{aligned}\Delta T_{\rm eff,\ vdw} = e_0 + e_1 \\ \times \exp\Big[e_2 + \Big(e_3 + e_6 \\ \times \exp\left[e_7 + e_8 g_x + e_9 T_x + \big(e_{10} + e_{11}\right. \\ \left.\times \exp[e_{12} + e_{13} g_x + e_{14} T_x + e_{15} y_x]\big) y_x\right]\Big) g_x + e_4 T_x + e_5 y_x\Big],\end{aligned} \tag{4.8}$$

$$\begin{aligned}\Delta\log\left({\rm H/He}\right)_{\rm vdw} = f_0 + \Big(f_1 + f_6 \\ \times \exp\Big[f_7 + f_8 g_x + \\ f_9 T_x + (f_{10} + f_{11}\exp[f_{12} + f_{13} g_x + f_{14} T_x + f_{15} y_x]) y_x\Big]\Big) \\ \times \exp[f_2 + f_3 g_x + f_4 T_x + f_5 y_x],\end{aligned} \tag{4.9}$$

and the values of the fitted coefficients can be found in Table 4.2. Because van der Waals line broadening remains uncertain, it may be adequate to use a multiplicative free parameter to these correction functions to illustrate how line broadening could be corrected to match the observations.

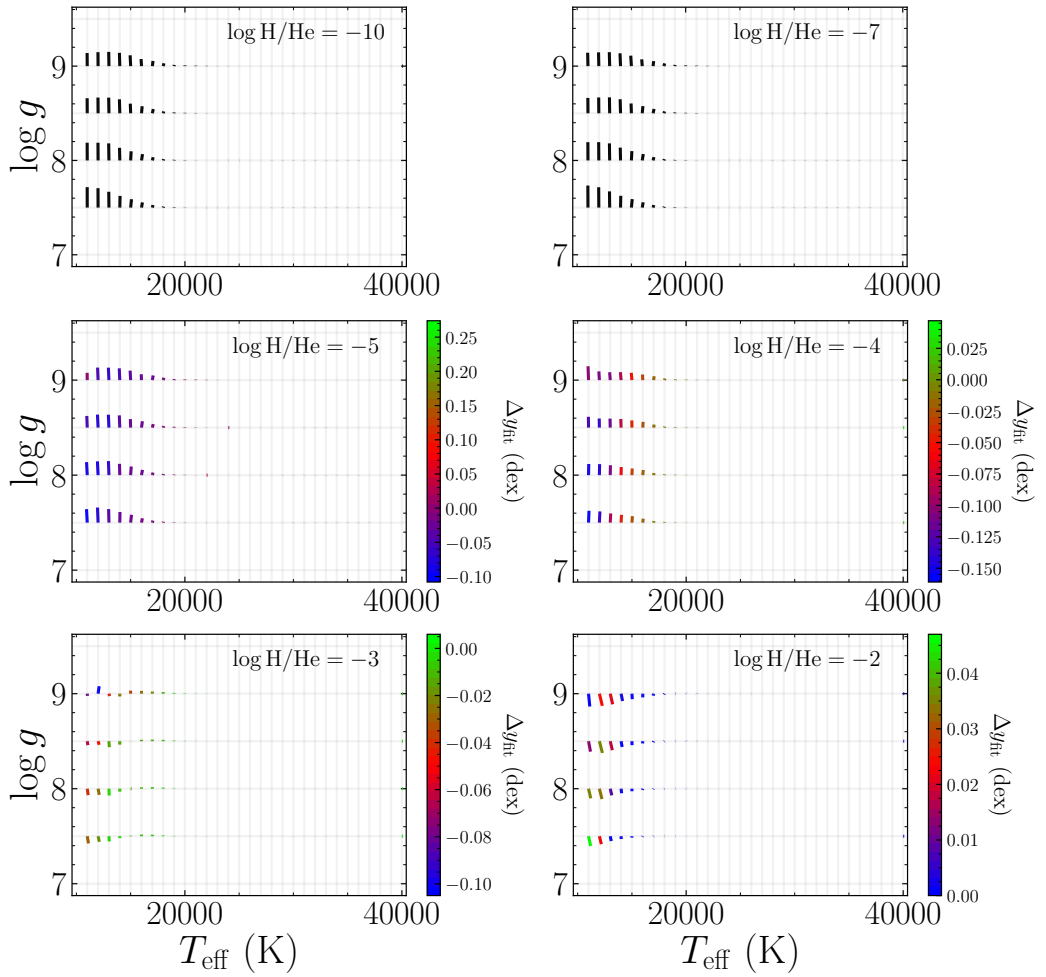

Figure 4.10: The corrections between two types of van der Waals line broadening. The intersections of the light grey lines denote the atmospheric parameters determined using the adapted Deridder and van Rensbergen [1976] broadening. The coloured lines which extend from the intersections indicate the size of the correction. The end-point away from the intersection gives the values of the corresponding atmospheric parameters when Unsold [1955] broadening is used. The colours of the lines represent the hydrogen abundance correction, which are omitted for very low hydrogen abundances.

Table 4.2: The fitted coefficients of the van der Waals correction functions described in Eqs. 4.7, 4.8 and 4.9

Coeff.		Coeff.		Coeff.	
d_0	1.354503e-05	e_0	−8.048437e-03	f_0	−2.270021e-04
d_1	−2.129736e+00	e_1	1.691468e-02	f_1	3.606112e+00
d_2	2.285596e+00	e_2	−5.845098e-01	f_2	−2.589784e+00
d_3	−6.941645e+00	e_3	3.311933e-01	f_3	−9.132723e-01
d_4	7.303697e+00	e_4	−9.525062e-02	f_4	−2.830694e+00
d_5	−8.526167e-01	e_5	2.450207e-02	f_5	−6.040429e+00
d_6	−2.027013e+00	e_6	−4.539866e+00	f_6	−1.296512e-09
d_7	1.920717e+00	e_7	6.474893e+00	f_7	−5.299115e+00
d_8	−8.975828e-01	e_8	−6.583532e-01	f_8	−6.659703e+00
d_9	1.259352e+00	e_9	−8.687359e+00	f_9	5.898993e+00
d_{10}	−9.500635e-01	e_{10}	9.742149e-01	f_{10}	4.629177e+01
d_{11}	−2.873445e+00	e_{11}	−1.348958e+01	f_{11}	−3.197353e-07
d_{12}	1.377208e+00	e_{12}	2.491540e+01	f_{12}	−9.639373e+00
d_{13}	1.345794e-01	e_{13}	1.094585e+02	f_{13}	8.545292e+00
d_{14}	−5.075663e-01	e_{14}	−8.256914e+01	f_{14}	3.598632e+00
d_{15}	−5.002648e+00	e_{15}	−1.018644e+00	f_{15}	3.651746e+01

As an illustration we apply these corrections to the Genest-Beaulieu and Bergeron [2019b] sample. Due to the way the corrections were derived, they have to be subtracted from the values of the atmospheric parameters derived using the Deridder and van Rensbergen [1976] broadening theory, such that

$$\begin{aligned} \log\left(\mathrm{H/He}\right)_{\mathrm{U}} &= \log\left(\mathrm{H/He}\right)_{\mathrm{D}} + 10 \times \Delta\log\left(\mathrm{H/He}\right)_{\mathrm{vdw}}, \\ \log g_{\mathrm{U}} &= \log g_{\mathrm{D}} - 7 \times \Delta\log g_{\mathrm{vdw}} \\ T_{\mathrm{eff,\ U}} &= T_{\mathrm{eff,\ D}} - 10\,000 \times \Delta T_{\mathrm{eff,\ vdw}}, \end{aligned} \tag{4.10}$$

where D and U denote the parameters derived using models with Deridder and van Rensbergen [1976] and Unsold [1955] line broadenings, respectively. In Fig. 4.11 we show a comparison between the photometric and van der Waals corrected spectroscopic surface gravities. From the plot, it is clear that the Unsold [1955] theory does lead to higher values of surface gravities at low effective temperatures. Using Deridder and van Rensbergen [1976] broadening is, however, not the final answer, since this theory was adapted in the DB and DBA case to better fit observations when using 1D model atmospheres [Beauchamp et al., 1996]. Instead, the aim should be to determine a better prescription of van der Waals line broadening. Additionally, it is therefore not surprising that 1D models produce a slightly better agreement with *Gaia* observations compared to 3D models when using Deridder and van Rens-

bergen [1976]. In Fig. 4.11 we also show a comparison between spectroscopic and photometric surface gravities, when the SDSS spectroscopic parameters of Genest-Beaulieu and Bergeron [2019b] are corrected for both the van der Waals broadening and 3D effects. We see that in this case, the 3D models show a better agreement with observations, hinting that Unsold [1955] van der Waals broadening is closer to the real prescription of the broadening. However, this combination of corrections still leaves an irregular $\log g$ distribution below $T_{\rm eff} \approx 14\,000$ K. We conclude that 3D corrections should be employed alongside properly adjusted line broadening using Eqs. 4.7, 4.8 and 4.9 until a better prescription is developed.

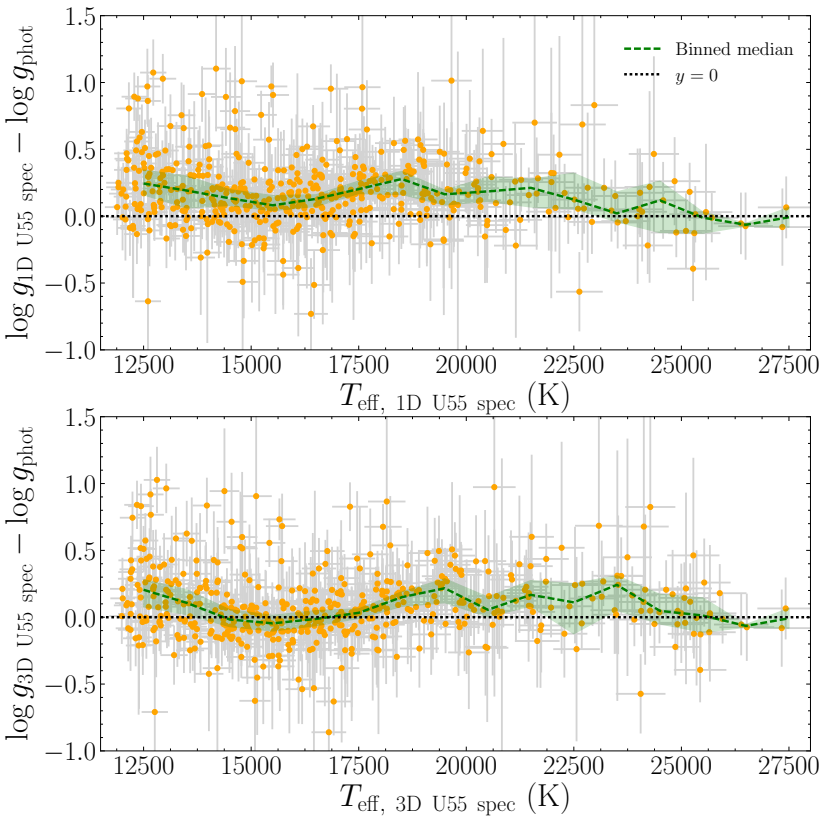

Figure 4.11: A comparison between the spectroscopically and photometrically-derived surface gravities corrected for van der Waals broadening only (top plot) and corrected both for van der Waals broadening and 3D effects (bottom plot). Solid orange circles represent the difference in surface gravities with errors shown in light grey. The running median in bins of 1000 K is shown in dashed green, with the 95% confidence limit being represented by the green colour blocked area. For reference, the dotted black line illustrates a one-to-one agreement.

4.4.2 Non-ideal effects

In this section we derive corrections due to non-ideal gas perturbations from neutral atoms (i.e. neutral helium) on the atomic levels of light-absorbing helium atoms. To do this, we calculate new grids of 1D ATMO models with different parametrisations of the Hummer and Mihalas [1988] theory currently used in all DB model atmospheres. We use different multiplicative factors to the Bohr radius $r_{\rm B}$, namely $r_{\rm B}$=[0.25,0.75,1.00], which are then used to scale the size of neutral helium and hydrogen atoms. The standard 1D ATMO grid used in previous sections was calculated at $r_{\rm B} = 0.5$ and we shall use this grid as a reference for fitting. All previous studies using the ATMO code have relied on this parametrisation [Bergeron et al., 2011; Rolland et al., 2018; Genest-Beaulieu and Bergeron, 2019a,b]. The derived corrections for surface gravity and effective temperature are shown in Fig. 4.12. We omit the hydrogen abundance corrections because they are insignificant, at most a few per cent. Similarly to van der Waals broadening corrections, we find a significant effect on surface gravity. Increasing the value of $r_{\rm B}$ from 0.5 to 1.0 results in an increase of around 0.4 dex in most extreme cases. For the highest hydrogen abundances ($\log {\rm H/He} = -2.0$), we find that the non-ideal effects do not change with varying value of $r_{\rm B}$, and indeed the surface gravity corrections act in the opposite direction. The reason why $r_{\rm B}$ does not seem to have much effect on models with $\log {\rm H/He} = -2.0$ is because the hydrogen lines are so strong that they overwhelm the fitting in that particular range of effective temperature.

Because the agreement of current 1D and 3D spectroscopic parameters with *Gaia* is reasonable and the non-ideal and line broadening corrections are partially degenerate, we argue that the commonly used value of $r_{\rm B} = 0.5$ is still an optimal choice. However, a more physical treatment of non-ideal effects will be needed before we can verify the accuracy of 3D corrections in this regime.

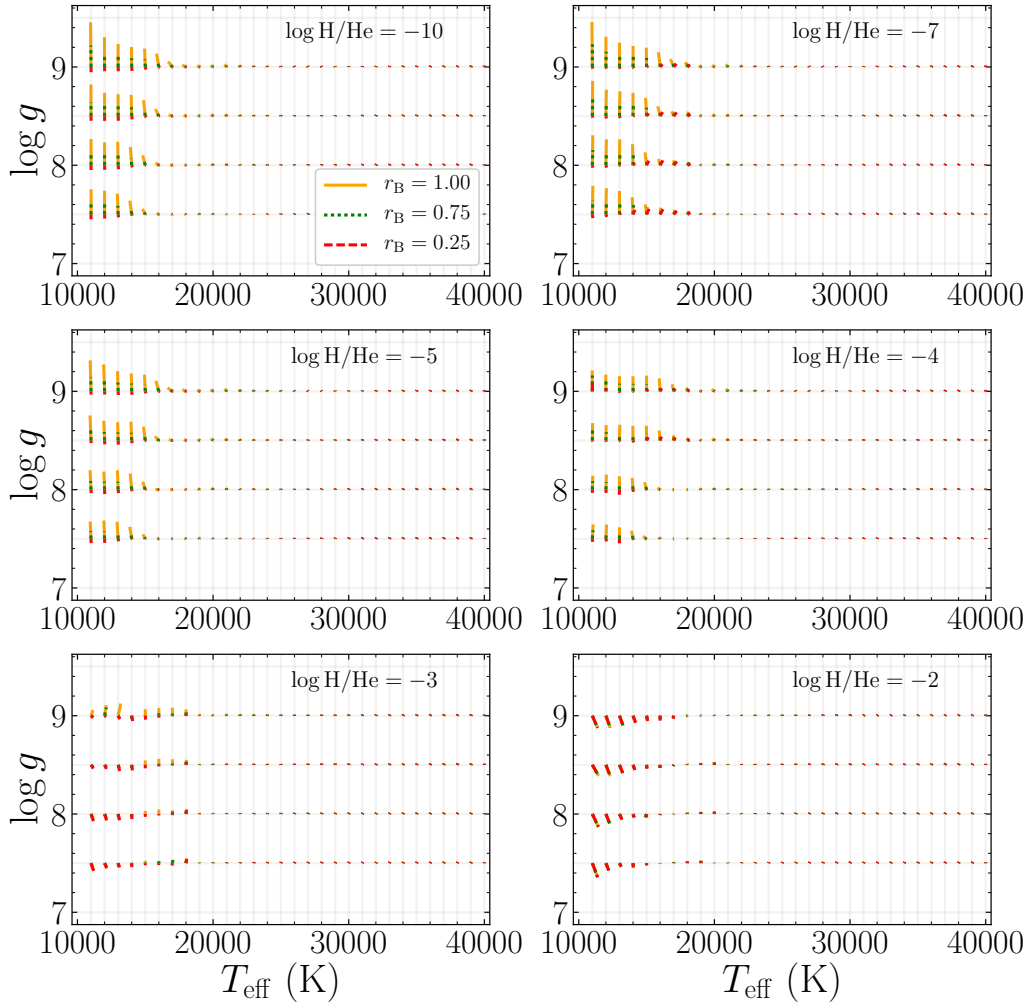

Figure 4.12: The corrections in surface gravity and effective temperature arising from varying the value of the multiplying factor to the Bohr radius, r_B, in the Hummer and Mihalas [1988] non-ideal gas theory with respect to the standard value of 0.5. In solid orange, dotted green and dashed red we show the corrections for $r_B = 1.0$, 0.75 and 0.25, respectively. The hydrogen abundance is indicated on each sub plot.

4.4.3 Comparison between He- and H-atmosphere white dwarfs

A comparison of the atmospheric parameter distributions for both DA and DB/DBA white dwarfs can help to understand systematic trends. Line broadening physics is dramatically different between the two spectral types, i.e. in warmer DA white dwarfs, hydrogen is broadened by the linear Stark effect, while helium is subject to the quadratic Stark effect and van der Waals broadening. As a consequence, if there were any issues caused by microphysics we expect systematic trends to be different

between spectroscopic parameters of DA and DB stars. In contrast *Gaia* photometric parameters have a much weaker dependence on atmospheric composition above 12 000 K [Bergeron et al., 2019] and the median masses of DA and DB stars are found to be the same to within a few per cent [Tremblay et al., 2019b].

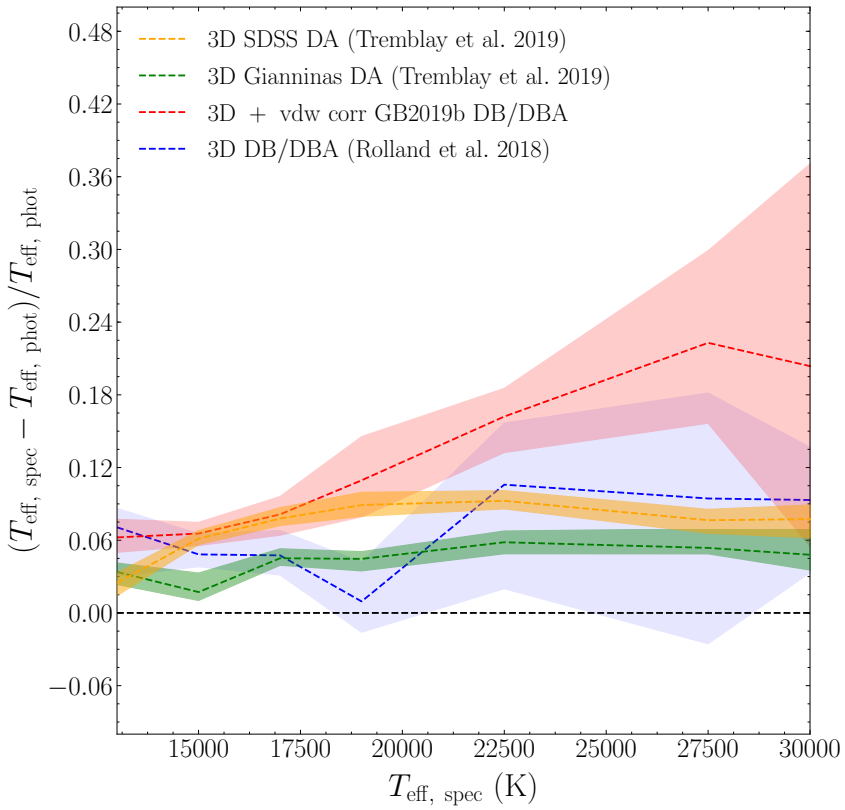

Figure 4.13: A comparison between the effective temperatures derived using spectroscopic and *Gaia* photometric observations for samples of DA and DB/DBA white dwarfs. The median fractional difference of each sample was plotted in bins of 2000 K for $T_{\rm eff} \leq 20\,000$ K and of 5000 K above that temperature. The difference in effective temperatures for the SDSS DA sample of Tremblay et al. [2019b], with spectroscopic S/N > 20 and 3D corrections, is shown in dashed orange. The dashed green curve corresponds to the DA sample of Gianninas et al. [2011] with 3D corrections (see Tremblay et al. 2019b for the comparison with *Gaia*). In dashed red and dashed blue the difference is shown for the SDSS DB/DBA sample of Genest-Beaulieu and Bergeron [2019b] and the DB/DBA sample of Rolland et al. [2018], respectively, both corrected for 3D effects presented in this work. The Genest-Beaulieu and Bergeron [2019b] sample is also corrected for Unsold [1955] van der Waals broadening (using corrections from Section 4.4.1), while Rolland et al. [2018] is already using this type of line broadening. The coloured areas represent the corresponding 95% confidence limit on the medians calculated using bootstrapping. The dashed black line indicates a perfect agreement between spectroscopy and photometry.

In Fig. 4.13 we compare the effective temperatures derived from spectroscopic and *Gaia* photometric observations of several different samples of DA and DB/DBA white dwarfs. In the plot we show the binned median of the fractional difference of each sample in bins of 2 000 K for $12\,000 \leq T_{\rm eff} \leq 20\,000$ K, and bins of 5 000 K for $T_{\rm eff} > 20\,000$ K. We rely on the same DB/DBA sample of Genest-Beaulieu and Bergeron [2019b] as discussed previously, using our 3D corrections and also the Unsold [1955] prescription of van der Waals broadening (with original atmospheric parameters corrected according to Section 4.4.1). We also use the DB/DBA sample of Rolland et al. [2018] where we have applied our new 3D DB/DBA corrections. The sample of Rolland et al. [2018] already uses the Unsold [1955] prescription of van der Waals broadening. Our DA white dwarf samples are drawn from SDSS [Tremblay et al., 2019b], where we have restricted to spectroscopic S/N > 20, and Gianninas et al. [2011]. In both cases we have applied 3D DA corrections [Tremblay et al., 2013c]. These DA samples are effectively the same as the 3D spectroscopic samples described in Tremblay et al. [2019b]. All spectroscopic samples have been cross matched with the *Gaia* white dwarf catalogue of Gentile Fusillo et al. [2019a,b] to obtain photometric atmospheric parameters based on dereddened photometry.

The different samples show similar offsets between photometric and spectroscopic effective temperatures. The offset is not obviously caused by calibration issues of SDSS spectra [Kleinman et al., 2004; Tremblay et al., 2019b], since the samples of Gianninas et al. [2011] and Rolland et al. [2018] do not use SDSS data. An issue with the approximate treatment of dereddening in Gentile Fusillo et al. [2019a] is unlikely because there is no obvious correlation between the observed offset and distance [Tremblay et al., 2019b], e.g. the offset is similar even for bright DA white dwarfs within 40 pc [Tremblay et al., 2020] for which reddening is expected to be negligible. It cannot be due to 3D effects, as 1D DB/DBA models predict a similar offset (see Fig. 4.8) and 3D effects for DA white dwarfs are essentially negligible above a temperature of 13 000 K. It is unlikely to be caused by microphysics issues, such as van der Waals or Stark broadening, as the offset seems to be more or less constant over the entire range of effective temperatures, and is very similar for DA and DB stars, whereas line opacities vary significantly as a function of effective temperature and spectral type. Therefore, they are are unlikely to cause offsets of similar magnitude. Therefore, this leaves the possibility that the offset is due to calibration issues with *Gaia* colours, which are the direct input in the determination of photometric effective temperatures, given that the sensitivity of surface gravity to colours is weak. Similar offsets have been observed in other studies of photometric *Gaia* data [Maíz Apellániz and Weiler, 2018; Tremblay et al., 2019b; Genest-Beaulieu and

Bergeron, 2019a; Tremblay et al., 2020], for example, Maíz Apellániz and Weiler [2018] suggest an offset of 0.0032dex in *Gaia* G magnitude. Our work provides robust constraints based on 3D spectroscopic parameters of both DA and DB white dwarfs. The calibration of *Gaia* astrometry [Lindegren et al., 2018] is not expected to have a significant role in the determination of surface temperatures. Finally, the larger scatter observed for DB/DBA samples above $T_{\rm eff} \approx 20\,000$ K could be explained by spectral fitting issues regarding the maximum strength of He I lines as discussed in this work. For DA white dwarfs spectral fitting is straightforward in this temperature range.

In Fig. 4.14 we show a comparison between the spectroscopically- and photometrically-derived surface gravities. The remnant high-$\log g$ issue for DB and DBA white dwarfs can be seen in the (3D and Unsold [1955] van der Waals broadening corrected) Rolland et al. [2018] and Genest-Beaulieu and Bergeron [2019b] samples below $T_{\rm eff} \approx 15\,000$ K. Similarly to the effective temperature comparison, the agreement between spectroscopically- and photometrically-derived surface gravities is not perfect. When deriving the photometric atmospheric parameters, the temperature almost only depends on observed colours, while for a fixed temperature value and mass-radius relation, the surface gravity only depends on mean absolute flux. Therefore, it means that if an offset is observed in effective temperature and is caused by *Gaia* colour calibration, then an offset similar in shape is likely to be seen in surface gravities, as the radius must compensate for the offset in temperature to match absolute fluxes. However, the diagnostic potential is complicated by the fact that the spectroscopic effective temperatures and surface gravities have different sensitivities and possibly different systematics with respect to the line profiles. For DA white dwarfs in Fig. 4.14 we find that photometric $\log g$ values are systematically lower. This results in larger radii, which compensate for the lower photometric $T_{\rm eff}$ values in keeping the same absolute fluxes, and is therefore entirely consistent with a colour calibration issue. In contrast the DB white dwarfs in both samples show an irregular behaviour, which could suggest that issues with line profiles dominate or are similar in strength to colour calibration issues.

In general, it appears that when comparing the spectroscopic results to external constraints, both DA and DB/DBA white dwarfs behave in a similar fashion. This indicates that 3D DB/DBA atmospheric models are comparable to their DA counterparts in terms of precision.

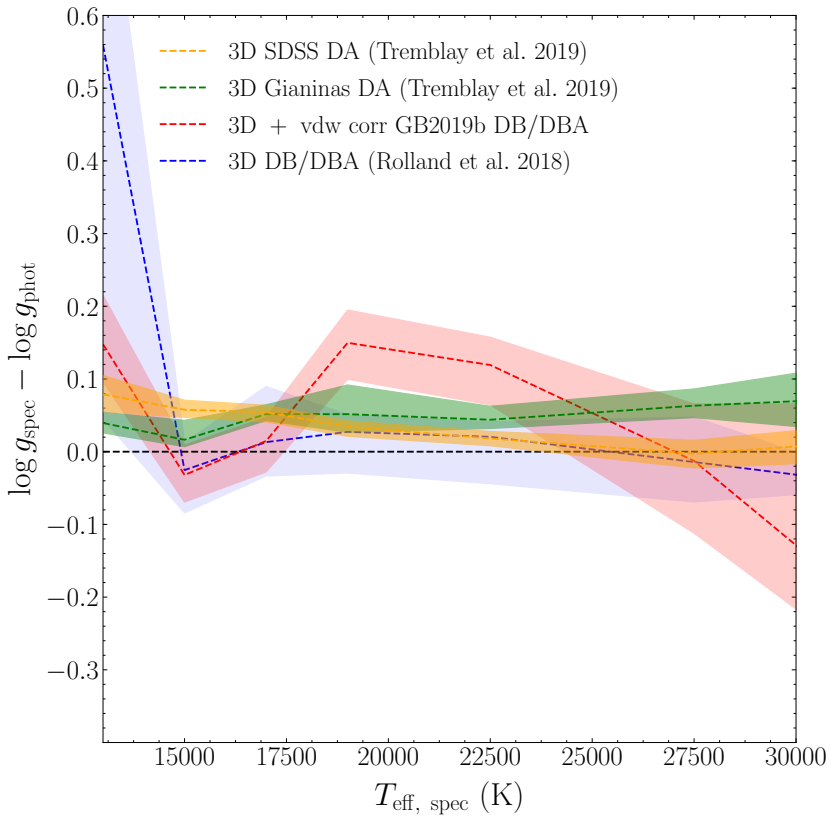

Figure 4.14: Same as Fig. 4.13 but for a comparison between the surface gravities derived using spectroscopic and *Gaia* photometric observations for samples of DA and DB/DBA white dwarfs.

4.5 Conclusions

Using 282 3D atmospheric models of DB and DBA white dwarfs, we have determined the corrections for hydrogen abundance, surface gravity and effective temperature due to a more physical treatment of convection. We find significant surface gravity corrections for $T_{\rm eff} \lesssim 16\,000$ K where the high-log g problem was historically reported for these types of white dwarfs. When applying our 3D corrections to the spectroscopic sample of Genest-Beaulieu and Bergeron [2019b] we find a similar agreement between 1D and 3D spectroscopic parameters when compared with *Gaia* data. We nevertheless recommend using 3D parameters as a standard starting point because of the superior input physics. We provide 3D correction functions that can applied to 1D atmospheric parameters from any study and with any input model atmospheres.

The currently employed Deridder and van Rensbergen [1976] theory of van der Waals broadening has been specifically adapted to produce a smooth distribution of 1D atmospheric parameters for $T_{\rm eff} \lesssim 16{,}000\,{\rm K}$, albeit this has not been updated for the most recent constraints from *Gaia* DR2. Nevertheless, it is not surprising that 3D corrections do not lead to a better agreement with *Gaia* photometry and astrometry in this regime. When applying 3D corrections to spectroscopically derived values relying on the Unsold [1955] theory of van der Waals broadening, we find that 3D results are in better agreement with *Gaia*. However, we stress that the treatment of non-ideal effects due to neutral helium atoms also plays a significant role in this low temperature regime and that it is degenerate with the choice of the line broadening theory. This highlights the fact that the treatment of the microphysics for cool DB and DBA white dwarfs needs to be revisited.

By comparing spectroscopic and photometric atmospheric parameters of various samples of DA, DB and DBA white dwarfs, we have been able to identify a prominent offset in effective temperature and a possible smaller offset in surface gravity. By ruling out a number of possibilities that could be responsible for such an offset, we conclude that it is most likely caused by the *Gaia* colour calibration. A similar offset has been reported in other studies. In general, it seems that the offsets are remarkably similar for both DA and DB/DBA white dwarfs. Thus, the atmospheric models of DB and DBA white dwarfs can be considered to be of similar precision and accuracy to that of DA models. In the following chapter, we extend the usefulness of 3D atmospheric models by using them to calibrate the mixing length parameter at the bottom of the convection zone, which can then, for example, be used to calculate more accurate envelope and evolutionary models of DB and DBA white dwarfs.

Chapter 5

MLT parameter calibration for 3D DB and DBA white dwarfs

Sanity
I feel like I've been floating endlessly
Pray for me
'Cause I've been chasing wine with alchemy
I took everything they gave me
I'm still begging for more
Call the exorcist, the hypnotist
They can't find a cure

A Pill to Crush
Evalyn

5.1 Introduction

White dwarfs evolve by cooling, as they are unable to fuse matter in their degenerate cores. As they cool, superficial convection zones develop in their envelopes and grow bigger with decreasing effective temperature, $T_{\rm eff}$ [Tassoul et al., 1990]. This means that both the structure and evolutionary models of white dwarfs can be affected by uncertainties arising from the treatment of convective energy transport. Thus, in this chapter, the 3D DB and DBA atmospheric models are used to calibrate the mixing length parameter at the bottom of the convection zone, which can be used in aforementioned models. In Sect. 5.2 we present the grids of 3D DB and DBA atmospheric models and 1D envelope structures used for the calibration of the mixing length parameter. Sect. 5.3 describes the general properties of the 3D

convection zones and the differences with 1D convection zones. The calibration method is described in Sect. 5.4 and results are discussed in Sect. 5.5. We conclude in Sect. 5.6.

Until recently, the standard white dwarf models used for the atmosphere and the interior have been 1D, where convection is treated using the ML2 version [Tassoul et al., 1990] of the mixing length theory, MLT [Böhm-Vitense, 1958]. As an improvement, another 1D theory of convection, CMT (abbreviation for authors' names, Canuto and Mazzitelli 1991, 1992), and its refined version CGM (abbreviation for authors' names, Canuto et al. 1996), have also been used in modelling white dwarf evolution [Althaus and Benvenuto, 1996, 1997; Benvenuto and Althaus, 1999]. Unlike MLT, CMT does not rely on the approximation of single-sized convective eddies and instead considers a full range of eddy sizes. Unfortunately, similarly to MLT, CMT depends on the local conditions of the atmosphere [Ludwig et al., 1999], which is a restrictive approximation as convection is a non-local process. This assumption was subsequently removed in non-local 1D envelope models of white dwarfs [Montgomery and Kupka, 2004]. Given that convection is inherently a 3D process, the dimensionality issue was first improved by 2D atmospheric models of DA white dwarfs developed by Ludwig et al. [1993], Ludwig et al. [1994] and Freytag et al. [1996].

More recently, the first 3D models for pure-hydrogen atmosphere (DA) [Tremblay et al., 2013b,a,c; Kupka et al., 2018] and pure-helium atmosphere (DB) [Cukanovaite et al., 2018] (Chap. 3) white dwarfs have been developed. In 3D models convection is non-local, is treated from first principles and the models do not depend on any free parameters, although numerical parameters do exist. Spectroscopic corrections derived from 3D models have been tested against *Gaia* DR2 data [Gaia Collaboration et al., 2018] by comparing the observed parallaxes for samples of DA and DB/DBA white dwarfs with spectroscopically-derived parallaxes with and without 3D corrections [Tremblay et al., 2019b]. 3D DA corrections to the 1D models were shown to be in excellent agreement with the observational data. For the DB/DBA samples, the 3D DB corrections were not a clear improvement upon predicted 1D parallaxes. This has been attributed to remaining uncertainties in the microphysics of DB and DBA models.

In this chapter, we focus on the calibration of the mixing length parameter at the bottom of the convection zone for 3D DB and DBA models, similar to what has been achieved for 3D DA models [Tremblay et al., 2015b]. We use the grid of 3D DBA models consisting of 235 simulations alongside the recently published grid of 47 3D DB models. Our calibration of mixing length parameter is relevant for the overall

thermal and mixing properties of the convection zone. It differs in purpose to the calibration of the mixing length parameter based on a detailed spectroscopic analysis performed by Bergeron et al. [2011]. This is because the spectral light forming layers for DB and DBA stars are always near or above the top of the convection zone. Additionally, due to the dynamic nature of convection, the mixing length parameter varies throughout the white dwarf structure [Ludwig et al., 1994; Tremblay et al., 2015b]. Therefore, no single 1D synthetic spectrum at a given value of the mixing length parameter can reproduce the entirety of a 3D spectrum [Cukanovaite et al., 2018] (Chap. 3).

Our calibration is of relevance to many applications. For example, it is currently not possible to compute 3D evolutionary models of any star. Instead, 1D stellar evolution models have been improved by calibrating the mixing length parameter based on 3D atmospheric models and allowing it to vary accordingly as the star evolves [Trampedach et al., 2014; Magic et al., 2015; Salaris and Cassisi, 2015; Mosumgaard et al., 2018; Sonoi et al., 2019]. Such a calibration has already been performed for DA white dwarfs [Tremblay et al., 2015b], but has not been done for DB and DBA stars.

Additionally, the position of the theoretical blue edge of the instability strip for V777 Her (DBV) white dwarfs is heavily dependent on the assumed convective efficiency at the bottom of the convection zone [Fontaine and Brassard, 2008; Córsico et al., 2009; Van Grootel et al., 2017]. Larger values of the mixing length parameter result in larger effective temperature of the blue edge. The current empirical blue edge of the strip is defined by PG0112+104 at $T_{\rm eff} \approx 31\,000$ K (at $\log g \approx 7.8$) [Shipman et al., 2002; Provencal et al., 2003; Hermes et al., 2017], approximately 2 000 K higher than the current theoretical blue edge of $T_{\rm eff} \approx 29\,000$ K (at $\log g \approx 7.8$) calculated at the spectroscopically-calibrated ML2/α = 1.25 [Van Grootel et al., 2017]. This suggests that higher convective efficiency is needed to correctly model the empirical blue edge.

Calibration of the mixing length parameter at the bottom of the convection zone can also provide more accurate convection zone sizes for DB and DBA white dwarfs. This is needed in order to understand the accretion of planetesimals onto white dwarfs, including the mixing of the different accreted chemical elements within the convection zone and their diffusion at its bottom (or floating in the case of hydrogen). These events are frequent around DB and DBA white dwarfs [Kleinman et al., 2013; Veras, 2016] and could explain the origin of hydrogen in DBA stars [Gentile Fusillo et al., 2017]. However, for a full 3D description of the accretion-diffusion scenario, convective overshoot must also be accounted for [Kupka et al.,

2018; Cunningham et al., 2019], which is outside the scope of the current work.

5.2 Numerical setup

5.2.1 3D atmospheric models

Using the CO^{5}BOLD radiation-hydrodynamics code [Freytag et al., 2002; Wedemeyer et al., 2004; Freytag et al., 2012; Freytag, 2013, 2017], we have calculated 285 3D DB and DBA models with 12 000 K $\lesssim T_{\rm eff} \lesssim$ 34 000 K, $7.5 \leq \log g \leq 9.0$ and $-10.0 \leq \log {\rm H/He} \leq -2.0$, where $\log {\rm H/He}$ is the logarithm of the ratio of the number of hydrogen-to-helium atoms in the atmosphere. Fig. 5.1 illustrates the atmospheric parameter values of our 3D simulations. Appendix B also lists basic information about the 3D models, including their atmospheric parameters, simulation box sizes, running times and intensity contrasts. For DB models we use $\log {\rm H/He} = -10.0$ as this low hydrogen abundance practically describes a pure-helium composition. The abundance range chosen covers the majority of observed hydrogen abundances in DB/DBA samples [Bergeron et al., 2011; Koester and Kepler, 2015; Rolland et al., 2018]. For all abundances, models with $\log g = 7.5$ only extend up to 32 000 K due to convective energy transport being negligible at higher effective temperatures for this particular surface gravity. Currently, there are no known low-mass helium-dominated atmosphere white dwarfs, which would be formed as a consequence of binary evolution [Tremblay et al., 2019b; Genest-Beaulieu and Bergeron, 2019a]. This indicates that binary evolution does not produce helium-dominated atmosphere white dwarfs. Therefore, we do not calculate models with $\log g < 7.5$.

For all simulations the top boundary is located at $\log \tau_{\rm R} \lesssim -5.0$, where $\log \tau_{\rm R}$ is the logarithm of the Rosseland optical depth. The bottom boundaries are around $\log \tau_{\rm R} = 3.0$, however, some closed bottom simulations had to be extended deeper to justify the enforcement of zero vertical velocity. In most extreme cases, the models had to be vertically extended to 230 grids points, increasing $\log \tau_{\rm R}$ to around 4.

The 3D models are spatially- and temporally-averaged in order to extract the relevant atmospheric stratifications, i.e. entropy, temperature, pressure and convective flux as functions of $\log \tau_{\rm R}$. The spatial average is performed over constant geometric height, unlike in Cukanovaite et al. [2018] (Chaps. 3 and 4) where the spatial average was done over contours of constant $\log \tau_{\rm R}$. The temporal average is

performed over the last quarter of the simulation, i.e. the last quarter of the total run time given in Tabs. B.1-B.6.

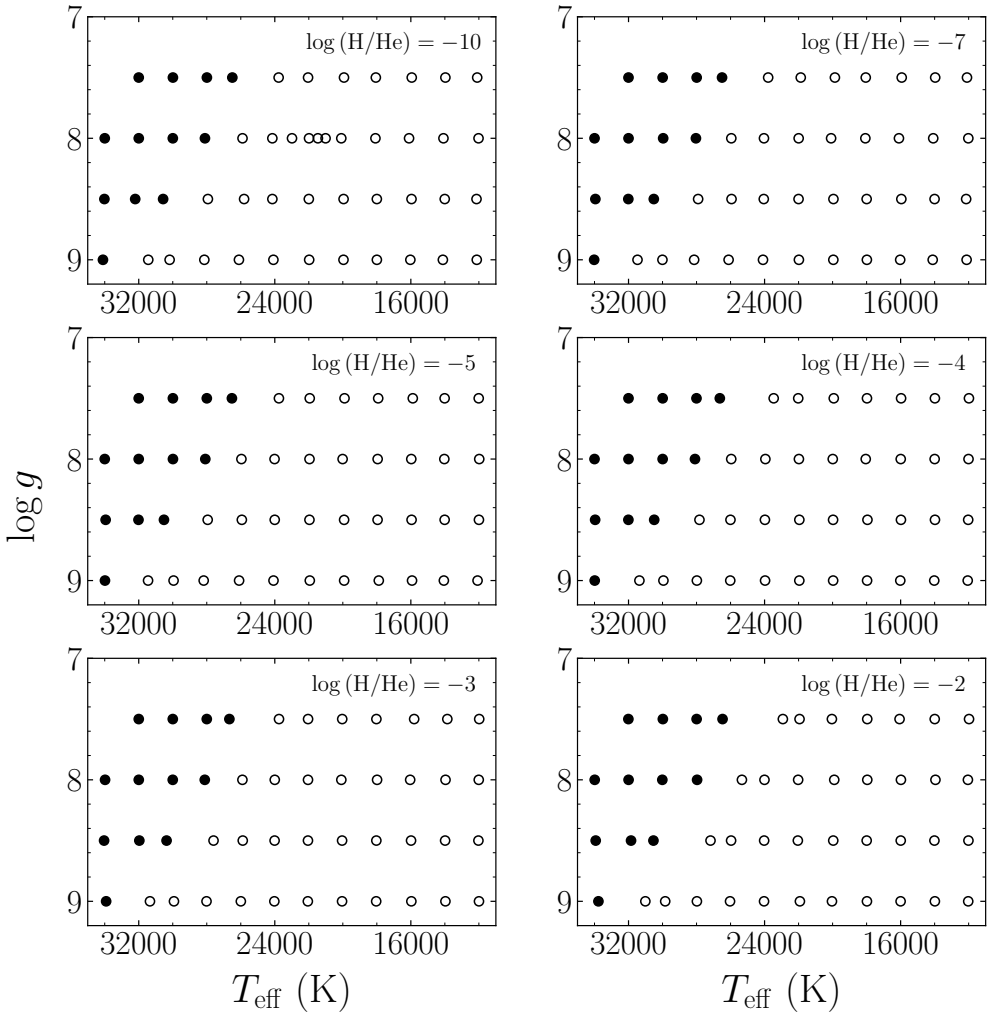

Figure 5.1: The abundances, surface gravities and effective temperatures of the 3D models presented in this paper. Open and filled circles denote the models with open and closed bottom boundaries, respectively.

5.2.2 1D envelope models

In order to find a mixing length value that best matches the nature of 3D convection zones, we use the updated 1D DB and DBA envelope models of Van Grootel et al. [2017] and Fontaine et al. [2001], which span the same parameter range as our 3D atmospheric models but also different values of the mixing length parameter, namely $0.4 \leq \mathrm{ML2}/\alpha \leq 1.4$ in steps of 0.1. The envelopes rely on non-

grey upper boundary conditions extracted from the atmospheric models of Bergeron et al. [2011], and on the non-ideal EOS of Saumon et al. [1995]. Turbulent pressure is not included in the envelope structures.

For the majority of 3D models the inflowing entropy at the base of the convection zone (the input parameter for open bottom models which controls effective temperature of the model) is used for the calibration of the mixing length parameter. In order to have a common entropy zero-point between the 1D envelopes and 3D atmospheres, we re-calculate the 1D entropy from the temperature and pressure at the base of the 1D envelope convection zone. The entropy is re-calculated with and without partial degeneracy to demonstrate the degeneracy effects. Fig. 5.2 shows the entropy at the bottom of the convection zone as a function of effective temperature for select models. At high effective temperatures the partial degeneracy is negligible as the chemical potential of free electrons has a large negative value. Partial degeneracy becomes important for models with cool effective temperatures due to their low temperatures and high densities. For the $\log \mathrm{H/He} = -10.0$ grid, our first-order partial degeneracy correction begins to break down for models with lowest effective temperatures, which are not plotted in Fig. 5.2, namely $T_{\mathrm{eff}} \lesssim 14\,000$, 14 000, 16 000, 18 000 K for models with $\log g = 7.5$, 8.0, 8.5, 9.0, respectively. Similar behaviour is observed for the DBA grid. Below these effective temperatures convection in envelopes is almost fully adiabatic everywhere and becomes independent of the particular choice of the mixing length parameter. Therefore, we do not attempt the calibration of the mixing length parameter in that particular effective temperature regime (see Sect. 5.4). We find that partial degeneracy is more important for DB/DBA models with low effective temperatures than DA models with low effective temperatures (see Fig. 1 of Tremblay et al. 2015b) possibly due to the higher densities of DB models.

From 1D envelopes we also extract the ratio $\log (M_{\mathrm{CVZ}}/M_{\mathrm{tot}})$, where M_{CVZ} is the mass of the convection zone integrated from the surface of the white dwarf to the bottom of the convection zone and M_{tot} is the total mass of the white dwarf. An example of this is shown in Fig. 5.3. As expected, varying the value of the mixing length parameter for models where superadiabatic convection is important has a significant effect on the mass of the convection zone. The change can be as much as ≈ 4 dex for DB and DBA models with $\log g = 7.5$, and ≈ 3 dex for models with $\log g = 9.0$. By calibrating the mixing length parameter with our 3D models (see Sect. 5.4) we can narrow down the uncertainty on the mixed mass within the convection zone.

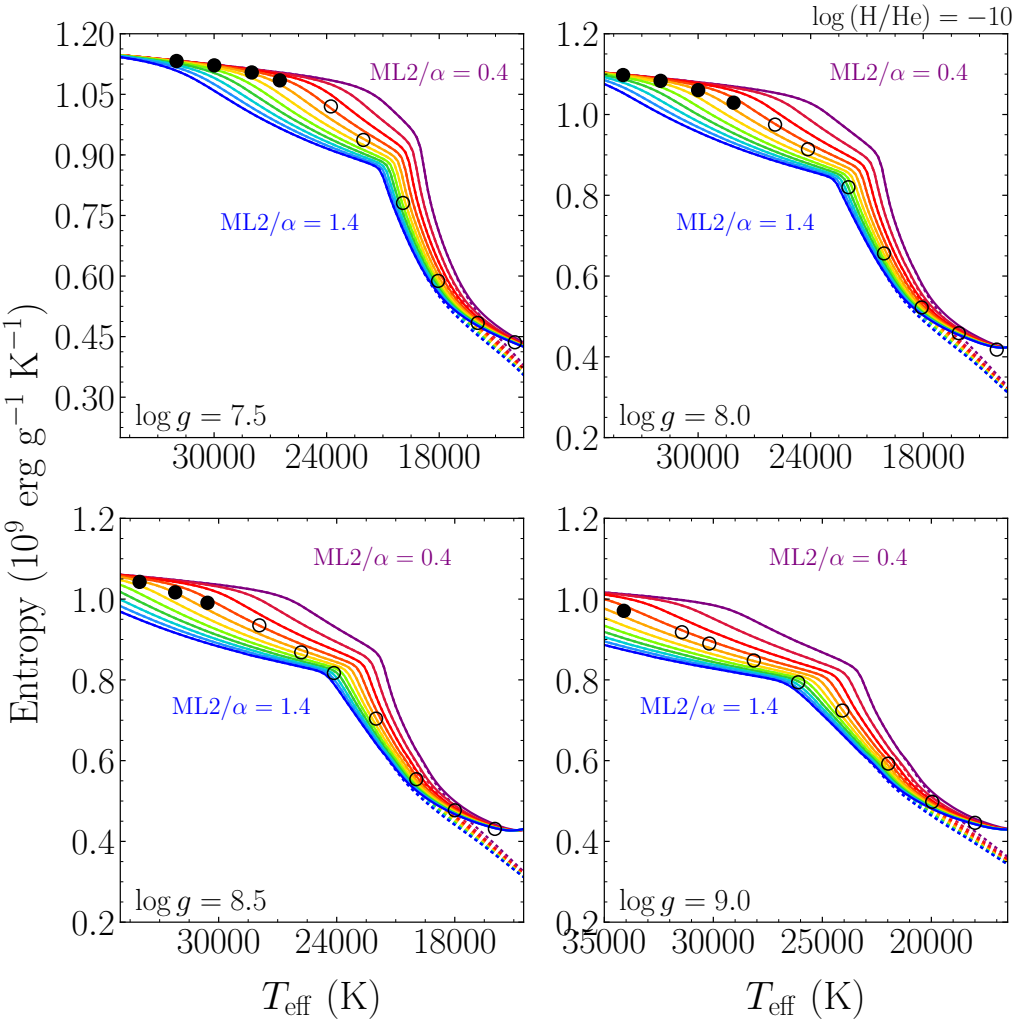

Figure 5.2: The specific entropy at the bottom of the convection zone defined by the Schwarzschild criterion as a function of effective temperature for 3D DB open (open circles) and closed (filled circles) bottom models, and for 1D DB envelopes with different values of the mixing length parameter. The value of the mixing length parameter decreases by increments of 0.1 from the dark blue line (ML2/α = 1.4) all the way up to the dark purple line (ML2/α = 0.4). We show the 1D entropies with (solid lines) and without (dashed lines) partial degeneracy effects taken into account. The surface gravities of the models are indicated on the panels.

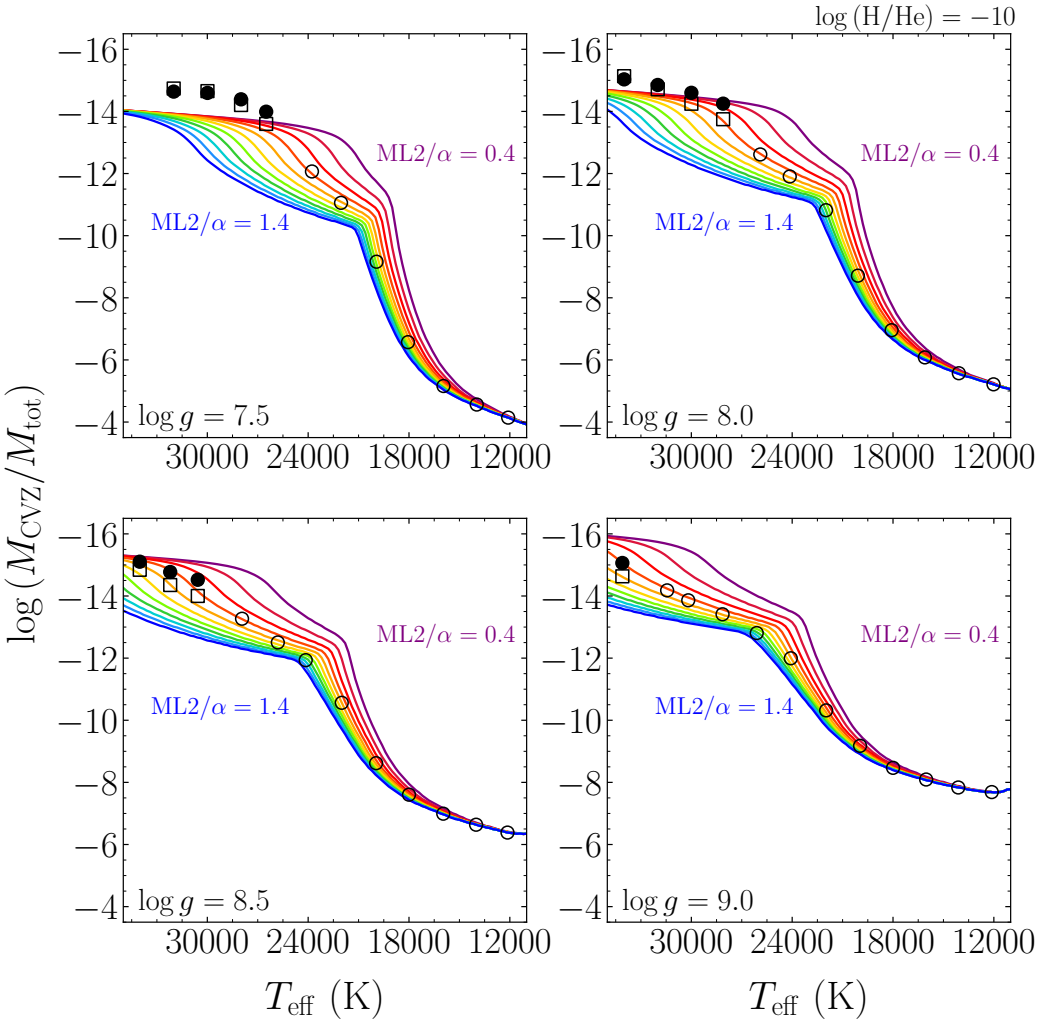

Figure 5.3: The fraction of the convection zone mass to the total mass of the white dwarf as a function of effective temperature for 3D DB models and 1D DB envelopes (solid lines) with different values of the mixing length parameter. The value of the mixing length parameter decreases by increments of 0.1 from the dark blue line (ML2/α = 1.4) all the way up to the dark purple line (ML2/α = 0.4). The Schwarzschild boundaries for the 3D open bottom models are indicated by open circles; filled circles represent the Schwarzschild boundary for closed bottom 3D models; open squares represent the flux boundary for closed bottom 3D models.

The convection zone size increases with decreasing surface gravity and decreasing effective temperature [Fontaine and van Horn, 1976]. Shallower convection zones are expected for DBA models as the presence of hydrogen increases the total opacity, decreasing the atmospheric density and pressure [Fontaine and van Horn, 1976]. This is also seen for late-type stars with increased metallicity [Magic et al., 2013]. The decrease in density and pressure results in higher adiabatic entropy (see

Sec. 5.3), and therefore lower convective efficiency (and entropy jump, see Sec. 5.5.1) and smaller convection zones [Magic et al., 2013]. Fig. 5.4 shows $\log(M_{\rm CVZ}/M_{\rm tot})$ for the $\log {\rm H/He} = -2.0$ grid. By comparing Figs. 5.3 and 5.4 it is clear that the presence of hydrogen does indeed shrink the convection zones.

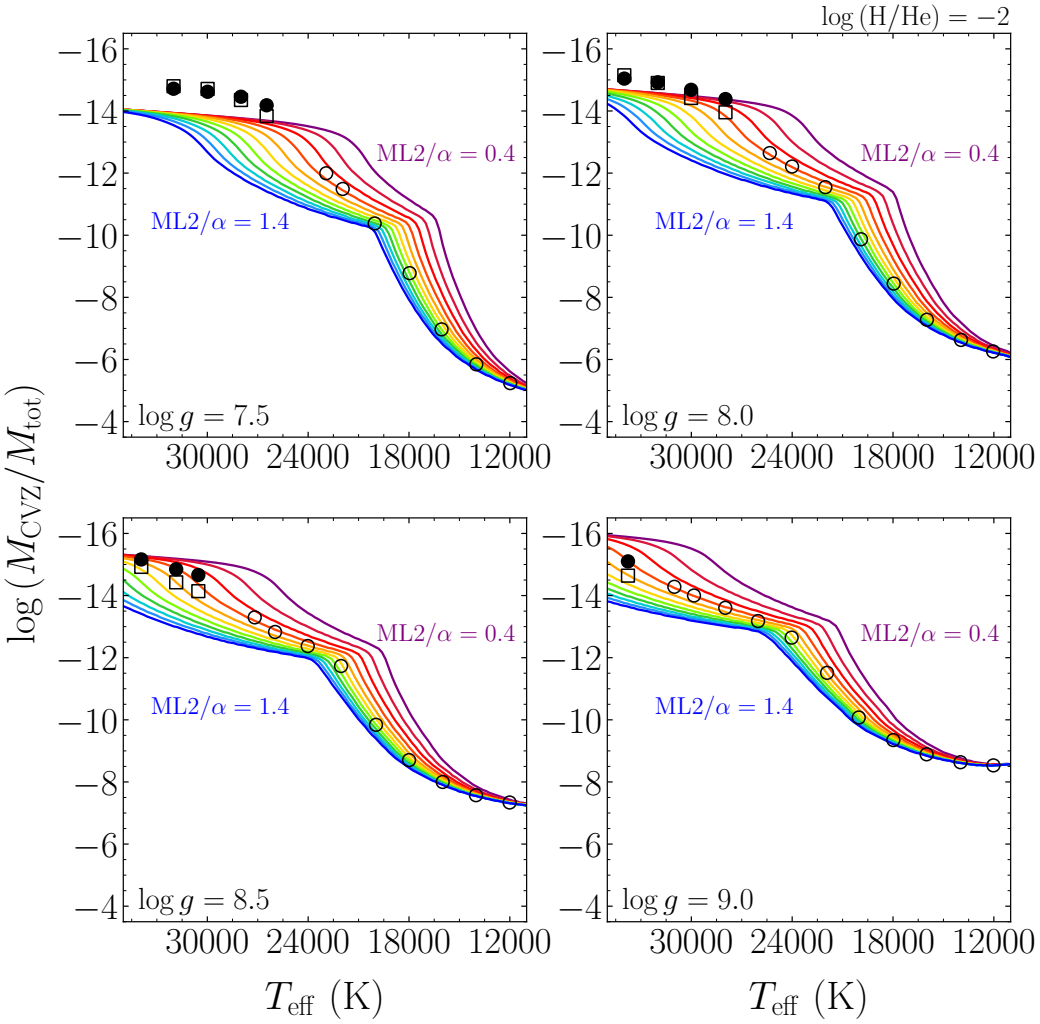

Figure 5.4: Same as Fig. 5.3, but for a DBA grid with $\log {\rm H/He} = -2.0$.

5.3 The convection zone

The envelopes of cool DA and DB white dwarfs are convective, with the top of the convection zone almost perfectly overlapping with the photospheric layers [Tassoul et al., 1990], meaning that convection is essential for modelling both atmospheres and envelopes of cool white dwarfs. In 1D atmospheric and envelope models

the convective layers are defined by the Schwarzschild criterion

$$\left(\frac{\partial \ln T}{\partial \ln P}\right)_{\text{radiative}} > \left(\frac{\partial \ln T}{\partial \ln P}\right)_{\text{adiabatic}}, \tag{5.1}$$

where T and P are the temperature and pressure. Therefore, only those layers that locally satisfy this inequality are able to transport energy through convection, leading to abrupt and clearly-defined boundaries of the convection zone in 1D. This is a limited approximation of the turbulent nature of convection, which is better explored with the use of 3D models. There are at least two ways one can define convection zone boundaries and subsequently convection zone sizes in 3D simulations. In the following we use the Schwarzschild criterion (the Schwarzschild boundary) and the zero convective flux (the flux boundary) definitions.

The Schwarzschild criterion can be rewritten in terms of the entropy gradient with respect to $\log \tau_{\text{R}}$, such that the convective layers are defined by

$$\frac{\mathrm{d}s}{\mathrm{d}\tau_{\text{R}}} > 0 \ , \tag{5.2}$$

where s is the entropy and both $\log \tau_{\text{R}}$ and s are averages over constant values of geometric depth. We use this definition to determine the edges of the convection zone in both 1D and $\langle$3D$\rangle$ entropy stratifications, focusing on the bottom boundary, defining it to be the Schwarzschild boundary.

Unlike in the 1D case, the 3D convective energy is transported even beyond the Schwarzschild boundary. This is due to the acceleration of the overdense convective downdrafts in the layers just above the base of the convection zone. In response, because of mass conservation warm material is transported upwards, resulting in a positive convective flux [Tremblay et al., 2015b]. We define the flux boundary to be the region where the ratio of convective-to-total flux goes to zero. The convective flux, F_{conv}, is calculated using

$$F_{\text{conv}} = \left\langle \left(e_{\text{int}} + \frac{P}{\rho}\right) \rho u_z \right\rangle + \left\langle \frac{\mathbf{u}^2}{2} \rho u_z \right\rangle - e_{\text{tot}} \langle \rho u_z \rangle, \tag{5.3}$$

where e_{int} is the internal energy per gram, ρ is the density, u_z is the vertical velocity, $\mathbf{u}$ is the velocity vector and e_{tot} is the total energy, defined as

$$e_{\text{tot}} = \frac{\langle \rho e_{\text{int}} + P + \rho \frac{\mathbf{u}^2}{2} \rangle}{\langle \rho \rangle}. \tag{5.4}$$

The first term of Eq. 5.3 is the enthalpy flux, the second term is the kinetic energy

flux and the third term is the mass flux weighted energy flux, which is subtracted in order to correct for any non-zero mass flux arising in the numerical simulations. This definition is identical to the one used in Tremblay et al. [2015b]. Some authors, for instance Cattaneo et al. [1991] and Canuto [2007], have referred to the sum of enthalpy and kinetic energy flux as "convected" flux. In general, convective flux is a synonym for enthalpy flux only. By adding kinetic energy flux, the "convective flux" boundary is moved closer to the Schwarzschild boundary, as kinetic energy is always negative for simulations presented here, which have standard granulation topology of slow and broad upflows surrounded by fast and narrow downflows. Therefore, the calibrated values of the mixing length parameter, which are based on the enthalpy and kinetic flux boundary will be smaller than the calibrated values based on enthalpy flux alone [Kupka et al., 2018; Tremblay et al., 2015b]. As shown by Kupka et al. [2018] the boundary associated with the enthalpy flux indicates where downflows become hotter than their surroundings, which is related to buoyancy, the driving mechanism of convection. Therefore, the definition of convective flux based on enthalpy flux would be crucial in studies of downflows. However, for consistency with previous work of Tremblay et al. [2015b] we use the definition of "convective" flux as defined in Eq. 5.3. In MLT, convective flux refers to enthalpy flux only, as kinetic flux is zero everywhere.

Figs. 5.5 and 5.6 demonstrate the Schwarzschild and flux boundaries, respectively. In the case of helium-dominated atmosphere white dwarfs, at higher effective temperatures there are two convectively-unstable regions related to He I and He II ionization. These zones can either be separated by a convectively stable region or merge into one convection zone depending on the effective temperature. This can also happen for a model at the same effective temperature, but for different definitions of the convection zone as shown in Figs. 5.5 and 5.6, where the model at $T_{\rm eff} \approx 28\,000$ K has two clearly defined and separated convectively-unstable regions in terms of the Schwarzschild criterion, yet in terms of the flux criterion the two helium zones are indistinguishable, since the flux boundary penetrates deeper. At the highest effective temperatures only the He II convection zone remains as He I is fully ionised.

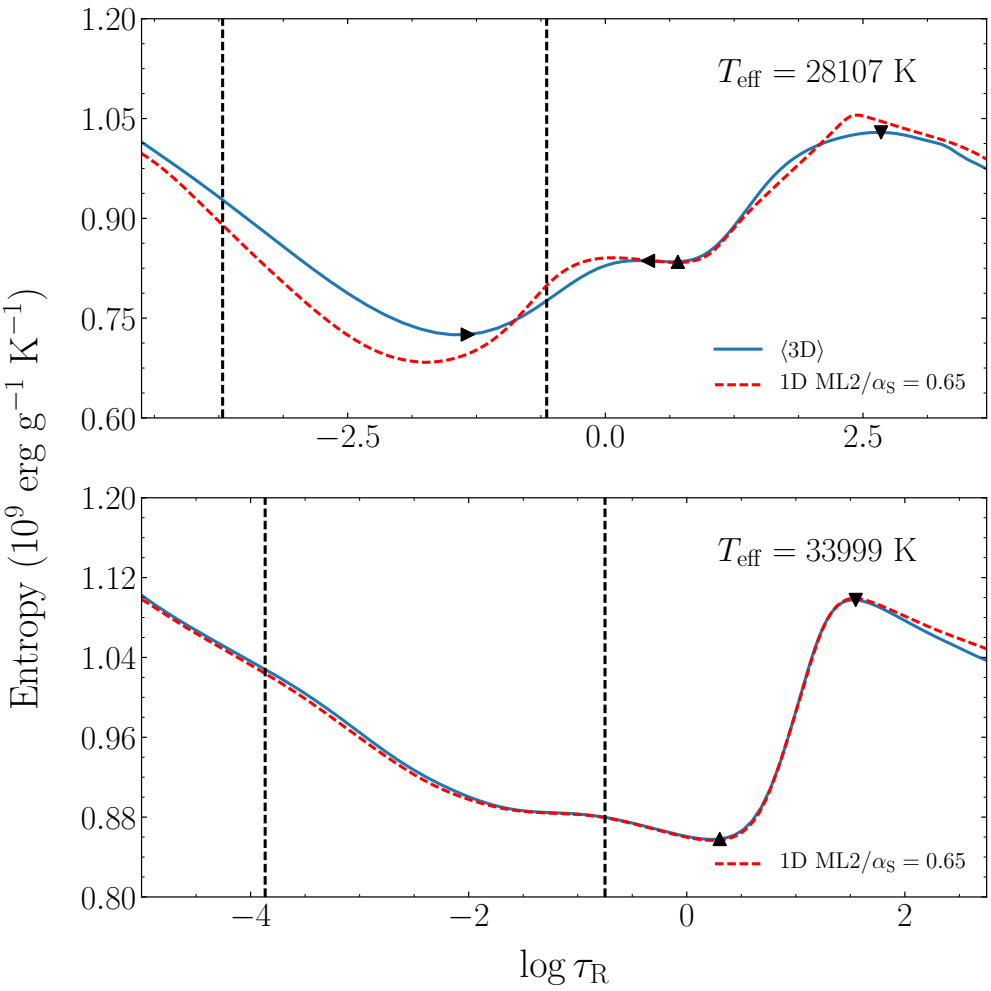

Figure 5.5: Entropy stratifications of two 3D closed bottom models with $\log g = 8.0$ and $\log \mathrm{H/He} = -10.0$ are shown as solid blue lines. The dashed black lines indicate the flux-forming region for wavelengths 3500 Å to 7200 Å, representing the atmosphere of the white dwarf in terms of visible light. 1D models calculated at calibrated ML2/$\alpha_{\rm S}$ are shown as dashed red lines. According to the Schwarzschild criterion, at $T_{\rm eff} \approx 28\,000$ K there are two convectively unstable regions due to He I and He II ionization. The top and bottom of the first convective region is denoted by right- and left-pointing triangles, respectively. The second convective region is indicated by upward- and downward-pointing triangles. The two convective regions are separated by a small region which is convectively stable in terms of the Schwarzschild criterion. At $T_{\rm eff} \approx 34\,000$ K, according to the Schwarzschild criterion there is only one convective region (He II) left, which is denoted by the upward- and downward-pointing triangles.

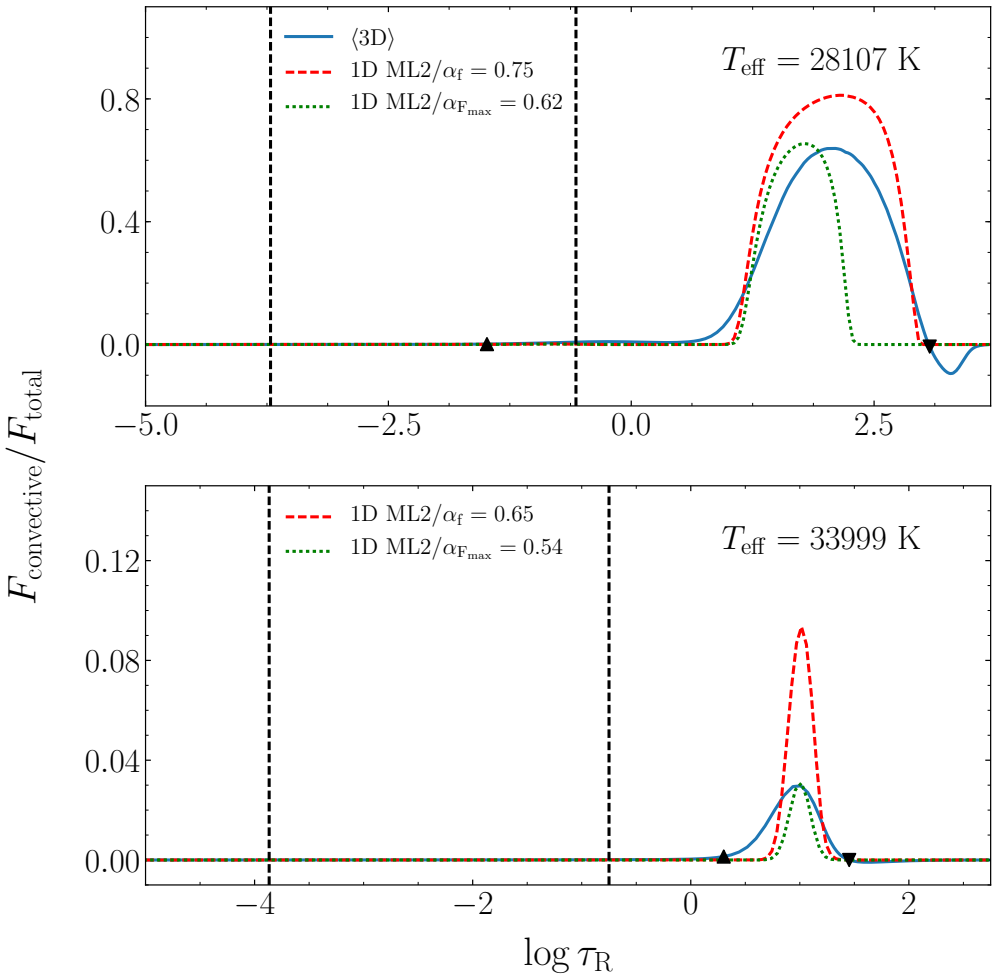

Figure 5.6: The ratio of the convective-to-total flux as a function of the $\log \tau_{\rm R}$ for two 3D closed bottom models with $\log g = 8.0$ and $\log {\rm H/He} = -10.0$ is shown in solid blue. The upward- and downward-pointing triangles denote the top and bottom flux boundaries of the convection zone, respectively. The dashed black lines represent the flux-forming region for wavelengths 3500 Å to 7200 Å. Red dashed lines show the 1D models calculated at calibrated ML2/$\alpha_{\rm f}$, and green dotted lines show 1D models calculated at ML2/$\alpha_{\rm F_{max}}$ (see Sect. 5.5.2). Unlike the Schwarzschild boundary, at $T_{\rm eff} \approx 28\,000$ K the two convectively-unstable regions are inseparable in terms of the flux due to the dynamics of the downdrafts. Beyond the flux boundary, a region of negative flux related to convective overshoot is observed.

In Fig. 5.6 we see a region beyond the flux boundary where the ratio of convective-to-total flux becomes negative. This is the convective overshoot region, where the negative convective flux is due to the convective downflow plumes being warmer than the surroundings [Zahn, 1991; Tremblay et al., 2015b]. This is because

the plumes travel too fast to exchange heat with the surroundings. There is no equivalent region in 1D models and therefore we do not attempt to calibrate the mixing length in any form to describe this region. However, overshoot is important for convective mixing studies. For DA white dwarfs it has been shown that more material can be mixed in the convection zone even beyond the negative flux region (the velocity overshoot region), impacting the mass, abundances, and diffusion times of accreted metals [Freytag et al., 1996; Koester, 2009; Kupka et al., 2018; Cunningham et al., 2019]. This is still unexplored for helium-rich atmospheres.

5.4 The calibration method

5.4.1 Closed bottom models

For the closed bottom 3D models (examples shown in Figs. 5.5 and 5.6) both the Schwarzschild and flux boundaries can be directly probed and the $\langle 3D \rangle$ temperature and pressure values at the two boundaries can be extracted. Similarly, from 1D envelope structures we also have access to the temperature and pressure at the bottom of the 1D Schwarzschild boundary. These quantities are displayed in Figs. 5.7 and 5.8.

For each 3D model with given atmospheric parameters, we interpolate over 1D envelopes with the same atmospheric parameters but varying values of the mixing length parameter, in order to find the value of the mixing length parameter that gives the same temperature and pressure at the base of either the Schwarzschild or the flux boundary of the 3D convection zone. We refer to these calibrated values of the mixing length parameter as ML2/$\alpha_{\rm S}$ and ML2/$\alpha_{\rm f}$ for the Schwarzschild and the flux boundaries, respectively. The calibrated mixing length parameters between temperature and pressure generally agree within ≈ 0.05 even in the most extreme cases such as models with $\log g = 9.0$ shown in Figs. 5.7 and 5.8. Therefore, we take an average of the two values of the mixing length parameter. This gives us an indication of the average temperature gradient in the vicinity of the base of the convection zone.

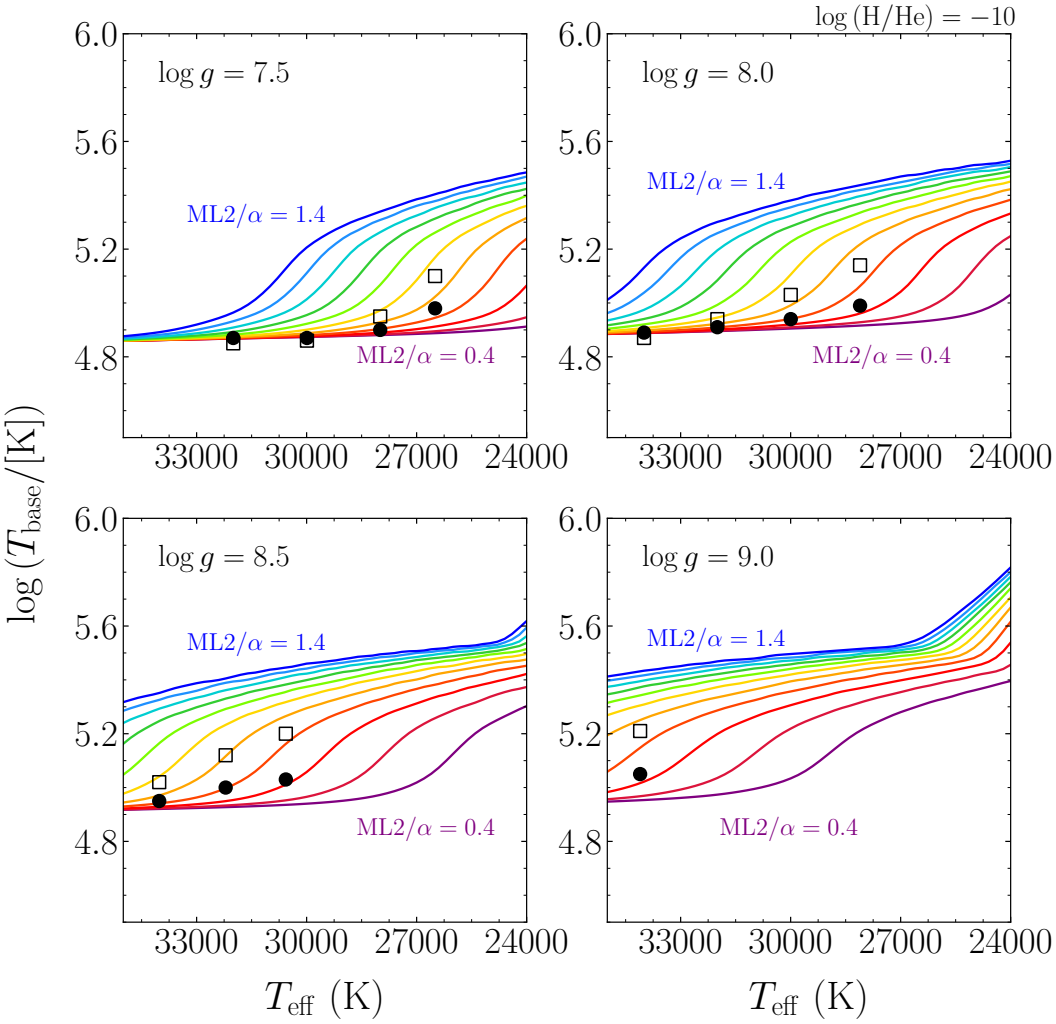

Figure 5.7: The logarithm of the temperature at the base of the convection zone as a function of effective temperature for DB white dwarfs. The solid lines are 1D envelope temperatures at the Schwarzschild boundary for varying values of the mixing length parameter. The value of the mixing length parameter decreases by increments of 0.1 from the dark blue line (ML2/α = 1.4) all the way down to the dark purple line (ML2/α = 0.4). The solid circles represent the temperature of closed bottom 3D models at the Schwarzschild boundary, the open squares are the temperatures of closed bottom 3D models at the flux boundary. The surface gravities are indicated on the plots.

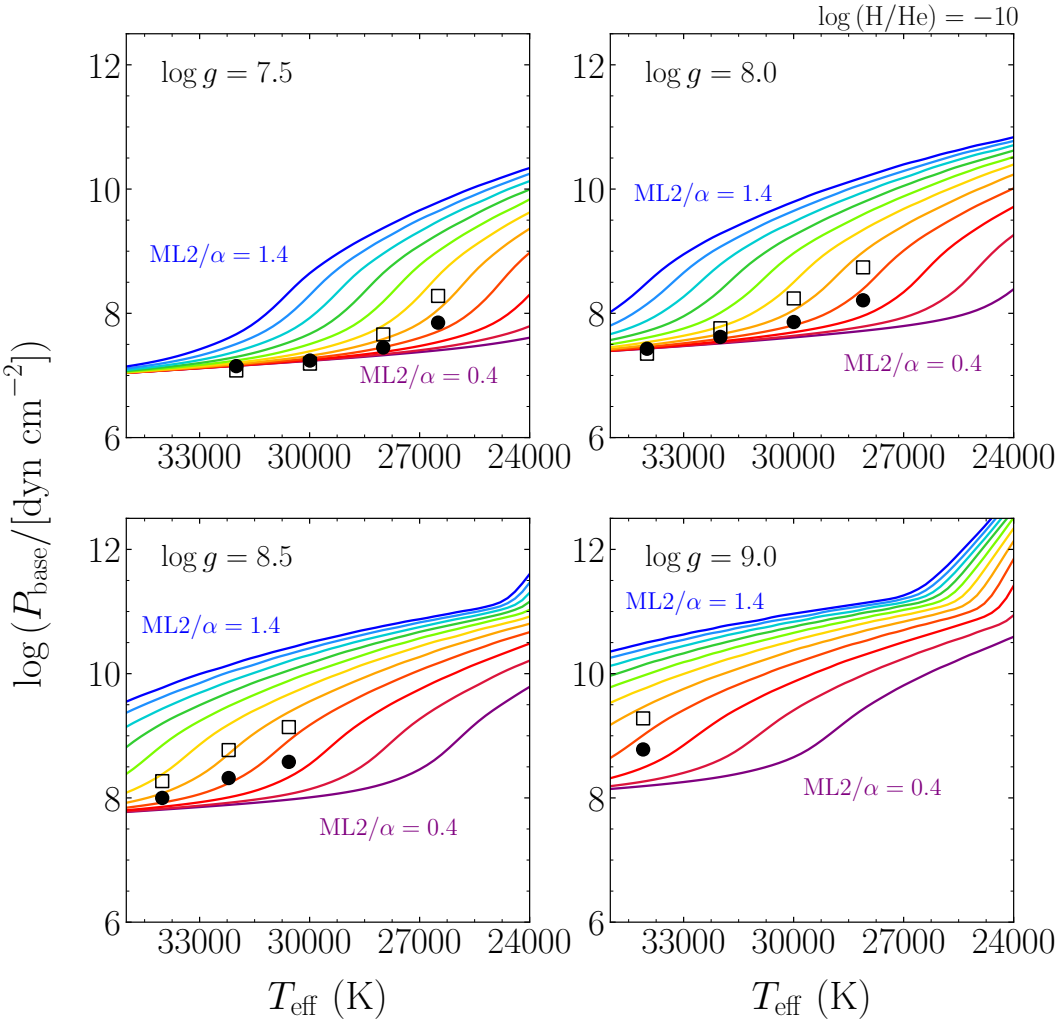

Figure 5.8: Similar to Fig. 5.7 but for pressure at the base of the convection zone.

A larger value of the mixing length parameter means that the convection zone extends deeper into the envelope and thus both the temperature and pressure are larger at the base. As effective temperatures increases for models with $\log g = 7.5$ and 8.0, the envelopes with different values of the mixing length parameter start to converge, yet we can still deduce that the calibrated value of the mixing length parameter in this range of effective temperatures must be on the lower end of our mixing length parameter range, meaning that the convective efficiency is very low.

The blue edge of the DBV instability strip is thought to be related to recombination of the main constituent of the atmosphere, which also causes convection to set in. Figs. 5.7 and 5.8 show that our 3D models indicate that a lower value of the mixing length parameter (around 0.7-0.8) than 1.25 (the value used by Van Grootel

et al. [2017] to determine the theoretical blue edge) best represents the base of the convection zone both for Schwarzschild and flux boundaries. In general, with the lowering of the value of the mixing length parameter, convection will occur later in the white dwarf's evolution (i.e. at lower effective temperatures). The theoretical location of the blue edge of the instability strip should therefore be at a lower effective temperature than predicted by current studies.

With closed bottom models we can also directly calculate $\log(M_{\rm CVZ}/M_{\rm tot})$ for either convection zone boundary. In Figs. 5.3 and 5.4 we compare 3D $\log(M_{\rm CVZ}/M_{\rm tot})$ to the predictions of 1D envelopes. Unlike the DA case [Tremblay et al., 2015b] we do not find that mass-calibrated values of the mixing length parameter are similar to the temperature- and pressure-calibrated values of the mixing length parameter. As the mass is calculated independently of either temperature or pressure, a disagreement is not unexpected since 1D models cannot reproduce all of the dynamic quantities of 3D models. This is clearly shown in Figs. 5.5 and 5.6, where we plot $\langle$3D$\rangle$ structures and corresponding 1D atmospheric models of Bergeron et al. [2011] calculated at calibrated ML2/$\alpha_{\rm S}$ and ML2/$\alpha_{\rm f}$ values, respectively. As expected, the $\langle$3D$\rangle$ and 1D structures agree in the vicinity of either boundary, but the overall 1D and $\langle$3D$\rangle$ structures do not agree well. For all closed bottom models at $\log g = 7.5$ and 8.0, the masses included in the 3D convection zones diverge off the 1D envelope predictions, such that they are much smaller than what is possible to achieve in 1D within our range of mixing length parameters.

In Figs. 5.3 and 5.4 the flux and the Schwarzschild boundary reversals are observed, where the flux boundary is now inside the Schwarzschild boundary. This is also observed in 3D DA models. As mentioned previously, the reversal is due to kinetic energy flux. If the kinetic energy is neglected then the boundary reversal is not observed [Kupka et al., 2018; Tremblay et al., 2015b]. Such a reversal does not occur in 1D models, as kinetic energy flux is not considered.

For studies in need of the physical conditions near the base of the convection zone, the calibrations shown in Figs 5.7 and 5.8 and listed in Tabs. B.13 to B.18 of Appendix B should be used. The masses listed in those tables are the 1D convection zone masses found from 1D envelopes calculated at 3D calibrated values of the mixing length parameter. For studies where such approximations are not adequate, the direct use of 3D structures are beneficial.

5.4.2 Open bottom models

For open bottom models we are unable to probe the bottom of the convection zone as our simulations are not deep enough. We can, however, exploit the fact that

in 3D models a fraction of upflows from the bottom of the deep convection zone retain their adiabatic entropy almost all the way up to the observable atmospheric layers by not interacting with neighbouring downflows via heat exchange [Stein and Nordlund, 1989]. Therefore, none of the plumes will have entropy higher than this, but they can lose entropy due to interactions with surroundings. This means that the spatially- and temporally-resolved entropy has a plateau corresponding to the adiabatic entropy value and it can be used to calibrate the mixing length parameter [Steffen, 1993; Ludwig et al., 1999]. Example entropy plateaus are shown in Fig. 5.9 for $\log \mathrm{H/He} = -10.0$ and $\log \mathrm{H/He} = -2.0$ models, where we also plot the temporally- and horizontally-averaged entropy stratifications. The averaged entropy is smaller than the adiabatic entropy because it also considers the small entropy of the downflows. For CO^{5}BOLD the adiabatic entropy value is the inflowing entropy input parameter and an entropy plateau is observed in all open bottom simulations.

For each 3D model with given atmospheric parameters, we interpolate over the 1D envelopes with different values of mixing length parameter and with the same atmospheric parameters to find the 1D entropy at the bottom of the Schwarzschild boundary that best matches the 3D adiabatic entropy. We show this in Fig. 5.2. The entropy of closed bottom models is also shown, but for these models we do not use the entropy to calibrate. This is because we have already calibrated the mixing length parameter directly in Sec. 5.4.1 and generally for closed bottom models the upflows are not adiabatic in any portion of the convection zone.

The adiabatic entropy value is for the 3D Schwarzschild boundary only. We cannot access the flux boundary for open bottom models. Instead, we use the results from closed bottom models to estimate the value of the mixing length parameter that best represents the flux boundary for open bottom models. For closed bottom models that do not show the flux and Schwarzschild boundary reversal we find the relation ML2/α_f= 1.17 ML2/α_S with a standard deviation of around 3%. A similar result of ML2/α_f= 1.16 ML2/α_S with a standard deviation of around 3% was found for 3D DA models [Tremblay et al., 2015b].

In Figs. 5.3 and 5.4 we show the $\log\left(M_\mathrm{CVZ}/M_\mathrm{tot}\right)$ value for both open and closed bottom models with $\log \mathrm{H/He} = -10.0$ and -2.0, respectively. Unlike the closed bottom case, we cannot directly access the bottom of either convection zone boundary for open bottom models. Thus, the masses for open bottom 3D models are extracted from the 1D envelopes with value of the mixing length parameter that best matches the 3D adiabatic entropy.

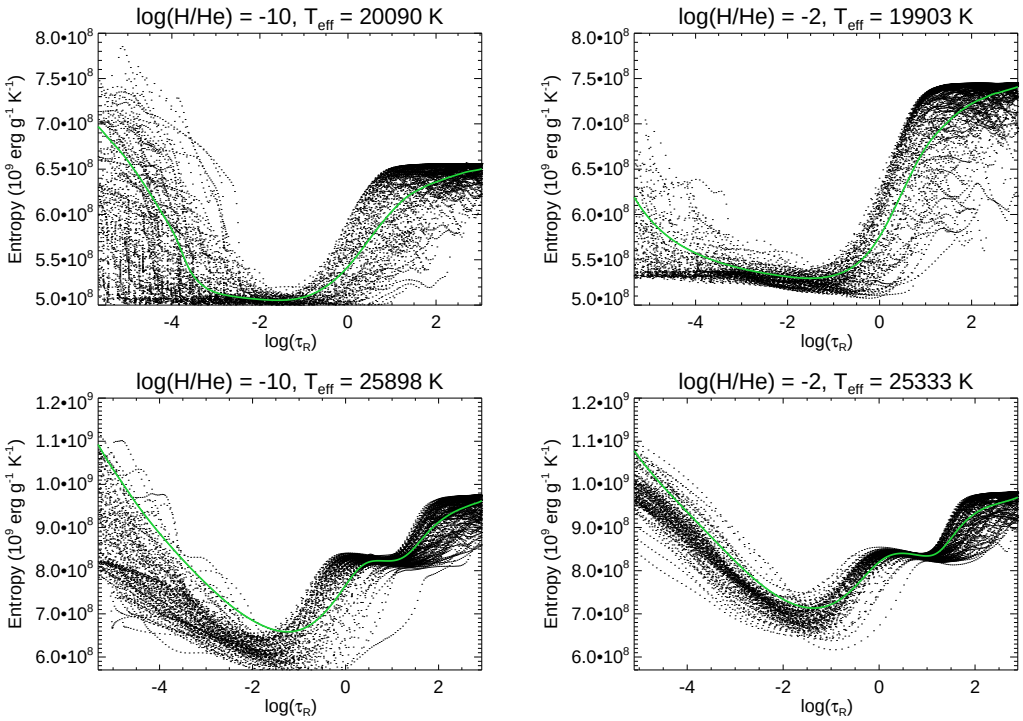

Figure 5.9: The spatially- and temporally- resolved entropy for 3D open bottom models with $\log g = 8.0$. The top two plots show the entropy stratification when only the He I convection is present, whereas the bottom two panels show models with both He I and He II convection zones. In green we plot the averaged entropy over constant geometric depth and time. Although the average entropy does not reach the adiabatic value near the bottom of the simulation, it is clear that the spatially- and temporally- resolved entropy has a plateau at deeper layers, which corresponds to the inflowing entropy, an input parameter of our 3D models.

As mentioned earlier and shown in Fig. 5.2, at the lowest effective temperatures the envelopes with different values of mixing length parameter converge to the same solution as convection becomes adiabatic and insensitive to the mixing length parameter even in the upper atmosphere. In these cases, the derived mass fraction does not change significantly between the different values of the mixing length parameter. Therefore, we propose not to interpolate for the best matching mixing length parameter, but to set it to 1.0 for both Schwarzschild and flux boundaries.

5.5 Discussion

The calibrated values of the mixing length parameter are shown in Figs. 5.10 and 5.11 for the Schwarzschild and flux boundaries, respectively. They are also given in Appendix B. In all cases, the values of the mixing length parameter are smaller than what is often used in evolutionary models, i.e. ML2/α = 1.25. This means that 3D models predict lower convective efficiencies and smaller convection zone sizes. Given that the value of 1.25 is based on matching observed and model spectra and therefore describes the convective efficiency in the photosphere, it is not unexpected that it is different to the convective efficiency at the bottom of the convection zone. Interestingly, the mean convective efficiency for DB/DBA white dwarfs is very similar, or only slightly larger, to that of DA stars [Tremblay et al., 2015b]. This indicates that convective efficiency at the bottom of the convection zone is similar for DA and DB/DBA white dwarfs.

The plateaus observed in Figs. 5.10 and 5.11 for $T_{\rm eff} \lesssim 18\,000$ K are artificial. They are the consequence of fixing the value of ML2/$\alpha_{\rm S}$ = ML2/$\alpha_{\rm f}$= 1.0 for effective temperatures where the structures become insensitive to the mixing length parameter. A similar effect can be observed for $T_{\rm eff} \gtrsim 30\,000$ K, where the calibration is forced to values of 0.65 for both ML2/$\alpha_{\rm S}$ and ML2/$\alpha_{\rm f}$, as none of the 1D values of the mixing length parameter can reproduce the boundaries of the 3D convection zone. Since the convective zone is in any case very small and inefficient in this regime, the fixed value may not be a concern for some applications. If on the other hand, detailed convective properties are required, it is more appropriate to directly use 3D models that include velocity overshoot (see Sect. 5.5.3).

The peaks observed in Figs. 5.10 and 5.11 which seem to shift to higher effective temperatures for higher surface gravities, are associated with the knee-like feature of the 1D envelopes seen in Figs. 5.2, 5.3 and 5.4, which we suggest is related to the disappearance of the He II convection zone as the white dwarf evolves to lower effective temperature. This transition is different in 3D, potentially because of the non-local coupling of the two convection zones. The knee-feature also means that the calibration of mixing length parameter is more sensitive in that region compared to other regions.

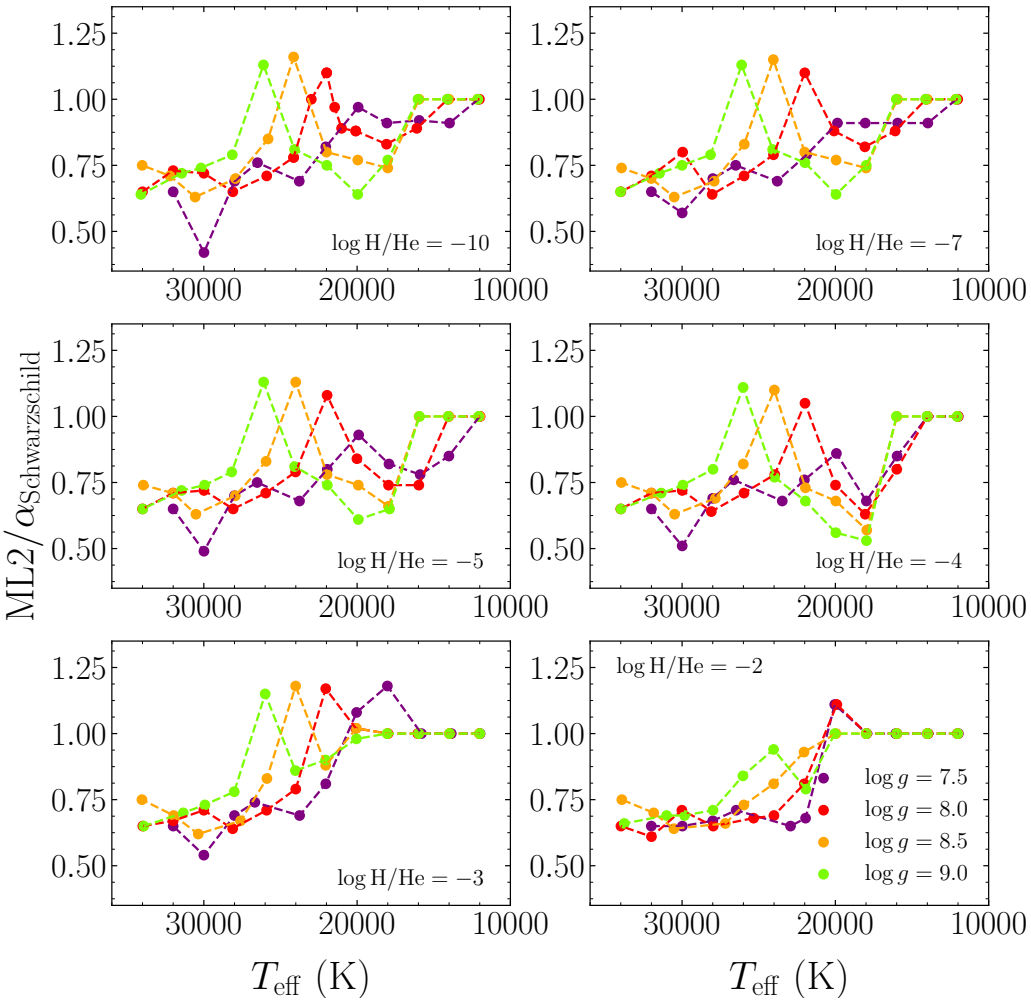

Figure 5.10: The calibrated mixing length parameter based on the Schwarzschild boundary is plotted as solid colour points which are connected for clarity for the same surface gravity. The hydrogen abundance is indicated on each panel.

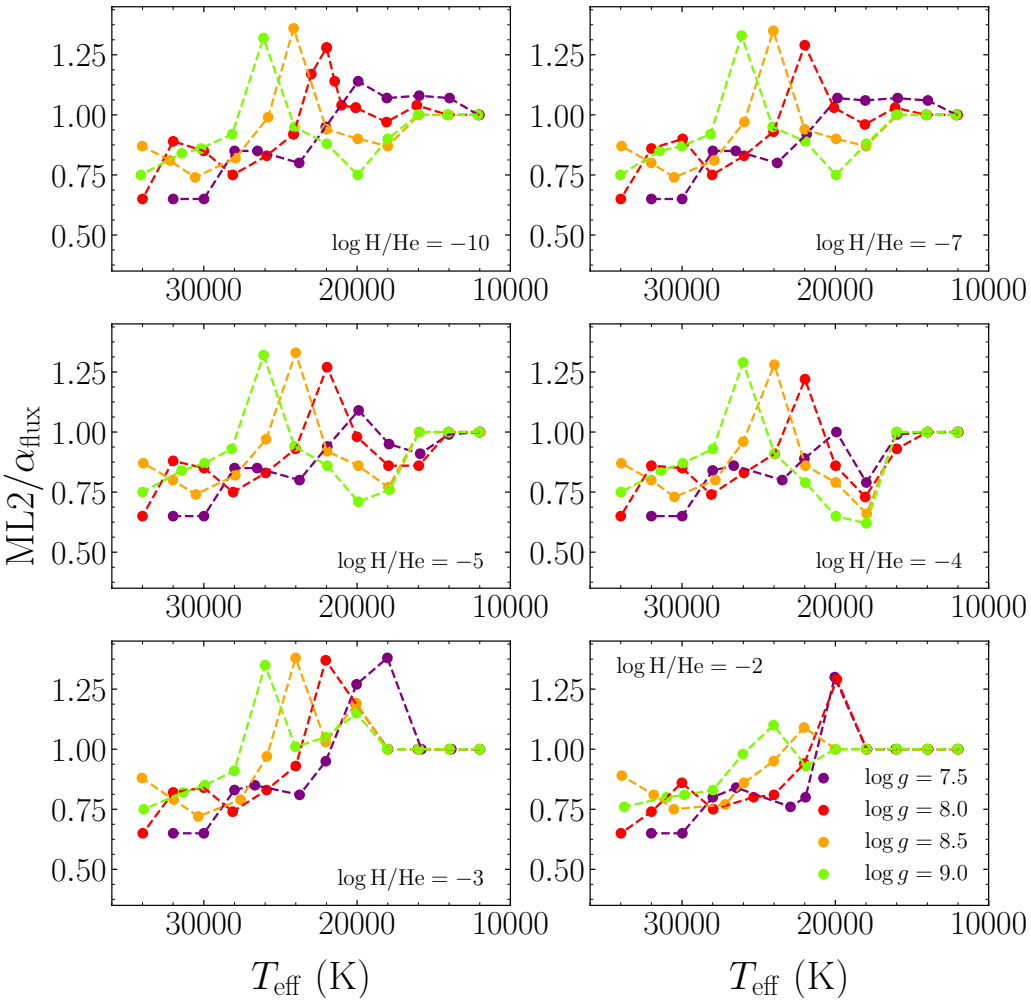

Figure 5.11: Same as Fig. 5.10 but for the flux boundary.

5.5.1 Calibration of the entropy jump

Studies such as Magic et al. [2015] have performed calibrations of the mixing length parameter for solar-like stars based on the entropy jump associated with superadiabatic convection. Examples of such entropy jumps can be seen in Figs. 5.5 and 5.9 for closed and open bottom models, respectively. In their calibration, Magic et al. [2015] define the jump as the difference between the constant entropy value of the adiabatic convection zone and the entropy minimum for both 1D and 3D models. We use a similar method to investigate more clearly the variations of the mixing length parameter as a function of effective temperature.

To perform the calibration we do not use the evolutionary models presented

in Sec. 5.2.2. Instead, we use the 1D atmospheric models of Bergeron et al. [2011]. This grid of models spans the same range of atmospheric parameters as our 3D and 1D envelope grids, but also values of the mixing length parameter in the range $0.5 \leq \mathrm{ML2}/\alpha \leq 1.5$ in steps of 0.25. We define the entropy jump, s_{jump}, as

$$s_{\mathrm{jump}} = s(\log \tau_{\mathrm{R}} = 2) - s_{\mathrm{min}}, \tag{5.5}$$

where $s(\log \tau_{\mathrm{R}} = 2)$ is the entropy at $\log \tau_{\mathrm{R}} = 2$ and s_{min} is the minimum entropy value. In the 3D case, the entropy stratification is temporally- and spatially-averaged, with the spatial average being performed over constant geometric height as before. We calculate s_{jump} both for the 3D atmospheric models, and for 1D atmospheric models calculated at different values of the mixing length parameter. We then find the value of the mixing length parameter, which we refer to as $\mathrm{ML2}/\alpha_{\mathrm{s_{jump}}}$, that best represents the given $\langle \mathrm{3D} \rangle$ entropy jump. In late-type stars, the entropy jump was found to decrease for increasing values of the mixing length parameter [Magic et al., 2015]. This is because as convection becomes more efficient, smaller temperature gradients in the superadiabatic layers are needed to transport the same flux [Sonoi et al., 2019]. This relation holds for DB and DBA 1D models where the entropy minimum is located at the top of the He I convection zone (see Fig. 5.9 for example). It breaks down when the He I convection zone disappears or when the entropy minimum moves to the top of the He II convection zone. This happens for the majority of 3D closed bottom models, and therefore we only perform $\mathrm{ML2}/\alpha_{\mathrm{s_{jump}}}$ calibration for 3D open bottom models.

We show the $\mathrm{ML2}/\alpha_{\mathrm{s_{jump}}}$ values for DB white dwarfs in Fig. 5.12. Similar results were found for DBA white dwarfs. For all surface gravities apart from 7.5, the peaks observed in $\mathrm{ML2}/\alpha_{\mathrm{s_{jump}}}$ are at the same effective temperatures as the peaks observed for $\mathrm{ML2}/\alpha_{\mathrm{S}}$ and $\mathrm{ML2}/\alpha_{\mathrm{f}}$. By looking at the structures directly, the peaks in Figs. 5.10 and 5.11 are associated with the disappearance of the second-hump in the entropy profile due to He II convection zone as the white dwarf cools to lower effective temperature. Examples of double peaked entropy profiles are shown in Fig. 5.9.

For atmospheric parameters where convection is sensitive to the value of the mixing length parameter (e.g. the calibrated value of the mixing length parameter is not fixed in Figs. 5.10 and 5.11), we find reasonable agreement between the $\mathrm{ML2}/\alpha_{\mathrm{s_{jump}}}$, $\mathrm{ML2}/\alpha_{\mathrm{S}}$ and $\mathrm{ML2}/\alpha_{\mathrm{f}}$ calibrations.

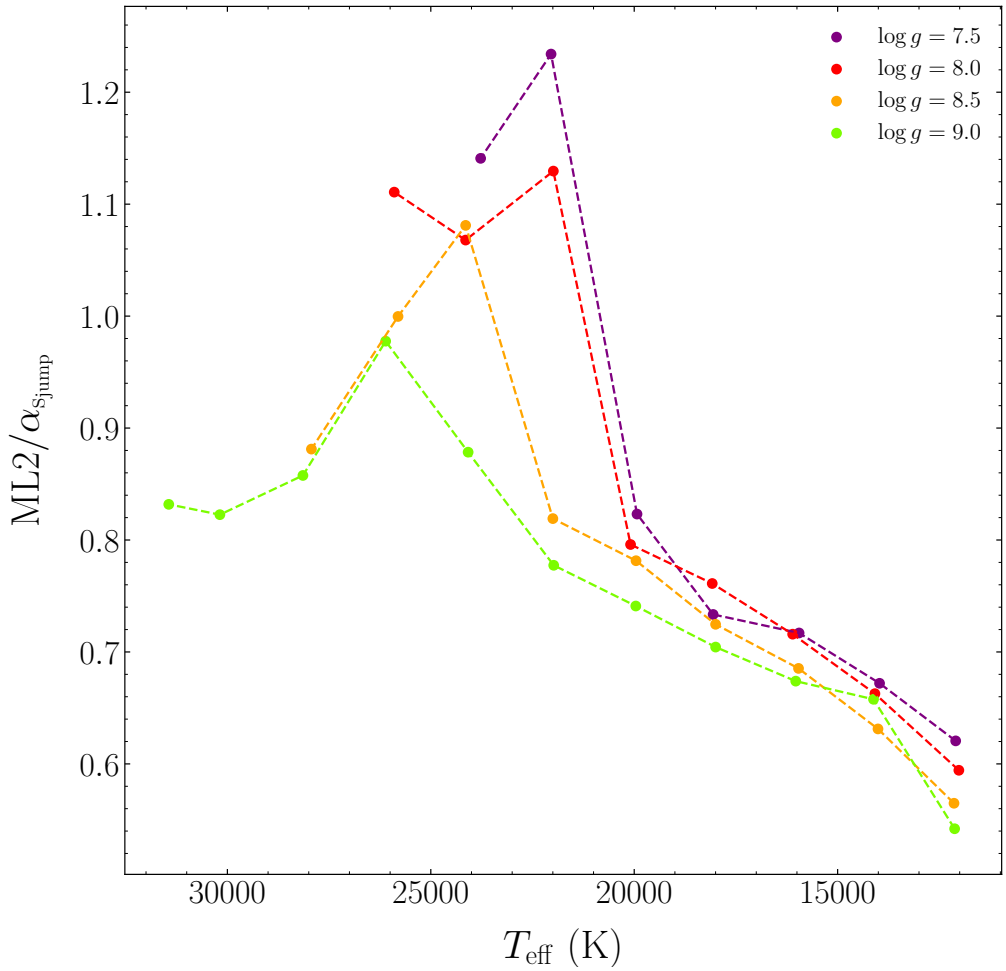

Figure 5.12: The calibrated mixing length parameter based on the entropy jump for open bottom 3D DB models. The solid colour points represent the ML2/$\alpha_{\mathrm{s_{jump}}}$ values and are connected for clarity based on their surface gravity.

Magic et al. [2015] found that their values of the mixing length parameter based on the entropy jump were higher than the values of the mixing length parameter based on the adiabatic entropy (ML2/α_{S}). They attribute this to the 1D entropy minimum being lower than the $\langle$3D$\rangle$ entropy minimum, which is also the case for our models with lower effective temperatures. This explains why at low effective temperatures we find ML2/α_{S} and ML2/α_{f} values that are larger than the value of ML2/$\alpha_{\mathrm{s_{jump}}}$ (for example, $T_{\mathrm{eff}} \lesssim 20\,000$ K for DB models with $\log g = 8.0$).

From the studies of ML2/$\alpha_{\mathrm{s_{jump}}}$, ML2/$\alpha_{\mathrm{S}}$ and ML2/α_{f} it is apparent that the peaks in values of the mixing length parameter are observed close to the red edge of the DBV instability region. This means that in terms of the 3D picture, the mixing

length changes quite rapidly in the region where pulsations are empirically observed to stop. As current DBV studies use ML2/$\alpha = 1.25$, and the peak is closer to this value than the calibrated values of the mixing length parameter at other effective temperatures, we expect that our calibration will not significantly alter the current theoretical DBV studies at the red edge of the instability strip.

5.5.2 Calibration of the maximum convective flux

An alternative way to calibrate the values of mixing length parameter for closed bottom models has been proposed by Tremblay et al. [2015b]. The calibration is based on the maximum value of the convective-to-total flux. This better represents the total amount of energy transported by convection as shown for DA white dwarfs by Tremblay et al. [2015b]. We perform this calibration for DB and DBA closed bottom models using the 1D atmospheric models of Bergeron et al. [2011], i.e. same grid that was used in Sec. 5.5.1, but with additional grids at ML2/$\alpha = 0.55$, 0.60, 0.65 and 0.70 as convective flux changes significantly with the value of the mixing length parameter. Our results are shown in Fig. 5.13. In Fig. 5.6, we confirm that ML2/$\alpha_{\mathrm{F_{max}}}$ calibration does indeed better reproduce the overall shape of DB (and DBA, although not shown) convection zones.

Overall, the ML2/$\alpha_{\mathrm{F_{max}}}$ calibrated values are similar to the ML2/α_{S} and ML2/α_{f} calibration. For most models we find inefficient convection resulting in small convection zones. Montgomery and Kupka [2004] performed an equivalent calibration of the maximum convective flux using their 1D non-local envelope models of DB white dwarfs. They found ML2/$\alpha \approx 0.5$ for DB models with $\log g = 8.0$ and 28 000 K $\leq T_{\mathrm{eff}} \leq$ 33 000 K, whereas we find $0.64 \gtrsim$ ML2/$\alpha \gtrsim 0.5$ for the same atmospheric parameter range. Both studies therefore suggest that convection is less efficient than what is currently assumed. When comparing DA and DB white dwarfs in the regime of very inefficient convection (closed bottom models in our case), Montgomery and Kupka [2004] found that for given $F_{\mathrm{convective}}/F_{\mathrm{total}}$, DB stars have lower values of ML2/$\alpha_{\mathrm{F_{max}}}$, but larger convection zone sizes. They attribute this to the He II convection zone being deeper than the H I counterpart, allowing the same amount of convective flux to be transported more efficiently and therefore with a smaller value of the mixing length parameter. Comparing our results to the 3D DA calibration of Tremblay et al. [2015b], we also find that DB white dwarfs have smaller ML2/$\alpha_{\mathrm{F_{max}}}$ values and larger convection zone sizes, in agreement with the findings of Montgomery and Kupka [2004].

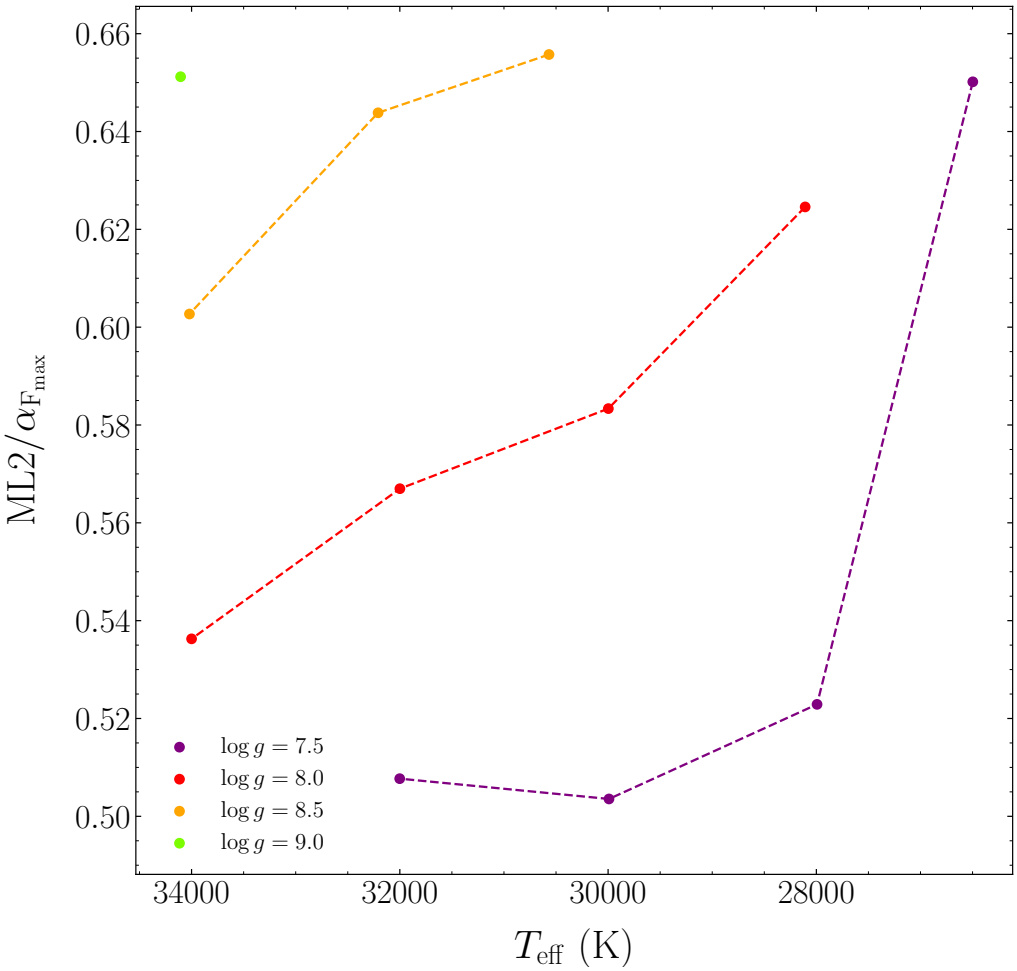

Figure 5.13: Same as Fig. 5.12, but for calibration of the mixing length parameter based on the maximum convective flux for 3D closed bottom models.

5.5.3 Calibration of velocities

Unlike in 1D models, in 3D simulations we expect there to be significant macroscopic diffusion at the bottom of the convection zone caused by momenta of downflows. We refer to this region as the velocity overshoot region, which overlaps with the flux overshoot region shown in Fig. 5.6 where negative flux is found. The velocity overshoot both includes and extends beyond the flux overshoot region. The overshoot region can be thought of as an extension to the more traditional convection zones discussed in this chapter, especially for studies of metal diffusion in the atmospheres of white dwarfs. If included, it would mean larger convection

zones than presented in this chapter. In Fig. 5.14 we compare the velocities of our ⟨3D⟩ and 1D structures. In 1D the convective velocities are non-zero only inside the Schwarzschild convection zone, whereas in 3D, the velocities are significant even beyond the Schwarzschild and flux boundaries. As long as these convective velocities result in a macroscopic diffusion process that is more efficient than microscopic diffusion, metals are expected to be fully mixed in the convection zone rather than diffuse out of it. Convective overshoot could also significantly enhance the dredge-up of carbon from the interior [Dufour et al., 2005] if the size of the superficial helium layer is small enough to allow convection to reach the underlying carbon layer.

Macroscopic diffusion can only be studied in 3D models with closed bottoms. This is because macroscopic diffusion has to be studied directly and therefore both the bottom of the convection zone and the layers underneath are needed. Yet, it is expected that all 3D models, including those with open bottoms, will have overshoot both at the bottom and top of their convection zones, due to the dynamics of the convective flows. In order to study velocity overshoot for effective temperatures at which we currently only have open bottom models, a new grid of deep closed bottom models would have to be calculated.

Cunningham et al. [2019] have recently performed an in-depth study of overshoot in 3D DA closed models, finding that the mass over which metals can mix can be as much as 3 dex larger than currently used. Such a study for 3D DB and DBA models is beyond the scope of the current paper. As such, we do not attempt to perform any calibration of the mixing length parameter based on velocities.

5.5.4 Impact of metals on size of the convection zone

In order to test the effect of metals on the size of the convection zone, we calculate two sets of 3D models with and without metals at two select values of effective temperature. We use the 1D atmospheric code of Koester [2010] to calculate the input equations of state and opacity tables. When including metals, we use the metal composition and abundances of SDSS J073842.56+183509.06 determined by Dufour et al. [2012], as well as their determined hydrogen abundance of $\log \mathrm{H/He} = -5.73 \pm 0.17$. We base our atmospheric composition on this white dwarf because it is one of the most polluted objects with 14 elements heavier than helium present in its atmosphere. Our aim is not to replicate exactly the atmospheric parameters determined by Dufour et al. [2012] but rather to study the effect of strong metal pollution on 3D models.

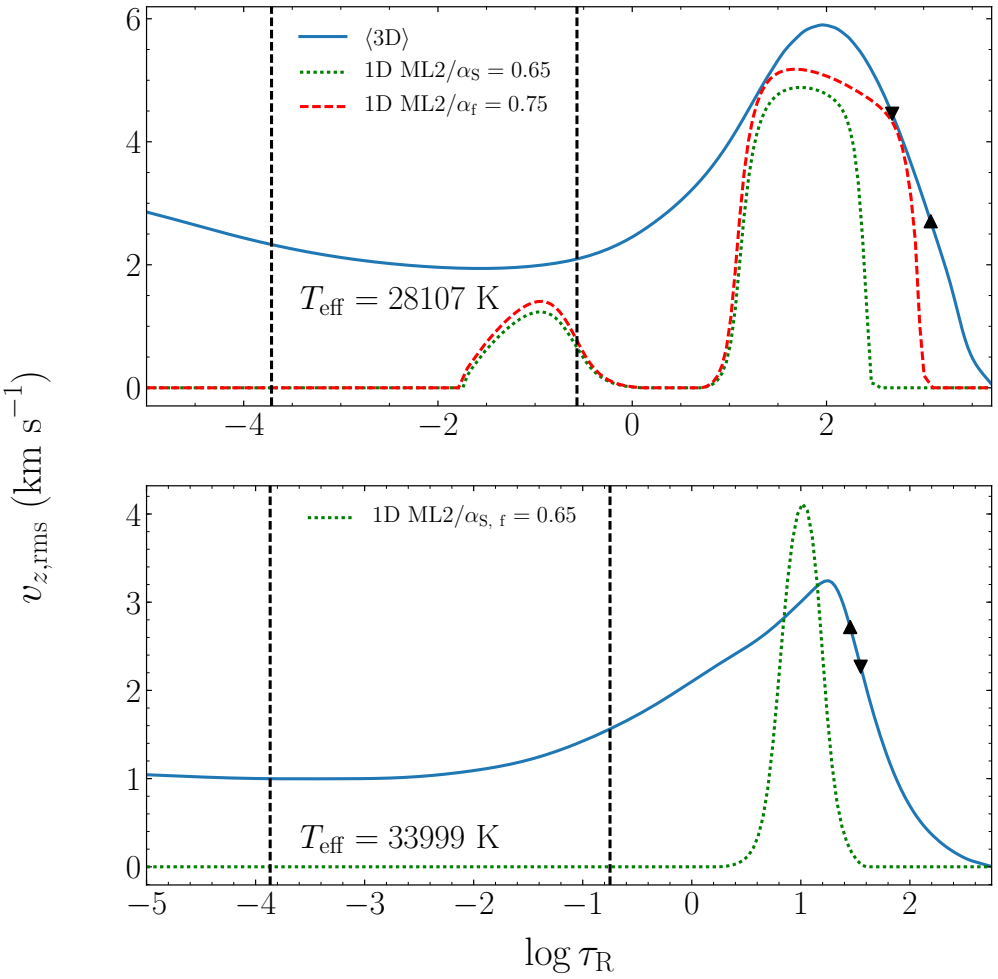

Figure 5.14: The vertical root mean square velocity as a function of $\log \tau_R$ at two different effective temperatures for DB models with $\log g = 8.0$. The ⟨3D⟩ $v_{z,\rm rms}$ is shown in solid blue. The 1D models with ML2/α = ML2/α_S and ML2/α_f are shown as dotted green and red dashed lines, respectively. The bottom of the Schwarzschild and flux boundaries are shown as downward- and upward-pointing triangles. The dashed black lines indicate the top and bottom of the optical light forming region. The 1D structures are unable to reproduce ⟨3D⟩ velocities especially outside the convective regions. In the upper layers ($\log \tau_R <$ -3), the ⟨3D⟩ convective velocities have an important contribution from waves in the simulation.

We start our models from two computed simulations of the 3D DBA grid with $\log$ H/He $= -5.0$, $\log g = 8.0$ and $T_{\rm eff} \approx 14\,000$ K and $\approx 20\,000$ K. As hydrogen abundance is ultimately controlled by the input tables, the hydrogen abundance of the starting model does not matter, but for convergence it is desirable to start with the closest available hydrogen abundance. Although, a value of $\log g = 8.4 \pm 0.2$ was

determined by Dufour et al. [2012], we instead use $\log g = 8.0$, more in line with the recent determination of $\log g = 8.05 \pm 0.15$ by Gentile Fusillo et al. [2019a,b].

As the effective temperature is only recovered after the model is run, for each set of models we tried to achieve an agreement of around 100 K between the models with and without metals. We find that including our selected metal-rich composition in a 3D model decreases the effective temperature by around 1 500 K given the specified inflowing entropy at the bottom boundary (using the same entropy zero point). Recall, that the inflowing entropy at the bottom boundary sets the resulting effective temperature of the model for a given EOS and opacity table. For example, the effective temperature of one of the metal-poor models is 13 975 K, whereas the effective temperature of the metal-rich version is 12 497 K with the same physical conditions at the bottom, i.e. the same entropy value. In order to get an agreement of $\approx$ 100 K between metal-rich and metal-poor models, we had to increase the entropy of the inflowing material at the bottom boundary for the metal-rich model. From Figs. 5.2 and 5.3 it is clear that higher inflowing entropy means higher effective temperature and smaller convection zone. Therefore, we can speculate that with the inclusion of metals, the size of the convection zone becomes smaller for the same effective temperature. This is not unexpected, since similarly to hydrogen, metals increase the total opacity.

To find the mass of the convection zone we utilise the envelope code described in Koester and Kepler [2015] with our calibrated mixing length parameter. The code takes the last point in a given $\langle$3D$\rangle$ atmospheric structure as a starting point for calculating the corresponding envelope. The envelope code is 1D and therefore depends on the mixing length theory. As per our calibration based on 3D models with $\log \mathrm{H/He} = -5.0$, $\log g = 8.0$, we use ML2/$\alpha = 1.0$ and 0.80 for $T_{\mathrm{eff}} \approx 14\,000$ K and 20 000 K models, respectively. We do not perform any additional mixing length parameter calibration beyond what has been described in previous sections. The total mass of the white dwarf is assumed to be $0.59\mathrm{M}_{\odot}$ with a radius of $0.0127\mathrm{R}_{\odot}$. The Saumon et al. [1995] equation of state is used and only hydrogen and helium atoms are considered. Metals are ignored as they do not impact the envelope structure as long as they are trace species. Therefore, the difference in the mass of the convection zone between the metal-rich and metal-poor models arises from the fact that the 3D atmospheric structures are different (see Fig. 5.15). In Tab. 5.1 we show the change in the mass of the convection zone with the addition of metals. We find that in the $T_{\mathrm{eff}} \approx 14\,000$ K case, the mass of the convection zone decreases by a factor of 2 (or 0.31 dex) when metals are included. For the $T_{\mathrm{eff}} \approx 20\,000$ K case, a similar change of 0.45 dex is observed. In both cases it would mean that for the

same metal abundance observed, the total mass of metals present would be smaller using the appropriate metal-rich model atmosphere. For $T_{\rm eff} \approx 14\,000$ K, the change in the mass of the convection zone with the inclusion of metals can be mimicked by increasing the hydrogen abundance from $\log {\rm H/He} = -5.0$ to -3.0. Similarly, at $T_{\rm eff} \approx 20\,000$ K, the increase of $\log {\rm H/He}$ from -5.0 to somewhere between -3.0 and -2.0 gives a change in mass similar to the effect of metals.

In terms of the 3D picture, the effect of metals on the size of the convection zone is moderate, especially since SDSS J073842.56+183509.06 is one of the most heavily polluted white dwarfs. However, the effect of metals on spectroscopic 3D corrections for effective temperature and surface gravity are still to be explored. Fig. 5.15 suggests that changes in the structure of the light forming layers are important especially at lower Teff.

Table 5.1: Change in the convection zone mass from addition of metals (DBAZ) in a helium-rich DBA white dwarf. The DBAZ models use the metal abundances of SDSS J073842.56+183509.06 determined by Dufour et al. [2012].

$\log g$	$T_{\rm eff}$ (K)	Change in convection zone mass (dex)
8.0	$\approx 14\,000$ K	-0.31
8.0	$\approx 20\,000$ K	-0.45

5.6 Summary

With 285 3D CO^{5}BOLD atmospheric models of DB and DBA white dwarfs, we have calibrated the mixing length parameter for the use of 1D envelope and evolutionary models. Our results are applicable for studies in need of convection zone sizes, for example for asteroseismological and remnant planetary systems analyses.

As the nature of the convection zone boundaries is more complex in 3D than in 1D, two definitions of the boundary were used for calibration, the Schwarzschild and flux boundaries. Overall, values of both ML2/$\alpha_{\rm S}$ or ML2/$\alpha_{\rm f}$ are lower than what is typically used in envelope and evolutionary models, meaning that convection is less efficient in 3D models. On average, for models with $\log g = 8.0$ and $18\,000$ K $\lesssim T_{\rm eff} \lesssim 30\,000$ K, we find ML2/$\alpha_{\rm S} \approx 0.80$ and ML2/$\alpha_{\rm f} \approx 0.9$. This is similar to mixing length parameters calibrated for 3D DA white dwarfs [Tremblay et al., 2015b].

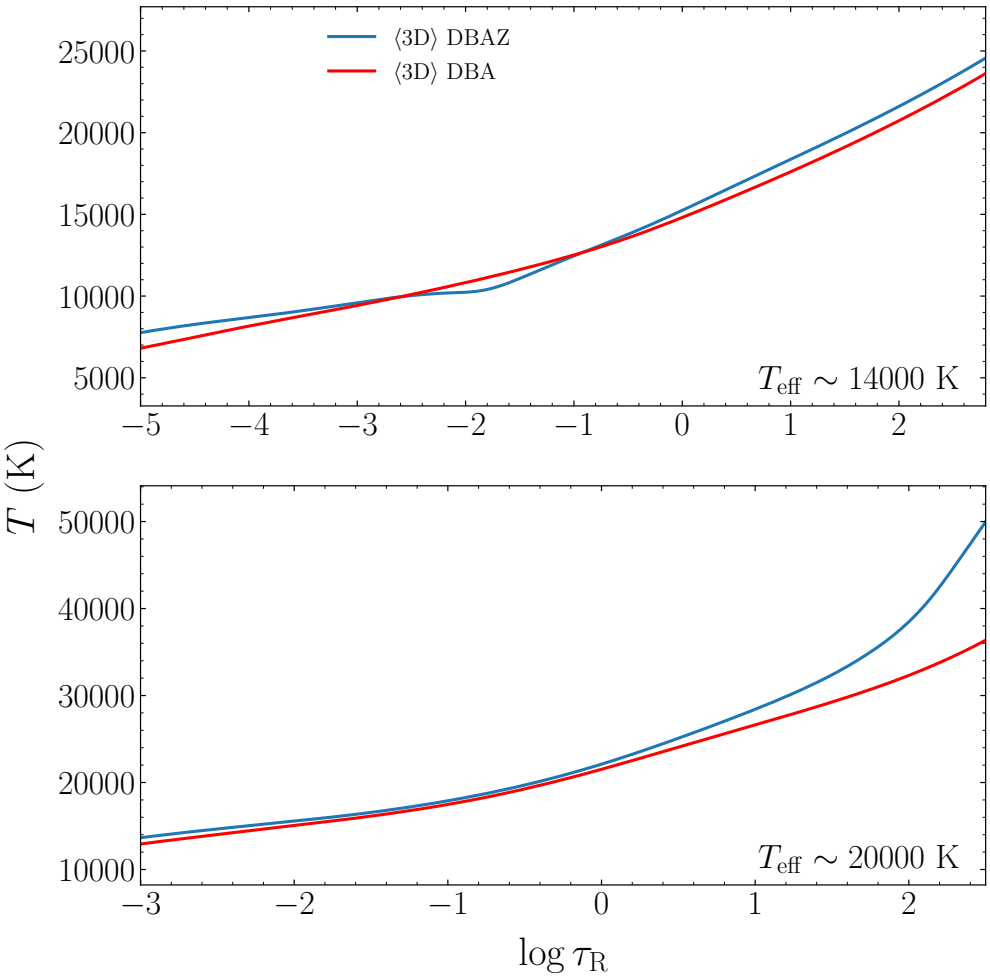

Figure 5.15: Temperature stratification of 3D models with and without metals at two different effective temperatures. The ⟨3D⟩ structures for 3D DBAZ models are shown in solid blue, whereas the metal-poor 3D models are in plotted in solid red.

Near the blue edge of the DBV instability strip, we find that the calibrated values of the mixing length parameter are much lower than the value of 1.25 recently used in the theoretical seismological study of Van Grootel et al. [2017]. Therefore, in 3D, efficient convective energy transport sets in at a lower effective temperature. As the set-in of significant energy transport by convection is related to the blue edge of the strip, the 3D results would potentially mean lower effective temperature of the theoretical blue edge. Note that compared to the empirical blue edge of $T_{\rm eff} \approx 31\,000$ K at $\log g \approx 7.8$ [Shipman et al., 2002; Provencal et al., 2003; Hermes et al., 2017], the current 1D theoretical blue edge of $T_{\rm eff} \approx 29\,000$ K at $\log g \approx 7.8$ is already too low in comparison (see Fig. 4 of Van Grootel et al. 2017).

In terms of determining the effective temperatures and surface gravities from spectroscopy, we recommend using ML2/$\alpha = 1.25$ (but see Chaps. 3 and 4 for details of 3D DB/DBA corrections). However, it is clear that the actual efficiency of convection in the atmosphere has little to do with the ML2/$\alpha = 1.25$ value calibrated from spectroscopic observations.

The current evolutionary models of white dwarfs can be improved by including our calibrated values of the mixing length parameter. 3D models also provide the best available estimate for the masses of convection zones of DB and DBA white dwarfs which are relevant for studies of remnant planetary systems. We illustrate this by calculating example 3D DBAZ models. However, our calibration does not consider velocity overshoot which could increase the mixing mass by orders of magnitude. In most of the models presented here, however, we cannot currently do any overshoot studies as the convection zones are too large to model. For the select few models at the highest effective temperatures of our grid, the overshoot region can be directly accessed and could be used for direct investigation, similar to what has been achieved for DA white dwarfs [Cunningham et al., 2019].

Convection is not expected to have any direct impact on the derived ages of white dwarfs, up until the convection zone grows large enough to reach the core, which directly couples the degenerate core to the surface [Tremblay et al., 2015b]. This occurs at $T_{\rm eff} \sim 5\,000$ K for DA white dwarfs [Tassoul et al., 1990; Tremblay et al., 2015b] and $\sim 10\,000$ K for DB white dwarfs [Tassoul et al., 1990; MacDonald and Vennes, 1991]. However, at these effective temperatures convection is adiabatic and therefore loses its sensitivity to the mixing length parameter. Therefore, we do not expect our calibration of the mixing length parameter to have any direct impact on the ages derived from evolutionary models. However, the 3D models can have an indirect effect on age determinations due to 3D spectroscopic corrections for surface gravities and effective temperatures.

Chapter 6

Summary

This thesis presented the first-ever 3D atmospheric models for DB and DBA white dwarfs calculated with the radiation-hydrodynamics code called CO^{5}BOLD. The 3D models treat convective energy transport from first principles, which is a significant improvement upon the commonly used 1D models. The atmospheric models calculated using 1D codes rely on the mixing length approximation, which depends on a free parameter known as the mixing length. 3D codes do not rely on free parameters, but numerical parameters exist. However, these parameters were tested and their effects were found to be smaller than typical observational errors. Another important shortcoming in the 3D models is the numerical treatment of microphysics, but by carefully choosing reference 1D models, convective effects can be isolated, and these uncertainties can be effectively eliminated.

6.1 3D spectroscopic corrections

In the first part of the thesis, the 3D spectroscopic corrections to the atmospheric parameters of hydrogen abundance, surface gravity and effective temperature were derived. Due to the limitations of current calculations of 3D synthetic spectra, two methods of calculating helium-line spectra were used. The two types of spectra are known as 1.5D and $\langle$3D$\rangle$ and they represent two extremes of combining nearby grid-points in the 3D simulations, with 1.5D enlarging the horizontal fluctuations. This means that the real 3D spectrum lies somewhere between these two extremes. Both 1.5D and $\langle$3D$\rangle$ spectra lead to similar sized corrections when taking into account typical observation errors. Given that $\langle$3D$\rangle$ spectra would result in the smallest possible 3D corrections, the $\langle$3D$\rangle$ corrections were used as the final result.

The corrections for hydrogen abundance were found to be unimportant. Sig-

nificant corrections for surface gravities were found below $T_{\rm eff} \approx 20\,000$ K, although the value of the temperature depends on the hydrogen abundance, with more hydrogen in the atmosphere leading to the corrections becoming significant at lower effective temperature range. The 3D spectra result in lower surface gravities when compared to 1D. The corrections in $\log g$ can be as much as 0.4 dex. Historically, high-$\log g$ values for DB and DBA white dwarfs have been observed below $T_{\rm eff} \approx 16\,000$ K in numerous studies [Beauchamp et al., 1996; Bergeron et al., 2011; Koester and Kepler, 2015; Rolland et al., 2018; Genest-Beaulieu and Bergeron, 2019a,b]. Yet, from the 3D models, we do get corrections at larger effective temperatures if the hydrogen abundance becomes very small. Given that large surface gravities are not reported above this temperature, this could indicate that only a minute amount of white dwarfs in the DB/DBA white dwarf samples are close to a pure-helium composition. The 3D corrections for effective temperature are comparable to observational errors. For ease of user application, we provide 3D correction functions, which can also be used in conjunction with any 1D DB and DBA atmospheric models.

To test the spectroscopic corrections, the *Gaia* DR2 astrometric and photometric data was compared to the Genest-Beaulieu and Bergeron [2019b] DB and DBA spectroscopic sample. It was found that both 1D and 3D spectroscopic atmospheric parameters agree similarly with *Gaia* data. However, the adapted Deridder and van Rensbergen [1976] treatment of van der Waals line broadening used in 1D atmospheric models has been deliberately adjusted to match observations [Beauchamp et al., 1996]. Thus, when 3D corrections are applied alongside the Deridder and van Rensbergen [1976] broadening, a worse agreement with *Gaia* data is found. In this work, it is shown that using the older version of van der Waals line broadening by Unsold [1955] alongside 3D models produces a better agreement with *Gaia*. Taking into account the superior physics of 3D models, it is clear that there are issues with the microphysics that need to be addressed in DB and DBA models. Alongside the van der Waals line broadening, there is also the uncertainty in line broadening caused by non-ideal effects due to the relatively large densities in white dwarf atmospheres, leading to significant perturbations of helium absorbers by neighbouring neutral helium atoms. The impact of this has been investigated and shown to be degenerate with van der Waals broadening.

6.2 3D MLT calibration

To extend the application of the 3D atmospheric models of DB and DBA white dwarfs, the calibration of the mixing length parameter for the bottom of the convec-

tion zone was performed. This calibration is useful for studies in need of convection zone masses and of parameters at the bottom of the convection zone. Applications include investigations in to the chemical composition of remnant planetary debris accreting and diffusing into the interiors of white dwarfs, as well as white dwarf asteroseismology. However, the calibration does not take into account convective overshoot, which can increase the convective zone masses by orders of magnitude [Cunningham et al., 2019]. Due to current computational limitations not allowing the simulation of large convection zones, the study of convective overshoot is not possible for most models presented in this thesis, thus this calibration is currently the best estimate available. Additionally, an accurately calibrated mixing length parameter is important for envelope and evolutionary models of DB and DBA models, which currently cannot be calculated in 3D due to computational limitations. It can also be used to understand the spectral changes arising from convective mixing and dilution in hot white dwarfs [MacDonald and Vennes, 1991].

Convective energy transport is more complex in 3D models than in 1D. Therefore, the convection zone boundaries are more difficult to define in 3D. In this work, two definitions of the bottom boundary were used, the Schwarzschild and flux boundaries. The Schwarzschild boundary was used for open bottom models, where the convection zone is too large to be simulated vertically. The calibration for this type of boundary relied on the entropy of the adiabatic upflows. The flux boundary was used for closed bottom models, where the convective flux goes to zero. The entropy or temperature and pressure of the 3D models at each of these boundaries were compared with the parameters of 1D envelope models calculated at different values of the mixing length parameter. The calibrated mixing length value was the value that gave the best-matching parameters.

In this thesis, it is found that the calibrated value of the mixing length parameter (≈ 0.8) is lower than the most commonly used value of ML2/$\alpha = 1.25$, meaning that 3D models predict lower convective efficiency. The value of the calibrated mixing length parameter for DB and DBA white dwarfs is similar to the calibrated value of the mixing length parameter of 3D DA models [Tremblay et al., 2015b], indicating that convective transport is similar in both types of stellar remnants. One example consequence of the calibrated value of mixing length parameter is the effect it will have on the empirical blue edge of the DBV instability strip. Based on 1D theoretical models the blue edge is already too cool ($T_{\rm eff} \approx 29\,000$ K at $\log g \approx 7.8$ [Van Grootel et al., 2017]) when compared to the observational blue edge ($T_{\rm eff} \approx 31\,000$ K at $\log g \approx 7.8$ [Shipman et al., 2002; Provencal et al., 2003; Hermes et al., 2017]). As 3D models predict lower efficiency of convection, it means

that onset of efficient convection, which is related to the blue edge, will occur at a lower effective temperature, worsening the current agreement between theoretical predictions and observational results.

6.3 Future work

The future of DB and DBA white dwarf modelling lies in the improvement of line broadening treatments. The two most important uncertainties at the low effective temperature regime are the van der Waals broadening and perturbations of helium absorbers due to non-ideal gas effects. However, from comparisons with *Gaia* data it is clear that there are also issues at temperatures where these effects become negligible, in the regime where Stark broadening becomes important, thus some attention should be drawn to this type of broadening as well. In order to improve these issues, detailed theoretical or experimental work needs to be performed [Montgomery et al., 2015].

There are several avenues of utilising the current 3D atmospheric models of DB and DBA white dwarfs to aid future research of these stars. One such way is to include the calibration of the mixing length parameter in 1D envelope and evolutionary models of DB and DBA white dwarfs. The calibration of the mixing length parameter can also be used in asteroseismological studies of the deep interior of white dwarfs. Additionally, 3D structures can directly be used in asteroseismological modelling ensuring more physical treatment of convection. This is especially relevant since pulsating DBV white dwarfs are subject to so-called convective driving, where convective flux plays an important role in the excitation and observed amplitude of pulsation modes [Fontaine and Brassard, 2008].

Recently, the issue of emission cores in the He I 5876 Å line in DB and DBA white dwarfs has been investigated by Klein et al. [2020]. They attribute this to a temperature inversion near the surface of the atmosphere with one of the proposed causes being 3D effects, such as increased radiative cooling or overshoot. Radiative cooling would cause the upper layers to be cooler when compared to 1D models. As a response, the lower down layers could thus become hotter, leading to temperature inversion in the atmosphere. Overshoot in the upper layers would mean that the convection zone in 3D models can extend to higher up layers of the atmosphere when compare to 1D models. This would change the temperature structure of the atmosphere and could potentially lead to a temperature inversion near the surface. The 3D DB and DBA model structures can thus be used to either confirm or eliminate the 3D effects as the cause. In order to fully asses this, the use of

full 3D synthetic spectra codes such as Linfor3D might be beneficial to simulate the most realistic profile of the line, which can then be directly compared to observations.

Another avenue to explore in terms of 3D modelling would involve the computation of metal-rich atmosphere white dwarfs, work which has already been initiated in this thesis. This could lead to more accurate chemical compositions for the parent accreted bodies, providing insight into the diversity of rocky exo-asteroids [Zuckerman et al., 2010]. Related to this would be the study of convective overshoot in the atmospheres of DB and DBA white dwarfs, which can already be performed for the closed bottom simulations. Such work would provide more accurate estimates of the parent body masses.

The *Gaia* DR2 white dwarf catalogue of Gentile Fusillo et al. [2019a] has increased the number of white dwarfs by an order of magnitude. This, in combination with the spectroscopic information released from multi-object spectroscopic surveys such as SDSS-V [Kollmeier et al., 2017], DESI [DESI Collaboration et al., 2016b,a], 4MOST [de Jong et al., 2016] and WEAVE [Dalton et al., 2012, 2016], means that white dwarf spectroscopic information will also increase ten-fold. Thus, new and improved 3D atmospheric models, alongside line broadening improvements, will be essential to study these spectra. Additionally, a large number of rarer objects are expected to be found, such as massive helium-rich atmosphere white dwarfs which could have formed as a result of stellar mergers [Richer et al., 2019; Pshirkov et al., 2020]. Thus, 3D models can be expanded to study these peculiar objects also.

More improvements can also be made in terms of the numerical parametrisation of the simulations. Larger simulations which will become possible with computational improvements, will lead to the ability to simulate more of the convection zone or simulate it with greater precision. More complex phenomena can also be included in CO^{5}BOLD and explored for helium-dominated atmosphere white dwarfs, such as magnetic fields and the presence of dust particles [Freytag et al., 2012]. Once the microphysics is improved, it can also be included in the 3D atmosphere models.

In all, 3D atmosphere modelling has allowed for a significant improvement in our understanding of convection in the atmospheres of DB and DBA white dwarfs. Additionally, it has allowed us to identify missing physics in the current models. With these models, significant advancements in other aspects of white dwarf research are on the horizon.

Appendix A

Python 3D DBA spectroscopic correction functions

The following Python code can be used to determine the 3D corrections for given 1D $\log \mathrm{H/He}$, $\log g$ and T_{eff} values. Brief description of how to use the code is also provided. The 3D corrections should only be applied to spectroscopically-determined 1D atmospheric parameters in the ranges $7.5 \leq \log g \leq 9.1$ dex, $11\,900 \leq T_{\mathrm{eff}} \leq 33\,900$ K and $-10.0 \leq \log \mathrm{H/He} \leq -2.0$ dex.

```
import numpy as np
"""coefficients of correction function.
corr_g_x -> coefficients for log(g) correction function
corr_t_x -> coefficients for Teff correction function
corr_y_x -> coefficients for log(H/He) correction function"""
corr_g_x = [  7.78980378e-05,  -1.24678964e-01,
2.26643820e-01,   7.34619109e+00,
  -4.95618648e+00,   9.31949412e-01,  -2.70682476e-03,
8.47497762e+00,
   3.13916897e+00,  -6.49325446e+00,   1.90907434e+00,
-5.27204063e+00,
   9.79168675e+00,   2.15044078e+00,   4.42834455e+00,
-1.00893139e+02]
corr_t_x = [  -1.50741476e-03,   1.56723133e-02,
-4.02862191e-01,  -4.16098578e+00,
   3.08774593e+00,   2.17254602e-01,  -1.77379411e-02,
-6.21423204e-01,
  -1.38832346e+01,   5.00270182e+00,   1.52048260e-02,
4.74907475e+00,
   9.44761787e+00,  -3.17258673e+00,  -2.92209394e-01,
-3.89830203e+01,]
corr_y_x = [  6.82099077e-04,  -5.54974701e+00,
1.57704162e+01,   3.28321463e+00,
   1.10683877e+00,  -3.79492811e+01,  -4.39666652e+00,
6.79944714e+00,
  -5.94840004e+00,   3.87450827e+00,  -9.91733926e+00,
-8.30112716e-01,
  -1.14903810e+01,  -2.79453315e-01,  -5.36529860e-02,
2.40314969e+01]
""" Correction functions:
corr_g -> log(g) correction function
corr_t -> Teff correction function
corr_y -> log(H/He) correction function """
def corr_g(x,u1,v1,w1):
    if u1 < 7.5 or u1 > 9.1 or v1 < 11900.0 or v1 > 33900 or w1 > -2.0:
        a = 0.*u1
    elif w1 < -10.0:
        w1=-10.0
    else:
        u = (u1 - 7.0)/7.0
        v = (v1 - 10000.0)/10000.0
        w = w1/(-10.)
        a = (x[0]+x[1]*np.exp(x[2]+x[3]*u+(x[4]+(x[6]+x[11]*np.exp(
        x[12]+x[13]*u+
        x[14]*v+x[15]*w))*np.exp(x[7]+x[8]*u+x[9]*v+x[10]*w))*v
        +x[5]*w))
    return a
```

```
def corr_t(x,u1,v1,w1):
    if (u1 < 7.5 or u1 > 9.1 or v1 < 11900.0 or v1 > 33900 or w1 > -2.0
        or w1 < -10.0):
        a = 0.*u1
    elif w1 < -10.0:
        w1=-10.0
    else:
        u = (u1 - 7.0)/7.0
        v = (v1 - 10000.0)/10000.0
        w = w1/(-10.)
        a = (x[0]+x[1]*np.exp((x[2]+x[6]*np.exp(x[7]+(x[8]+x[11]*np.exp(
        x[12]+x[13]*u+x[14]*v+x[15]*w))*u+x[9]*v+x[10]*w))+x[3]*u+x[4]*v
        +x[5]*w))
    return a
def corr_y(x,u1,v1,w1):
    if (u1 < 7.5 or u1 > 9.1 or v1 < 11900.0 or v1 > 33900 or w1 > -2.0
        or w1 < -10.0):
        a = 0.*u1
    elif w1 < -10.0:
        w1=-10.0
    else:
        u = (u1 - 7.0)/7.0
        v = (v1 - 10000.0)/10000.0
        w = w1/(-10.)
        a = (x[0]+x[1]*np.exp(x[2]+(x[3]+x[6]*np.exp(x[7]+x[8]*u+(x[9]+
        x[11]*np.exp(x[12]+x[13]*u+x[14]*v+x[15]*w))*v+x[10]*w))*u+
        x[4]*v+x[5]*w))
    return a
""" How to use:
For example, you want to find 3D log(g) correction for a 1D
spectroscopically-determined values of
log(H/He) = -5.3, log(g) = 8.45, Teff = 13540 K. Can also use
lists of Teff, logg, logH/He."""
correction_in_logg = corr_g(corr_g_x,8.45,13540,-5.3)
"""This will give the correction in log(g) which must be ADDED to
1D log(g) value in
order to correct for 3D effects.
Same procedure can be repeated for 3D Teff and log(H/He) corrections."""
correction_in_teff = corr_t(corr_t_x,8.45,13540,-5.3)
correction_in_loghhe = corr_y(corr_y_x,8.45,13540,-5.3)
corrected_logg = 8.45 + correction_in_logg
corrected_teff = 13540 + 10000.*correction_in_teff
corrected_loghhe = -5.3 - 10.*correction_in_loghhe
```

Appendix B

Additional information on 3D DBA models

Tabs. B.1 to B.6 list some basic parameters of the 3D simulations. This includes the surface gravity of a given simulation, its effective temperature, the size of the box the simulation was run in, the run time and the relative bolometric intensity contrast averaged over space and time.

Tabs. B.7 to B.12 list the parameters needed for the mixing length calibration of 3D open bottom models, as well as the results of the calibration. For each 3D simulation, its surface gravity, effective temperature and the adiabatic entropy used for ML2/$\alpha_{\rm S}$ calibration is included. Also given are the ML2/$\alpha_{\rm S}$, $\log\left(M_{\rm CVZ}/M_{\rm tot}\right)$, T and P values for the Schwarzschild boundary. $\log\left(M_{\rm CVZ}/M_{\rm tot}\right)$, temperature and pressure are found from the 1D envelope calculated at ML2/$\alpha_{\rm S}$. The same parameters are also given for the flux boundary. As the flux boundary cannot be directly accessed for open bottom models, we instead use the relation ML2/$\alpha_{\rm f}$ = 1.17 ML2/$\alpha_{\rm S}$ to find ML2/$\alpha_{\rm f}$.

Tabs. B.13 to B.18 list the parameters needed for the calibration of the mixing length for 3D closed bottom models, as well as the results of the calibration. For each 3D simulation, its surface gravity and effective temperature are given. The mixing length calibration for closed bottom model relies on the spatially- and temporally-averaged 3D temperature and pressure at the bottom of the convection zone, and these parameters are given for both the Schwarzschild and flux boundaries. The ML2/$\alpha_{\rm S}$ and ML2/$\alpha_{\rm f}$ are also given, as well as the $\log\left(M_{\rm CVZ}/M_{\rm tot}\right)$ for each boundary.

Table B.1: Select parameters of the 3D DB model atmospheres, where $\delta I_{\rm rms}/\langle I\rangle$ is the relative bolometric intensity contrast averaged over space and time.

$\log g$	$T_{\rm eff}$ (K)	Box size (km × km × km)	Total run time (stellar s)	$\delta I_{\rm rms}/\langle I\rangle$ (%)
7.5	12098	1.22×1.22×0.58	33.6	3.6
7.5	13969	1.98×1.98×0.67	32.2	8.9
7.5	15947	2.86×2.86×1.19	32.2	16.4
7.5	18059	6.09×6.09×1.46	32.1	21.3
7.5	19931	11.96×11.96×2.39	34.7	23.4
7.5	22044	21.75×21.75×4.51	32.3	25.5
7.5	23774	23.96×23.96×4.78	31.7	24.3
7.5	26497	37.47×37.47×21.40	32.6	21.7
7.5	27993	31.22×31.22×10.77	14.7	17.5
7.5	29991	31.22×31.22×11.86	17.7	9.4
7.5	32001	33.48×33.48×14.00	48.3	4.8
8.0	12020	0.70×0.70×0.10	10.0	2.1
8.0	14083	0.79×0.79×0.24	10.2	6.0
8.0	16105	0.94×0.94×0.18	10.1	11.9
8.0	18082	1.23×1.23×0.35	13.0	17.0
8.0	20090	2.00×2.00×0.58	12.5	19.4
8.0	21014	5.19×5.19×0.97	11.9	21.0
8.0	21465	5.19×5.19×0.97	11.0	21.6
8.0	21987	5.19×5.19×0.97	8.7	22.3
8.0	22988	8.62×8.62×1.41	11.6	24.2
8.0	24144	8.62×8.62×1.41	11.7	23.8
8.0	25898	8.62×8.62×1.56	10.0	21.1
8.0	28107	12.63×12.63×4.93	16.8	20.3
8.0	29997	12.63×12.63×5.12	13.5	19.2
8.0	31999	12.63×12.63×3.28	5.0	14.8
8.0	33999	12.63×12.63×3.42	5.3	7.9
8.5	12139	0.25×0.25×0.05	3.6	1.5
8.5	14007	0.25×0.25×0.04	5.7	3.6
8.5	15961	0.34×0.34×0.05	3.5	7.6
8.5	18000	0.39×0.39×0.13	3.6	12.6
8.5	19955	0.60×0.60×0.20	4.0	15.5

Continued on next page

Table B.1 continued.

$\log g$	$T_{\rm eff}$ (K)	Box size (km × km × km)	Total run time (stellar s)	$\delta I_{\rm rms}/\langle I \rangle$ (%)
8.5	21999	1.03×1.03×0.26	3.2	17.8
8.5	24143	1.78×1.78×0.37	3.7	22.1
8.5	25805	2.37×2.37×0.44	3.5	22.3
8.5	27934	2.53×2.53×0.59	2.9	20.6
8.5	30567	4.53×4.53×1.97	4.6	19.5
8.5	32208	4.53×4.53×2.12	3.8	18.9
8.5	34020	4.53×4.53×1.92	3.7	17.6
9.0	12124	0.06×0.06×0.01	3.4	0.8
9.0	14117	0.07×0.07×0.01	2.0	2.3
9.0	16029	0.11×0.11×0.02	1.1	5.0
9.0	17998	0.12×0.12×0.03	1.1	8.7
9.0	19961	0.14×0.14×0.05	1.0	11.7
9.0	21978	0.20×0.20×0.07	1.0	13.6
9.0	24082	0.39×0.39×0.10	1.1	17.2
9.0	26109	0.76×0.76×0.13	0.6	20.6
9.0	28143	0.76×0.76×0.16	1.0	20.6
9.0	30184	0.86×0.86×0.20	1.1	17.4
9.0	31440	0.86×0.86×0.20	3.2	17.2
9.0	34105	1.43×1.43×0.84	2.3	18.3
Concluded				

Table B.2: Select parameters of 3D DBA model atmospheres with $\log \mathrm{H/He} = -7$.

$\log g$	$T_{\rm eff}$ (K)	Box size (km × km × km)	Total run time (stellar s)	$\delta I_{\rm rms}/\langle I \rangle$ (%)
7.5	12098	1.22×1.22×0.58	32.8	3.6
7.5	13967	1.98×1.98×0.67	31.7	8.8
7.5	15936	2.86×2.86×1.19	35.0	16.3
7.5	18051	6.09×6.09×1.46	34.1	21.0
7.5	19865	11.96×11.96×2.44	32.6	22.3
7.5	21873	21.75×21.75×4.04	37.8	22.7
7.5	23789	23.96×23.96×4.80	32.1	24.4
7.5	26501	37.47×37.47×21.40	33.2	22.1
7.5	27993	31.22×31.22×10.77	16.0	17.2
7.5	29993	31.22×31.22×11.86	18.3	10.2
7.5	32002	33.48×33.48×14.00	34.4	4.5
8.0	12019	0.70×0.70×0.11	10.8	2.1
8.0	14083	0.79×0.79×0.24	10.9	5.9
8.0	16099	0.94×0.94×0.19	10.1	11.9
8.0	18074	1.23×1.23×0.35	10.3	17.0
8.0	20088	2.00×2.00×0.58	10.2	19.4
8.0	21996	5.19×5.19×0.97	11.4	22.3
8.0	24036	8.62×8.62×1.41	10.4	24.0
8.0	25956	8.62×8.62×1.56	10.2	21.1
8.0	28037	12.63×12.63×4.93	18.2	20.6
8.0	29963	12.63×12.63×5.12	10.5	20.2
8.0	32000	12.63×12.63×3.28	5.5	14.4
8.0	33999	12.63×12.63×3.42	5.4	8.5
8.5	12147	0.25×0.25×0.05	3.1	1.5
8.5	14004	0.25×0.25×0.04	3.8	3.6
8.5	15958	0.34×0.34×0.05	3.3	7.6
8.5	17998	0.39×0.39×0.13	3.6	12.6
8.5	19951	0.60×0.60×0.20	3.4	15.5
8.5	22002	1.03×1.03×0.26	3.1	17.9
8.5	24047	1.78×1.78×0.37	3.3	22.1
8.5	25943	2.37×2.37×0.44	3.4	22.1
8.5	27907	2.53×2.53×0.59	3.2	20.6
8.5	30514	4.53×4.53×1.97	4.2	19.7
8.5	32012	4.53×4.53×2.12	3.7	19.0
8.5	33949	4.53×4.53×1.92	3.2	17.1
9.0	12120	0.06×0.06×0.01	1.1	0.8
9.0	14114	0.07×0.07×0.01	1.0	2.3
9.0	16026	0.11×0.11×0.02	1.0	4.9
9.0	17985	0.12×0.12×0.03	1.0	8.7
9.0	19957	0.14×0.14×0.04	1.1	11.7
9.0	21982	0.20×0.20×0.07	1.1	13.6
9.0	24093	0.39×0.39×0.10	1.1	17.1
9.0	26115	0.76×0.76×0.13	1.1	20.7
9.0	28141	0.76×0.76×0.16	1.1	20.6
9.0	30006	0.86×0.86×0.20	1.0	17.8
9.0	31472	0.86×0.86×0.20	1.3	16.7
9.0	34021	1.43×1.43×0.84	2.0	18.3

Table B.3: Select parameters of 3D DBA model atmospheres with $\log \mathrm{H/He} = -5$.

$\log g$	T_{eff} (K)	Box size (km × km × km)	Total run time (stellar s)	$\delta I_{\mathrm{rms}}/\langle I \rangle$ (%)
7.5	12009	1.22×1.22×0.59	33.1	3.4
7.5	14013	1.98×1.98×0.67	33.0	9.0
7.5	15886	2.86×2.86×1.19	33.9	15.7
7.5	17920	6.09×6.09×1.46	31.8	21.0
7.5	19900	11.96×11.96×2.44	32.2	23.1
7.5	21946	21.75×21.75×4.51	32.6	24.7
7.5	23757	23.96×23.96×4.80	32.2	24.2
7.5	26522	37.47×37.47×21.40	36.4	22.1
7.5	27998	31.22×31.22×10.77	15.8	17.7
7.5	29992	31.22×31.22×11.86	26.6	9.7
7.5	32002	33.48×33.48×14.00	24.0	5.1
8.0	11978	0.70×0.70×0.11	10.2	2.1
8.0	14031	0.79×0.79×0.24	9.9	5.7
8.0	15974	0.94×0.94×0.19	11.5	11.3
8.0	17952	1.23×1.23×0.35	10.4	16.9
8.0	20012	2.00×2.00×0.58	12.7	19.4
8.0	21959	5.19×5.19×0.97	10.1	22.2
8.0	24014	8.62×8.62×1.41	10.0	24.0
8.0	25963	8.62×8.62×1.56	9.9	20.6
8.0	28086	12.63×12.63×4.93	12.4	20.7
8.0	29989	12.63×12.63×5.12	10.1	18.9
8.0	32002	12.63×12.63×3.28	10.3	14.7
8.0	34000	12.63×12.63×3.42	10.1	8.2
8.5	11996	0.25×0.25×0.05	4.0	1.3
8.5	14012	0.25×0.25×0.04	3.7	3.5
8.5	15957	0.34×0.34×0.05	3.7	7.6
8.5	17956	0.39×0.39×0.13	3.6	12.7
8.5	19924	0.60×0.60×0.20	4.0	15.5
8.5	21962	1.03×1.03×0.26	3.7	17.8
8.5	24004	1.78×1.78×0.37	3.7	21.9
8.5	25938	2.37×2.37×0.45	3.7	22.2
8.5	27946	2.53×2.53×0.59	3.5	20.3
8.5	30517	4.53×4.53×1.97	4.1	19.5
8.5	32015	4.53×4.53×2.12	4.3	19.0
8.5	33947	4.53×4.53×1.92	3.6	17.4
9.0	12077	0.06×0.06×0.01	1.1	0.8
9.0	14059	0.07×0.07×0.01	1.1	2.2
9.0	15930	0.11×0.11×0.02	1.0	4.7
9.0	17885	0.12×0.12×0.03	1.0	8.7
9.0	19922	0.14×0.14×0.04	1.1	11.8
9.0	21942	0.20×0.20×0.07	1.1	13.6
9.0	24076	0.39×0.39×0.10	1.1	17.1
9.0	26099	0.76×0.76×0.13	1.0	20.6
9.0	28181	0.76×0.76×0.16	1.0	20.6
9.0	29952	0.86×0.86×0.20	1.0	17.8
9.0	31452	0.86×0.86×0.20	1.0	17.2
9.0	33986	1.43×1.43×0.84	2.3	18.3

Table B.4: Select parameters of 3D DBA model atmospheres with $\log \mathrm{H/He} = -4$.

$\log g$	T_{eff} (K)	Box size (km × km × km)	Total run time (stellar s)	$\delta I_{\mathrm{rms}}/\langle I \rangle$ (%)
7.5	11983	1.22×1.22×0.58	32.0	3.5
7.5	13985	1.98×1.98×0.67	31.8	9.0
7.5	15973	2.86×2.86×1.19	34.0	16.0
7.5	17979	6.09×6.09×1.46	34.2	20.4
7.5	19932	11.96×11.96×2.75	34.5	22.2
7.5	22021	21.75×21.75×4.51	32.2	23.8
7.5	23464	23.96×23.96×4.80	31.0	23.7
7.5	26632	37.47×37.47×21.40	34.4	21.9
7.5	28004	31.22×31.22×10.77	15.8	17.3
7.5	29993	31.22×31.22×11.86	19.8	9.4
7.5	32002	33.48×33.48×14.00	10.9	5.3
8.0	12008	0.70×0.70×0.11	10.0	2.2
8.0	13999	0.79×0.79×0.24	10.1	5.8
8.0	15994	0.94×0.94×0.19	10.3	11.4
8.0	18052	1.23×1.23×0.35	10.1	17.1
8.0	19991	2.00×2.00×0.58	10.2	19.5
8.0	21981	5.19×5.19×1.02	10.0	22.0
8.0	23953	8.62×8.62×1.41	10.3	23.3
8.0	25961	8.62×8.62×1.56	10.2	20.6
8.0	28092	12.63×12.63×4.93	10.2	21.1
8.0	29994	12.63×12.63×5.12	11.9	19.4
8.0	32002	12.63×12.63×3.28	10.4	14.5
8.0	34000	12.63×12.63×3.42	10.1	8.0
8.5	12027	0.25×0.25×0.05	3.8	1.4
8.5	13981	0.25×0.25×0.04	3.7	3.6
8.5	15982	0.34×0.34×0.06	4.1	7.6
8.5	17951	0.39×0.39×0.13	3.8	13.0
8.5	19972	0.60×0.60×0.20	3.8	15.8
8.5	21956	1.03×1.03×0.26	3.8	18.0
8.5	23980	1.78×1.78×0.37	3.9	21.9
8.5	26006	2.37×2.37×0.46	3.6	21.5
8.5	27829	2.53×2.53×0.59	3.7	20.8
8.5	30490	4.53×4.53×1.97	3.8	19.4
8.5	32008	4.53×4.53×2.12	4.0	19.0
8.5	33963	4.53×4.53×1.92	3.3	17.4
9.0	12055	0.06×0.06×0.01	1.1	0.9
9.0	14023	0.07×0.07×0.01	1.0	2.2
9.0	16020	0.11×0.11×0.02	1.0	4.9
9.0	17972	0.12×0.12×0.03	1.1	9.3
9.0	19968	0.14×0.14×0.04	1.1	12.2
9.0	21957	0.20×0.20×0.07	1.0	13.9
9.0	23971	0.39×0.39×0.10	1.0	17.2
9.0	26018	0.76×0.76×0.13	1.0	20.5
9.0	27982	0.76×0.76×0.16	1.0	20.6
9.0	29948	0.86×0.86×0.20	1.0	17.8
9.0	31360	0.86×0.86×0.20	1.0	17.0
9.0	33988	1.43×1.43×0.84	1.7	18.3

Table B.5: Select parameters of 3D DBA model atmospheres with $\log \mathrm{H/He} = -3$.

$\log g$	$T_{\rm eff}$ (K)	Box size (km × km × km)	Total run time (stellar s)	$\delta I_{\rm rms}/\langle I \rangle$ (%)
7.5	11980	1.22×1.22×0.37	31.7	3.3
7.5	13855	1.98×1.98×0.67	36.3	8.8
7.5	15805	2.86×2.86×1.19	34.6	16.2
7.5	18026	6.09×6.09×1.46	32.1	21.2
7.5	20035	11.96×11.96×2.53	33.0	23.3
7.5	22043	21.75×21.75×4.51	31.6	24.8
7.5	23752	23.96×23.96×4.89	31.4	24.5
7.5	26670	37.47×37.47×21.40	35.7	21.0
7.5	28000	31.22×31.22×10.77	15.2	17.2
7.5	29999	31.22×31.22×11.86	22.8	8.8
7.5	32000	33.48×33.48×14.00	23.0	4.3
8.0	12007	0.70×0.70×0.12	11.9	2.1
8.0	13961	0.79×0.79×0.14	10.5	5.8
8.0	16040	0.94×0.94×0.19	10.1	11.6
8.0	17985	1.23×1.23×0.36	10.4	17.0
8.0	20088	2.00×2.00×0.58	10.1	19.5
8.0	22047	5.19×5.19×0.99	10.8	22.5
8.0	24002	8.62×8.62×1.41	10.4	24.0
8.0	25904	8.62×8.62×1.56	10.4	21.2
8.0	28118	12.63×12.63×4.93	11.4	21.4
8.0	30001	12.63×12.63×5.12	11.0	18.9
8.0	31999	12.63×12.63×3.28	10.0	14.1
8.0	33980	12.63×12.63×3.42	9.9	8.1
8.5	12027	0.25×0.25×0.05	3.8	1.3
8.5	13985	0.25×0.25×0.05	3.5	3.5
8.5	15988	0.34×0.34×0.06	3.4	7.6
8.5	18029	0.39×0.39×0.13	3.7	12.8
8.5	20043	0.60×0.60×0.20	3.6	15.7
8.5	22050	1.03×1.03×0.27	3.8	18.0
8.5	24011	1.78×1.78×0.37	3.4	22.0
8.5	25884	2.37×2.37×0.46	3.6	22.1
8.5	27602	2.53×2.53×0.59	3.1	21.5
8.5	30364	4.53×4.53×1.97	3.2	19.2
8.5	31965	4.53×4.53×2.12	5.2	18.8
8.5	34038	4.53×4.53×1.92	3.6	17.3
9.0	11994	0.06×0.06×0.01	1.0	0.8
9.0	13967	0.07×0.07×0.01	1.1	2.1
9.0	15970	0.11×0.11×0.02	1.1	4.8
9.0	18038	0.12×0.12×0.03	1.2	9.0
9.0	20045	0.14×0.14×0.04	1.0	12.0
9.0	22057	0.20×0.20×0.07	1.0	13.8
9.0	24026	0.39×0.39×0.10	1.0	17.1
9.0	25997	0.76×0.76×0.13	1.0	20.6
9.0	28015	0.76×0.76×0.16	1.0	20.6
9.0	29929	0.86×0.86×0.20	1.0	18.3
9.0	31340	0.86×0.86×0.20	1.0	17.5
9.0	33917	1.43×1.43×0.84	1.0	18.6

Table B.6: Select parameters of 3D DBA model atmospheres with $\log \mathrm{H/He} = -2$.

$\log g$	$T_{\rm eff}$ (K)	Box size (km × km × km)	Total run time (stellar s)	$\delta I_{\rm rms}/\langle I \rangle$ (%)
7.5	11977	1.98×1.98×0.67	39.8	9.0
7.5	13995	2.86×2.86×1.19	38.3	15.0
7.5	16063	6.09×6.09×1.46	40.0	17.7
7.5	17963	6.09×6.09×1.46	73.4	20.2
7.5	20042	21.75×21.75×3.39	36.8	20.6
7.5	21944	21.75×21.75×4.59	33.9	18.2
7.5	22925	23.96×23.96×5.01	32.8	21.8
7.5	26471	37.47×37.47×21.40	33.7	19.7
7.5	27996	31.22×31.22×11.11	16.6	16.1
7.5	29982	31.22×31.22×11.86	24.1	8.0
7.5	32009	33.48×33.48×14.00	24.0	4.0
8.0	12044	0.79×0.79×0.16	14.0	5.8
8.0	13953	0.94×0.94×0.20	12.8	10.6
8.0	15983	1.23×1.23×0.36	14.4	14.3
8.0	17961	1.23×1.23×0.38	19.9	17.1
8.0	19903	3.40×3.40×0.69	23.1	18.4
8.0	22026	8.62×8.62×1.43	11.0	17.6
8.0	24006	8.62×8.62×1.53	11.9	19.3
8.0	25333	8.62×8.62×1.67	12.4	18.1
8.0	27968	12.63×12.63×4.93	11.5	20.2
8.0	30013	12.63×12.63×5.12	10.4	18.3
8.0	31997	12.63×12.63×3.39	10.2	12.5
8.0	33989	12.63×12.63×3.51	10.0	7.0
8.5	12013	0.25×0.25×0.05	5.1	3.4
8.5	14013	0.34×0.34×0.06	4.4	7.1
8.5	15994	0.39×0.39×0.13	6.1	10.6
8.5	17996	0.60×0.60×0.20	4.4	13.7
8.5	19962	0.60×0.60×0.20	7.1	15.1
8.5	22044	1.78×1.78×0.38	3.6	15.8
8.5	24025	2.37×2.37×0.46	3.5	19.7
8.5	25969	2.53×2.53×0.59	3.8	16.1
8.5	27179	3.80×3.80×0.62	4.6	17.4
8.5	30535	4.53×4.53×2.05	7.9	18.4
8.5	31852	4.53×4.53×2.12	3.5	18.7
8.5	33930	4.53×4.53×1.92	3.4	16.9
9.0	12025	0.07×0.07×0.01	1.2	2.0
9.0	13986	0.11×0.11×0.02	1.3	4.4
9.0	16001	0.12×0.12×0.03	1.6	7.3
9.0	17981	0.14×0.14×0.04	1.4	10.2
9.0	20038	0.14×0.14×0.05	2.0	12.0
9.0	21923	0.41×0.41×0.08	2.9	12.9
9.0	24031	0.76×0.76×0.13	1.0	17.7
9.0	26031	0.76×0.76×0.16	2.0	16.9
9.0	27980	0.86×0.86×0.20	1.1	16.3
9.0	29843	0.86×0.86×0.21	1.3	16.0
9.0	31011	0.86×0.86×0.22	2.3	16.7
9.0	33770	1.43×1.43×0.84	3.2	18.2

Table B.7: MLT calibration for open bottom 3D DB models, where 3D $s_{\rm env}$ is the 3D adiabatic entropy used for calibration, ML2/$\alpha_{\rm S}$ is the calibrated ML2/α value for Schwarzschild boundary, $\log{(M_{\rm CVZ}/M_{\rm tot})_{\rm S}}$ is $\log{(M_{\rm CVZ}/M_{\rm tot})}$ for Schwarzschild boundary, $(\log T_{\rm b})_{\rm S}$ is the 1D calibrated temperature at the Schwarzschild boundary, $(\log P_{\rm b})_{\rm S}$ is the 1D calibrated pressure at the Schwarzschild boundary. The same parameters are also given for the flux boundary and are denoted by subscript 'f'.

$\log g$	$T_{\rm eff}$ (K)	3D $s_{\rm env}$ (10^9 erg g^{-1} K^{-1})	ML2/$\alpha_{\rm S}$	$\log{(M_{\rm CVZ}/M_{\rm tot})_{\rm S}}$	$(\log T_{\rm b})_{\rm S}$ (K)	$(\log P_{\rm b})_{\rm S}$ (dyn cm^{-2})	ML2/$\alpha_{\rm f}$	$\log{(M_{\rm CVZ}/M_{\rm tot})_{\rm f}}$	$(\log T_{\rm b})_{\rm f}$ (K)	$(\log P_{\rm b})_{\rm f}$ (dyn cm^{-2})
7.5	12098	0.40	1.00	−4.14	6.68	16.96	1.00	−4.14	6.68	16.96
7.5	13969	0.44	0.91	−4.56	6.63	16.53	1.07	−4.54	6.63	16.55
7.5	15947	0.48	0.92	−5.16	6.52	15.93	1.08	−5.11	6.54	15.99
7.5	18059	0.59	0.91	−6.57	6.25	14.51	1.07	−6.40	6.28	14.69
7.5	19931	0.78	0.97	−9.16	5.74	11.92	1.14	−8.72	5.83	12.36
7.5	22044	0.94	0.82	−11.06	5.42	10.02	0.95	−10.82	5.46	10.26
7.5	23774	1.02	0.69	−12.07	5.24	9.01	0.80	−11.62	5.33	9.45
8.0	12020	0.38	1.00	−5.21	6.59	16.87	1.00	−5.21	6.59	16.87
8.0	14083	0.42	1.00	−5.57	6.56	16.51	1.00	−5.57	6.56	16.51
8.0	16105	0.46	0.89	−6.08	6.48	16.00	1.04	−6.05	6.49	16.04
8.0	18082	0.52	0.83	−6.96	6.32	15.12	0.97	−6.86	6.34	15.23
8.0	20090	0.66	0.88	−8.71	5.98	13.37	1.03	−8.45	6.04	13.63
8.0	21014	0.66	0.89	−9.92	5.75	12.16	1.04	−9.56	5.82	12.52
8.0	21465	0.75	0.97	−10.38	5.67	11.70	1.14	−9.97	5.74	12.11
8.0	21987	0.78	1.10	−10.82	5.59	11.26	1.28	−10.38	5.67	11.70
8.0	22988	0.82	1.00	−11.39	5.49	10.68	1.17	−11.25	5.52	10.83
8.0	24144	0.82	0.78	−11.90	5.41	10.17	0.92	−11.69	5.45	10.38
8.0	25898	0.87	0.71	−12.61	5.30	9.46	0.83	−12.27	5.36	9.81
8.5	12139	0.37	1.00	−6.38	6.47	16.70	1.00	−6.38	6.47	16.70
8.5	14007	0.40	1.00	−6.64	6.47	16.44	1.00	−6.64	6.47	16.44
8.5	15961	0.43	1.00	−6.99	6.43	16.09	1.00	−6.99	6.43	16.09
8.5	18000	0.48	0.74	−7.60	6.33	15.47	0.87	−7.55	6.34	15.53
8.5	19955	0.55	0.77	−8.62	6.14	14.46	0.90	−8.47	6.17	14.60
8.5	22000	0.70	0.80	−10.56	5.77	12.52	0.94	−10.26	5.84	12.82
8.5	24143	0.82	1.16	−11.93	5.54	11.14	1.36	−11.65	5.59	11.43
8.5	25805	0.87	0.85	−12.50	5.45	10.57	0.99	−12.34	5.48	10.74
8.5	27934	0.94	0.70	−13.27	5.33	9.81	0.82	−12.97	5.38	10.10
9.0	12124	0.35	1.00	−7.69	6.28	16.39	1.00	−7.69	6.28	16.39
9.0	14117	0.38	1.00	−7.84	6.34	16.24	1.00	−7.84	6.34	16.24
9.0	16029	0.41	1.00	−8.09	6.33	15.99	1.00	−8.09	6.33	15.99
9.0	17998	0.45	0.77	−8.47	6.29	15.61	0.90	−8.44	6.30	15.64
9.0	19961	0.50	0.64	−9.18	6.17	14.90	0.75	−9.10	6.18	14.97
9.0	21978	0.59	0.75	−10.32	5.97	13.76	0.88	−10.13	6.01	13.94
9.0	24082	0.72	0.81	−12.00	5.66	12.08	0.95	−11.72	5.71	12.36
9.0	26109	0.79	1.13	−12.81	5.53	11.27	1.32	−12.58	5.57	11.49
9.0	28143	0.85	0.79	−13.41	5.43	10.67	0.92	−13.25	5.46	10.83
9.0	30184	0.89	0.74	−13.86	5.37	10.22	0.86	−13.63	5.41	10.45
9.0	31440	0.92	0.72	−14.18	5.32	9.90	0.84	−13.89	5.37	10.19

Table B.8: Same as Tab. B.7 but for MLT calibration of open bottom 3D DBA models with $\log \mathrm{H/He} = -7$.

$\log g$	$T_{\rm eff}$ (K)	3D $s_{\rm env}$ (10^9 erg g^{-1} K^{-1})	ML2/$\alpha_{\rm S}$	$\log(M_{\rm CVZ}/M_{\rm tot})_{\rm S}$	$(\log T_{\rm b})_{\rm S}$ (K)	$(\log P_{\rm b})_{\rm S}$ (dyn cm^{-2})	ML2/$\alpha_{\rm f}$	$\log(M_{\rm CVZ}/M_{\rm tot})_{\rm f}$	$(\log T_{\rm b})_{\rm f}$ (K)	$(\log P_{\rm b})_{\rm f}$ (dyn cm^{-2})
7.5	12098	0.40	1.00	−4.14	6.68	16.96	1.00	−4.14	6.68	16.96
7.5	13967	0.44	0.91	−4.56	6.63	16.53	1.06	−4.54	6.63	16.56
7.5	15936	0.48	0.91	−5.16	6.52	15.93	1.07	−5.11	6.54	15.99
7.5	18051	0.59	0.91	−6.57	6.25	14.51	1.06	−6.39	6.29	14.69
7.5	19865	0.79	0.91	−9.23	5.73	11.85	1.07	−8.76	5.82	12.32
7.5	21873	0.94	0.79	−11.06	5.41	10.02	0.92	−10.83	5.45	10.25
7.5	23789	1.02	0.69	−12.07	5.24	9.01	0.80	−11.62	5.33	9.45
8.0	12019	0.38	1.00	−5.21	6.59	16.87	1.00	−5.21	6.59	16.87
8.0	14083	0.42	1.00	−5.57	6.56	16.51	1.00	−5.57	6.56	16.51
8.0	16099	0.46	0.88	−6.08	6.48	16.00	1.03	−6.05	6.49	16.04
8.0	18074	0.52	0.82	−6.96	6.32	15.13	0.96	−6.86	6.34	15.23
8.0	20088	0.66	0.88	−8.71	5.98	13.37	1.03	−8.45	6.04	13.63
8.0	21996	0.82	1.10	−10.82	5.59	11.26	1.29	−10.38	5.67	11.70
8.0	24036	0.91	0.79	−11.87	5.42	10.21	0.93	−11.65	5.46	10.43
8.0	25956	0.97	0.71	−12.61	5.30	9.46	0.83	−12.27	5.36	9.81
8.5	12147	0.37	1.00	−6.38	6.47	16.69	1.00	−6.38	6.47	16.69
8.5	14004	0.40	1.00	−6.64	6.47	16.44	1.00	−6.64	6.47	16.44
8.5	15958	0.43	1.00	−6.99	6.43	16.09	1.00	−6.99	6.43	16.09
8.5	17998	0.48	0.74	−7.60	6.33	15.48	0.87	−7.55	6.34	15.53
8.5	19951	0.55	0.77	−8.62	6.14	14.46	0.90	−8.47	6.17	14.60
8.5	22002	0.70	0.80	−10.56	5.77	12.52	0.94	−10.26	5.84	12.82
8.5	24047	0.81	1.15	−11.90	5.54	11.17	1.35	−11.59	5.60	11.49
8.5	25943	0.87	0.83	−12.55	5.44	10.53	0.97	−12.38	5.47	10.69
8.5	27907	0.94	0.69	−13.27	5.33	9.81	0.81	−12.98	5.38	10.10
9.0	12120	0.35	1.00	−7.69	6.28	16.39	1.00	−7.69	6.28	16.39
9.0	14114	0.38	1.00	−7.84	6.34	16.24	1.00	−7.84	6.34	16.24
9.0	16026	0.41	1.00	−8.09	6.33	15.99	1.00	−8.09	6.33	15.99
9.0	17985	0.45	0.75	−8.47	6.29	15.61	0.88	−8.44	6.30	15.64
9.0	19957	0.50	0.64	−9.18	6.17	14.90	0.75	−9.10	6.18	14.97
9.0	21982	0.59	0.76	−10.32	5.97	13.76	0.89	−10.13	6.01	13.94
9.0	24093	0.72	0.81	−12.00	5.66	12.08	0.95	−11.72	5.71	12.36
9.0	26115	0.79	1.13	−12.81	5.53	11.27	1.33	−12.58	5.57	11.49
9.0	28141	0.85	0.79	−13.41	5.43	10.67	0.92	−13.25	5.46	10.83
9.0	30006	0.89	0.75	−13.80	5.38	10.27	0.87	−13.58	5.41	10.49
9.0	31472	0.92	0.72	−14.18	5.32	9.89	0.85	−13.89	5.37	10.19

Table B.9: Same as Tab. B.7 but for MLT calibration of open bottom 3D DBA models with $\log \mathrm{H/He} = -5$.

$\log g$	$T_{\rm eff}$ (K)	3D $s_{\rm env}$ (10^9 erg g^{-1} K^{-1})	ML2/$\alpha_{\rm S}$	$\log(M_{\rm CVZ}/M_{\rm tot})_{\rm S}$	$(\log T_{\rm b})_{\rm S}$ (K)	$(\log P_{\rm b})_{\rm S}$ (dyn cm^{-2})	ML2/$\alpha_{\rm f}$	$\log(M_{\rm CVZ}/M_{\rm tot})_{\rm f}$	$(\log T_{\rm b})_{\rm f}$ (K)	$(\log P_{\rm b})_{\rm f}$ (dyn cm^{-2})
7.5	12009	0.40	1.00	−4.13	6.69	16.98	1.00	−4.13	6.69	16.98
7.5	14013	0.44	0.85	−4.59	6.62	16.51	0.99	−4.56	6.63	16.54
7.5	15886	0.49	0.78	−5.22	6.51	15.88	0.91	−5.14	6.53	15.95
7.5	17920	0.59	0.82	−6.58	6.24	14.50	0.95	−6.40	6.28	14.68
7.5	19900	0.79	0.93	−9.24	5.73	11.84	1.09	−8.78	5.82	12.30
7.5	21946	0.94	0.80	−11.06	5.42	10.02	0.94	−10.83	5.46	10.25
7.5	23757	1.02	0.68	−12.07	5.24	9.01	0.80	−11.62	5.33	9.45
8.0	11978	0.38	1.00	−5.23	6.58	16.86	1.00	−5.23	6.58	16.86
8.0	14031	0.42	1.00	−5.56	6.56	16.52	1.00	−5.56	6.56	16.52
8.0	15974	0.46	0.74	−6.09	6.48	15.99	0.86	−6.05	6.49	16.04
8.0	17952	0.52	0.74	−6.97	6.31	15.11	0.86	−6.86	6.33	15.22
8.0	20012	0.66	0.84	−8.71	5.98	13.37	0.98	−8.45	6.04	13.63
8.0	21959	0.82	1.08	−10.82	5.59	11.26	1.27	−10.37	5.67	11.71
8.0	24014	0.91	0.79	−11.87	5.42	10.21	0.93	−11.65	5.46	10.43
8.0	25963	0.97	0.71	−12.61	5.30	9.46	0.83	−12.27	5.36	9.81
8.5	11996	0.36	1.00	−6.40	6.45	16.68	1.00	−6.40	6.45	16.68
8.5	14012	0.40	1.00	−6.66	6.46	16.42	1.00	−6.66	6.46	16.42
8.5	15957	0.43	1.00	−6.99	6.43	16.09	1.00	−6.99	6.43	16.09
8.5	17956	0.48	0.66	−7.65	6.32	15.43	0.77	−7.57	6.34	15.51
8.5	19924	0.56	0.74	−8.64	6.14	14.44	0.86	−8.51	6.16	14.57
8.5	21962	0.70	0.78	−10.56	5.78	12.52	0.92	−10.26	5.83	12.81
8.5	24004	0.81	1.13	−11.90	5.54	11.17	1.33	−11.58	5.60	11.50
8.5	25938	0.87	0.83	−12.55	5.44	10.53	0.97	−12.38	5.47	10.69
8.5	27946	0.94	0.70	−13.27	5.33	9.81	0.82	−12.97	5.38	10.10
9.0	12077	0.35	1.00	−7.68	6.28	16.40	1.00	−7.68	6.28	16.40
9.0	14059	0.38	1.00	−7.84	6.34	16.24	1.00	−7.84	6.34	16.24
9.0	15930	0.41	1.00	−8.07	6.33	16.01	1.00	−8.07	6.33	16.01
9.0	17885	0.45	0.65	−8.48	6.28	15.60	0.76	−8.45	6.29	15.63
9.0	19922	0.50	0.61	−9.20	6.16	14.87	0.71	−9.11	6.18	14.96
9.0	21942	0.59	0.74	−10.32	5.97	13.76	0.86	−10.13	6.01	13.94
9.0	24076	0.72	0.81	−12.01	5.66	12.07	0.94	−11.72	5.71	12.36
9.0	26099	0.79	1.13	−12.81	5.53	11.27	1.32	−12.58	5.57	11.50
9.0	28181	0.85	0.79	−13.41	5.43	10.66	0.93	−13.25	5.46	10.83
9.0	29952	0.89	0.74	−13.80	5.38	10.27	0.87	−13.58	5.41	10.50
9.0	31452	0.92	0.72	−14.18	5.32	9.89	0.84	−13.89	5.37	10.18

Table B.10: Same as Tab. B.7 but for MLT calibration of open bottom 3D DBA models with $\log \mathrm{H/He} = -4$.

$\log g$	$T_{\rm eff}$ (K)	3D $s_{\rm env}$ (10^9 erg g^{-1} K^{-1})	ML2/$\alpha_{\rm S}$	$\log(M_{\rm CVZ}/M_{\rm tot})_{\rm S}$	$(\log T_{\rm b})_{\rm S}$ (K)	$(\log P_{\rm b})_{\rm S}$ (dyn cm^{-2})	ML2/$\alpha_{\rm f}$	$\log(M_{\rm CVZ}/M_{\rm tot})_{\rm f}$	$(\log T_{\rm b})_{\rm f}$ (K)	$(\log P_{\rm b})_{\rm f}$ (dyn cm^{-2})
7.5	11983	0.40	1.00	−4.21	6.67	16.89	1.00	−4.21	6.67	16.89
7.5	13985	0.44	1.00	−4.61	6.62	16.48	1.00	−4.61	6.62	16.48
7.5	15973	0.49	0.85	−5.27	6.50	15.83	0.99	−5.21	6.51	15.88
7.5	17979	0.62	0.68	−7.01	6.16	14.08	0.79	−6.73	6.22	14.36
7.5	19932	0.82	0.86	−9.67	5.65	11.41	1.00	−9.11	5.75	11.97
7.5	22021	0.95	0.76	−11.16	5.40	9.92	0.89	−10.92	5.44	10.16
7.5	23465	1.01	0.68	−11.92	5.27	9.15	0.80	−11.53	5.35	9.55
8.0	12008	0.39	1.00	−5.30	6.57	16.78	1.00	−5.30	6.57	16.78
8.0	13999	0.42	1.00	−5.60	6.55	16.48	1.00	−5.60	6.55	16.48
8.0	15994	0.46	0.80	−6.11	6.47	15.97	0.93	−6.08	6.48	16.00
8.0	18052	0.54	0.63	−7.22	6.26	14.86	0.73	−7.08	6.29	15.00
8.0	19991	0.68	0.74	−8.98	5.92	13.10	0.86	−8.66	5.99	13.41
8.0	21981	0.83	1.05	−10.98	5.56	11.10	1.22	−10.50	5.65	11.57
8.0	23953	0.91	0.78	−11.88	5.42	10.20	0.91	−11.65	5.46	10.43
8.0	25961	0.97	0.71	−12.61	5.30	9.47	0.83	−12.27	5.36	9.81
8.5	12027	0.37	1.00	−6.45	6.45	16.63	1.00	−6.45	6.45	16.63
8.5	13981	0.40	1.00	−6.70	6.45	16.38	1.00	−6.70	6.45	16.38
8.5	15982	0.43	1.00	−7.04	6.42	16.04	1.00	−7.04	6.42	16.04
8.5	17951	0.49	0.57	−7.76	6.29	15.32	0.66	−7.67	6.31	15.41
8.5	19972	0.57	0.68	−8.81	6.11	14.27	0.79	−8.63	6.14	14.45
8.5	21956	0.72	0.73	−10.73	5.74	12.35	0.86	−10.39	5.81	12.68
8.5	23980	0.82	1.10	−11.95	5.53	11.13	1.28	−11.65	5.59	11.43
8.5	26006	0.88	0.82	−12.58	5.44	10.50	0.96	−12.41	5.46	10.67
8.5	27829	0.94	0.69	−13.26	5.33	9.82	0.80	−12.98	5.38	10.10
9.0	12055	0.35	1.00	−7.74	6.27	16.33	1.00	−7.74	6.27	16.33
9.0	14023	0.38	1.00	−7.88	6.33	16.20	1.00	−7.88	6.33	16.20
9.0	16020	0.41	1.00	−8.13	6.32	15.94	1.00	−8.13	6.32	15.94
9.0	17972	0.45	0.53	−8.57	6.27	15.50	0.62	−8.54	6.27	15.54
9.0	19968	0.51	0.56	−9.29	6.14	14.78	0.65	−9.20	6.16	14.87
9.0	21957	0.60	0.68	−10.45	5.94	13.62	0.79	−10.27	5.98	13.81
9.0	23971	0.72	0.77	−12.00	5.66	12.08	0.91	−11.72	5.71	12.36
9.0	26018	0.79	1.11	−12.80	5.53	11.27	1.29	−12.57	5.57	11.50
9.0	27982	0.84	0.80	−13.37	5.44	10.70	0.93	−13.23	5.46	10.85
9.0	29948	0.89	0.74	−13.81	5.38	10.27	0.87	−13.58	5.41	10.50
9.0	31360	0.92	0.71	−14.18	5.32	9.89	0.84	−13.89	5.37	10.18

Table B.11: Same as Tab. B.7 but for MLT calibration of open bottom 3D DBA models with $\log \mathrm{H/He} = -3$.

$\log g$	$T_{\rm eff}$ (K)	3D $s_{\rm env}$ (10^9 erg g^{-1} K^{-1})	ML2/$\alpha_{\rm S}$	$\log(M_{\rm CVZ}/M_{\rm tot})_{\rm S}$	$(\log T_{\rm b})_{\rm S}$ (K)	$(\log P_{\rm b})_{\rm S}$ (dyn cm^{-2})	ML2/$\alpha_{\rm f}$	$\log(M_{\rm CVZ}/M_{\rm tot})_{\rm f}$	$(\log T_{\rm b})_{\rm f}$ (K)	$(\log P_{\rm b})_{\rm f}$ (dyn cm^{-2})
7.5	11980	0.40	1.00	−4.56	6.59	16.54	1.00	−4.56	6.59	16.54
7.5	13855	0.44	1.00	−4.92	6.55	16.18	1.00	−4.92	6.55	16.18
7.5	15805	0.49	1.00	−5.51	6.45	15.58	1.00	−5.51	6.45	15.58
7.5	18026	0.59	1.18	−6.66	6.23	14.42	1.38	−6.50	6.26	14.59
7.5	20035	0.80	1.08	−9.39	5.70	11.69	1.27	−8.93	5.79	12.15
7.5	22043	0.94	0.81	−11.09	5.41	9.99	0.95	−10.85	5.45	10.23
7.5	23752	1.02	0.69	−12.05	5.25	9.02	0.81	−11.62	5.33	9.45
8.0	12007	0.38	1.00	−5.61	6.51	16.48	1.00	−5.61	6.51	16.48
8.0	13961	0.42	1.00	−5.92	6.48	16.16	1.00	−5.92	6.48	16.16
8.0	16040	0.46	1.00	−6.37	6.42	15.72	1.00	−6.37	6.42	15.72
8.0	17985	0.52	1.00	−7.13	6.28	14.95	1.00	−7.13	6.28	14.95
8.0	20088	0.66	1.02	−8.79	5.96	13.29	1.19	−8.53	6.02	13.55
8.0	22047	0.83	1.17	−10.89	5.57	11.18	1.37	−10.44	5.66	11.63
8.0	24002	0.91	0.79	−11.88	5.42	10.20	0.93	−11.66	5.45	10.42
8.0	25904	0.97	0.71	−12.61	5.30	9.47	0.83	−12.27	5.36	9.81
8.5	12027	0.37	1.00	−6.74	6.41	16.34	1.00	−6.74	6.41	16.34
8.5	13985	0.40	1.00	−6.96	6.40	16.11	1.00	−6.96	6.40	16.11
8.5	15988	0.43	1.00	−7.28	6.37	15.80	1.00	−7.28	6.37	15.80
8.5	18029	0.48	1.00	−7.80	6.29	15.28	1.00	−7.80	6.29	15.28
8.5	20043	0.56	1.02	−8.71	6.12	14.37	1.19	−8.57	6.15	14.51
8.5	22050	0.71	0.88	−10.63	5.77	12.45	1.03	−10.36	5.81	12.72
8.5	24011	0.81	1.18	−11.90	5.54	11.18	1.38	−11.61	5.59	11.47
8.5	25884	0.87	0.83	−12.56	5.44	10.52	0.97	−12.38	5.47	10.69
8.5	27602	0.94	0.67	−13.26	5.33	9.81	0.79	−12.97	5.38	10.10
9.0	11994	0.35	1.00	−8.06	6.22	16.02	1.00	−8.06	6.22	16.02
9.0	13967	0.38	1.00	−8.14	6.27	15.94	1.00	−8.14	6.27	15.94
9.0	15970	0.41	1.00	−8.32	6.28	15.75	1.00	−8.32	6.28	15.75
9.0	18038	0.45	1.00	−8.65	6.25	15.43	1.00	−8.65	6.25	15.43
9.0	20045	0.50	0.98	−9.24	6.15	14.83	1.15	−9.18	6.17	14.90
9.0	22057	0.60	0.90	−10.40	5.95	13.68	1.05	−10.23	5.99	13.84
9.0	24026	0.72	0.86	−11.97	5.67	12.11	1.01	−11.70	5.72	12.38
9.0	25997	0.79	1.15	−12.79	5.53	11.29	1.35	−12.57	5.57	11.51
9.0	28015	0.85	0.78	−13.42	5.43	10.65	0.91	−13.25	5.46	10.82
9.0	29929	0.89	0.73	−13.85	5.37	10.23	0.85	−13.62	5.41	10.46
9.0	31340	0.92	0.70	−14.23	5.31	9.84	0.82	−13.93	5.36	10.15

Table B.12: Same as Tab. B.7 but for MLT calibration of open bottom 3D DBA models with $\log \mathrm{H/He} = -2$.

$\log g$	$T_{\rm eff}$ (K)	3D $s_{\rm env}$ (10^9 erg g^{-1} K^{-1})	ML2/$\alpha_{\rm S}$	$\log(M_{\rm CVZ}/M_{\rm tot})_{\rm S}$	$(\log T_{\rm b})_{\rm S}$ (K)	$(\log P_{\rm b})_{\rm S}$ (dyn cm^{-2})	ML2/$\alpha_{\rm f}$	$\log(M_{\rm CVZ}/M_{\rm tot})_{\rm f}$	$(\log T_{\rm b})_{\rm f}$ (K)	$(\log P_{\rm b})_{\rm f}$ (dyn cm^{-2})
7.5	11977	0.45	1.00	−5.24	6.44	15.85	1.00	−5.24	6.44	15.85
7.5	13995	0.49	1.00	−5.84	6.35	15.24	1.00	−5.84	6.35	15.24
7.5	16063	0.56	1.00	−6.97	6.15	14.11	1.00	−6.97	6.15	14.11
7.5	17963	0.68	1.00	−8.78	5.80	12.30	1.00	−8.78	5.80	12.30
7.5	20042	0.88	1.11	−10.38	5.52	10.70	1.30	−10.23	5.55	10.85
7.5	21944	0.98	0.68	−11.49	5.34	9.59	0.80	−11.19	5.39	9.89
7.5	22925	1.02	0.65	−12.00	5.25	9.08	0.76	−11.60	5.33	9.48
8.0	12044	0.43	1.00	−6.26	6.37	15.82	1.00	−6.26	6.37	15.82
8.0	13953	0.46	1.00	−6.63	6.33	15.45	1.00	−6.63	6.33	15.45
8.0	15983	0.50	1.00	−7.28	6.22	14.80	1.00	−7.28	6.22	14.80
8.0	17961	0.58	1.00	−8.44	6.01	13.64	1.00	−8.44	6.01	13.64
8.0	19903	0.74	1.11	−9.87	5.75	12.21	1.29	−9.50	5.82	12.58
8.0	22026	0.88	0.81	−11.55	5.46	10.53	0.94	−11.40	5.48	10.67
8.0	24006	0.94	0.69	−12.21	5.36	9.86	0.81	−11.96	5.40	10.12
8.0	25333	0.98	0.68	−12.64	5.29	9.43	0.80	−12.30	5.35	9.78
8.5	12013	0.41	1.00	−7.34	6.28	15.74	1.00	−7.34	6.28	15.74
8.5	14013	0.44	1.00	−7.57	6.28	15.51	1.00	−7.57	6.28	15.51
8.5	15994	0.47	1.00	−8.00	6.22	15.08	1.00	−8.00	6.22	15.08
8.5	17996	0.52	1.00	−8.70	6.10	14.37	1.00	−8.70	6.10	14.37
8.5	19962	0.63	1.00	−9.84	5.90	13.24	1.00	−9.84	5.90	13.24
8.5	22044	0.80	0.93	−11.73	5.56	11.35	1.09	−11.28	5.64	11.80
8.5	24025	0.86	0.81	−12.38	5.46	10.70	0.95	−12.23	5.48	10.84
8.5	25969	0.90	0.73	−12.83	5.39	10.25	0.86	−12.63	5.43	10.45
8.5	27179	0.94	0.66	−13.30	5.32	9.78	0.77	−13.01	5.37	10.07
9.0	12025	0.39	1.00	−8.53	6.15	15.54	1.00	−8.53	6.15	15.54
9.0	13986	0.42	1.00	−8.63	6.19	15.44	1.00	−8.63	6.19	15.44
9.0	16001	0.45	1.00	−8.89	6.18	15.19	1.00	−8.89	6.18	15.19
9.0	17981	0.48	1.00	−9.35	6.11	14.73	1.00	−9.35	6.11	14.73
9.0	20038	0.55	1.00	−10.07	6.00	14.00	1.00	−10.07	6.00	14.00
9.0	21923	0.68	0.79	−11.51	5.73	12.56	0.93	−11.23	5.79	12.85
9.0	24031	0.78	0.94	−12.65	5.54	11.43	1.10	−12.31	5.60	11.77
9.0	26031	0.83	0.84	−13.18	5.46	10.90	0.98	−13.05	5.48	11.02
9.0	27980	0.87	0.71	−13.61	5.40	10.47	0.83	−13.43	5.43	10.65
9.0	29843	0.91	0.69	−14.00	5.34	10.07	0.81	−13.75	5.38	10.33
9.0	31011	0.93	0.69	−14.28	5.30	9.79	0.80	−14.00	5.35	10.08

Table B.13: MLT calibration for closed bottom 3D DB models, where $\langle 3\mathrm{D}\rangle\ T_{\rm b,\,S}$ is the $\langle 3\mathrm{D}\rangle$ temperature at the bottom of the Schwarzschild boundary, $\langle 3\mathrm{D}\rangle\ P_{\rm b,\,S}$ is the $\langle 3\mathrm{D}\rangle$ pressure at the bottom of the Schwarzschild boundary, ML2/$\alpha_{\rm S}$ is the calibrated ML2/α value for the Schwarzschild boundary and $\log(M_{\rm CVZ}/M_{\rm tot})_{\rm S}$ is the $\log(M_{\rm CVZ}/M_{\rm tot})$ for the Schwarzschild boundary. The same parameters are also given for the flux boundary and are denoted with a subscript 'f'.

$\log g$	$T_{\rm eff}$	$\langle 3\mathrm{D}\rangle\ T_{\rm b,\,S}$	$\langle 3\mathrm{D}\rangle\ P_{\rm b,\,S}$	ML2/$\alpha_{\rm S}$	$\log(M_{\rm CVZ}/M_{\rm tot})_{\rm S}$	$\langle 3\mathrm{D}\rangle\ T_{\rm b,\,f}$	$\langle 3\mathrm{D}\rangle\ P_{\rm b,\,f}$	ML2/$\alpha_{\rm f}$	$\log(M_{\rm CVZ}/M_{\rm tot})_{\rm f}$
7.5	26497	4.98	7.85	0.76	−13.20	5.10	8.28	0.85	−12.76
7.5	27993	4.90	7.45	0.69	−13.63	4.95	7.66	0.85	−13.41
7.5	29991	4.87	7.24	0.42	−13.84	4.86	7.19	0.65	−13.82
7.5	32001	4.87	7.15	0.65	−13.91	4.85	7.08	0.65	−13.91
8.0	28107	4.99	8.21	0.65	−13.94	5.14	8.74	0.75	−13.36
8.0	29997	4.94	7.86	0.72	−14.24	5.03	8.24	0.85	−13.84
8.0	31999	4.91	7.62	0.73	−14.47	4.94	7.76	0.89	−14.31
8.0	33999	4.89	7.43	0.65	−14.63	4.87	7.35	0.65	−14.63
8.5	30567	5.03	8.58	0.63	−14.59	5.20	9.14	0.74	−13.96
8.5	32208	5.00	8.32	0.71	−14.80	5.12	8.77	0.81	−14.33
8.5	34020	4.95	8.00	0.75	−15.09	5.02	8.27	0.87	−14.80
9.0	34105	5.05	8.78	0.64	−15.38	5.21	9.28	0.75	−14.81

Table B.14: Same as Tab. B.13 but for MLT calibration of closed bottom 3D DBA models with $\log \mathrm{H/He} = -7$.

$\log g$	$T_{\rm eff}$	$\langle 3D \rangle$ $T_{\rm b,\,S}$	$\langle 3D \rangle$ $P_{\rm b,\,S}$	ML2/$\alpha_{\rm S}$	$\log(M_{\rm CVZ}/M_{\rm tot})_{\rm S}$	$\langle 3D \rangle$ $T_{\rm b,\,f}$	$\langle 3D \rangle$ $P_{\rm b,\,f}$	ML2/$\alpha_{\rm f}$	$\log(M_{\rm CVZ}/M_{\rm tot})_{\rm f}$
7.5	26501	4.98	7.84	0.75	−13.21	5.11	8.29	0.85	−12.75
7.5	27993	4.90	7.46	0.70	−13.63	4.95	7.66	0.85	−13.40
7.5	29993	4.87	7.25	0.57	−13.83	4.87	7.21	0.65	−13.82
7.5	32002	4.87	7.16	0.65	−13.91	4.85	7.06	0.65	−13.91
8.0	28037	4.98	8.18	0.64	−13.97	5.13	8.72	0.75	−13.38
8.0	29963	5.00	8.04	0.80	−14.01	5.12	8.49	0.90	−13.55
8.0	32000	4.91	7.60	0.71	−14.48	4.94	7.73	0.86	−14.35
8.0	33999	4.89	7.43	0.65	−14.63	4.87	7.35	0.65	−14.63
8.5	30514	5.03	8.59	0.63	−14.58	5.21	9.15	0.74	−13.94
8.5	32012	4.99	8.33	0.70	−14.80	5.14	8.83	0.80	−14.26
8.5	33949	4.95	8.00	0.74	−15.09	5.02	8.28	0.87	−14.79
9.0	34021	5.06	8.82	0.65	−15.33	5.21	9.29	0.75	−14.79

Table B.15: Same as Tab. B.13 but for MLT calibration of closed bottom 3D DBA models with $\log \mathrm{H/He} = -5$.

$\log g$	$T_{\rm eff}$	$\langle 3D \rangle$ $T_{\rm b,\,S}$	$\langle 3D \rangle$ $P_{\rm b,\,S}$	ML2/$\alpha_{\rm S}$	$\log(M_{\rm CVZ}/M_{\rm tot})_{\rm S}$	$\langle 3D \rangle$ $T_{\rm b,\,f}$	$\langle 3D \rangle$ $P_{\rm b,\,f}$	ML2/$\alpha_{\rm f}$	$\log(M_{\rm CVZ}/M_{\rm tot})_{\rm f}$
7.5	26522	4.97	7.83	0.75	−13.23	5.10	8.27	0.85	−12.77
7.5	27998	4.90	7.46	0.70	−13.63	4.95	7.66	0.85	−13.41
7.5	29992	4.87	7.25	0.49	−13.84	4.86	7.19	0.65	−13.82
7.5	32002	4.87	7.16	0.65	−13.91	4.85	7.08	0.65	−13.91
8.0	28086	4.98	8.19	0.65	−13.95	5.13	8.73	0.75	−13.38
8.0	29989	4.94	7.87	0.72	−14.24	5.03	8.24	0.85	−13.84
8.0	32002	4.91	7.61	0.71	−14.48	4.94	7.75	0.88	−14.32
8.0	34000	4.89	7.43	0.65	−14.63	4.87	7.35	0.65	−14.63
8.5	30517	5.02	8.59	0.63	−14.58	5.21	9.16	0.74	−13.93
8.5	32015	5.00	8.36	0.71	−14.76	5.14	8.83	0.80	−14.27
8.5	33947	4.95	8.00	0.74	−15.09	5.02	8.29	0.87	−14.78
9.0	33986	5.06	8.82	0.65	−15.33	5.21	9.30	0.75	−14.79

Table B.16: Same as Tab. B.13 but for MLT calibration of closed bottom 3D DBA models with $\log \mathrm{H/He} = -4$.

$\log g$	$T_{\rm eff}$ (K)	$\langle 3D \rangle$ $T_{\rm b,\,S}$ (K)	$\langle 3D \rangle$ $P_{\rm b,\,S}$ (dyn cm^{-2})	ML2/$\alpha_{\rm S}$	$\log(M_{\rm CVZ}/M_{\rm tot})_{\rm S}$	$\langle 3D \rangle$ $T_{\rm b,\,f}$ (K)	$\langle 3D \rangle$ $P_{\rm b,\,f}$ (dyn cm^{-2})	ML2/$\alpha_{\rm f}$	$\log(M_{\rm CVZ}/M_{\rm tot})_{\rm f}$
7.5	26632	4.97	7.81	0.76	−13.24	5.09	8.23	0.86	−12.81
7.5	28004	4.90	7.45	0.69	−13.64	4.94	7.64	0.84	−13.43
7.5	29993	4.87	7.25	0.51	−13.84	4.86	7.19	0.65	−13.82
7.5	32002	4.87	7.15	0.65	−13.91	4.85	7.07	0.65	−13.91
8.0	28092	4.98	8.17	0.64	−13.97	5.12	8.68	0.74	−13.42
8.0	29994	4.94	7.87	0.72	−14.23	5.04	8.25	0.85	−13.82
8.0	32003	4.91	7.60	0.71	−14.48	4.94	7.73	0.86	−14.35
8.0	34000	4.89	7.43	0.65	−14.63	4.87	7.35	0.65	−14.63
8.5	30490	5.03	8.61	0.63	−14.56	5.20	9.15	0.73	−13.95
8.5	32008	5.00	8.35	0.71	−14.77	5.13	8.81	0.80	−14.29
8.5	33963	4.95	8.00	0.75	−15.09	5.01	8.27	0.87	−14.80
9.0	33988	5.06	8.83	0.65	−15.33	5.21	9.30	0.75	−14.79

Table B.17: Same as Tab. B.13 but for MLT calibration of closed bottom 3D DBA models with $\log \mathrm{H/He} = -3$.

$\log g$	$T_{\rm eff}$ (K)	$\langle 3D \rangle$ $T_{\rm b,\,S}$ (K)	$\langle 3D \rangle$ $P_{\rm b,\,S}$ (dyn cm^{-2})	ML2/$\alpha_{\rm S}$	$\log (M_{\rm CVZ}/M_{\rm tot})_{\rm S}$	$\langle 3D \rangle$ $T_{\rm b,\,f}$ (K)	$\langle 3D \rangle$ $P_{\rm b,\,f}$ (dyn cm^{-2})	ML2/$\alpha_{\rm f}$	$\log (M_{\rm CVZ}/M_{\rm tot})_{\rm f}$
7.5	26670	4.95	7.74	0.74	−13.34	5.06	8.15	0.85	−12.91
7.5	28000	4.90	7.44	0.69	−13.65	4.94	7.61	0.83	−13.45
7.5	29999	4.87	7.24	0.54	−13.84	4.85	7.15	0.65	−13.82
7.5	32000	4.87	7.15	0.65	−13.92	4.84	7.05	0.65	−13.92
8.0	28118	4.98	8.14	0.64	−13.99	5.11	8.64	0.74	−13.45
8.0	30001	4.94	7.83	0.71	−14.27	5.02	8.18	0.84	−13.90
8.0	31999	4.90	7.58	0.67	−14.51	4.93	7.68	0.82	−14.40
8.0	33980	4.89	7.43	0.65	−14.63	4.87	7.36	0.65	−14.63
8.5	30364	5.03	8.59	0.62	−14.58	5.20	9.14	0.72	−13.96
8.5	31965	4.99	8.30	0.69	−14.81	5.12	8.77	0.79	−14.31
8.5	34038	4.95	7.99	0.75	−15.10	5.01	8.26	0.88	−14.81
9.0	33917	5.06	8.84	0.65	−15.31	5.21	9.31	0.75	−14.77

Table B.18: Same as Tab. B.13 but for MLT calibration of closed bottom 3D DBA models with $\log \mathrm{H/He} = -2$.

$\log g$	$T_{\rm eff}$ (K)	$\langle 3D \rangle$ $T_{\rm b,\,S}$ (K)	$\langle 3D \rangle$ $P_{\rm b,\,S}$ (dyn cm^{-2})	ML2/$\alpha_{\rm S}$	$\log (M_{\rm CVZ}/M_{\rm tot})_{\rm S}$	$\langle 3D \rangle$ $T_{\rm b,\,f}$ (K)	$\langle 3D \rangle$ $P_{\rm b,\,f}$ (dyn cm^{-2})	ML2/$\alpha_{\rm f}$	$\log (M_{\rm CVZ}/M_{\rm tot})_{\rm f}$
7.5	26471	4.93	7.67	0.71	−13.43	5.02	8.04	0.84	−13.04
7.5	27996	4.89	7.38	0.67	−13.70	4.91	7.50	0.80	−13.57
7.5	29982	4.87	7.22	0.65	−13.84	4.85	7.13	0.65	−13.84
7.5	32009	4.86	7.12	0.65	−13.93	4.84	7.04	0.65	−13.93
8.0	27968	4.96	8.07	0.65	−14.05	5.09	8.54	0.75	−13.56
8.0	30013	4.93	7.77	0.71	−14.32	4.99	8.06	0.86	−14.01
8.0	31998	4.90	7.53	0.61	−14.55	4.91	7.58	0.74	−14.50
8.0	33989	4.88	7.41	0.65	−14.65	4.86	7.33	0.65	−14.65
8.5	30535	5.01	8.45	0.64	−14.69	5.17	8.99	0.75	−14.10
8.5	31852	4.98	8.25	0.70	−14.86	5.10	8.70	0.81	−14.39
8.5	33930	4.94	7.95	0.75	−15.14	5.00	8.20	0.89	−14.87
9.0	33770	5.05	8.78	0.66	−15.36	5.20	9.27	0.76	−14.81

Bibliography

Ali A.W. and Griem H.R., 1965. *Physical Review*, 140(4A):1044–1049.

Ali A.W. and Griem H.R., 1966. *Physical Review*, 144(1):366–366.

Allende Prieto C. et al., 2013. *A&A*, 550:A103.

Althaus L.G. and Benvenuto O.G., 1996. *MNRAS*, 278:981–984.

Althaus L.G. and Benvenuto O.G., 1997. *MNRAS*, 288:L35–L38.

Althaus L.G. et al., 2005. *A&A*, 440:L1–L4.

Althaus L.G. et al., 2010. *A&ARv*, 18:471–566.

Asplund M. et al., 1999. *A&A*, 343:507–518.

Barstow M.A. et al., 1993. *MNRAS*, 264:16.

Battich T., Althaus L.G., and Córsico A.r.H., 2020. *arXiv e-prints*, arXiv:2003.13602.

Beauchamp A., Wesemael F., and Bergeron P., 1997. *ApJS*, 108(2):559–573.

Beauchamp A. et al., 1995. *ApJ Lett.*, 441:L85.

Beauchamp A. et al., 1996. In C.S. Jeffery and U. Heber, editors, *Hydrogen Deficient Stars*, volume 96 of *Astronomical Society of the Pacific Conference Series*, 295.

Beauchamp A. et al., 1999. *ApJ*, 516:887–891.

Bédard A., Bergeron P., and Fontaine G., 2017. *ApJ*, 848:11.

Bellinger E.P. et al., 2020. *MNRAS*, 491(4):4752–4767.

Benvenuto O.G. and Althaus L.G., 1999. *MNRAS*, 303:30–38.

Bergeron P., Ruiz M.T., and Leggett S.K., 1997. *ApJS*, 108(1):339–387.

Bergeron P., Saumon D., and Wesemael F., 1995. *ApJ*, 443:764.

Bergeron P., Wesemael F., and Fontaine G., 1991. *ApJ*, 367:253.

Bergeron P. et al., 1988. *ApJ*, 332:964.

Bergeron P. et al., 1990. *ApJ Lett.*, 351:L21–L24.

Bergeron P. et al., 2011. *ApJ*, 737(1):28.

Bergeron P. et al., 2015. In P. Dufour, P. Bergeron, and G. Fontaine, editors, *19th European Workshop on White Dwarfs*, volume 493 of *Astronomical Society of the Pacific Conference Series*, 33.

Bergeron P. et al., 2019. *ApJ*, 876(1):67.

Bethe H.A., 1939. *Phys. Rev*, 55(5):434–456.

Blöcker T., 2001. *Ap&SS*, 275:1–14.

Bohlin R.C., Gordon K.D., and Tremblay P.E., 2014. *PASP*, 126(942):711.

Böhm K.H., 1968. *Ap&SS*, 2(3):375–383.

Böhm-Vitense E., 1958. *Z. Astrophys.*, 46:108.

Böhm-Vitense E., 1989. *Introduction to stellar astrophysics. Vol 2: Stellar atmospheres*. Press Syndicate of the University of Cambridge.

Bohr N., 1913. *Philosophical Magazine*, 26:1–25.

Boltzmann L., 1884. *Annalen der Physik*, 258(6):291–294.

Brummell N.H., Clune T.L., and Toomre J., 2002. *ApJ*, 570:825–854.

Caffau E. et al., 2007. *A&A*, 470(2):699–708.

Camisassa M.E. et al., 2020. *arXiv e-prints*, arXiv:2008.03028.

Canuto V.M., 2007. In F. Kupka, I. Roxburgh, and K.L. Chan, editors, *Convection in Astrophysics*, volume 239 of *IAU Symposium*, 3–18.

Canuto V.M., Goldman I., and Mazzitelli I., 1996. *ApJ*, 473:550.

Canuto V.M. and Mazzitelli I., 1991. *ApJ*, 370:295–311.

Canuto V.M. and Mazzitelli I., 1992. *ApJ*, 389:724–730.

Carroll B.W. and Ostlie D.A., 2007. *An Introduction to Modern Astrophysics*. Addison-Wesley.

Cattaneo F. et al., 1991. *ApJ*, 370:282–294.

Chabrier G., 2003. *PASP*, 115(809):763–795.

Chandrasekhar S., 1931. *ApJ*, 74:81.

Christy R.F., 1966. *ApJ*, 144:108.

Córsico A.H. et al., 2009. In *Journal of Physics Conference Series*, volume 172 of *Journal of Physics Conference Series*, 012075.

Córsico A.H. et al., 2019. *A&ARv*, 27(1):7.

Cukanovaite E. et al., 2018. *MNRAS*, 481(2):1522–1537.

Cukanovaite E. et al., 2019. *MNRAS*, 490(1):1010–1025.

Cummings J.D. et al., 2018. *ApJ*, 866(1):21.

Cunningham T. et al., 2019. *MNRAS*, 488(2):2503–2522.

Dalton G. et al., 2012. In *Ground-based and Airborne Instrumentation for Astronomy*, volume 8446 of *Society of Photo-Optical Instrumentation Engineers (SPIE) Conference Series*, 84460P.

Dalton G. et al., 2016. In *Ground-based and Airborne Instrumentation for Astronomy*, volume 9908 of *Society of Photo-Optical Instrumentation Engineers (SPIE) Conference Series*, 99081G.

de Jong R.S. et al., 2016. In *Ground-based and Airborne Instrumentation for Astronomy*, volume 9908 of *Society of Photo-Optical Instrumentation Engineers (SPIE) Conference Series*, 99081O.

de Vaucouleurs G., 1978. *ApJ*, 223:351–363.

Deridder G. and van Rensbergen W., 1976. *A&AS*, 23:147.

DESI Collaboration et al., 2016a. *arXiv e-prints*, arXiv:1611.00036.

DESI Collaboration et al., 2016b. *arXiv e-prints*, arXiv:1611.00037.

Dreizler S. and Werner K., 1993. *A&A*, 278:199–208.

Dufour P., Bergeron P., and Fontaine G., 2005. *ApJ*, 627(1):404–417.

Dufour P. et al., 2012. *ApJ*, 749:6.

Dupuis J. et al., 1992. *ApJS*, 82:505.

Eisenstein D.J. et al., 2006. *ApJS*, 132(2):676–691.

Eldridge J.J., Mattila S., and Smartt S.J., 2007. *MNRAS*, 376(1):L52–L56.

Fantin N.J. et al., 2019. *ApJ*, 887(2):148.

Farihi J., Gänsicke B.T., and Koester D., 2013. *Science*, 342:218–220.

Farihi J. et al., 2010. *MNRAS*, 404(4):2123–2135.

Fermi E., 1926. *Zeitschrift für Physik*, 36(11-12):902–912.

Fontaine G. and Brassard P., 2008. *PASP*, 120(872):1043.

Fontaine G., Brassard P., and Bergeron P., 2001. *PASP*, 113(782):409–435.

Fontaine G. and van Horn H.M., 1976. *ApJS*, 31:467–487.

Fontaine G. and Wesemael F., 1987. In A.G.D. Philip, D.S. Hayes, and J.W. Liebert, editors, *IAU Colloq. 95: Second Conference on Faint Blue Stars*, 319–326.

Fontaine G. et al., 2015. In P. Dufour, P. Bergeron, and G. Fontaine, editors, *19th European Workshop on White Dwarfs*, volume 493 of *Astronomical Society of the Pacific Conference Series*, 113.

Fowler R.H., 1926. *MNRAS*, 87:114–122.

Freytag B., 2013. *Memorie della Societa Astronomica Italiana Supplementi*, 24:26.

Freytag B., 2017. *Memorie della Societa Astronomica Italiana*, 88:12.

Freytag B., Ludwig H.G., and Steffen M., 1996. *A&A*, 313:497–516.

Freytag B., Steffen M., and Dorch B., 2002. *Astronomische Nachrichten*, 323:213–219.

Freytag B. et al., 2012. *Journal of Computational Physics*, 231(3):919–959.

Gaia Collaboration et al., 2018. *A&A*, 616:A1.

Gänsicke B.T. et al., 2019. *New Astron. Rev.*, 576(7785):61–64.

García-Berro E. and Oswalt T.D., 2016. 72:1–22.

Genest-Beaulieu C. and Bergeron P., 2019a. *ApJ*, 871(2):169.

Genest-Beaulieu C. and Bergeron P., 2019b. *ApJ*, 882(2):106.

Gentile Fusillo N.P. et al., 2017. *MNRAS*, 468(1):971–980.

Gentile Fusillo N.P. et al., 2019a. *MNRAS*, 482(4):4570–4591.

Gentile Fusillo N.P. et al., 2019b. *VizieR Online Data Catalog*, 748.

Gentile Fusillo N.P. et al., 2020. *MNRAS*, 491(3):3613–3623.

Giammichele N. et al., 2018. *New Astron. Rev.*, 554(7690):73–76.

Gianninas A., Bergeron P., and Ruiz M.T., 2011. *ApJ*, 743(2):138.

Gianninas A. et al., 2010. *ApJ*, 720(1):581–602.

Girven J. et al., 2012. *ApJ*, 749(2):154.

Grimm-Strele H. et al., 2015. *New Astronomy*, 34:278–293.

Hansen B.M.S., 1999. *ApJ*, 520(2):680–695.

Hayashi C., 1966. *ARA&A*, 4:171.

Heger A. et al., 2003. *ApJ*, 591(1):288–300.

Heisenberg W., 1927. *Zeitschrift fur Physik*, 43(3-4):172–198.

Hermes J.J. et al., 2017. *ApJ*, 835(2):277.

Herwig F., 2001. *Stellar Evolution and Nucleosynthesis of Post-AGB Stars*, volume 265 of *Astrophysics and Space Science Library*, 249.

Höfner S. and Olofsson H., 2018. *A&ARv*, 26(1):1.

Holberg J.B., Bergeron P., and Gianninas A., 2008. *AJ*, 135(4):1239–1248.

Hollands M.A. et al., 2018. *MNRAS*, 480(3):3942–3961.

Hummer D.G. and Mihalas D., 1988. *ApJ*, 331:794.

Ibeling D. and Heger A., 2013. *ApJ Lett.*, 765(2):L43.

Iben I. J. and Renzini A., 1983. *ARA&A*, 21:271–342.

Iben Icko J., 1991. *ApJS*, 76:55.

Iben Icko J. and Laughlin G., 1989. *ApJ*, 341:312.

Isern J. et al., 1997. *ApJ*, 485(1):308–312.

John T.L., 1994. *MNRAS*, 269:871.

Joyce S.R.G. et al., 2018. *MNRAS*, 479(2):1612–1626.

Jura M., 2003. *ApJ Lett.*, 584(2):L91–L94.

Kalirai J.S., 2012. *New Astron. Rev.*, 486(7401):90–92.

Kepler S.O. et al., 2015. *MNRAS*, 446:4078–4087.

Kepler S.O. et al., 2019. *MNRAS*, 486(2):2169–2183.

Klein B. et al., 2020. *arXiv e-prints*, arXiv:2006.07483.

Kleinman S.J. et al., 2004. *ApJ*, 607(1):426–444.

Kleinman S.J. et al., 2013. *ApJS*, 204:5.

Koester D., 2009. *A&A*, 498:517–525.

Koester D., 2010. *Memorie della Societa Astronomica Italiana*, 81:921–931.

Koester D. and Chanmugam G., 1990. *Reports on Progress in Physics*, 53(7):837–915.

Koester D. and Kepler S.O., 2015. *A&A*, 583:A86.

Koester D., Wegner G., and Kilkenny D., 1990. *ApJ*, 350:329.

Kollmeier J.A. et al., 2017. *arXiv e-prints*, arXiv:1711.03234.

Kritcher A.L. et al., 2020. *New Astron. Rev.*, 584(7819):51–54.

Kupka F. and Muthsam H.J., 2017. *Living Reviews in Computational Astrophysics*, 3:1.

Kupka F., Zaussinger F., and Montgomery M.H., 2018. *MNRAS*, 474:4660–4671.

Lamb D.Q. and van Horn H.M., 1975. *ApJ*, 200:306–323.

Lambert D.L., 1981. *The chemical composition of red giants - The first dredge-up phase*, volume 88 of *Astrophysics and Space Science Library*, 115–134.

Liebert J., Bergeron P., and Holberg J.B., 2005. *ApJS*, 156(1):47–68.

Liebert J., Dahn C.C., and Monet D.G., 1988. *ApJ*, 332:891.

Lindegren L. et al., 2018. *A&A*, 616:A2.

Ludwig H.G., Freytag B., and Steffen M., 1999. *A&A*, 346:111–124.

Ludwig H.G., Jordan S., and Steffen M., 1993. In M.A. Barstow, editor, *NATO Advanced Science Institutes (ASI) Series C*, volume 403 of *NATO Advanced Science Institutes (ASI) Series C*, 471.

Ludwig H.G., Jordan S., and Steffen M., 1994. *A&A*, 284:105–117.

Ludwig H.G. and Steffen M., 2008. In N.C. Santos, L. Pasquini, A.C.M. Correia, and M. Romaniello, editors, *Proceedings of Precision Spectroscopy in Astrophysics*, ESO Astrophysics Symposia, 133.

MacDonald J. and Vennes S., 1991. *ApJ*, 371:719–738.

Madej J., 1994. *A&A*, 286:515–522.

Magic Z., Weiss A., and Asplund M., 2015. *A&A*, 573:A89.

Magic Z. et al., 2013. *A&A*, 557:A26.

Maíz Apellániz J. and Weiler M., 2018. *A&A*, 619:A180.

Manser C.J., 2018. *The gaseous component to planetary debris discs at white dwarfs.* PhD thesis, University of Warwick.

Manser C.J. et al., 2019. *Science*, 364(6435):66–69.

Martin W.C., 1960. *Journal of the Optical Society of America (1917-1983)*, 50(2):174.

Martin W.C., 1987. *Phys. Rev. A*, 36(8):3575–3589.

McGraw J.T., 1977. *The ZZ Ceti Stars - a New Class of Pulsating White Dwarfs.* Ph.D. thesis, Texas Univ., Austin.

Mestel L., 1952. *MNRAS*, 112:583.

Metcalfe T.S. et al., 2005. *A&A*, 435(2):649–655.

Miller Bertolami M.M. and Althaus L.G., 2006. *A&A*, 454(3):845–854.

Montgomery M.H. and Kupka F., 2004. *MNRAS*, 350:267–276.

Montgomery M.H. et al., 2015. *High Energy Density Physics*, 17:168–174.

Mosumgaard J.R. et al., 2018. *MNRAS*, 478:5650–5659.

Narayan G. et al., 2019. *ApJS*, 241(2):20.

Nordlund A., 1982. *A&A*, 107:1–10.

Oswalt T.D. and Barstow M.A., 2013. *Planets, Stars and Stellar Systems Vol. 4*.

Paquette C. et al., 1986a. *ApJS*, 61:177–195.

Paquette C. et al., 1986b. *ApJS*, 61:197–217.

Pauli W., 1925. *Zeitschrift für Physik*, 31(1):765–783.

Pelletier C. et al., 1986. *ApJ*, 307:242.

Provencal J.L. et al., 2003. In *NATO ASIB Proc. 105: White Dwarfs*, volume 105, 235.

Pshirkov M.S. et al., 2020. *arXiv e-prints*, arXiv:2007.06514.

Raddi R. et al., 2015. *MNRAS*, 450:2083–2093.

Reader J. et al., 1980. *Wavelengths and transition probabilities for atoms and atomic ions: Part 1. Wavelengths, part 2. Transition probabilities.*

Reindl N. et al., 2014a. *A&A*, 572:A117.

Reindl N. et al., 2014b. *A&A*, 566:A116.

Richer H.B. et al., 2019. *ApJ*, 880(2):75.

Rolland B., Bergeron P., and Fontaine G., 2018. *ApJ*, 857(1):56.

Salaris M. and Cassisi S., 2015. *A&A*, 577:A60.

Saumon D., Chabrier G., and van Horn H.M., 1995. *ApJS*, 99:713.

Saumon D. et al., 1994. *ApJ*, 424:333.

Sbordone L. et al., 2010. *A&A*, 522:A26.

Schatzman E., 1948. *New Astron. Rev.*, 161(4080):61–62.

Schönberg M. and Chandrasekhar S., 1942. *ApJ*, 96:161.

Schwarzschild M. and Härm R., 1965. *ApJ*, 142:855.

Shipman H.L. et al., 2002. In *American Astronomical Society Meeting Abstracts #200*, volume 200 of *American Astronomical Society Meeting Abstracts*, 72.06.

Sion E.M. et al., 1983. *ApJ*, 269:253–257.

Sonoi T. et al., 2019. *A&A*, 621:A84.

Stancil P.C., 1994. *ApJ*, 430:360.

Steffen M., 1993. In W.W. Weiss and A. Baglin, editors, *IAU Colloq. 137: Inside the Stars*, volume 40 of *Astronomical Society of the Pacific Conference Series*, 300.

Steffen M., Ludwig H.G., and Freytag B., 1995. *A&A*, 300:473.

Stein R.F. and Nordlund A., 1989. *ApJ Lett.*, 342:L95–L98.

Strittmatter P.A. and Wickramasinghe D.T., 1971. *MNRAS*, 152:47.

Suleimanov V. et al., 2007. In R. Napiwotzki and M.R. Burleigh, editors, *15th European Workshop on White Dwarfs*, volume 372 of *Astronomical Society of the Pacific Conference Series*, 217.

Taam R.E., 1980. *ApJ*, 237:142–147.

Tassoul M., Fontaine G., and Winget D.E., 1990. *ApJS*, 72:335.

Trampedach R. et al., 2014. *MNRAS*, 445:4366–4384.

Tremblay P.E. and Bergeron P., 2008. *ApJ*, 672:1144-1152.

Tremblay P.E. and Bergeron P., 2009. *ApJ*, 696(2):1755–1770.

Tremblay P.E. et al., 2010. *ApJ*, 712(2):1345–1358.

Tremblay P.E. et al., 2011. *A&A*, 531:L19.

Tremblay P.E. et al., 2013a. *A&A*, 557:A7.

Tremblay P.E. et al., 2013b. *A&A*, 552:A13.

Tremblay P.E. et al., 2013c. *A&A*, 559:A104.

Tremblay P.E. et al., 2014. *ApJ*, 791(2):92.

Tremblay P.E. et al., 2015a. *ApJ*, 809:148.

Tremblay P.E. et al., 2015b. *ApJ*, 799(2):142.

Tremblay P.E. et al., 2017. *MNRAS*, 465:2849–2861.

Tremblay P.E. et al., 2019a. *New Astron. Rev.*, 565(7738):202–205.

Tremblay P.E. et al., 2019b. *MNRAS*, 482(4):5222–5232.

Tremblay P.E. et al., 2020. *MNRAS*.

Unsold A., 1955. *Physik der Sternatmospharen, MIT besonderer Berucksichtigung der Sonne*. Berlin.

Van Grootel V. et al., 2012. *A&A*, 539:A87.

Van Grootel V. et al., 2017. In P.E. Tremblay, B. Gaensicke, and T. Marsh, editors, *20th European White Dwarf Workshop*, volume 509 of *Astronomical Society of the Pacific Conference Series*, 321.

van Horn H.M., 1968. *ApJ*, 151:227.

van Horn H.M., 1971. In W.J. Luyten, editor, *White Dwarfs*, volume 42 of *IAU Symposium*, 97.

Vanderburg A. et al., 2015. *New Astron. Rev.*, 526(7574):546–549.

Veras D., 2016. *Royal Society Open Science*, 3:150571.

Vögler A., Bruls J.H.M.J., and Schüssler M., 2004. *A&A*, 421:741–754.

Voss B. et al., 2007. *A&A*, 470:1079–1088.

Wares G.W., 1944. *ApJ*, 100:158.

Wedemeyer S. et al., 2004. *A&A*, 414:1121–1137.

Werner K. and Herwig F., 2006. *PASP*, 118(840):183–204.

Wesemael F., Green R.F., and Liebert J., 1985. *ApJS*, 58:379–411.

Winget D.E., van Horn H.M., and Hansen C.J., 1981. *ApJ Lett.*, 245:L33–L36.

Winget D.E. et al., 1982. *ApJ Lett.*, 262:L11–L15.

Winget D.E. et al., 1987. *ApJ Lett.*, 315:L77.

Winget D.E. et al., 2004. *ApJ Lett.*, 602(2):L109–L112.

Woosley S.E. and Heger A., 2015. *ApJ*, 810(1):34.

Zahn J.P., 1991. *A&A*, 252:179–188.

Zuckerman B. and Becklin E.E., 1987. *New Astron. Rev.*, 330(6144):138–140.

Zuckerman B. et al., 2007. *ApJ*, 671(1):872–877.

Zuckerman B. et al., 2010. *ApJ*, 722(1):725–736.